Sound propagation in wedge shaped ocean channels

Wang, Liansheng

Award date:
1989

Awarding institution:
University of Bath

SOUND PROPAGATION IN WEDGE SHAPED OCEAN CHANNELS

Submitted by

Liansheng Wang

for the degree of Ph. D. of the

University of Bath

1989

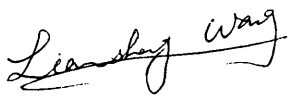

ProQuest LLC
789 East Eisenhower Parkway
P.O. Box 1346
Ann Arbor, MI 48106-1346

ACKNOWLEDGMENTS

I would like to thank Professor H. O. Berktay for his helpful suggestions, and Dr. N. G. Pace for his indispensable advice and supervision.

I am very grateful to Harbin Shipbuilding Engineering Institute, which provides me the financial support to study in U. K.

ABSTRACT

The work in this thesis is to study the field generated by a harmonic point source in a wedge shaped ocean channel. Uniformly asymptotic approximations of Buckingham's theoretical models for perfect wedge and penetrable wedge are obtained by stationary phase method. The approximate representations can be used to predict the fields in perfect and penetrable wedges rapidly with a satisfactory accuracy compared with numerical evaluation of the exact solutions. Theoretical results are presented for the fields in perfect wedges and penetrable wedges. An experiment is carried out in a laboratory tank to measure in 3-dimensions the sound pressure fields for a source far away from the apex both in the water and in the bottom in wedge shaped water channels with a sand bottom. Comparisons are made between the experimental results and the theoretical results.

CONTENTS

LIST OF SYMBOLS

A	Constant
a	Non-dimensional function of range and cross range in perfect wedge, $a = rr'/R_0^2$
$\tilde{a}$	Non-dimensional function of range and cross range in penetrable wedge, $\tilde{a} = \tilde{r}\tilde{r}'/\tilde{R}_0^2$
a_0	Constant
$\mathrm{Ai}(\xi)$	Airy function
B_s	Bandwidth of signal transmitting and receiving system
b_1	Sound velocity for shear wave in bottom
C	Function in characteristic equation for shallow water propagation
$C(\xi)$	Airy function
$C_a(\xi)$, $C_b(\xi)$	Incomplete Airy functions
c_0	Sound velocity in water
c_1	Sound velocity in bottom
d	Difference between the distances from the source **S** and the virtual image **I** to the receiver **R**
d_c	Difference between the distances from the source **S** and the critical image to the receiver **R**
d_{s1} , d_{s2}	Distances from the virtual images corresponding to stationary points to receiver in $z = 0$ plane
d_1	Distance from the source **S** to the receiver **R**
d_2	Distance from the virtual image **I** to the receiver **R**
$E\{\xi\}$	Maximum integer of ξ
f	Frequency

$f(\sigma), \tilde{f}(\sigma)$	Analytic functions
$G(s)$	General function
$G(0)$	Zero order approximation of $G(s)$
g	Ratio of the densities of bottom and water $g = \rho_1/\rho_0$
H	Water depth in shallow water channel
h_c	Water depth at which a mode is cutoff in a wedge
$H_0^{(1)}$	Zero-order first kind Hunkel function
$H_{\pm 0}$	Positive and negative sides of the interface of water and bottom in a shallow water channel
$h_{1,2}$	Analytic functions
I	Virtual image
$I_{e_\pm}$	Contributions from endpoints of integral
I_ν	Mode coefficients
$I_3, I_\pm$	Integrals
$I_{\sigma_{1,2}}$	Contributions from the stationary points of integral
J_0, J_m, J_ν	Zero order, the mth order and the νth order Bessel functions
j	Symbol for $\sqrt{-1}$
k	Wave number in water $k = 2\pi/\lambda$
k_1	Wave number in bottom $k_1 = 2\pi/\lambda_1$
k_z	Vertical component of the wave number in water
k_{1z}	Vertical component of the wave number in bottom
k_{zn}	Vertical component of the wave number for the nth mode in water
k'_1, k''_1	Real and imaginary parts of wave number k_1
k'_{zn}, k''_{zn}	Real and imaginary parts of k_{zn}

k_b	Attenuation coefficient in dB/mkHz
l	Integer
M_h	Number of mode sustained in a shallow water channel
M_w	Number of mode sustained in a wedge
m	Integer
m_ϕ	Average diameter of the grain size of the sedimental materials in ϕ-scale, ϕ is defined as $\phi = -\log_2$ (of grain diameter in millimeters)
N	Constant index
n	Refraction index $n = c_0/c_1$
P	Pressure in kg/cm^2
p	Stationary phase integration path in s plane
p_a, p_{ab}, p_b	Integration path in s plane
p_{br}	Amplitude of reflected wave from the bottom
p_i	Amplitude of incident wave at the interface of water and bottom
p_{sr}	Amplitude of reflected wave from the water surface
p'	Integration path in s plane
$\bar{p}$	Integration path in z plane
$\bar{p}_z$	Stationary phase integration path in z plane
Q	Source strength
$q(z), q_\pm(z)$	Analytic functions
$q^{(1)}(z), q_\pm^{(1)}(z)$	First order derivatives of $q(z), q_\pm(z)$
$q^{(2)}(z), q_\pm^{(2)}(z)$	Second order derivatives of $g(z), q_\pm(z)$
$q^{(3)}(z), q_\pm^{(3)}(z)$	Third order derivatives of $q(z), q_\pm(z)$
$\tilde{q}_-(\sigma)$	Analytic function

$\tilde{q}_-^{(2)}(\sigma)$	Second order derivative of $\tilde{q}_-(\sigma)$
R	Distance between the source and receiver
R	Receiver
r	Range from apex to receiver in a perfect wedge. In appendix C: range from source to receiver
r_c	Cut-off range for a mode in a wedge
r'	Range from apex to source in a perfect wedge
$\tilde{r}$	Range from apex to receiver in an effective wedge
$\tilde{r}'$	Range form apex to source in an penetrable wedge
R_0	Function of range and cross range in perfect wedge, $R_0 = \sqrt{r'^2+r^2+z^2}$
$\tilde{R}_0$	Function of range and cross range in penetrable wedge, $\tilde{R}_0 = \sqrt{\tilde{r}'^2+\tilde{r}^2+z^2}$
S	Salinity in $^\circ/_{\infty}$
S	Source
s	Complex variable
s_a, s_b	Endpoints of integral in s plane
$\hat{s}$	Amplitude of s
$s_{1,2}$	Stationary phase points in s plane
s_c , s_0	Complex constants
T	Temperature in °C
T_c	Time delay between the critical image and the source to receiver
T_s	Settling time for signal transmitting and receiving system
T_0	Pulse length
t	Complex variable
t_b	Complex function

t_c , t_0	Complex constants
V	Reflection coefficient
x	Range from the apex in horizontal plane
x_0	Source range from the apex in horizontal plane
y	Vertical axis
Z, Z_c, Z_s	Impedances of acoustic wave in water, compressional and shear waves in bottom
z	Cross range from the source. In chapter 3: complex variable. In appendix C: depth of receiver in shallow water channel
$\tilde{z}$	Coordinate of receiver in z axis
z_s	Stationary point
z_0	Depth of source in shallow water channel
α	Grazing angle at the interface of water and bottom. In chapter 3: Angular variable
α_c	Critical angle at water/bottom interface
α_1	Complementary angle of refraction angle at water/bottom interface
β	Angle between the ray from a virtual image to the receiver and the image plane
β_0	Initial elevation angle of sound ray at source
$\Gamma(\,)$	Gamma Function
γ_0	Initial azimuthal angle of sound ray at source
γ_1	Refraction angle of shear wave in bottom
Δ	Displacement of the bottom introduced by an effective wedge
Δ_0	Zero order approximation of Δ
$\delta(\,)$	Dirac Delta function
ε	Function of grazing angle
ε_v	Relative deviation in reflection coefficient

η	Complex constant
θ, θ'	Angles of receiver and source in perfect wedge
$\tilde{\theta}, \tilde{\theta}'$	Angles of receiver and source in penetrable wedge
θ_0	Wedge angle
λ	Wave length in water. In chapter 2: variable for Bessel transform
λ_1	Wave length in bottom
μ	Horizontal component of wave number k
μ_n	Horizontal component of wave number k for the nth mode
μ', μ''	Real and imaginary parts of μ
ν	Integer $\nu = m\pi/\theta_0$
ξ	Variable
ρ_0, ρ_1	Densities of water and bottom
$\sum_{\nu}$	Sum over all possible value ν
σ	Angle of virtual image to horizontal plane, complex variable
σ_c	Upper limit of integral Eq. (2.34)
σ_{cs}	Stationary point
σ_i	Angle of image plane
$\sigma_{1,2}$	Stationary phase points in σ plane
$\sigma'_{1,2}$	Real parts of $\sigma_{1,2}$
$\sigma''_{1,2}$	Imaginary parts of $\sigma_{1,2}$
$\tau(s)$	Analytic function
Φ	Velocity potential function of the sound field in a wedge
$\hat{\Phi}$	Fourier sine transform of Φ
$\hat{\hat{\Phi}}$	Fourier transform of $\hat{\Phi}$

$\hat{\hat{\Phi}}$	Bessel transform of $\hat{\Phi}$
ϕ_0 , ϕ_1	Incident and refraction angle at the interface of water and bottom
χ	Angular variable
ψ	Velocity potential function of sound field in shallow water channel
Ω	Complex constant
ω	Angular frequency $\omega = 2\pi f$

LIST OF FIGURES

1665m/s, 2 --- Measured sound pressure.

Fig. C5 The normalized sound pressure in the water channel, the parameters are the same as in Fig. C4. 1 --- Predicted sound pressure by Eq. (C.10) with 0.78dB/λ attenuation in the bottom, 2 --- Predicted sound pressure by Eq. (C.10) with 1dB/λ attenuation in the bottom, 3 --- Measured sound pressure.

Fig. C6 The normalized sound pressure in the water channel, the parameters are the same as in Fig. C3. 1 --- Predicted sound pressure by Eq. (C.10) with 0.78dB/λ attenuation in the bottom, 2 --- Measured sound pressure.

Fig. C7 The normalized sound pressure in the water channel, the parameters are the same as in Fig. C3. 1 --- Predicted sound pressure by Eq. (C.10) with 1dB/λ attenuation in the bottom, 2 --- Measured sound pressure.

Chapter 1. INTRODUCTION

A wedge shaped water channel is generally defined as a water domain that is bounded by the horizontal water surface and a sloping bottom. In the oceans, all the continental slopes, the continental shelves and the areas near coastline can be approximated as wedge shaped channels, and even the ocean basins and the sea mountains can also be considered as wedges since they have the same profile in the slope direction. Sound propagation in a wedge shaped channel has some special features such as refraction of sound rays in the horizontal plane and, a shadow zone near the apex of the wedge and, intramode interference and mode penetration into the bottom in a penetrable wedge. All the features are caused by the sloping bottom of the wedge as the sound wave is repeatly reflected between the water surface and the bottom. As a very important aspect of sound propagation in the oceans, the wedge problem has received a lot of attentions in the underwater acoustics world.

1.1 Review of the previous works

The studies of the wave propagation phenomena including diffraction, refraction and reflection in wedge-shaped wave guide have been one of interesting topics for a long time. Considering the half-plane as a wedge with an angle of 2π, the wave diffraction was investigated by Sommerfeld[1] as early as at the end of last century. Bromwich[2] and Carslaw[3] extended the work of Sommerfeld to a wedge of any angle.

In underwater acoustics, the sound field in wedge-shaped ocean channels has also been studied extensively in theory and in experiment. Weston[4] applied ray theory in a wedge and explained the mechanism of the ray curvature in horizontal plane, he introduced a method to describe the horizontal refraction by using Snell's Law. Kuznetsov[5] conducted an analysis of a point source field in a wedge with perfect boundaries by method of geometric acoustics, he showed the ray's curvature and the caustic in the wedge and gave some experiment results to confirm the theory. Weinberg and Burridge[6] showed the horizontal rays and the envelopes of different modes by means of horizontal ray theory. Harrison[7,8] analyzed horizontal ray curvature more thoroughly than any previous studies by using ray invariant similar to that given by Weston[9]. More recently, Tindle and Deane[10] employed ray theory with beam displacement to calculate the sound field in a shallow water over a sloping bottom. The method they used can predict sound field very well in shallow water channel. Rousseau, Jacobson and Siegmann[11] examined the effects of a sloping ocean bottom on three dimensional ray arrivals and on incoherent total field transmission loss by using ray theory.

Normal mode theory introduced by Pekeris[12] for explanation of explosive sound propagation in shallow water has also been applied to wedge-shaped water channels. For a certain class of ocean domains, such as isovelocity wedge-shaped channels with perfectly reflecting boundaries (i.e. "ideal" or "perfect" wedges), exact solutions can be obtained using the normal mode method. Sakharova[13] deduced an asymptotic representation of the sound field of a point source in an "ideal" wedge based on the rigorous solution which is a contour integral given by Sommerfeld[14]. The representation is a summation of normal waves. Bradley[15], Bradley and Hudimac[16] derived a exact solution of the acoustic field in an "ideal" wedge. On using integral transforms, Buckingham[17] derived an exact solution for the field in a perfect wedge with a wedge angle equal to a submultiple of π, and an approximate representation was given which has a larger range of validity than that of the Bradley and Hudimac's solution[15,16].

In practice, there is no ideal wedge-shape channel in the ocean because the bottom of the ocean is not a perfectly reflecting surface. It has been found that 79% of ocean slopes are covered with at least 200m of sediment[18]. Therefore a more realistic approximation of the bottom of the wedge-shaped ocean channel is a fast bottom, that is, a water/fluid sediment interface that shows a critical grazing angle. A ray traveling through the ocean that is incident upon this type of bottom either will be totally internally reflected, a process accompanied by a phase shift, or it will penetrate the sediment depending on whether the grazing angle is less than or greater than the critical value. Such a bottom is referred to be penetrable.

There is no exactly analytical solution for the acoustic field in a wedge-shaped ocean channel with a penetrable bottom because the Helmholtz equation can not be separated anymore. However, many approximate solutions have been developed for this problem.

Kuznetsov[19] presented an approximate normal mode solution by applying nonrigorous separation to the wave equation. The solution may be used to describe the sound field only in the wave-guide zone. Eby *et al*[20] introduced adiabatic approximation quantified by Pierce[21] and Milder[22] to extend the method of normal mode. The theory assumed the coupling between normal modes are negligible to a guided-wave propagation in a medium varying slowly with horizontal coordinates in addition to varying with the vertical coordinate. According to this assumption, a normal mode adapts itself locally without energy exchanging with other normal modes when it is propagating in a horizontally varying medium. Graves *et al*[23] applied the adiabatic mode method to the wedge-shaped ocean with a perfectly reflecting bottom. Their results agreed well with the exact solution of Bradley and

Hudimac[16], especially when the slopes are more gradual. This suggests that mode coupling exists and it should be taken into account when the medium change is not very small. McDaniel[24,25] derived equations for energy transfer between normal modes and applied the equations in shallow water sound propagation. Chwieroth *et al*[26] studied the mode coupling in a special case of the acoustic propagation in a ocean channel with a parabolic profile. Nagl *et al*[27] also applied the adiabatic mode theory to some real situations and compared the results with experimental results. Agreement was good for the deep water channel case, but not for the shallow water with a variable depth, which was considered as an effect of mode coupling. Koch *et al* [28] used an adiabatic normal mode solution to study some physical mechanisms relevant to acoustic propagation to some of environmental parameters associated with these mechanisms. They pointed out that propagation is sensitive to the shallow water sediment attenuation but not to the slope angle. By the same approach, Koch[29] concluded that the variation of the acoustic field levels with source or receiver depth may be more substantial than variation in level associated with the dependence of propagation on sediment attenuation or sediment type. In order to examine the adiabatic normal mode theory, Tindle, Hobaek and Muir[30,31] conducted a model experiment to investigate the downslope propagation of lower-order normal modes in a shallow water wedge with a penetrable bottom. The results support the theory except the assumption of vertical wave fronts. In a recent experiment, Hobaek and Westwood[32] also measured the up slope wave front curvature in a sand bottom wedge, their results indicate that the wave front is a circular arc with the center around the apex. The adiabatic mode method will fail to predict the sound field when the normal mode reaches the mode cutoff depth where the mode is coupled into a continuous spectrum and penetrates into the bottom.

A variant of the adiabatic approximation have been developed to deal with a simple range dependent environment like a wedge[33,34]. This method simplifies the wedge as stairsteps, and on each step, normal mode method can be used, the backgoing of the wave is taken into account by considering the boundary conditions between steps. It is possible to use this method to examine the backscattering caused by the wedge slope.

Another important approximate method is the Parabolic Equation(PE) approximation introduced by Tappert[35]. Jensen and Kuperman[36] used a PE algorithm to calculate the sound upslope propagation in a wedge with a penetrable bottom. Their results revealed that when a mode reaches its cutoff depth, its energy propagates into the bottom and radiates away into the sediment in the form of well-defined modal beams. The mode coupling to lower modes is very little. Their work stimulated several analytical investigations of the 2-D penetrable wedge. Topuz and Felsen[37] have formulated a

solution in term of "intrinsic mode" that is valid through mode cutoff region. By using Airy's function, Pierce[38] extended the adiabatic normal mode solution to the regions where the mode cutoff occurs. Kamel and Felsen[39] generalized the theory of characteristic Green's function(resolvents) to accommodate weak nonseparability as in a penetrable wedge. Arnold and Felsen[40] employed the ray and local mode equivalence to solve the penetrable wedge problem. All these analytical investigations concerned with the acoustic field in a penetrable wedge agreed well with Jensen and Kuperman[36].

The conventional PE model[35] is a narrow angle approximation. It introduces a phase error when used to predict sound propagation in ocean channel[41]. Some wide-angle PE models[42,43,44] have been developed to improve the performance of the PE algorithms. The wide-angle PE[43] was employed by Dosso and Chapman[45] to compute the downslope propagation loss over a continental slope, the comparison was made with their experimental data, which is in excellent agreement.

As we already know that the sound field in a wedge is 3-dimensional, so that most of works mentioned before are not capable to describe the field in a penetrable wedge. Some 3-D PE models[46,47,48,49] have also been developed which can handle 3-D propagation problems such as sound propagation through mesoscale eddies and directivity effects of sonar arrays[50]. More improvements are still needed for 3-dimensional PE to be used to predict the whole field in a penetrable wedge.

In order to find an analytic solution which can be used in a penetrable wedge, Buckingham[51] suggested an "effective wedge" to model the wedge with a penetrable bottom, then the solution[17] for the ideal wedge can be apply to the "effective wedge" with a little mathematical amendment[52] which excludes the sound rays with incident angles less than the critical angle on the water/bottom interface. Some numerical examples given by this solution demonstrate some phenomena of propagation in a penetrable wedge which are apparently different from that in an ideal wedge, such as an inner zone is formed where the rays which have grazing angles greater than critical value penetrate the interface of the water and the bottom, and travel away from the water column, and a more narrow shadow zone caused by phase shift resulted from the total internal reflection. Between the inner zone and the shadow zone, there is an outer zone where the intermode interference happens.

There are more theoretical works presented recently. Pao *et al* [53] analyzed the propagation of sound wave for a point source in a penetrable wedge by applying the generalized ray method, though the analysis is carried out in the time domain, the approach may give a new way to the solution for

the field with a CW source. Westwood[54,55] developed complex ray methods for the acoustic interaction at a fluid-fluid interface and used the result to shallow water and 2-D wedge problem. The agreement is very good between his approach and the fast field programme[56] in shallow water case and the 2-D coupled mode[57] in penetrable wedge case. There is no doubt that his approach can be used to 3-D wedge problem.

Compared with the theoretical studies, there are far less experimental studies especially on the 3-D sound field in the wedge-shaped ocean channel. Wood[58] showed an interference pattern on the bottom of a wedge-like water column. In his experiment, he put a glass plate painted with water soluble paint into the water to form a water wedge between the water surface and the glass plate. the variation of sound level was recorded on the plate when the region was insonified with a CW signal, a typical interference pattern caused by the horizontal ray propagation was obtained, and from this result, a cutoff range from the apex of the wedge was specified. However, no quantitative comparisons with a theoretical model were made. Kuznetsov[59] studied the normal modes propagating from a wedge into a half-space. In his experiment, a tapered vessel filled with liquid in which the sound speed is less than the sound speed in the water was placed into water. The vertex of the vessel was perpendicular to the surface of the water. By the arrangement of the experiment, he could scan the field in the water to get a profile of the field corresponding to a z=constant plane. The results showed the normal modes propagated into the half-space from the wedge and the mode exit sites where those normal modes were cutoff. The results were in good agreement with the results predicted by the theory. But his measurements were confined to the half-space domain under the wedge. Borchardt[60] carried out a model experiment to measure 3-D sound field in a wedge with penetrable bottom and compared the results with a computation model developed by Coppens[61] by applying image theory. But his measurements were also limited due to the experiment conditions. Doolittle, Tolstoy, and Buckingham[62,63] confirmed the horizontal refraction of sound propagation in a sea test by measuring the bearing shift of the array. Glegg and Yoon[64] conducted an experiment in an "ideal" wedge, they put an air-filled plexiglass wedge into a water tank to model a wedge with presure-release boundaries. Their experimental results are in good agreement with the theoretical solution of Buckingham[17].

It is the purpose of this thesis to investigate the correspondence between the theoretical solutions for the sound field in a penetrable wedge[17,51,52] and a comprehensive model experiment. The features of the field are revealed and analyzed, and comparisons made between the predicted field and the experimental results.

1.2 Outline of the thesis

In chapter 1, the problem of sound propagation in a wedge is introduced. A review of the previous works and the aim of the project is given.

Chapter 2 describes the geometry of the wedge problem and introduces Buckingham's analytic solutions[17,51,52] for a harmonic point source in a perfect wedge and in a penetrable wedge.

Starting with an introduction about the stationary phase method (SPM), the analytic solutions are evaluated by SPM to obtain uniformly asymptotic approximations in Chapter 3. Comparisons are made between the exact solutions, which can not be expressed explicitly, and the approximate representations obtained. It is shown that the approximate representations can be used to predicted the sound field in wedges rapidly with a satisfactory accuracy. The different features of the "wedge mode" and the "shallow water mode" are also revealed. The restrictions on using the approximate representations are discussed.

A laboratory experiment which measured sound pressure in a tank with a sand bottom is detailed in chapter 4, which includes the configuration of the experimental apparatus and, the schematic drawing of the gantry system which is able to carry a receiver measuring sound pressure 3-dimensionally and, the procedures of the measurement carried out. In order to provide reasonable parameters for the theoretical prediction of the sound field in penetrable wedges, the sound velocity in the sand bottom was determined by measuring the relative reflection coefficient and the density of the water saturated sand.

Chapter 5 gives some predicted fields in perfect wedges and penetrable wedges by the approximate representations derived in chapter 3. The parameters for the penetrable problems were the same as used in the experiment. The results are analyzed and explained in term of normal mode theory and ray theory.

The experimental results are given in chapter 6. These results includes sound pressure as a function of range and water depth in the water column and in the sand bottom, and sound pressure as a function of range and cross range in wedges with different angles. In order to help to interpret the nature of the sound fields in wedges, the sound fields in shallow water channel were also measured. Comparisons are made with the numerical results in chapter 5.

A summary of the thesis and some general conclusions drawn from present work is in Chapter 7.

All the appendices are at the end of the thesis. Appendix A describes the using of a long pulse sine signal in the tank as a continuous wave. The detail of the control of the signal transmitting and receiving by the computer is in appendix B. Appendix C introduces sound propagation in shallow water in theory. Some experimental results are given, which are useful in two ways. One is the results showed the sound velocity obtained in chapter 4 is reasonable, and the other is the results will help to explain sound propagation in a wedge.

Chapter 2. THEORY

2.1 Introduction

Buckingham's theoretical models[17,51,52] for a point source in wedges with perfect reflecting boundaries and a penetrable bottom are used to predict the acoustic fields. Firstly, the analytic solution for a perfect wedge[17] is introduced, which describes the field in terms of normal mode. The mode coefficients which are expressed as integrals are a function of range (out from the apex) and cross range (parallel to the apex). The features of the field in a wedge are embodied in the mode coefficients. Secondly, the concept of the "effective bottom"[51] is detailed. Then the analytic solution for a penetrable wedge[52] are described, which is obtained by applying the analytic solution for a perfect wedge[17] in a new coordinate system introduced by the "effective bottom". The mode coefficients which are also expressed as integrals become a function of the critical angle on the water/bottom interface in a penetrable wedge.

2.2 Acoustic field in a wedge with perfectly reflecting boundaries

The wedge we are concerned is shown in Fig. 2.1, where points S and R represent a point source and a point receiver (or field point), respectively. They are not necessarily in the same plane perpendicular to the apex of the wedge. The angle of the wedge is θ_0.

A cylindrical coordinate system with z-axis running along the apex of the wedge is employed, since this is the natural choice for the problem. The water surface is chosen to coincide with the $\theta = 0$ plane. So that the bottom is the θ_0 plane. The source is put in the z=0 plane which passes through the origin (only for convenience) and in the position of $S(r', \theta', 0)$, while the receiver which can be anywhere in the wedge, is assigned the position $R(r, \theta, z)$, r' and r are the ranges of the source and the receiver out from the apex, z is the cross range of the receiver, θ' and θ are referred to the water surface as shown in Fig. 2.1.

The sound field for a harmonic point source in the wedge with perfect pressure-release boundaries can be described by the inhomogeneous Helmholtz equation:

$$\nabla^2\Phi(r,\theta,z)+k^2\Phi(r,\theta,z)=-Q\delta(\vec{r}-\vec{r}_0) \tag{2.1}$$

with boundary conditions,

$$\Phi(r,0,z)=0 \tag{2.2a}$$

$$\Phi(r,\theta_0,z)=0 \tag{2.2b}$$

where, for the cylindrical coordinate system used,

$$\nabla^2=\frac{\partial^2}{\partial r^2}+\frac{1}{r}\frac{\partial}{\partial r}+\frac{1}{r^2}\frac{\partial^2}{\partial \theta^2}+\frac{\partial^2}{\partial z^2} \tag{2.3a}$$

and

$$\delta(\vec{r}-\vec{r}_0)=\frac{\delta(r-r')}{r}\delta(z)\delta(\theta-\theta') \tag{2.3b}$$

where Q is the source strength, $\delta(\ )$ is the Dirac Delta function, $k=\omega/c_0$ is the wave number, ω is angular frequency and c_0 is the velocity of the sound in the medium. Φ is the velocity potential function, from which the sound pressure P can be found as $P = \rho_0\omega\Phi$ for a harmonic source. ρ_0 is the density of the medium. On using the expressions (2.3a) and (2.3b), Eq. (2.1) becomes:

$$\frac{\partial^2\Phi}{\partial r^2}+\frac{1}{r}\frac{\partial\Phi}{\partial r}+\frac{1}{r^2}\frac{\partial^2\Phi}{\partial \theta^2}+\frac{\partial^2\Phi}{\partial z^2}+k^2\Phi=-Q\frac{\delta(r-r')}{r}\delta(\theta-\theta')\delta(z) \tag{2.4}$$

There are several ways of solving Eq. (2.4) when the boundaries are perfect reflecting surfaces. One method, which has an advantage of eliminating the need to select arbitrary functions that will satisfy the boundary conditions, is to apply a sequence of integral transforms to both sides of Eq. (2.4), and subsequently to perform the inverse transforms to arrive at the solution.

Firstly we use finite Fourier sine transform, since this ensures that the pressure-release condition is satisfied on the both boundaries. The transform pair are as follows:

$$\hat{\Phi}(r,\nu,z)=\int_0^{\theta_0}\Phi(r,\theta,z)\sin(\nu\theta)d\theta \tag{2.5a}$$

$$\Phi(r,\theta,z)=\frac{2}{\theta_0}\sum_{\nu}\hat{\Phi}(r,\nu,z)\sin(\nu\theta) \tag{2.5b}$$

where $\nu=m\pi/\theta_0$ and m is a positive integer. The symbol $\sum_{\nu}$ is used to mean a sum over all possible value of m. After transforming Eq. (2.4), we obtain

$$\frac{\partial^2\hat{\Phi}}{\partial r^2}+\frac{1}{r}\frac{\partial\hat{\Phi}}{\partial r}-\frac{\nu^2}{r^2}\hat{\Phi}+\frac{\partial^2\hat{\Phi}}{\partial z^2}+k^2\hat{\Phi}=-Q\frac{\delta(r-r')}{r}\sin(\nu\theta')\delta(z) \tag{2.6}$$

Secondly we use Fourier transform in Z-coordinate. The transform pair for this transform are as follows:

$$\hat{\Phi}(r,\nu,\xi)=\int_{-\infty}^{+\infty}\Phi(r,\nu,z)e^{-j\xi z}dz \tag{2.7a}$$

$$\Phi(r,\nu,z)=\frac{1}{2\pi}\int_{-\infty}^{+\infty}\hat{\Phi}(r,\nu,\xi)e^{jz\xi}d\xi \tag{2.7b}$$

Fourier transforming Eq. (2.6), we have

$$\frac{\partial^2\hat{\Phi}}{\partial r^2}+\frac{1}{r}\frac{\partial\hat{\Phi}}{\partial r}-\frac{\nu^2}{r^2}\hat{\Phi}-\xi^2\hat{\Phi}+k^2\hat{\Phi}=-Q\frac{\delta(r-r')}{r}\sin(\nu\theta') \tag{2.8}$$

The last transform is Hankel transform with transform pair:

$$\hat{\hat{\Phi}}(\lambda,\nu,\xi)=\int_0^{\infty}\hat{\Phi}(r,\nu,\xi)J_\nu(\lambda r)rdr \tag{2.9a}$$

$$\hat{\Phi}(r,\nu,\xi)=\int_0^{\infty}\hat{\hat{\Phi}}(\lambda,\nu,\xi)J_\nu(\lambda r)\lambda d\lambda \tag{2.9b}$$

On taking Hankel transform of Eq. (2.8), we find that

$$(k^2-\xi^2-\lambda^2)\hat{\hat{\Phi}}=-QJ_\nu(\lambda r')\sin(\nu\theta') \tag{2.10}$$

then

$$\hat{\hat{\Phi}}=-Q\frac{J_\nu(\lambda r')\sin(\nu\theta')}{k^2-\xi^2-\lambda^2} \tag{2.11}$$

Now, using inverse transforms to Eq. (2.11) to find the solution of the equation. Starting with the inverse Fourier transform:

$$\hat{\Phi}(\lambda,\nu,z)=\frac{1}{2\pi}\int_{-\infty}^{+\infty}-Q\frac{J_\nu(\lambda r')\sin(\nu\theta')}{k^2-\xi^2-\lambda^2}e^{j\xi z}d\xi \tag{2.12}$$

There are two poles at $k_z=\pm\sqrt{k^2-\lambda^2}$ on the complex ξ plane. Considering the wave is outgoing in z-direction, it must satisfy $\Phi\to 0$ when $|z|\to\infty$, so we have to choose $k_z=\sqrt{k^2-\lambda^2}$ for $z>0$ and $k_z=-\sqrt{k^2-\lambda^2}$ for $z<0$. Performing contour integration along a path as shown in Fig. 2.2, the following expression is obtained:

$$\hat{\Phi}(\lambda,\nu,z)=\frac{jQ}{2}\frac{J_\nu(\lambda r')\sin(\nu\theta')}{\sqrt{k^2-\lambda^2}}e^{j\sqrt{k^2-\lambda^2}\,|z|} \tag{2.13}$$

Next, the inverse Hankel transform of Eq. (2.13) is

$$\Phi(r,\nu,z)=\frac{jQ}{2}\sin(\nu\theta')\int_0^{\infty}\frac{J_\nu(\lambda r)J_\nu(\lambda r')}{\sqrt{k^2-\lambda^2}}e^{j\sqrt{k^2-\lambda^2}\,|z|}\lambda d\lambda \tag{2.14}$$

Finally, using inverse finite Fourier transform on Eq. (2.14) to arrive at the solution:

$$\Phi(r,\theta,z)=\frac{Q}{\theta_0}\sum_\nu I_\nu\sin(\nu\theta)\sin(\nu\theta') \tag{2.15}$$

where

$$I_\nu(r,r',z)=j\int_0^{\infty}\frac{e^{j\sqrt{k^2-\lambda^2}\,|z|}}{\sqrt{k^2-\lambda^2}}J_\nu(\lambda r)J_\nu(\lambda r')\lambda d\lambda \tag{2.16}$$

We can see that the acoustic field of a harmonic point source in a wedge with pressure-release boundaries is a sum of the orthogonal normal modes. The mode coefficient I_ν is function of range r (out from the apex of the wedge) and cross-range z (parallel to the apex).

In order to simplify the I_ν, suppose the wedge angle θ_0 is a submultiple of π, thus $\nu=\frac{m\pi}{\theta_0}$ is an integer. Applying the addition theorem of the Bessel function;

$$J_0(R_1)=\sum_{m=-\infty}^{+\infty}J_m(r_1)J_m(r_2)e^{jm\sigma}$$

$$=J_0(r_1)J_0(r_2)+2\sum_{m=1}^{\infty}J_m(r_1)J_m(r_2)\cos(m\sigma) \tag{2.17}$$

where $R_1=(r_1^2+r_2^2-2r_1r_2\cos\sigma)^{1/2}$, making use of the orthogonality of the cosine function, after multiplying both sides of Eq. (2.17) with cos(nσ) and integrating the product from 0-π over σ, i.e.

$$\int_0^{\pi}J_0(R_1)\cos(n\sigma)d\sigma=\int_0^{\pi}\left[J_0(r_1)J_0(r_2)+2\sum_{m=1}^{\infty}J_m(r_1)J_m(r_2)\cos(m\sigma)\right]\cos(n\sigma)d\sigma \tag{2.18}$$

we can obtain

$$J_m(r_1)J_m(r_2)=\frac{1}{\pi}\int_0^{\pi}J_0(R_1)\cos(m\sigma)d\sigma \tag{2.19}$$

now

$$I_\nu(r,r',z)=\frac{j}{\pi}\int_0^{\pi}\cos(\nu\sigma)\int_0^{\infty}\frac{e^{j\sqrt{k^2-\lambda^2}\,|z|}}{\sqrt{k^2-\lambda^2}}J_0\left(\lambda\sqrt{r^2+r'^2-2rr'\cos\sigma}\right)\lambda d\lambda d\sigma \tag{2.20}$$

The inner integration of the Eq. (2.20) is the sound field of a harmonic point source in an infinite homogeneous medium. The Eq. (2.20) can be expressed as

$$I_\nu(r,r',z)=\frac{1}{\pi}\int_0^{\pi}\cos(\nu\sigma)\frac{e^{-jkR}}{R}d\sigma=\frac{1}{2\pi}\int_{-\pi}^{+\pi}\cos(\nu\sigma)\frac{e^{-jkR}}{R}d\sigma \tag{2.21}$$

where $R=(r^2+r'^2-2rr'\cos\sigma+z^2)^{1/2}$ is the distance between the source and the receiver, with $\sigma=\theta'-\theta$.

Apparently, Eq. (2.21) means that the coefficient of a particular normal mode is determined by the total contribution of the "virtual images" with the strength $\cos(\nu\sigma)$ distributed continuously along the circle centered at the apex of the wedge with a radius which is equal to the distance from the apex of the wedge to the point source.

The solution in Eqs. (2.15) and (2.21) is exact only for a wedge angle which is a submultiple of π, when there is no diffraction from the apex of the wedge. However, for very small wedge angles, successive submultiples of π form a quasicontinuum and the diffracted component of the field is always insignificant. Thus the solution given in Eqs. (2.15) and (2.21) accurately represents the field in very small angle wedges with perfectly reflecting boundaries regardless of whether θ_0 is a submultiple of π.

2.3 Effective wedge

In the ocean, there is no perfectly reflecting bottom. Most of the wedge-shaped ocean channels have a bottom that is covered with thick sediment[18] such as sand, silt, and clay. These sediments are saturated with water, therefore they can be considered approximately as fluids in which the sound velocity is greater than the sound velocity in the water. A sound ray propagating in the channel with such kind of bottom can be trapped if its incident angle upon the bottom is greater than the critical angle. While a ray with an incident angle less than the critical angle will be attenuated very quickly in the channel because it penetrates into the sediment and travels away from the water column. In underwater acoustics applications, the field in the water column is usually of greater concern than that in the sediment. It is reasonable to consider only the trapped sound rays in an ocean channel with a penetrable bottom. When the rays are propagating in the channel, they undergo a totally internal reflecting process in the bottom. The reflected wave has the same amplitude as the incident wave but a phase delay. It appears as if that the sound rays are reflected by a perfectly reflecting bottom which is lying below the actual bottom interface. This is referred to as the "effective" pressure-release bottom.

Consider a ray which is incident at the interface between two fluids at grazing angle α as shown in Fig. 2.3. a. The densities and the sound velocities of the upper and the lower fluids are (ρ_0, c_0) and (ρ_1, c_1), respectively, with relative values $g=\frac{\rho_1}{\rho_0}>1$ (where the inequality represents the practical requirement that the lower medium should support the upper one) and $n=\frac{c_0}{c_1}<1$(where the inequality indicates that the "fast" bottom with a critical angle α_c is considered). Since $n=\cos\alpha_c$, the reflection coefficient for a plane wave[65] for the interface is

$$V=\frac{g\sin\alpha-j\sqrt{\cos^2\alpha-\cos^2\alpha_c}}{g\sin\alpha+j\sqrt{\cos^2\alpha-\cos^2\alpha_c}} \tag{2.22}$$

We are concerned here only with grazing angles less than the critical, where total internal reflection occurs, since above this region most of the energy penetrates the bottom and, in the present context, is no longer of interest. When $\alpha<\alpha_c$ there is a phase change on reflection, 2ε which from Eq. (2.22) can be expressed as

$$2\varepsilon=2\tan^{-1}\left[\frac{(\cos^2\alpha-\cos^2\alpha_c)^{1/2}}{g\sin\alpha}\right] \tag{2.23}$$

There will be the same phase change if a ray is reflected from a pressure-release surface a distance Δ below the actual interface Fig. 2.3. b, where

$$\Delta=\frac{\left(\frac{\pi}{2}-\varepsilon\right)}{k\sin\alpha} \tag{2.24}$$

From the Eq. (2.23), ε is zero when $\alpha=\alpha_c$. Then,

$$\Delta=\Delta_c=\frac{\pi}{2k\sin\alpha_c} \tag{2.25}$$

We are now interested in examining how Δ varies with the grazing angle α, still assuming of course that $\alpha\leq\alpha_c$. From Eqs.(2.23) and (2.24), after some simple algebraic rearrangement, the displacement of the effective pressure-release surface can be expressed as

$$\Delta=(kx\sin\alpha_c)^{-1}\tan^{-1}\left\{\frac{gx}{(1-x)^{1/2}}\right\} \tag{2.26}$$

where

$$x=\frac{\sin\alpha}{\sin\alpha_c} \tag{2.27}$$

Taking Taylor series expansion of Eq. (2.26) about x=0, the expression becomes

$$\Delta=\Delta_0\left[1+\frac{(2.2g^2)}{6}x^2+...\right] \qquad 0\le x\le 1 \tag{2.28}$$

where the zero-term is

$$\Delta_0=\frac{g}{k\sin\alpha_c} \tag{2.29}$$

which is the constant value of the displacement discussed by Weston[9].

It is expected that the displacement Δ is at least approximately independent of grazing angle, in which case, the concept of effective pressure release bottom could be useful. Fig. 2.4 shows Δ/Δ_0 as a function of x from the Eq. (2.26) with different values of g. Obviously, Δ is weakly dependent on grazing angle α.

In practice, the relative density of the continental shelf and slope sediments consisting of various proportion of sand, silt, and clay ranges from 1.4 to 1.8[66]. The value falls in the range where the effective bottom is only weakly dependent on grazing angle. This justifies replacing the actual, penetrable bottom in the wedge with a parallel effective pressure release bottom, as shown in Fig. 2.5. Then the solution for the "ideal" wedge can be used here in a new coordinate system in which the z-axis (the apex of the "effective wedge") is parallelly shifted a distance of $\Delta_0/\sin\theta_0$ on $\theta=0$ plane. The receiver and the source in the new system are $\tilde{S}$ ($\tilde{r}'$, θ', z) and $\tilde{R}(\tilde{r}, \tilde{\theta}, z)$. When the angle of the wedge is small, the relations between the old system and the new one for the coordinates of the receiver are

$$\tilde{r}\approx r+\frac{\Delta\cos\theta}{\sin\theta_0} \tag{2.30a}$$

$$\tilde{\theta}\approx\frac{r\theta}{\tilde{r}}=\frac{\theta}{1+\frac{\Delta\cos\theta}{r\sin\theta_0}} \tag{2.30b}$$

because θ_0 is small, Eqs. (2.30a) and (2.30b) can be simplified as

$$\tilde{r}\approx r+\frac{\Delta}{\theta_0} \tag{2.31a}$$

$$\tilde{\theta}\approx\theta\left[1/\left(1+\Delta/r\theta_0\right)\right] \tag{2.31b}$$

The change for the coordinates of the source to the new system is the same as that of the receiver.

2.4 Acoustic field in a wedge with a penetrable bottom

Changing the solution for the acoustic field in an ideal wedge with a perfectly reflecting bottom from the old coordinate system into in the new system derived in the previous section, a new solution can be written as

$$\Phi(\tilde{r},\tilde{\theta},z)=\frac{Q}{\theta_0}\sum_{\nu} I_\nu(\tilde{r},\tilde{r}',z)\sin\nu\tilde{\theta}\sin\nu\tilde{\theta}' \tag{2.32}$$

where

$$I_\nu(\tilde{r},\tilde{r}',z)=\frac{1}{2\pi\tilde{R}_0}\int_{-\pi}^{+\pi}\cos(\nu\sigma)\frac{\exp\left\{-jk\tilde{R}_0\left[1-2\tilde{a}\cos(\sigma)\right]^{1/2}\right\}}{\left[1-2\tilde{a}\cos(\sigma)\right]^{1/2}}d\sigma \tag{2.33}$$

where $\tilde{R}_0=(\tilde{r}'^2+\tilde{r}^2+z^2)^{1/2}$ and $\tilde{a}=\tilde{r}'\tilde{r}/\tilde{R}_0^2$.

The new solution can be used to describe approximately the sound field in a wedge with a penetrable bottom, but a modification to the Eq. (2.33) has to be made. In an ideal wedge, Eq. (2.33) takes account of all the virtual images in the circle. In a penetrable wedge, only the virtual images whose ray arrives at the receiver with a grazing angle upon the bottom less than the critical angle will contribute significantly to the field. Therefore the modification to Eq. (2.33) is the change on the limit of the integral as follows

$$I_\nu(\tilde{r},\tilde{r}',z)=\frac{1}{\pi}\int_0^{\sigma_c}\cos(\nu\sigma)\frac{e^{-ik\tilde{R}}}{\tilde{R}}d\sigma \tag{2.34}$$

where

$$\begin{aligned}\tilde{R}&=\tilde{R}_0(1-2\tilde{a}\cos\sigma)^{1/2}\\&=[(\tilde{r}'\cos\sigma-\tilde{r})^2+\tilde{r}'^2\sin^2\sigma+z^2]^{1/2}\end{aligned} \tag{2.35}$$

and $\sigma_c \leq \pi$ depends on the source and the receiver coordinates.

Now we are going to decide the value of σ_c. For the sake of simplicity in deriving σ_c a zero-wedge-angle approximation is adopted in which the wedge surfaces and the source and the receiver points are all compressed into $\sigma=0$ plane. This approximation may break down around the source position, but elsewhere, for the very small wedge angles of interests, it introduces little error in the final expression for the field. An immediate advantage of the approximation is the symmetry it introduces about the $\sigma=0$ plane, making it necessary to consider only those image sources in the reduced interval $(0,\pi)$. Fig. 2.6 shows the semicircular distribution of virtual images centered on the apex $\tilde{O}$ of the effective wedge.

The criterion we require in connection with the penetrable wedge is that none of the rays from the image sources should cross any image plane with a grazing angle greater than the critical grazing angle α_c. This sets an upper limit $\sigma_c \leq \pi$ on the value σ can take in the integral for the mode coefficients, since those rays from image sources where $\sigma > \sigma_c$ penetrate the bottom before reaching the receiver and can not therefore contribute to the field.

The source/receiver configuration in Fig. 2.6 is such that $\tilde{r} < \vec{r}$, which is the condition discussed below. When $\vec{r} < \tilde{r}$ an analogous argument applies, but with $\tilde{r}$ and $\vec{r}$ interchanged. In the Cartesian coordinate system, the ray from the image **I** to the receiver **R** can be described by the equation

$$\frac{x-\vec{r}\cos(\theta)}{\vec{r}\cos(\theta)-\tilde{r}} = \frac{y-\vec{r}\sin(\theta)}{\vec{r}\sin(\theta)} = \frac{z}{+\tilde{z}} \tag{2.36}$$

where the coordinates of the receiver in the effective wedge are $R(\tilde{r}, 0, -\tilde{z})$ in the Cartesian coordinate system given in Fig. 2.6. The ray will encounter a number of image planes along its path. The image planes assumed to be distributed continuously in σ can be presented as

$$y = \tan(\sigma_i)x \tag{2.37}$$

According to the Eqs. (2.36) and (2.37), the angle between the ray and the image plane satisfies

$$\sin(\beta) = \frac{\left|[\vec{r}\cos(\sigma)-\tilde{r}]\tan(\sigma_i)-\vec{r}\sin(\sigma)\right|}{\sqrt{[\vec{r}\cos(\sigma)-\tilde{r}]^2+[\vec{r}\sin(\sigma)]^2+\tilde{z}^2}\sqrt{\tan^2(\sigma_i)+1}}$$

$$= \frac{\left|[\vec{r}\cos(\sigma)-\tilde{r}]\sin(\sigma_i)-\vec{r}\sin(\sigma)\cos(\sigma_i)\right|}{\sqrt{[\vec{r}\cos(\sigma)-\tilde{r}]^2+[\vec{r}\sin(\sigma)]^2+\tilde{z}^2}}$$

$$=\left(\frac{[\tilde{r}'\cos(\sigma)-\tilde{r}]^2+[\tilde{r}'\sin(\sigma)]^2}{[\tilde{r}'\cos(\sigma)-\tilde{r}]^2+[\tilde{r}'\sin(\sigma)]^2+\tilde{z}^2}\right)^{1/2}|\sin(\chi-\sigma_i)| \tag{2.38}$$

where

$$\cot(\chi)=\frac{\tilde{r}'\cos(\sigma)-\tilde{r}}{\tilde{r}'\sin(\sigma)} \tag{2.39}$$

There are two cases to investigate, corresponding to positive and negative values of $\cot(\chi)$.

When $\chi<\pi/2$ [i.e. $\tilde{r}'\cos(\sigma)>\tilde{r}$], $\sin(\beta)$ is a monotonic function of σ_i, there is no turning point in this case, $\sin(\beta)$ decreases as σ_i increases, so the maximum of β occurs when $\sigma_i=0$. Since only those rays which intersect the image plane with a grazing angle less than the critical grazing angle α_c should be taken into account, so β is set equal to the critical angle α_c and substitute into Eq. (2.38) yield

$$\sin(\alpha_c)=\frac{\tilde{r}'\sin(\sigma_c)}{\sqrt{\tilde{r}'^2-2\tilde{r}'\tilde{r}\cos(\sigma_c)+\tilde{r}^2+\tilde{z}^2}} \tag{2.40}$$

It is resulted in

$$\cos(\sigma_c)=\left(\tilde{r}/\tilde{r}'\right)\sin^2(\alpha_c)+\cos(\alpha_c)\left[1-\left(\tilde{r}/\tilde{r}'\right)^2\sin^2(\alpha_c)-\left(\tilde{z}/\tilde{r}'\right)^2\tan(\alpha_c)\right]^{1/2} \tag{4.41}$$

Now σ_c must satisfy the requirement that $\chi<\pi/2$ or equivalently, $\tilde{r}'\cos(\sigma_c)-\tilde{r}>0$, under such a condition, we can find

$$\tilde{z}<z_1=\sqrt{(\tilde{r}'^2-\tilde{r}^2)}\cot(\alpha_c) \tag{2.42}$$

Eq. (2.42) identifies the inner zone of the modal field where the intermode interference is absent, and Eq. (2.41) specifies σ_c, the upper limit on the integral for the mode coefficients within the zone.

when $\chi\geq\pi/2$ [i.e. $\tilde{r}'\cos(\sigma)\leq\tilde{r}$], the Eq. (2.38) has a maximum, the elevation of the image plane associated with this maximum is

$$\sigma_c=\chi-\pi/2 \tag{2.43}$$

Thus within the condition in Eq. (2.43) on σ_i, we set β equal to its maximum allowed value α_c to obtain from Eq. (2.38)

$$\sin(\alpha_c)=\left\{\frac{[\tilde{r}\cos(\sigma_c)-\tilde{r}]^2+[\tilde{r}\sin(\sigma_c)]^2}{[\tilde{r}\cos(\sigma_c)-\tilde{r}]^2+[\tilde{r}\sin(\sigma_c)]^2+\tilde{z}^2}\right\}^{1/2} \tag{2.44}$$

Then we have

$$\cos(\sigma_c)=[\tilde{r}^2+\tilde{r}^2-\tilde{z}^2\tan^2(\alpha_c)]/2\tilde{r}\tilde{r} \tag{2.45}$$

The maximum value σ_c can take is π, corresponding to a value of $\tilde{z}=z_2$, where

$$z_2=(\tilde{r}+\tilde{r})\cot(\alpha_c) \tag{2.46}$$

Eq. (2.45) is valid and specifies the upper limit σ_c when $\tilde{z}$ falls in the transition zone $z_1\leq|\tilde{z}|\leq z_2$. Finally when the receiver is far away from the source in a zone $|\tilde{z}|\geq z_2$, the upper limit of the integral is

$$\sigma_c=\pi \tag{2.47}$$

Eqs. (2.33) and (2.35) with conditions in Eqs. (2.41), (2.45), (2.47) provide a approximate theoretical description of the acoustic field in penetrable wedges with a small angle. It is valid every where in the wedge except the vicinity of the source.

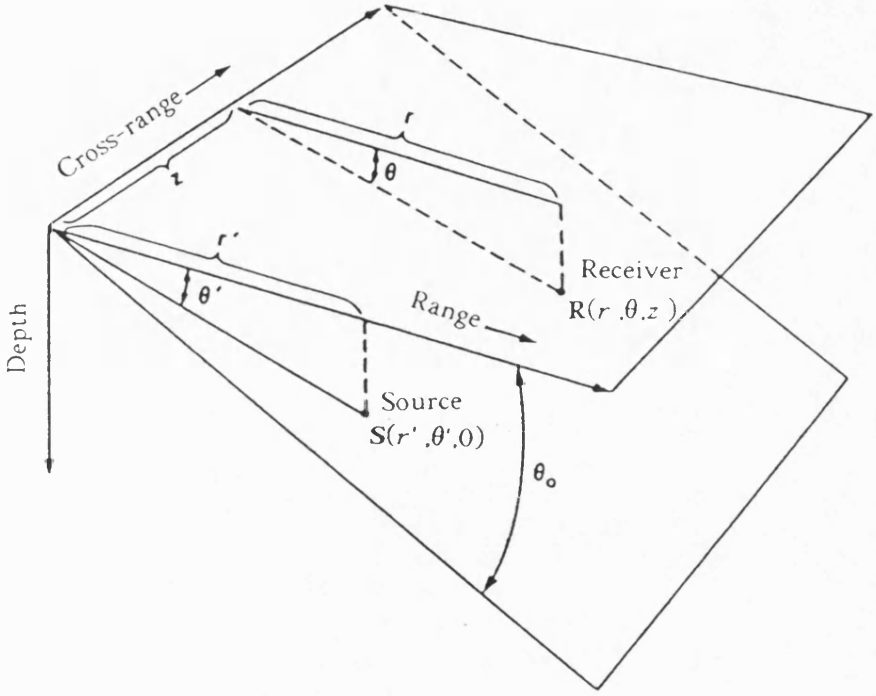

Fig. 2.1 Geometry of simple wedge with source at $S(r',\theta',0)$ and receiver at $R(r,\theta,z)$. The cross-range or z axis runs along the apex, while the range or r axis runs transversely to z axis toward to deeper water, θ is the angular coordinate originated on the horizontal surface of the wedge.

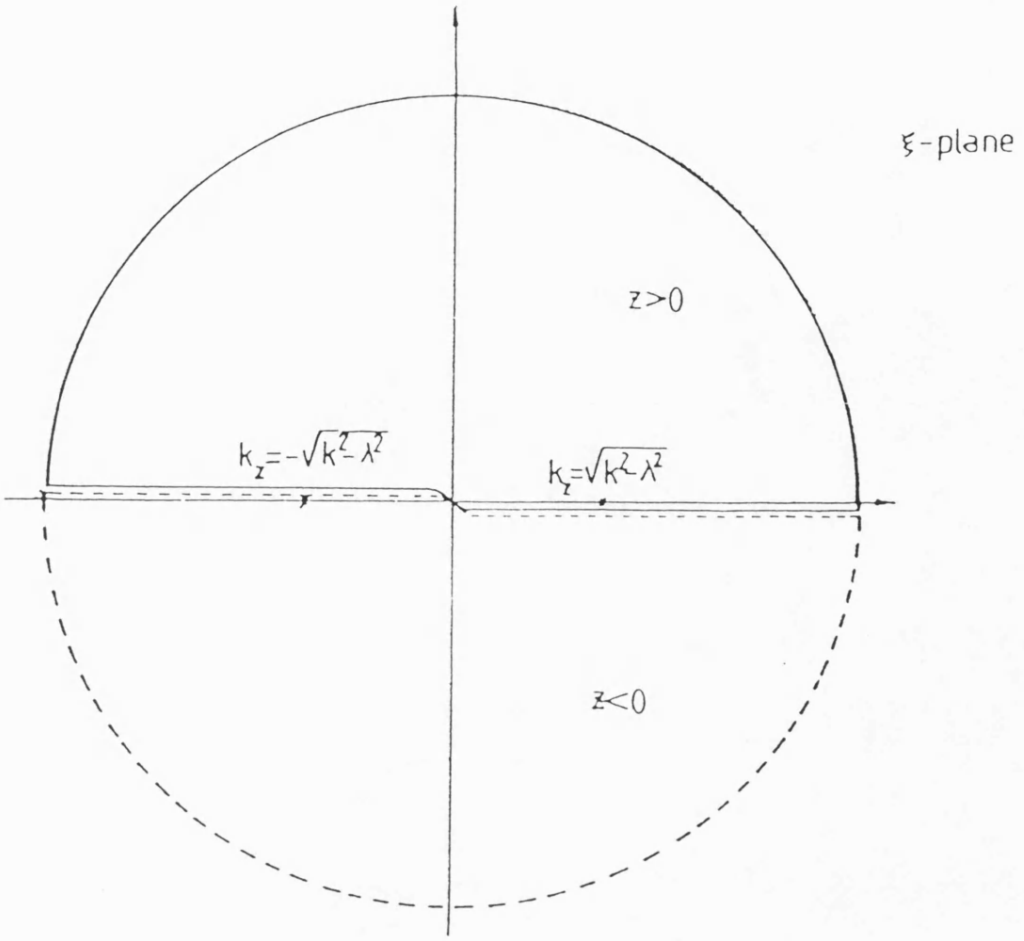

Fig. 2.2 The closed contour path for the integral in Eq. (2.12).

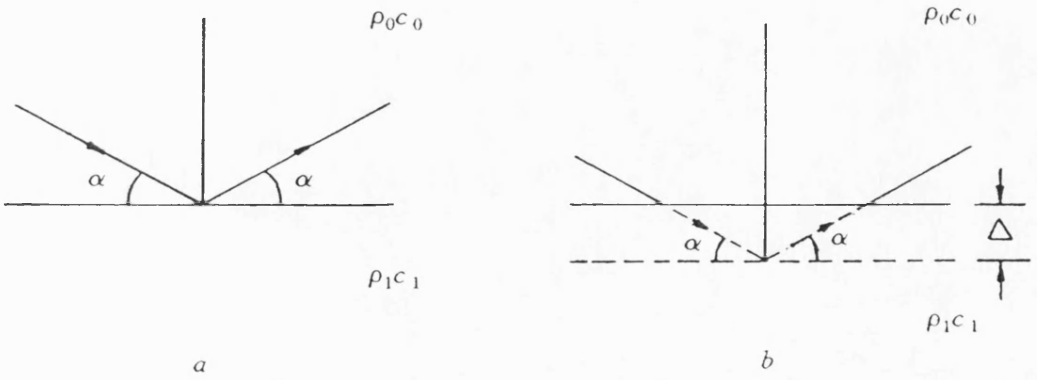

Fig. 2.3 a) Total internal reflection of a ray and, b) a reflection with the same phase shift from a effective pressure-release surface.

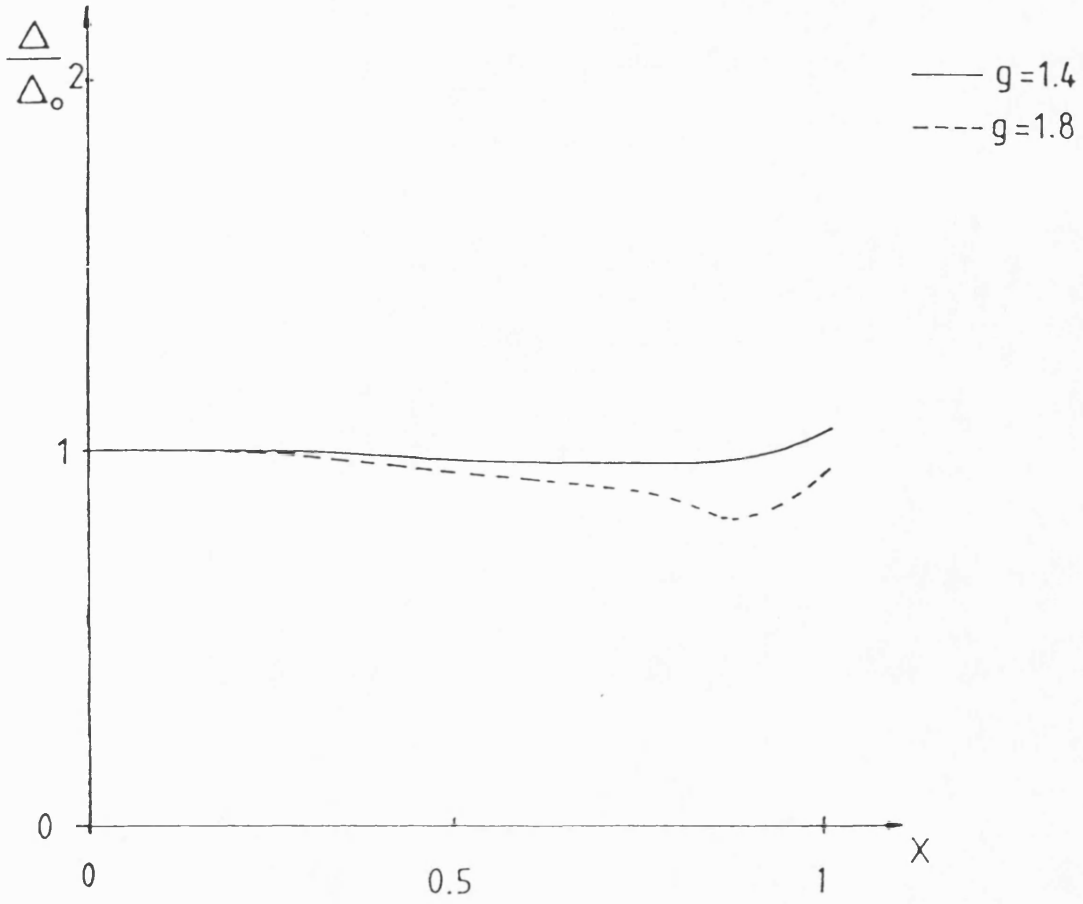

Fig. 2.4 Normalized displacement as the function of the grazing angle with different values of g.

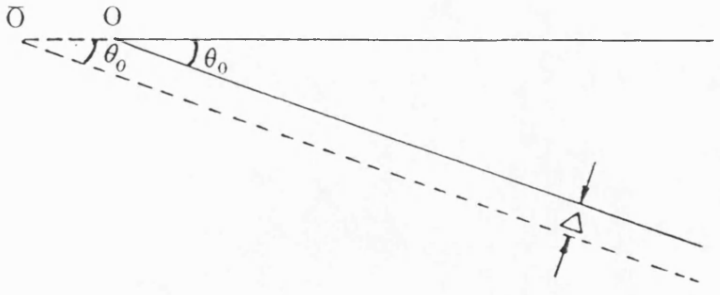

Fig. 2.5 Wedge with penetrable bottom and apex O and effective wedge with pressure-release bottom and apex $\bar{O}$.

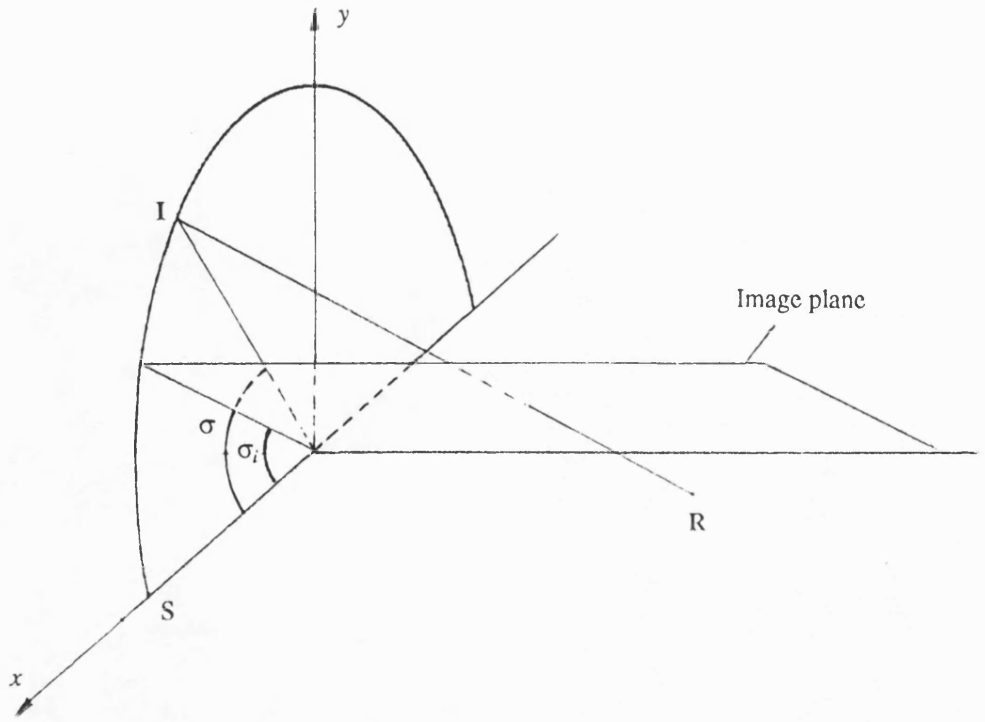

Fig. 2.6 Distribution of the "virtual images" and the ray path from image I to receiver R intersecting the image plane.

Chapter 3. APPROXIMATE EVALUATION OF THE ANALYTIC SOLUTIONS

The stationary-phase method (SPM) is introduced first in this chapter. Uniform asymptotic approximations of the mode coefficients given in chapter 2 for perfect wedge and for penetrable wedge are obtained by applying SPM. The approximate representations are applicable provided either the source or the receiver is far away from the apex, or the source and the receiver are well separated, and they are valid everywhere in a wedge. One of the major advantages of the representations is that, in comparison with numerical integration, the acoustic field in a wedge can be predicted rapidly with a satisfactory accuracy.

3.1 Stationary-phase method (SPM)

Some acoustic fields can be expressed by integral representations like Eqs. (2.21) and (2.34) that can not be evaluated in closed form. In many applications, however, the integrals contain a large parameter, Ω, in term of which the integrals may be approximated. Consider the integral of the following type

$$I(\Omega)=\int_{\bar{p}} f(z)e^{\Omega q(z)}dz \tag{3.1}$$

where $f(z)$ and $q(z)$ are analytic functions of the complex variable z along an integration path $\bar{p}$ with endpoints at infinity.

Suppose that Ω is real and, at the point z_s on the $\bar{p}$, $\mathrm{Im}\, q(z)$ has a minimum value so that $\mathrm{Im}\, q(z)>\mathrm{Im}\, q(z_s)$ on the remainder of the path. Since Ω is large, it follows that $\arg e^{[\Omega q(z)]}$ changes slowly at the vicinity of z_s and very rapidly away from z_s. If $f(z)$ is a regular and slowly varying function on the path, the integral in Eq. (3.1) may be approximated by the path contribution from the vicinity of z_s, since the contribution from the remainder of the path will be little because of the highly oscillating term $e^{\Omega q(z)}$. The point(s), where the maximum contribution to the integral occurs, are stationary points of function $q(z)$, defined by the vanishing of one or more the derivatives of $q(z)$. In general, the stationary points may not on the given contour $\bar{p}$, but on some other path $\bar{p}_z$. Then the contour $\bar{p}$ may be deformed into $\bar{p}_z$ by using Cauchy's theorem.

Since only the vicinity of the various stationary points traversed by the path $\bar{p}$ is relevant, it is unnecessary to deal completely with the generally complicated function $q(z)$; instead a finite number of terms in the power-series expansion of $q(z)$ about z_s characterizes the asymptotic evaluation for

large Ω. This feature can be exploited in a rigorous manner by transforming the given integral into a "canonical" form, wherein the function $q(z)$ is replaced by another function, a polynomial that describes in the simplest fashion the relevant stationary point arrangement at z_s. The transformation will be phrased in terms of a new variable s and the polynomial $\tau(s)$:

$$\tau(s)=q(z) \tag{3.2}$$

the point z_s in the complex z plane being chosen to correspond to $s=0$ in the complex s plane. Thus, Eq. (3.1) leads to the transformed integral

$$I(\Omega)=\int_{p'} G(s)e^{\Omega\tau(s)}ds \tag{3.3}$$

where

$$G(s)=f(z)\frac{dz}{ds}, \qquad \frac{dz}{ds}=\frac{\tau^{(1)}(s)}{q^{(1)}(z)} \tag{3.4}$$

with the superscript (1) denoting the first derivative with respect to the argument. p' represents the mapping onto the s plane of the path $\bar{p}$ in the z plane.

After the transformation, $I(\Omega)$ in the s plane is approximated most simply on a contour p, which passes in the vicinity of the origin and along which the phase of $\exp[\Omega\tau(s)]$ changes rapidly away from $s=0$. The desired contour p in the s plane, along which Re $\tau(s)=$*constant* and Im $\tau(s)>$Im $\tau(0)$ away from a region about $s=0$, constitutes a mapping into the s plane of the path $\bar{p}_z$ in the z plane. Generally, p' will not be identical with p, and in any ensuing deformation of p' into p, the presence of singularities of the integrand in Eq. (3.3) may have to be taken into account.

Assume now that the integral in Eq. (3.3) is to be evaluated over the desired contour p and that $G(s)$ is regular and slowly varying in the vicinity of $s=0$. For large values of Ω the dominant contribution to the integral in Eq. (3.3) arises from the vicinity of the origin since the phase of $e^{\Omega\tau(s)}$ is stationary about $s=0$. One may therefore write

$$I(\Omega)=\int_{p} G(s)e^{\Omega\tau(s)}ds \approx G(0)\int_{p} e^{\Omega\tau(s)}ds \qquad \Omega\to\infty \tag{3.5}$$

where the symbol $\approx$ means "approximately represented by" and $G(0)$ is the value of the regular function $G(s)$ at $s=0$. The last integral in Eq. (3.5) represents a "canonical" integral that provides a first-order approximation to the integral $I(\Omega)$ of Eq. (3.1).

The above remarks serve to highlight the motivation for a proper choice of the transformation (3.2). Firstly, Im $\tau(s)$ along p should increase most rapidly away from $s=0$ so that the major contribution to the integral arises from the vicinity of the origin in the s plane, and Im $\tau(0)$ should be as small as possible. These requirements imply that the stationary points of $\tau(s)$ [the zeros of $\tau^{(1)}(s)$] are situated near $s=0$. Viewed in the z plane, the path $\bar{p}_z$ (corresponding to p in s plane) passes near one or more of the pertinent stationary points z_s of $q(z)$ [zeros of $q^{(1)}(z)$], and Im $q(z)$ increases along $\bar{p}_z$ away from the neighborhood of z_s. Thus, the transformation (3.2) should be chosen so that the neighborhood of the pertinent stationary points z_s in the z plane is mapping into the neighborhood of $s=0$ in the s plane. Secondly, the mapping derivative dz/ds in Eq. (3.4) must be finite near s=0 in order to assure the assumed regularity of $G(s)$ near $s=0$. Therefore, $\tau(s)$ must be selected so that at the points s_s the derivative $\tau^{(1)}(s)$ possesses zeros of the same order as those of $q^{(1)}(z)$ at z_s, where the points s_s in the s plane correspond to z_s in the z plane. The simplest $\tau(s)$ meeting these requirements will yield the simplest comparison integral on the right hand side of Eq. (3.5).

According to the principles set out above, two cases of interest are considered here. One deals with a single isolated stationary point, and the other deals with two neighboring single stationary points.

Case 1. when $q^{(1)}(z)$ has a zero at z_s, and no other zeros nearby, the pertinent polynomial $\tau(s)$ is

$$q(z)=\tau(s)=q(z_s)-s^2 \tag{3.6}$$

in which $s=0$ corresponds to $z=z_s$, and $\frac{dz}{ds}=\frac{\tau^{(1)}(s)}{q^{(1)}(z)}$ is finite at $s=0$. It is clear that the path

$$s=\hat{s}e^{\pm j\frac{\pi}{4}} \tag{3.7}$$

will satisfy the requirement for Re $\tau(s)=constant$, where $\hat{s}$ is the amplitude of s, and the sign of the argument of s is decided by the requirement that $\tau(s)$ has a minimum at $s=0$. Thus, the integral in Eq. (3.3) becomes

$$I(\Omega)=e^{\Omega q(z_s)}\int_{-\infty e^{\pm j\frac{\pi}{4}}}^{+\infty e^{\pm j\frac{\pi}{4}}} G(s)e^{-\Omega s^2}ds \tag{3.8}$$

with $G(s)$ given via Eq. (3.5) as

$$G(s)=f(z)\frac{dz}{ds}, \qquad \frac{dz}{ds}=\frac{\tau^{(1)}(s)}{q^{(1)}(z)}=\frac{-2s}{q^{(1)}(z)} \tag{3.9}$$

Since $G(s)$ is assumed regular near $s=0$, it can be expanded into a power series

$$G(s)=G(0)+G^{(1)}(0)s+G^{(2)}(0)\frac{s^2}{2!}+\cdots+G^{(n)}\frac{s^n}{n!}+\cdots \tag{3.10}$$

which converges uniformly inside a circle with a finite radius r centered at $s=0$, r being the distance to the nearest singularity of $G(s)$. Upon applying L'Hopital's rule to the indeterminate form for dz/ds in Eq. (3.9) when $s=0$ (*i.e.*, $z=z_s$), one evaluates the first coefficient of the expansion as

$$G(0)=f(z_s)\left(\frac{dz}{ds}\right)_{s=0}, \qquad \left(\frac{dz}{ds}\right)_{s=0}=\left(\frac{-2}{q^{(2)}(z_s)}\right)^{1/2} \tag{3.11}$$

where $q^{(2)}(z_s)\neq 0$ at the first-order stationary point. Since arg (ds) is $\pm\frac{\pi}{4}$ along the path of integration and, in particular, at $s=0$, arg (dz/ds) at $s=0$ must be chosen equal to arg (dz)-$(\pm\pi/4)$ at z_s along the constant level path. The requirement specifies the square root function in Eq. (3.11). If $G(s)$ is approximated by $G(0)$ only, the first-order asymptotic approximation for $I(\Omega)$ in Eq. (3.3) is obtained:

$$I(\Omega)\approx G(0)e^{\Omega q(z_s)}\int_{-\infty e^{\pm j\frac{\pi}{4}}}^{+\infty e^{\pm j\frac{\pi}{4}}} e^{-\Omega s^2}ds \tag{3.12}$$

or, by Eq. (3.11), noting that the integral in Eq. (3.12) equals $\sqrt{\pi/\Omega}$:

$$I(\Omega)\approx\left(\frac{-2\pi}{\Omega q^{(2)}(z_s)}\right)^{1/2} f(z_s)e^{\Omega q(z_s)} \qquad \Omega\to\infty \tag{3.13}$$

Case 2. when $q^{(1)}(z)$ has two simple zeros $z_{1,2}$, one may select

$$q(z)=\tau(s)=a_0+\eta s-\frac{s^3}{3} \tag{3.14}$$

where a_0 and η are constants. Since $\tau^{(1)}(s)$ has two simple zeros at $s_{1,2}=\pm\sqrt{\eta}$, let $s_1=\sqrt{\eta}$ correspond to z_1 and $s_2=-\sqrt{\eta}$ correspond to z_2 to assure the regularity of dz/ds at $s_{1,2}$. From the ensuing relations

$$q(z_1)=\tau(\sqrt{\eta})=a_0+\frac{2}{3}\eta^{3/2} \tag{3.15a}$$

$$q(z_2)=\tau(-\sqrt{\eta})=a_0-\frac{2}{3}\eta^{3/2} \tag{3.15b}$$

one obtains the following expressions for a_0 and η in terms of $q(z_1)$ and $q(z_2)$:

$$a_0=\tau(0)=\frac{1}{2}[q(z_1)+q(z_2)] \tag{3.16}$$

$$\frac{2}{3}\eta^{3/2}=\frac{1}{2}[q(z_1)-q(z_2)] \tag{3.17}$$

Consider η is multivalued from Eq (3.17), special attention must be given to the choice of the proper branch of $(\eta^{3/2})^{2/3}$ required for the evaluation of η. Upon substituting Eq. (3.14) into Eq. (3.3), one obtains

$$I(\Omega)=\int f(z)e^{\Omega q(z)}dz=\int_p G(s)e^{\Omega\tau(s)}ds=e^{\Omega\tau(0)}\int_p G(s)e^{\eta s-\frac{s^3}{3}}ds \tag{3.18}$$

where p is the integration path mapped from z plane to s plane, and

$$G(s)=f(z)\frac{dz}{ds} \tag{3.19}$$

A uniformly asymptotic approximation of the integral I can be obtained with an expansion of $G(s)$ in series involving powers of the polynomial[67] $\xi=\tau^{(1)}(s)=\eta-s^2$

$$G(s)=f(z)\frac{dz}{ds}=\sum_{n=0}^{\infty}b_{n,0}\xi^n+\sum_{m=0}^{\infty}b_{m,1}\xi^m s \tag{3.20}$$

The coefficients $b_{n,0}, b_{m,1}$ can be obtained by repeated differentiation and use of the correspondences $z_1\longleftrightarrow s_1=\sqrt{\eta}$, $z_2\longleftrightarrow s_2=-\sqrt{\eta}$. Now the integral in Eq. (3.18) is written

$$I(\Omega)=e^{\Omega\tau(0)}\left\{\sum_{n=0}^{\infty}b_{n,0}\int\xi^n e^{\Omega(\eta s-\frac{s^3}{3})}ds+\sum_{m=0}^{\infty}b_{m,1}\int\xi^n s e^{\Omega(\eta s-\frac{s^3}{3})}ds\right\} \tag{3.21}$$

and the first order approximation of I is

$$I(\Omega)\simeq e^{\Omega\tau(0)}\left[\frac{b_{0,0}}{\Omega^{1/3}}C(\eta\Omega^{2/3})+\frac{b_{0,1}}{\Omega^{2/3}}C^{(1)}(\eta\Omega^{2/3})\right] \tag{3.22}$$

where

$$C(\Omega)=\int e^{\Omega t-\frac{t^3}{3}}dt \tag{3.23}$$

which is readily identified in terms of the Airy integrals for any specified allowable path p and $C^{(1)}(\Omega)$ is its derivative. The parameters $b_{0,0}, b_{0,1}$ can be found easily from Eq. (3.20)

$$b_{0,0}=\frac{1}{2}[G(s_1)+G(s_2)]=\frac{1}{2}[G(\sqrt{\eta})+G(-\sqrt{\eta})] \tag{3.24a}$$

$$b_{0,1}=\frac{[G(s_1)-G(s_2)]}{s_1-s_2}=\frac{1}{2\sqrt{\eta}}[G(\sqrt{\eta})-G(-\sqrt{\eta})] \tag{3.24b}$$

If the integral in Eq. (3.1) has finite endpoints, it can be evaluated in the same way as described before, and the contributions from the endpoints have to be taken into account. Fig. 3.1 shows the contour of integration with endpoints at s_a and s_b, and the integration path p through the stationary point. Connecting the path p_{ab} with p at the infinity by p_a and p_b, and applying Cauchy's theorem, one has

$$I_{ab}=I-I_a-I_b \tag{3.25}$$

where

$$I_a=\int_{p_a} G(s)e^{\Omega\tau(s)}ds\approx\frac{1}{\Omega}\frac{G(s_a)e^{\Omega\tau(s_a)}}{\tau^{(1)}(s_a)} \tag{3.26a}$$

$$I_b=\int_{p_b} G(s)e^{\Omega\tau(s)}ds\approx-\frac{1}{\Omega}\frac{G(s_b)e^{\Omega\tau(s_b)}}{\tau^{(1)}(s_b)} \tag{3.26b}$$

which are the first order approximations obtained by applying integration by parts.

3.2 Perfect wedge

From Eq. (2.21), the mode coefficient for a perfect wedge is now written as

$$I=\int_0^{\pi}\cos(\nu\sigma)\frac{\exp[-jkR_0\sqrt{1-2a\cos\sigma}]}{\sqrt{1-2a\cos\sigma}}d\sigma \tag{3.27}$$

$$I=\int_0^{\pi}\cos(\nu\sigma)\frac{\exp[-jkR_0\sqrt{1-2a\cos\sigma}]}{\sqrt{1-2a\cos\sigma}}d\sigma$$

where

$$R_0=\sqrt{r^2+r'^2+z^2}$$

$$a=\frac{rr'}{R_0^2}$$

$$k=2\pi/\lambda$$

$$\nu=m\pi/\theta_0$$

λ is wavelength

m is the mode number

θ_0 is the angle of the wedge

r is range from apex to receiver

r' is range from apex to source

z is cross–range from source to receiver

The factor $\frac{1}{\pi R_0}$ is omitted here from Eq. (2.21). Rewriting Eq. (3.27) as

$$I=(I_+ + I_-)/2 \tag{3.28}$$

where

$$I_\pm = \int_0^\pi f(\sigma) e^{jkR_0 q_\pm(\sigma)} d\sigma \tag{3.29}$$

with

$$f(\sigma) = \frac{1}{\sqrt{1-2a\cos\sigma}} \tag{3.30}$$

and

$$q_\pm(\sigma) = -[\pm v\sigma/kR_0 + \sqrt{1-2a\cos\sigma}] \tag{3.31}$$

Replacing Ω with kR_0 in Eq. (3.1), when kR_0 is large, Eq. (3.27) can be evaluated by Stationary-phase method (SPM) as mentioned in the previous section. The stationary points are determined by the derivative of Eq. (3.31). Upon taking the derivative of Eq. (3.31), one obtains

$$q_+^{(1)}(\sigma) = -\left[+\frac{v}{kR_0} + \frac{a\sin\sigma}{\sqrt{1-2a\cos\sigma}} \right] \tag{3.32a}$$

$$q_-^{(1)}(\sigma) = -\left[-\frac{v}{kR_0} + \frac{a\sin\sigma}{\sqrt{1-2a\cos\sigma}} \right] \tag{3.32b}$$

Eqs. (3.32a) and (3.32b) are periodic function of σ with the periodicity is equal to 2π, both have solutions on complex σ plane as $q_\pm^{(1)}(\sigma) = 0$, since the area of interest is confined in $[0,\pi]$ as given by the limits of the integral in Eq. (3.27), there is no solution to $q_+^{(1)}(\sigma)=0$ in this area, while two roots

can be found for $q_{-}^{(1)}(\sigma)=0$ as

$$\sigma_{1,2}=\arccos\frac{\nu^2\pm\sqrt{\nu^4-k^2R_0^2(\nu^2-a^2k^2R_0^2)}}{ak^2R_0^2} \tag{3.33}$$

which are the stationary points for I_- in Eq. (3.28). There are no stationary points for I_+ in Eq. (3.28). Since $\sigma_{1,2}$ are functions of the positions of the source and the receiver, they may be real or imaginary, or even identical determined by the value of the square root as it can be seen from Eq. (3.33). This characterizes the acoustic field into three parts, here referred to as the bright zone, the shadow zone and the caustic.

In the shadow zone, the term in the square root of Eq. (3.33) is less than zero, therefore, the stationary points become complex as followed;

$$\sigma_{1,2}=\arccos\left(\frac{\nu^2\pm jA}{ak^2R_0^2}\right) \tag{3.34}$$

where

$$A=\sqrt{k^2R_0^2(\nu^2-a^2k^2R_0^2)-\nu^4} \tag{3.35}$$

When σ is a complex variable, it can be written as

$$\sigma=\sigma'+j\sigma'' \tag{3.36}$$

Bearing it in mind that

$$\cos(\sigma)=\cos(\sigma'+j\sigma'')=\cos\sigma'\cosh\sigma''-j\sin\sigma'\sinh\sigma'' \tag{3.37}$$

and from Eq. (3.33), the following equations can be found

$$\cos\sigma'_{1,2}\cosh\sigma''_{1,2}=\frac{\nu^2}{ak^2R_0^2} \tag{3.38a}$$

$$\sin\sigma'_{1,2}\sinh\sigma''_{1,2}=\mp\frac{\sqrt{k^2R_0^2(\nu^2-a^2k^2R_0^2)-\nu^4}}{ak^2R_0^2} \tag{3.38b}$$

With some algebraic manipulations, one obtains,

$$\cosh\sigma''_1=\cosh\sigma''_2=\frac{\nu}{akR_0}\left(\frac{1+\sqrt{1-4a^2}}{2}\right)^{1/2} \tag{3.39a}$$

and

$$\sigma'_1=\sigma'_2=\arccos\left\{\frac{v}{kR_0}\left(\frac{2}{1+\sqrt{1-4a^2}}\right)^{1/2}\right\} \tag{3.39b}$$

Thus, there is $0\le\sigma'_1=\sigma'_2\le\pi/2$ in the region of interest, and according to Eq. (3.38b),

$$-\sigma''_1=\sigma''_2=\operatorname{arccosh}\left\{\frac{v}{akR_0}\left(\frac{1+\sqrt{1-4a^2}}{2}\right)^{1/2}\right\} \tag{3.40}$$

Therefore,

$$-\infty<\sigma''_1\le 0\,,\qquad 0\le\sigma''_2<\infty \tag{3.41}$$

It is interesting to notice that at the caustic, $\sigma_1=\sigma_2=\sigma_{cs}$, where

$$\cos\sigma_{cs}=\frac{m\frac{\lambda}{2}}{r'\theta_0}\,\frac{m\frac{\lambda}{2}}{r\theta_0} \tag{3.42}$$

and the locus of the caustic corresponding to th mth mode can be found by setting

$$v^4-k^2R_0^2(v^2-a^2k^2R_0^2)=0 \tag{3.43}$$

Simplifying Eq. (3.43), it is expressed as

$$r^2-\frac{z^2}{\left(\frac{2r'\theta_0}{m\lambda}\right)^2-1}=\left(\frac{m\lambda}{2\theta_0}\right)^2 \tag{3.44}$$

The maximum number of the normal modes sustained in a perfect wedge can be found by rearranging Eq. (3.44), which is given as

$$M_w=E\left\{\left[\frac{2}{r^2+r'^2+z^2+\sqrt{(r^2+r'^2+z^2)^2-4r^2r'^2}}\right]^{1/2}\left(\frac{rr'\theta_0}{\frac{\lambda}{2}}\right)\right\} \tag{3.45}$$

where E{ } means the maximum integer. It is obvious that M_w reaches the maximum value at $z=0$. So that we have

$$M_w=E\left\{\frac{r\theta_0}{\frac{\lambda}{2}}\right\} \tag{3.46}$$

for $r' > r$, and

$$M_w = E\left\{\frac{r'\theta_0}{\frac{\lambda}{2}}\right\} \tag{3.47}$$

for $r > r'$, which means the maximum number of the normal modes which can be detected by a receiver at range r in a perfect wedge is determined according to how many 1/2 wave-lengths can be accommodated along the arc which is equal to $r\theta_0$, and similarly, the maximum number of the normal modes excited by the source at range r' is determined according to how many 1/2 wave-length can be accommodated along the arc which is equal to $r'\theta_0$.

It can be seen that the loci of the caustics of all the modes sustained in the wedge in Eq. (3.44) are hyperbolic since

$$\left(\frac{2r'\theta_0}{m\lambda}\right)^2 - 1 \geq 0 \tag{3.48}$$

according to Eq. (3.47). By comparison with the shallow water channel with pressure-release boundaries, the elevation angle of the mth mode at the source in a perfect wedge is given by

$$\sin\beta_0 = \frac{m\frac{\lambda}{2}}{r'\theta_0} \tag{3.49}$$

Substitute Eq. (3.49) into Eq. (3.44), it is found that

$$r^2 = z^2\tan^2\beta_0 + r'^2\sin^2\beta_0 \tag{3.50}$$

which is the envelope of all rays corresponding to the mth mode given by Harrison in the Ray Invariant Theory[7,8]. This again reveals the well recognized relation between the ray theory and the normal mode theory. Fig. 3.2 shows the caustics of the first five modes for a point source 150λ away from the apex in a perfect wedge with a wedge angle $\theta_0 = 2°$, they are well defined beam in r–z plane, the areas outside the beams are the shadow zones of the different modes. It is found by Eq. (3.47), there are 10 modes excited by the source in this case. It can be seen that the higher mode, the narrower beam pattern. According to the ray-mode equivalence, a mode can be considered as the total contribution from all rays which have the same elevation angle at source as the mode has. When a ray travels away from the source in a perfect wedge, it is repeatedly reflected by the surface and the bottom, its heading is changed due to the reflections from the sloping bottom, this causes horizontal

refraction of sound rays and results in shadow zones for different modes. It is obvious that for rays with the same elevation angle at the source, the greater the elevation angle, the sharper the change in its heading, and consequently the wider the shadow zone for the mode. Eq. (3.49) indicates that a higher mode has a greater elevation angle than the lower modes, according to the ray-mode equivalence, higher modes corresponding to rays with greater elevation angles, therefore, the higher the mode, the wider the shadow zone, the lowest mode which has the smallest elevation angle can reach the largest area in the wedge as seen in Fig. 3.2.

It is found by Eqs. (3.42) and (3.44)

$$\cos\sigma_{cs}=\frac{m\frac{\lambda}{2}}{r'\theta_0}\frac{1}{\left[1+\frac{z^2}{r'^2-\left(\frac{m\lambda}{2\theta_0}\right)^2}\right]^{1/2}} \tag{3.51}$$

As would be expected that

$$\cos\sigma_{cs}=\frac{m\frac{\lambda}{2}}{r'\theta_0} \qquad z\to 0 \tag{3.52}$$

which means the caustic of the mth mode in the upslope direction is resulted from the ray with the same elevation angle as the mode at the source.

For a shallow water channel with perfect, parallel boundaries, the maximum number of the normal modes excited by a point source is

$$M_h=E\left\{\frac{H}{\frac{\lambda}{2}}\right\} \tag{3.53}$$

where H is the depth of the water. One difference between the "shallow water mode" and the "wedge mode" can be found by comparing Eqs. (3.47) and (3.53). In shallow water channel, M_h is the number of 1/2 wave-lengths which can be accommodated in the depth direction. In wedge-shaped channel, M_w is the number of 1/2 wave-lengths which can be accommodated along the arc which passes the source from the surface to the bottom rather than in the depth at the source position. Therefore, the wave-front is vertical straight in a shallow water channel and, a curvature centered at the apex with a radius r' in a wedge-shaped channel[63,64,65]. For a particular mode, the shortest cut-off

range is found at $z = 0$ by Eq. (3.44) as

$$r_c=\frac{m\lambda}{2\theta_0} \tag{3.54}$$

The depth of the water at the cut-off range is

$$h_c=r_c\tan(\theta_0)>r_c\theta_0 \tag{3.55}$$

Eq. (3.55) indicates the water depth at which a wedge mode is cut off can still sustain a shallow water mode. This is another difference between the "shallow water mode" and the "wedge mode". When wedge angle θ_0 is small, there is $h_c \approx r'\theta_0$, so that the maximum number of the modes excited in an ideal wedge can simply be estimated according to the depth at the source and, the number of the modes sustained in the wedge can be estimated according to the local depth as in a shallow water channel with the same depth.

There are two branch points introduced by the square root term $\sqrt{1-2a\cos\sigma}$ in Eq. (3.27) in the area of interest, which are $\sigma_{b_{1,2}} = \pm j\frac{2a}{1+\sqrt{1-4a^2}}$. Since they are away from the stationary points and they are not on the integration path as long as the source and the receiver are not at the same position, there will be no problem to employ SPM directly to evaluate the integral in Eq. (3.27).

In order to obtain an approximate representation of I_- in Eq (3.28), consider that there are two stationary points as given by Eq. (3.33), we can use the change of variable introduced in Eq. (3.14)

$$jq_-(\sigma)=\tau(s)=a_0+\eta s-\frac{s^3}{3} \tag{3.56}$$

where

$$a_0=\frac{j}{2}[q_-(\sigma_1)+q_-(\sigma_2)]=\tau(0) \tag{3.57}$$

$$\frac{2}{3}\eta^{3/2}=\frac{j}{2}[q_-(\sigma_1)-q_-(\sigma_2)] \tag{3.58}$$

Eq. (3.58) can also be expressed as

$$\frac{2}{3}\eta^{3/2}=\frac{1}{2}[q_-(\sigma_1)-q_-(\sigma_2)]e^{j\frac{\pi}{2}} \tag{3.59}$$

and consequentially,

$$\eta=\left\{\frac{3}{4}[q_-(\sigma_1)-q_-(\sigma_2)\right\}^{2/3} e^{j(\frac{\pi+2l\pi}{3})} \tag{3.60}$$

where l is an integer, $l=-2$ is a proper choice here, thus the above equation becomes

$$\eta=\left\{\frac{3}{4}[q_-(\sigma_1)-q_-(\sigma_2)]\right\}^{2/3} e^{-j\pi} \tag{3.61}$$

which is negative real. Thus by differentiating Eq. (3.56), one has

$$\left[\frac{d\sigma}{ds}\right]_{s=s_1}=\pm\left[\frac{-2\sqrt{\eta}}{jq_-^{(2)}(\sigma_1)}\right]^{1/2}=\pm j\left|\frac{2\sqrt{\eta}}{q_-^{(2)}(\sigma_1)}\right|^{1/2} \tag{3.62a}$$

$$\left[\frac{d\sigma}{ds}\right]_{s=s_2}=\pm\left[\frac{2\sqrt{\eta}}{jq_-^{(2)}(\sigma_2)}\right]^{1/2}=\pm j\left|\frac{2\sqrt{\eta}}{q_-^{(2)}(\sigma_2)}\right|^{1/2} \tag{3.62b}$$

where $\sigma_{1,2}\longleftrightarrow s_{1,2}$, $s_{1,2}=\pm\sqrt{\eta}$ and

$$q_-^{(2)}(\sigma)=-a\frac{\cos\sigma-a-a\cos^2\sigma}{(1-2a\cos\sigma)^{3/2}} \tag{3.63}$$

When $\sigma_1=\sigma_2=\sigma_{cs}$, $s_1=s_2=s=0$, one has

$$\left[\frac{d\sigma}{ds}\right]_{s=s_1}=\left[\frac{d\sigma}{ds}\right]_{s=s_2}=\left[\frac{d\sigma}{ds}\right]_{s=0}=\pm j\left[\frac{2}{q_-^{(3)}(\sigma_{cs})}\right]^{1/3} \tag{3.64}$$

where

$$q_-^{(3)}(\sigma_{cs})=a\sin\sigma_{cs}\frac{1-4a^2}{(1-2a\cos\sigma_{cs})^{5/2}} \tag{3.65}$$

The sign in Eqs. (3.63) and (3.65) should be determined by referring to the integration path.

For complex stationary points $\sigma_{1,2}$, Eq. (3.58) can be written as

$$\frac{2}{3}\eta^{3/2}=\frac{\nu\sigma''_2}{\Omega}-(1-4a^2)^{1/4}\sin(\alpha/2)\geq 0, \tag{3.66}$$

where $\Omega=kR_0$. Therefore η is positive real. And there are

$$\left[\frac{d\sigma}{ds}\right]_{s=s_2}=\pm j\left|\frac{2\sqrt{\eta}}{q_-^{(2)}(\sigma_1)}\right|^{1/2} e^{-j\frac{\alpha}{4}}, \qquad \left[\frac{d\sigma}{ds}\right]_{s=s_2}=\pm j\left|\frac{2\sqrt{\eta}}{q_-^{(2)}(\sigma_2)}\right|^{1/2} e^{j\frac{\alpha}{4}}, \tag{3.67}$$

$$f(\sigma_1)=\frac{e^{j\frac{\alpha}{2}}}{(1-4a^2)^{1/4}}, \qquad f(\sigma_2)=\frac{e^{-j\frac{\alpha}{2}}}{(1-4a^2)^{1/4}}, \tag{3.68}$$

$$\tau(0)=j\left[\frac{\nu\sigma'_1}{\Omega}-(1-4a^{2)^{1/4}}\cos(\alpha/2)\right], \tag{3.69}$$

where

$$\alpha=\tan^{-1}\frac{2A}{\Omega^2-2\nu^2}, \qquad 0\le\alpha\le\pi, \tag{3.70}$$

The sign in Eqs. (3.67) should be determined the same as in Eqs. (3.62) and (3.64).

To determine the contour of integration in the s plane, it suffices to consider the transformation in Eq. (3.56) as $\eta\to 0$ in order to establish the location of the endpoints of the transformed path. From Eq. (3.56),

$$jq_-(\sigma)=\tau(0)-\frac{s^3}{3} \qquad \eta\to 0 \tag{3.71}$$

since

$$\begin{aligned} jq_-(\sigma)-a_0 &= jq_-(\sigma)-\frac{j}{2}[q_-(\sigma_1)+q_-(\sigma_2)] \\ &\approx j\left\{q_-(\sigma_1)+\frac{q_-^{(2)}(\sigma_1)}{2!}(\sigma-\sigma_1)^2+\frac{q_-^{(3)}(\sigma_1)}{3!}(\sigma-\sigma_1)^3-\frac{1}{2}[q_-(\sigma_1)+q_-(\sigma_2)]\right\} \\ &= j\left\{\frac{1}{2}[q_-(\sigma_1)-q_-(\sigma_2)]+\frac{q_-^{(2)}(\sigma_1)}{2}(\sigma-\sigma_1)^2+\frac{q_-^{(3)}(\sigma_1)}{6}(\sigma-\sigma_1)^3\right\} \\ &= j\frac{q_-^{(3)}(\sigma_1)}{6}(\sigma-\sigma_1)^3 \qquad \eta\to 0 \end{aligned} \tag{3.72}$$

there is

$$s^3\approx-\frac{j}{2}q_-^{(3)}(\sigma_1)(\sigma-\sigma_1)^3 \tag{3.73}$$

then

$$s\approx\left[\frac{q_-^{(3)}(\sigma_1)}{2}\right]^{1/3}(\sigma-\sigma_1)e^{j(\frac{-\frac{\pi}{2}+2n\pi}{3})} \tag{3.74}$$

The proper choice for n is $n = 1$, therefore

$$s \approx \left[\frac{q_-^{(3)}(\sigma_1)}{2}\right]^{1/3}(\sigma-\sigma_1)e^{j\frac{\pi}{2}} \tag{3.75}$$

From Eq. (3.75), the sign in Eqs. (3.62), (3.64) and (3.67) is determined to be minus. Eq. (3.75) also indicates that the integration path in σ plane around the stationary points is mapped into the imaginary axis in s plane near $s = 0$. It is obvious that the imaginary axis in s plane is the desired integration path as it can be seen. On this integration path to the infinity, the Airy integral is given as[68]

$$C(x)=2\pi j\mathrm{Ai}(x). \tag{3.76}$$

With Eq. (3.76), the uniform asymptotic approximation for I_- in Eq. (3.28) is obtained as

$$I_-(\Omega)\approx 2\pi j e^{\Omega\tau(0)}\left[\frac{b_{0,0}}{\Omega^{1/3}}\mathrm{Ai}(\eta\Omega^{2/3})+\frac{b_{0,1}}{\Omega^{2/3}}\mathrm{Ai}^{(1)}(\eta\Omega 2/3)\right] \tag{3.77}$$

where

$$b_{0,0}=\frac{1}{j2}\left[f(\sigma_1)\left|\frac{2\sqrt{\eta}}{q_-^{(2)}(\sigma_1)}\right|^{1/2}+f(\sigma_2)\left|\frac{2\sqrt{\eta}}{q_-^{(2)}(\sigma_2)}\right|^{1/2}\right] \tag{3.78a}$$

and

$$b_{0,1}=\frac{1}{j2s_1}\left[f(\sigma_1)\left|\frac{2\sqrt{\eta}}{q_-^{(2)}(\sigma_1)}\right|^{1/2}-f(\sigma_2)\left|\frac{2\sqrt{\eta}}{q_-^{(2)}(\sigma_2)}\right|^{1/2}\right] \tag{3.78b}$$

for $\sigma_{1,2}$ are real, *i. e.* in the bright zone, and

$$b_{0,0}=\frac{1}{j2}\left[|f(\sigma_1)|\left|\frac{2\sqrt{\eta}}{q_-^{(2)}(\sigma_1)}\right|^{1/2}e^{j\frac{\alpha}{4}}+|f(\sigma_2)|\left|\frac{2\sqrt{\eta}}{q_-^{(2)}(\sigma_2)}\right|^{1/2}e^{-j\frac{\alpha}{4}}\right] \tag{3.79a}$$

and

$$b_{0,1}=\frac{1}{j2s_1}\left[|f(\sigma_1)|\left|\frac{2\sqrt{\eta}}{q_-^{(2)}(\sigma_1)}\right|^{1/2}e^{j\frac{\alpha}{4}}-|f(\sigma_2)|\left|\frac{2\sqrt{\eta}}{q_-^{(2)}(\sigma_2)}\right|^{1/2}e^{-j\frac{\alpha}{4}}\right] \tag{3.79b}$$

for $\sigma_{1,2}$ are imaginary, *i. e.* in the shadow zone.

The Airy function Ai(x) can be evaluated in a power series of x, which is[68]

$$\mathrm{Ai}(x)=\frac{1}{3^{2/3}}\sum_{n=0}^{\infty}\frac{3^{n/3}(-x)^n}{n!\Gamma[(2-n)/3]}. \tag{3.80}$$

But this series converges slowly if its argument x is large. Instead, the complete asymptotic expansions of Ai(x) for large argument are employed, they are

$$\mathrm{Ai}(-x)=\frac{1}{\sqrt{\pi}x^{1/4}}\left\{P(x)\sin(\frac{2}{3}x^{3/2}+\frac{\pi}{4})-Q(x)\cos(\frac{2}{3}x^{3/2}+\frac{\pi}{4})\right\},\quad x\to+\infty, \tag{3.81}$$

where

$$P(x)=\frac{1}{\sqrt{\pi}}\sum_{n=0}^{\infty}\frac{\Gamma(6n+\frac{1}{2})}{(4n)!}\frac{(-1)^n}{(9x^{3/2})^{2n}}, \tag{3.82a}$$

$$Q(x)=\frac{1}{\sqrt{\pi}}\sum_{n=0}^{\infty}\frac{\Gamma(6n+\frac{7}{2})}{(4n+2)!}\frac{(-1)^n}{(9x^{3/2})^{2n+1}}, \tag{3.82b}$$

and

$$\mathrm{Ai}(x)=\frac{1}{2\sqrt{\pi}x^{1/4}}e^{-2/3x^{3/2}}\sum_{n=0}^{\infty}\frac{\Gamma(3n+\frac{1}{2})}{\sqrt{\pi}(2n)!(-9x^{3/2})^n},\quad x\to+\infty. \tag{3.83}$$

When the stationary points $\sigma_{1,2}$ are not close to each other in the bright zone, $\eta\Omega^{2/3}$ is negative and large. On taking the first order approximation of Eq. (3.81) and from Eq. (3.77), one has

$$I_{-}=I_{\sigma_1}+I_{\sigma_2}, \tag{3.84}$$

where

$$I_{\sigma_{1,2}}=\left(\frac{2\pi}{\Omega\,|\,q_{-}^{(2)}(\sigma_{1,2})\,|}\right)^{1/2}f(\sigma_{1,2})e^{j\Omega q_{-}(\sigma_{1,2})\pm j\pi/4},\quad q_{-}^{(2)}(\sigma_{1,2})\gtrless 0. \tag{3.85}$$

Eqs. (3.84) and (3.85) are given by Doolittle *et al*[63], which are the contributions to the integral in Eq. (3.28) from the two isolate first order stationary points in the bright zone of a normal mode.

When the stationary points $\sigma_{1,2}$ are not close to each other in the shadow zone, $\eta\Omega^{2/3}$ is positive and large. On taking the first order approximation of Eq. (3.83) and from Eq. (3.77), one obtains

$$I_{-}=I_{\sigma_2}=\left\{\frac{-2\pi}{j\Omega q_{-}^{(2)}(\sigma_2)}\right\}^{1/2} f(\sigma_2)e^{j\Omega q_{-}(\sigma_2)}, \tag{3.86}$$

where

$$jq_{-}^{(2)}(\sigma_2)=\frac{Ae^{j(\pi-\frac{\alpha}{2})}}{\Omega^2(1-4a^2)^{1/4}}, \tag{3.87a}$$

$$jq_{-}(\sigma_2)=-\frac{v\sigma''_2}{\Omega}+(1-4a^2)^{1/4}\sin(\alpha/2)+j\left[\frac{v\sigma'_2}{\Omega}-(1-4a^2)^{1/4}\cos(\alpha/2)\right]. \tag{3.87b}$$

Eq. (3.86) is the contribution from the second stationary point σ_2 in the shadow zone. The contribution from the first stationary point σ_1 is excluded because it is not convergent. It can be seen that the amplitude of the mode in the shadow zone is exponentially attenuated with the increasing of σ''_2.

Near the caustic, $\sigma_1 \approx \sigma_2$, from Eqs. (3.77) and (3.80), I_{-} can be approximated by the first term,

$$I_{-}(\Omega)\approx 2\pi j e^{\Omega\tau(0)}\frac{b_{0,0}}{\Omega^{1/3}}\mathrm{Ai}(\eta\Omega^{2/3}). \tag{3.88}$$

where $b_{0,0}$ is given either by Eq. (3.78a) or by Eq. (3.79a) depending on the field point in the bright zone or the shadow zone of the mode. At the caustic, Where $\sigma_1 = \sigma_2 = \sigma_{cs}$, Eq. (3.88) becomes

$$I_{-}(\Omega)\approx 2\pi j e^{\Omega\tau(0)}\frac{b_{0,0}}{\Omega^{1/3}}\mathrm{Ai}(0) \tag{3.89}$$

where

$$b_{0,0}=-jf(\sigma_{cs})\left[\frac{2}{q_{-}^{(3)}(\sigma_{cs})}\right]^{1/3} \tag{3.90}$$

Comparing the representation in Eqs. (3.88) and (3.89) with those for an isolated stationary point as in Eqs. (3.85) and (3.86), it is found that the field intensity near caustics is higher due to the factor $(kR_0)^{1/3}$. From Eq. (3.90), it can be seen that $b_{0,0} \to \infty$ as $r \to r'$, which is the property of the sound field at the source.

Since Eq. (3.27) has finite endpoints, the contributions from the endpoints have to be taken into account. As mentioned in Sec. 3.1, the first-order approximations of the contributions from the endpoints are

$$I_{e_\pm}=\frac{1}{jkR_0}\left[\frac{f(\pi)}{q_\pm^{(1)}(\pi)}e^{jkR_0q_\pm(\pi)}-\frac{f(0)}{q_\pm^{(1)}(0)}e^{jkR_0q_\pm(0)}\right] \tag{3.91}$$

which is obtained by applying integration by parts to Eq. (3.27) and retaining $(kR_0)^{-1}$ terms. Thus the integral in Eq. (3.28) can be approximated by the sum of the contributions from each stationary point and the endpoints of the integral as

$$I=I_-+I_{e_+}+I_{e_-} \tag{3.92}$$

After simplifying Eq. (3.91), we have

$$I_{e_\pm}=\frac{2\sin(\nu\pi)}{\nu\sqrt{1+2a}}e^{jkR_0\sqrt{1+2a}} \tag{3.93}$$

where the contributions from $\sigma=0$ are canceled. If ν is an integer as required here, the contributions from the endpoint $\sigma=\pi$ vanish. Therefore, the integral in Eq. (3.27) can simply be written as

$$I\approx I_- \tag{3.94}$$

Although the contribution to the field from one mode can be considered as the total contributions from the "virtual images" distributed on a circle centered at the source as shown in Fig. 2.6, Eq. (3.94) indicates that in the bright zone only two "virtual images" with angle $\sigma_{1,2}$ as in Eq. (3.33) have the most significant contributions to the field. The same conclusion is found by using Ray Invariant Theory[7,8], that a receiver in bright zone can only receive two rays with the same elevation angle. So that the result of the stationary-phase method is a geometrical approximation of wave theory.

Eqs. (3.84), (3.85) are given by Doolittle *et al*[63], which can only be used in bright zone. Fig. 3.3 shows the integral in Eq. (3.27) as a function of the cross-range z evaluated by Eqs. (3.84) and (3.85) and by numerical integration with parameters, frequency f=411kHz, source position S(150λ,1°,0), wedge angle $\theta_0=2°$, the initial and the final positions of the receiver R(25λ,1°,0) and R(25λ,1°,300λ). Comparing the results in the bright zone, good agreement is found when the caustic is not close, the approximated representation behaves poorly near the caustic, and goes to infinity at the caustic. It means that big errors will occur if Eq. (3.85) is used to predict the field near caustics, and it will fail at caustics. It can not predict the field in shadow zone either.

With Eq. (3.77), the integral in Eq. (3.27) can be approximately evaluated in the bright zone, in the shadow zone, and in the vicinity of and at caustics. In order to compute the field rapidly, Eqs. (3.85) and (3.86) are used when the two stationary points are not close, and Eq. (3.87) is only used if

two stationary points are very close as it can be seen that only a few terms of Airy function in Eq. (3.81) are needed in this case. With the same parameters used in Fig. 3.3, Fig. 3.4 shows the improvement achieved by extending the asymptotic evaluation to the caustic and the shadow zone, and the comparison between the stationary-phase method and the numerical integration. Considering the stationary points as isolated points , curve 1 shows the result of the approximation given by the contributions from each indivadual stationary point. It agrees well with the numerical integration in both the bright zone and the shadow zone when caustic is not close, the error increases as the caustic is approached. Curve 2 is the result of the uniform asymptotic approximation Eq. (3.77), it indicates the approximate representation of the integral can predict the acoustic field very well from the bright zone to the caustic and from the caustic to the shadow zone for the given parameters. Another comparison is made between the two methods, with parameters the same as used by Tolstoy *et al*[69] in the evaluation of the sound field for a point source in a perfect wedge with a 1.2° slope. Fig. 3.5 shows the first mode coefficient as a function of range r in $z = 0.25$km plane calculated by the two methods. The difference between the two results is not distinguishable. Fig. 3.6a shows the amplitude of the velocity potential $|\Phi|$ of the acoustic field in the perfect wedge. Some features of the field are demonstrated in the figure. First, at the region very near the source, the field has circular rings of alternating high and low intensities. This means that in a wedge with a small angle, only a few bottom reflections are involved as the waves propagate away from the source, so that little difference from the horizontal bottom case can be seen. Further from the source, the effect of the bottom slope becomes apparent. Due to the successive reflections from the sloping bottom, sound energy tends to propagate in the downslope direction. High order modes, which undergo greater horizontal refraction because of their large elevation angles, are turned away at the further range from the apex as indicated by the caustic of each mode. A cross section of Fig. 3.6a is shown in Fig. 3.6b, which is the velocity potential $|\Phi|$ as a function of cross range (0-75km) at range 25km, the caustics can be seen clearly as indicated in the figure, beyond a cross range 61km, there is a periodic intramode interference pattern which means only the first mode exists at this range. To obtain the figure such as Fig. 3.6a by numerical integration, hundreds of hours of CPU time on a VAX 11/750 is required[69]. For the same problem, by the approximated representation, it takes less than one hour to run on an Apricot XI microcomputer.

3.3 Penetrable wedge

Comparing with the perfect wedge, the mode coefficient for a penetrable wedge in Eq. (2.34) has the same expression but a different endpoint in the integral. Since the endpoint is a function of

source and receiver positions and a certain critical angle, its value changes within a range $[0,\pi]$. To evaluate the integral in Eq. (2.34), the stationary points should be found first. Since

$$\tilde{q}_{\pm}=-[\pm\nu\sigma/k\tilde{R}_0+\sqrt{1-2\tilde{a}\cos\sigma}], \tag{3.95}$$

where $\tilde{R}_0=(\tilde{r}'^2+\tilde{r}^2+z^2)^{1/2}$ and $\tilde{a}=\tilde{r}'\tilde{r}/\tilde{R}_0^2$. Thus we have

$$\sigma_{1,2}=\arccos\frac{\nu^2\pm\sqrt{\nu^4-k^2\tilde{R}_0^2(\nu^2-\tilde{a}^2k^2\tilde{R}_0^2)}}{\tilde{a}k^2\tilde{R}_0^2} \tag{3.96}$$

Then the caustic of the mth mode can be obtained as the term under the square root equal to zero

$$\tilde{r}^2-\frac{z^2}{\left(\frac{2\tilde{r}\theta_0}{m\lambda}\right)^2-1}=\left(\frac{m\lambda}{2\theta_0}\right)^2 \tag{3.97}$$

Since the up endpoint of the integral in Eq. (2.34) may be close to or even traverses one or both of the stationary points, the contribution from the endpoint can not be determined in the same way as in Eq. (3.26) as $\sigma_c\to\sigma_{1,2}$, $\tilde{q}_-^{(1)}(\sigma)\to 0$. In order to deal with this case, the transformed integral for two stationary points may be written as

$$I_-(\Omega)=b_{0,0}\int_{s_a}^{s_b}e^{\Omega\tau(s)}ds+b_{0,1}\int_{s_a}^{s_b}se^{\Omega\tau(s)}ds+\frac{1}{\Omega}\int_{s_a}^{s_b}\frac{G(s)-b_{0,0}-sb_{0,1}}{s_1^2-s^2}\frac{d}{ds}e^{\Omega\tau(s)}ds, \tag{3.98}$$

where $\tau(s)$, $b_{0,0}$ and $b_{0,1}$ are given in Eqs. (3.14) and (3.24). The integrand $[G(s)-b_{0,0}-sb_{0,1}](s_1^2-s^2)^{-1}$ remains bounded at $s=s_{1,2}$, so that the third integral in Eq. (3.98) can be evaluated by integration by parts as

$$I_3=\frac{1}{\Omega}\frac{G(s)-b_{0,0}-sb_{0,1}}{s_1^2-s^2}e^{\Omega\tau(s)}\Bigg|_{s=s_a}^{s=s_b}+\frac{1}{\Omega}\int_{s_a}^{s_b}\frac{d}{ds}\left[\frac{G(s)-b_{0,0}-sb_{0,1}}{s_1^2-s^2}\right]e^{\Omega\tau(s)}ds. \tag{3.99}$$

Repeated use of integration by parts will produce higher order terms with increasing powers of Ω^{-1}. To a lowest order in Ω, the integral in Eq. (3.99) is omitted, and Eq. (3.98) gives

$$I_-(\Omega)\approx e^{\Omega\tau(0)}\left\{\frac{b_{0,0}}{\Omega^{1/3}}[C_a(\eta\Omega^{2/3})-C_b(\eta\Omega^{2/3})]+\frac{b_{0,1}}{\Omega^{2/3}}[C_a^{(1)}(\eta\Omega^{2/3})-C_b^{(1)}(\eta\Omega^{2/3})]\right\}$$

$$+\frac{1}{\Omega}\frac{G(s)-b_{0,0}-sb_{0,1}}{s_1^2-s^2}e^{\Omega\tau(s)}\Bigg|_{s=s_a}^{s=s_b} \tag{3.100}$$

where

$$C_a(\Omega)=\int_{s_a}^{\infty} e^{\Omega t-\frac{t^3}{3}}dt, \qquad C_b(\Omega)=\int_{s_b}^{\infty} e^{\Omega t-\frac{t^3}{3}}dt \tag{3.101}$$

which are the incomlpete Airy integrals. The endpoints in the transformed integral in Eq. (3.98) are determined according to

$$\tilde{q}_-(0)=\tau(s_a)=\tau(0)+\eta s_a-\frac{s_a^3}{3} \tag{3.102a}$$

$$\tilde{q}_-(\sigma_c)=\tau(s_b)=\tau(0)+\eta s_b-\frac{s_b^3}{3} \tag{3.102b}$$

where

$$\tau(0)=\frac{j}{2}[\tilde{q}_-(\sigma_1)+\tilde{q}_-(\sigma_2)] \tag{3.103a}$$

and

$$\frac{2}{3}\eta^{2/3}=\frac{j}{2}[\tilde{q}_-(\sigma_1)-\tilde{q}_-(\sigma_2)] \tag{3.103b}$$

The integration path for the integral in Eq. (3.98) can be chosen the same as described in the previous section. The coefficients $b_{0,0}$ and $b_{0,1}$ are readily given by Eqs. (3.78) or (3.79) with corresponding substitutions from perfect wedge to penetrable wedge.

There is no stationary point for $\tilde{q}_+(\sigma)$, so that its contribution to the integral in Eq. (2.34) is from the endpoints only, which can be given by Eq. (3.26) as

$$\tilde{I}_{e_+}=\frac{1}{jk\tilde{R}_0}\left[\frac{\tilde{f}(\sigma_c)}{\tilde{q}_+^{(1)}(\sigma_c)}e^{jk\tilde{R}_0\tilde{q}_+(\sigma_c)}-\frac{\tilde{f}(0)}{\tilde{q}_+^{(1)}(0)}e^{jk\tilde{R}_0\tilde{q}_+(0)}\right] \tag{3.104}$$

where

$$\tilde{f}(\sigma)=\frac{1}{\sqrt{1-2\tilde{a}\cos\sigma}} \tag{3.105}$$

The integral in Eq. (2.34) can be approximated as

$$\tilde{I}\approx\tilde{I}_-+\tilde{I}_{e_+} \tag{3.106}$$

If $\sigma_c \to \sigma_{1,2}$, $\sigma_1 \neq \sigma_2$, from the last term in Eq. (3.100), there is

$$t_b = \left.\frac{G(s)-b_{0,0}-sb_{0,1}}{s_1^2-s^2}\right|_{s=s_1} = \left.\frac{G^{(1)}(s)-b_{0,1}}{-2s}\right|_{s=s_1}. \tag{3.107}$$

When $\sigma_c = \sigma_1 = \sigma_2$, $s_b = s_1 = s_2 = 0$, Eq. (3.107) becomes $t_b = -G^{(2)}(0)/2$.

Fig. 3.7 shows the integral in Eq. (2.34) as a function of range r evaluated by Eq. (3.106) and numerical integration with parameters, frequency $f = 411$kHz, source position S(150λ,1°,0), wedge angle θ_0=2°, critical angle $\sigma_c = 27.5°$, the initial and the final positions of the receiver **R**(1λ,1°,0) and **R**(75λ,1°,0). For the given parameters, the stationary points are above both endpoints of the integral in Eq. (2.34) when the receiver is very near the apex, as the receiver moves towards to deeper water, one stationary point gets close to, and even traverses the up endpoint. In Fig. 3.7, the solid line is the result given by Eq. (3.106), and the dash line is the result obtained by numerical integration. Eq. (3.106) provides a result which agrees well with numerical integration in this case as shown in Fig. 3.7.

In another case, with the same conditions as in Fig. 3.7, but the receiver moves in z direction at a range 25λ away from the apex. One stationary point is within the endpoints all the time, and the other one gets close to, and traverses the up endpoint as the receiver moves away from $z = 0$ plane. By using Eq. (3.106), Fig. 3.8 shows the result (in solid line) is consistent with numerical integration (in dash line) through the whole region.

Near the caustics, it likely happens that endpoint is close to the stationary points. Fig. 3.9 shows the integral in Eq. (2.34) are evaluated by Eq. (3.106) (in solid line) and by numerical integration (in dash line) from $z = 0$ to $z = 400\lambda$ at range $r = 16\lambda$. The up endpoint of the integral is quite close to the two stationary points at cross range $z = 323\lambda$, where there are $\sigma_c = 1.549$, $\sigma_1 = 1.474$, $\sigma_2 = 1.589$. the agreement is very good especially when cross range z is large as it can be seen.

Comparing the results shown in Figs. 3.7, 3.8 and 3.9, it is found that the approximate representation gives better results when $k\tilde{R}_0$ becomes larger.

3.4 Discussion on the restriction of using SPM in wedge problem

As shown in Secs 3.2 and 3.3, SPM can be used to evaluate the acoustic field very well for the given parameters. It is important to find the limit of using SPM in any relevant situation. The only restriction on SPM applicable to wedge problem is that as mentioned in Sec. 3.1, the parameter

$\Omega = kR_0 \to \infty$, i.e.

$$kR_0 = \frac{2\pi(r^2 + r'^2 + z^2)^{1/2}}{\lambda} \to \infty \tag{3.108}$$

Eq. (3.108) means that if, compared with the wave length λ, the source is far away from the apex or, the receiver is far away from the apex or, the source and the receiver are far away from each other, SPM can provide a very good approximation to the field representation. In practice, most wedge shape ocean channels have a small wedge angle and, for any source which can excite normal modes in these channels, the range of the source must be quite large, thus SPM ia applicable to predicting the fields in these channels. Fig. 3.10 shows the first mode coefficient as a function of range r in the $z = 0$ plane in an ideal wedge, the wedge angle is 2°, the source is at range $r' = 14.5\lambda$ where the water column is just deep enough to sustain the first mode, the solid line is the result by numerical integration, the dash line is the result by SPM. The two results are consistent at large range and, only small errors are found close to the apex. This suggests that representations obtained by SPM can provide a satisfactory prediction of the acoustic field for a source at a range not shorter than the range at which only the lowest mode can be excited in a small angle wedge.

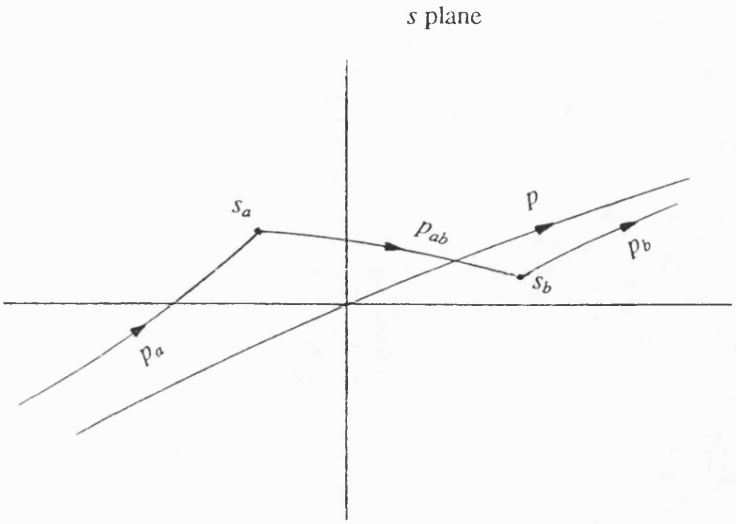

Fig. 3.1 Contours for evaluation of a finite integral.

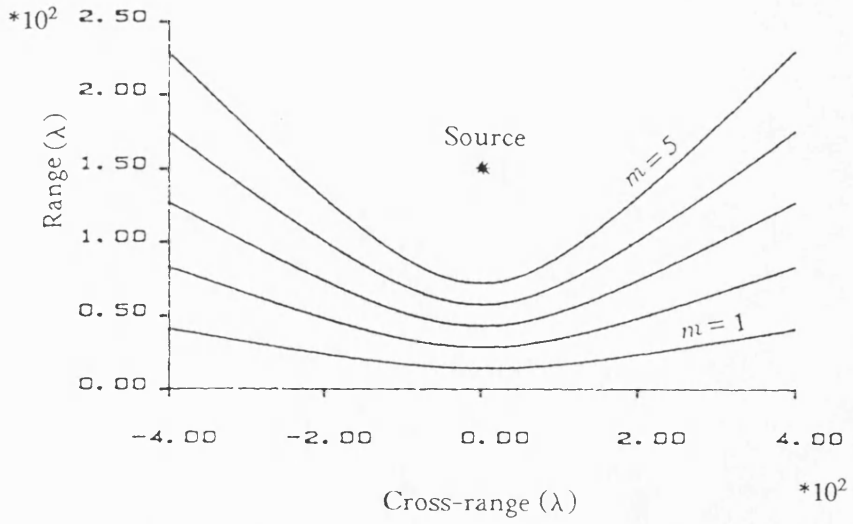

Fig. 3.2 Envelopes of the first five normal modes in an ideal wedge with 2° angle. The source at $r' = 150\lambda$.

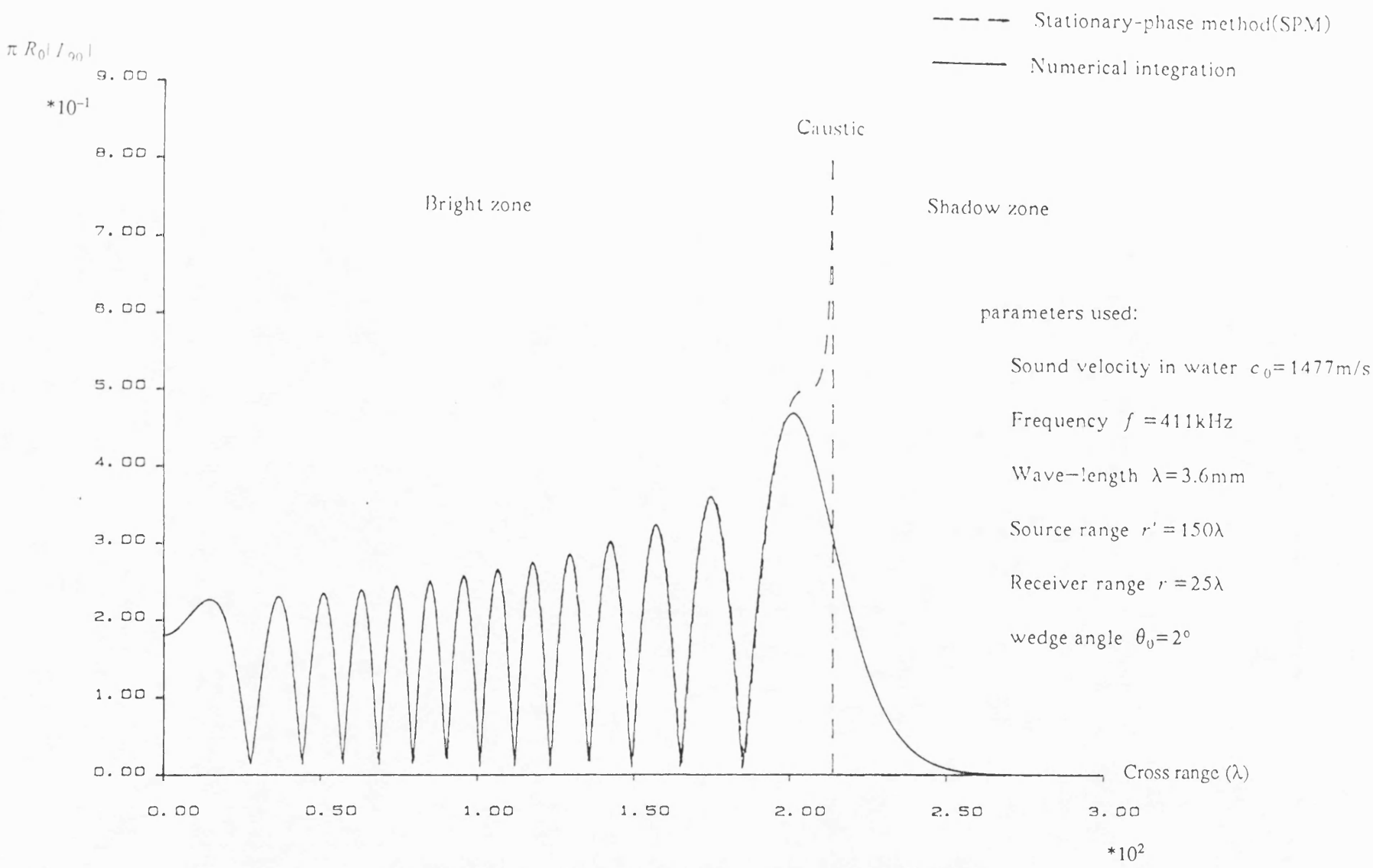

Fig. 3.3 The integral in Eq. (2.21) as a function of cross-range z evaluated by Eq. (3.85) and by numerical integration.

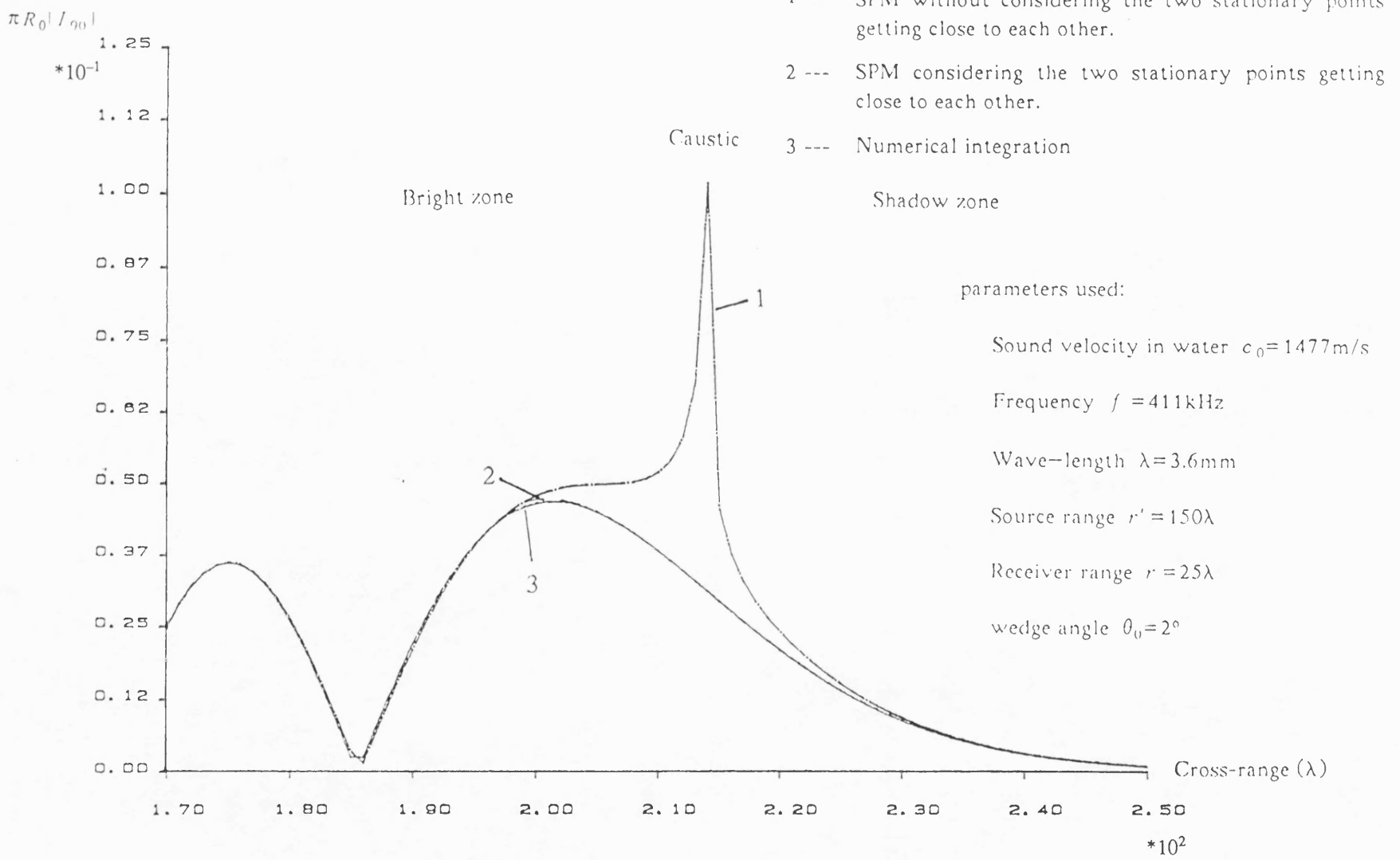

1 --- SPM without considering the two stationary points getting close to each other.

2 --- SPM considering the two stationary points getting close to each other.

3 --- Numerical integration

parameters used:

Sound velocity in water $c_0 = 1477$m/s

Frequency $f = 411$kHz

Wave-length $\lambda = 3.6$mm

Source range $r' = 150\lambda$

Receiver range $r = 25\lambda$

wedge angle $\theta_0 = 2°$

Fig. 3.4 The integral in Eq. (2.21) as a function of cross-range z evaluated by Eqs. (3.85), (3.86), (3.88), and by numerical integration.

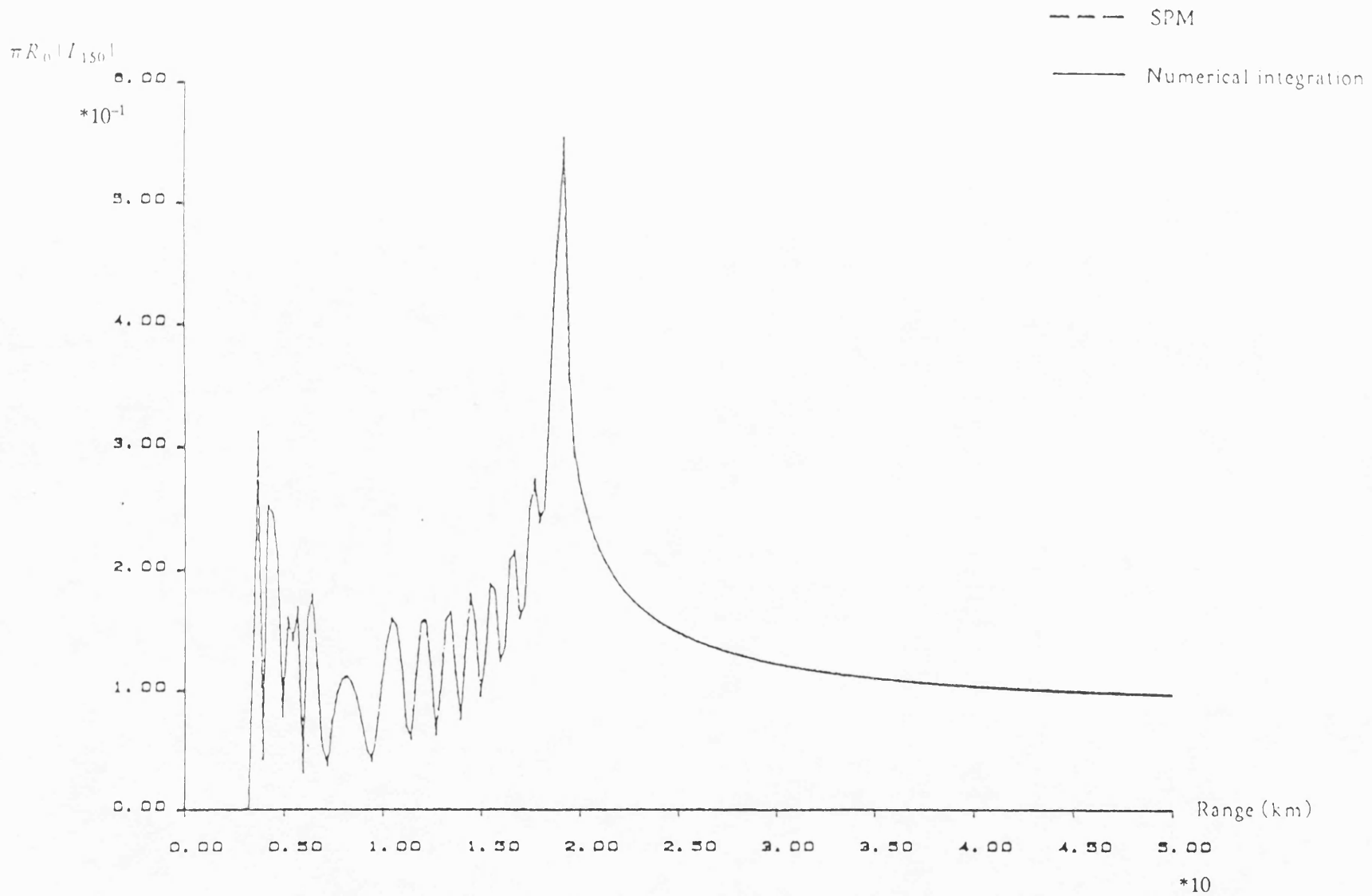

Fig. 3.5 The integral in Eq. (2.21) as a function of range r evaluated by Eqs. (3.85), (3.86), (3.88), and by numerical integration.

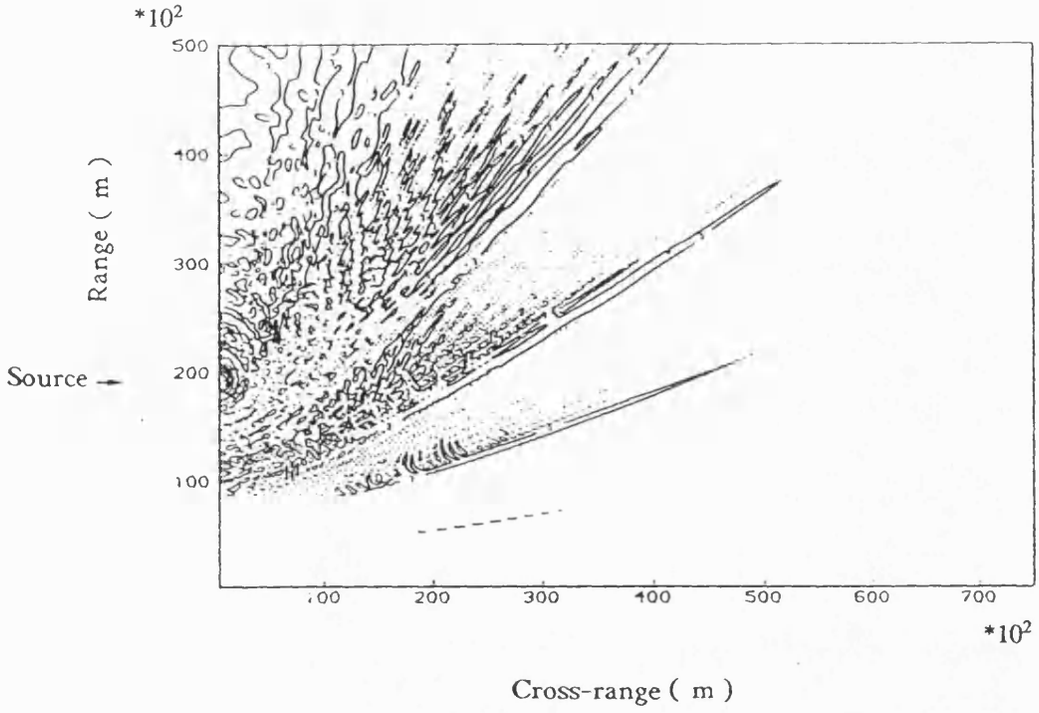

Fig. 3.6a Sound velocity potential $|\Phi|$ at the depth 80m as the function of range (0-50km) and cross-range (0-75km) for 10Hz source at 0 cross-range, 19.1km away from apex. Botom slope is 1.2 degrees, and bottom depth at source is 400m. The cross-range and the range were sampled every 0.25km.

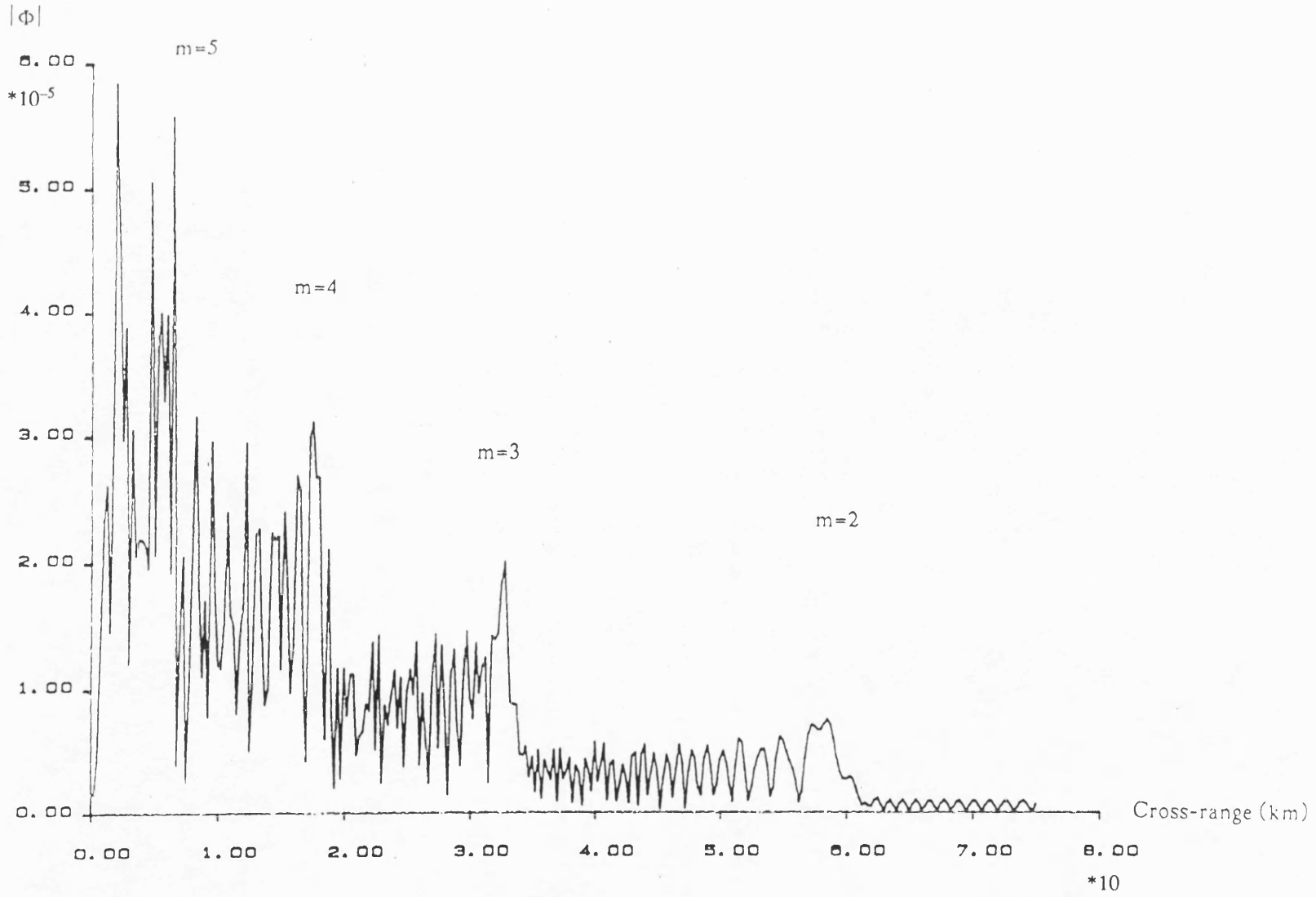

Fig. 3.6b A cross section of Fig. 3.6a at range 25km. The positions of the caustics are indicated.

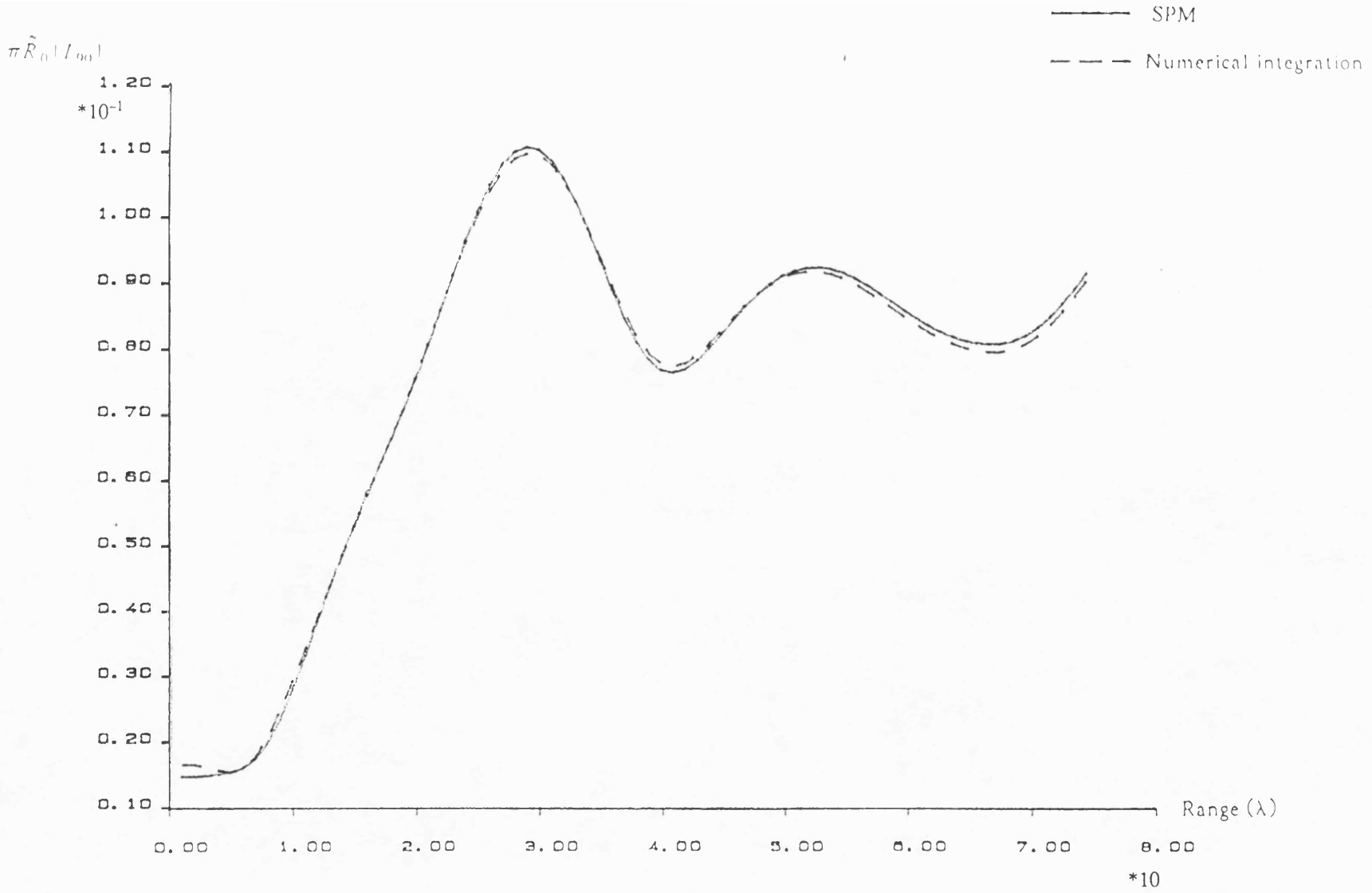

Fig. 3.7 The integral in Eq. (2.34) as a function of range r evaluated by Eq. (3.106) and by numerical integration.

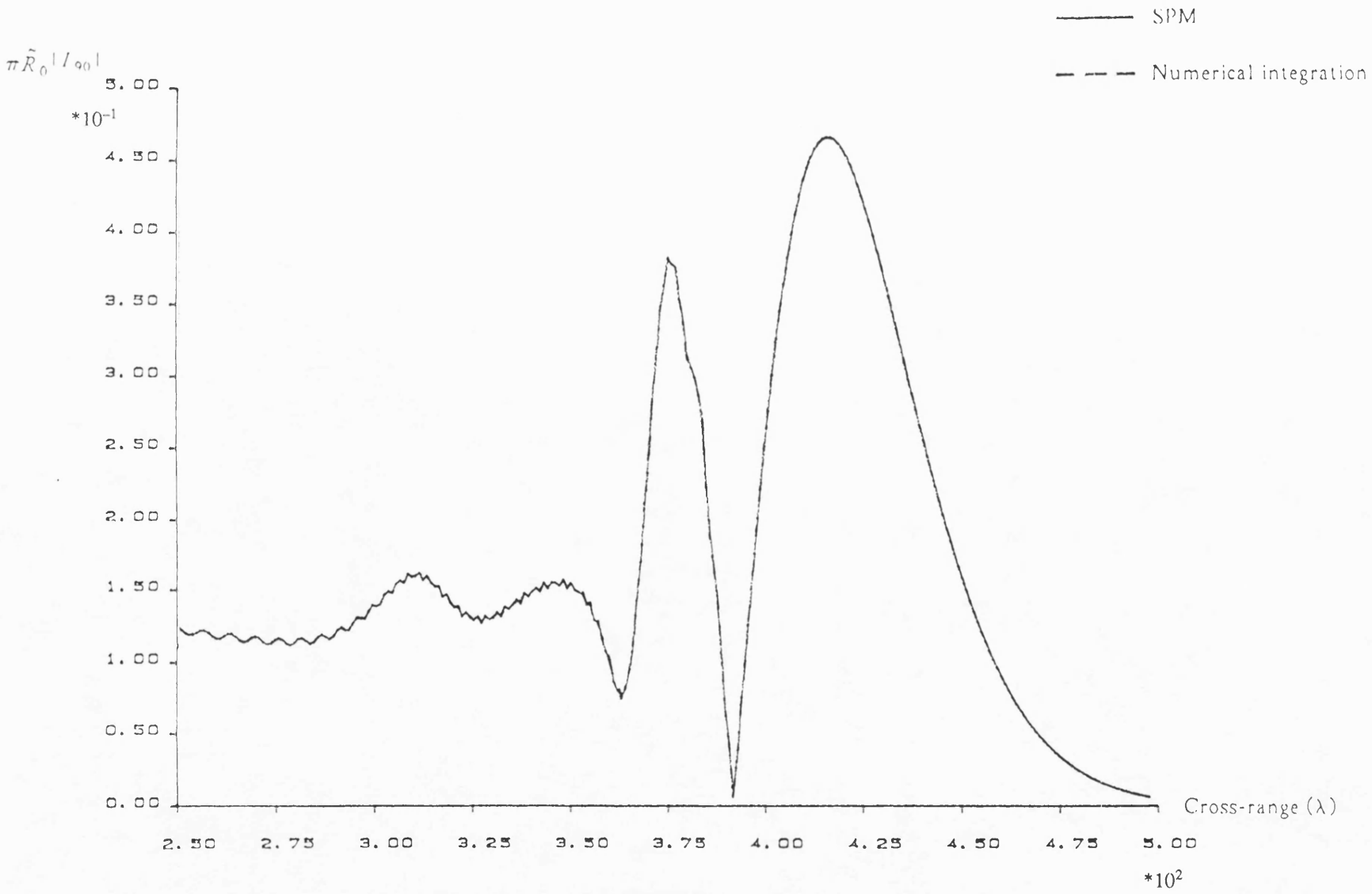

Fig. 3.8 The integral in Eq. (2.34) as a function of cross range z evaluated by Eq. (3.106) and by numerical integration.

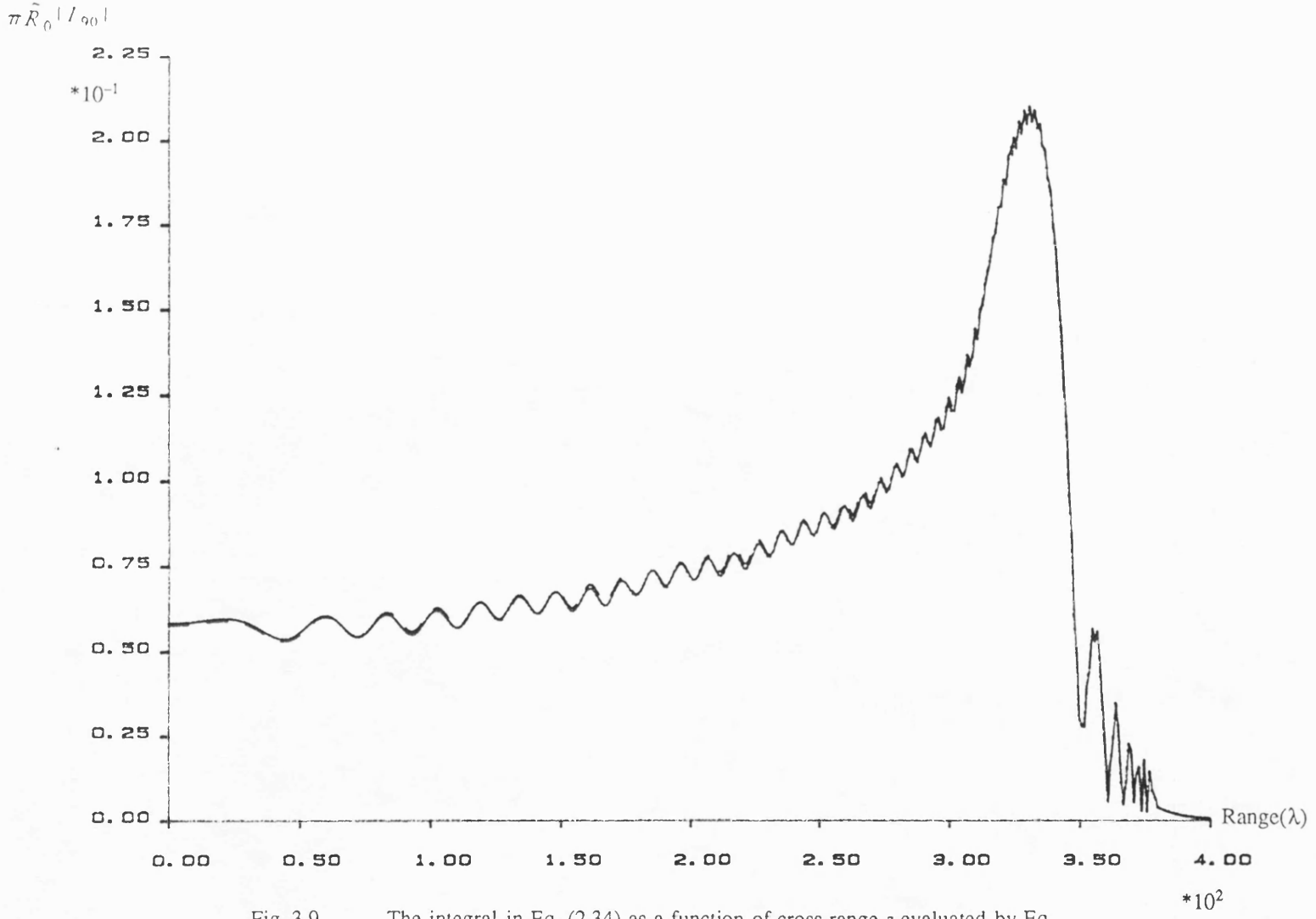

Fig. 3.9 The integral in Eq. (2.34) as a function of cross range z evaluated by Eq. (3.106) and by numerical integration.

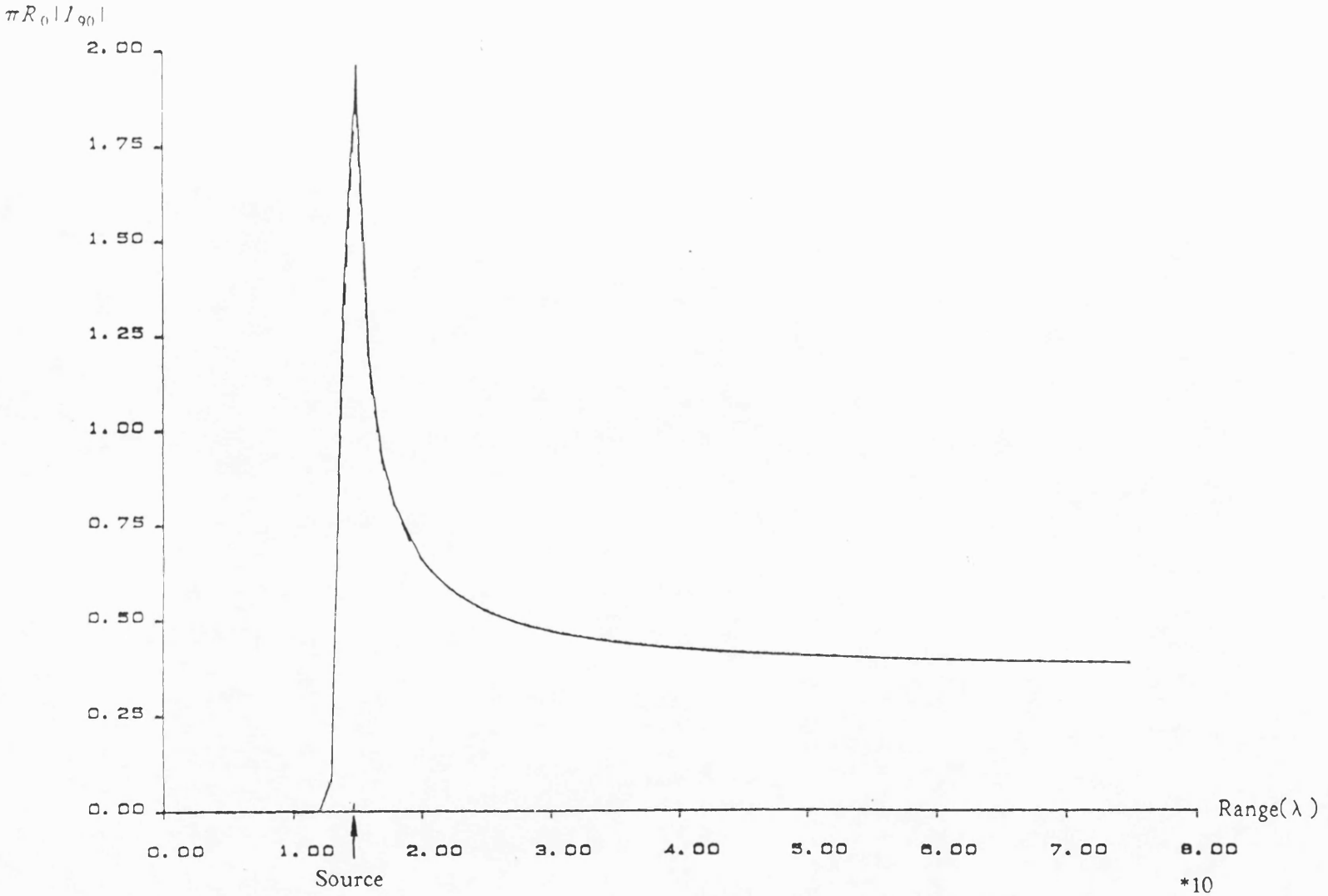

Fig. 3.10 The first mode coefficient (ordinate shows $\pi R_0 | I_{90} |$) in Eq. (2.21) as a function of range r evaluated by SPM (dash line) and by numerical integration (solid line) in $z = 0$ plane, the source at $r' = 15\lambda$, the wedge angle $\theta_0 = 2°$.

Chapter 4. EXPERIMENTAL WORK

4.1 Introduction

An experiment has been carried out in a laboratory tank to investigate three dimensional sound propagation in a wedge-shaped water channel with a penetrable bottom. A sand bottom was used in the experiment. The shear wave is assumed to be negligible here, therefore the sand bottom is considered as a fluid bottom. The sound velocity in the sand bottom is 1665m/s, which is greater than the sound velocity in the water, which is about 1477m/s. Under these conditions, a wedge-shaped channel with a fast fluid bottom can be modelled. A sophisticated system was designed and built to measure the sound pressure three dimensionally in the water and in the bottom as well. The configuration of the experiment is shown in Fig. 4.1. Pulsed signals were used to avoid the interference from the signals reflected by walls of the tank. The signal frequency was 411kHz, and the pulse length was decided according to the position of the source and the measured area. A detailed analysis of the pulse length and the valid measured area is in Appendix A. All the measurements were done automatically with accurate positioning under the control of an Apricot XI microcomputer.

4.2 Water tank

The water tank for the experiment is made of 6mm thick white polypropylene. Its inner dimensions are 1.98m long, 1.73m wide, and 0.25m deep. It was put into an angle steel frame to keep its shape. It was rested on a strong bench made of 75mm×75mm×6.5mm angle steel with 23mm thick plywood on the top. The bench is 2.35m long, 1.9m wide, and 0.28m high. A wedge-shaped water channel can be formed by lifting one end of the bench. It is not difficult to change the angle of the wedge by elevating the end up and down. Two hydraulic jacks were employed to lift the bench at one long end, and two aluminium tubes with alterable height were used to support the bench at the lifted end for a fixed angle.

4.3 Gantry system

A gantry as shown in Fig. 4.2 is designed and made for carrying and moving the hydrophone three dimensionally. The gantry spans over the tank. It is driven by two synchronized stepper motors (motor 3) to move in z-direction (along the tank) with a maximum range limit 2m. The carriage travelling in r-direction (across the tank) on the gantry is driven by one stepper motor (motor 2). The maximum travelling distance for the carriage is 1.55m. There was an apparatus on the carriage for

holding the hydrophone, it is also driven by a stepper motor (motor 1) to move up and down in vertical direction. So that the gantry system can move a hydrophone in 3-dimensions. The distance corresponding to the gantry and the carriage moved one step by the stepper motors is 0.3mm long which is about 1/12 of the wave length. In vertical direction, the resolution is 1mm/1200 steps. The movements of all four stepper motors are controlled by an Apricot XI microcomputer, so the positioning of the hydrophone is accurate.

In order to maintain the hydrophone in a horizontal plane wherever it is moved by the gantry, the rails on which the gantry is run have to be put in a horizontal plane. Four adjustable screws are used at four corners of the frame which supports the rails to adjust the heights of the rails. To check if the the rails are in the same horizontal plane, a thin metal rod was fixed vertically on the carriage with one end just touching the water surface near one corner of the tank, taking this point as a reference, moving the gantry to the other corners, and examining the height of the rod end with respect to the water surface. If the rod end is off the surface, the corresponding end of the rail needs to be adjusted. The horizontal plane was reached by adjusting the screws until the rod just touched the water surface at the all four corners of the tank. Fasten the screws to keep them in right positions. The error that the rails were not on the same plane was believed to be less then 0.2mm.

The running of the carriage on the gantry produces mechanical vibration, which can transmit into the water tank and may cause some errors in the measurement. In order to reduce this effect, the gantry is put on a separate base from the water tank.

4.4 Sand bottom

It is very important to keep the sand bottom free from air bubbles in the experiment, because the boundary condition will be different from the interested case if there are air bubbles in the sand bottom. So that the sand must be deaerated before used. The technique used here is to extract air from the sand in a vacuum vessel. The capacity of the vessel is about 50kg. Put dry sand into the vessel in an amount of about 2/3 of its capacity each time, keep pumping air out from the vessel for one hour at a pressure of 0.5 in Hg, then suck water into the vessel by the low pressure inside to immerse the sand in it. In this way, the air in the sand can be removed. To avoid air being trapped again, the deaerated sand can not be dumped directly from the vessel into the tank simply by turning the vessel upside down if the vessel is not immersed in the water. Since the water in the tank is not deep enough to immerse the vessel, the sand had to be dug out from the vessel and moved to the tank by a small bucket in order to keep the sand under the water all the time in the precess. The whole operation was

long and tedious.

The following problem was that the sand surface had to be levelled horizontally flat. Firstly, the sand was manually made roughly flat. Then a T-shaped scraper was used to make the sand bottom flat. Its working part was 0.43m long, made of 12mm×12mm×3mm angle aluminium, centrally fixed at one end of an aluminium tube which was 9mm in diameter and 0.46m long. The scraper was held on the gantry. Put the tank horizontally, by running the gantry along the tank repeatedly, the sand was levelled in a strip. Because the scraper only 0.43m long, it could only level a strip 0.43m wide each time, the tank is 1.73m across, so the whole bottom needed to be levelled with 5 strips parallelly. Special attention was paid to make the joint parts between these strips as flat as possible. The raising in the joint parts was less than 0.1mm. The unflatness caused by mounting error of the gantry was less than 0.2mm.

Crystal chlorine was put into the tank to inhibit biological growth which may produce air in the sand bottom at the early days of the experiment. Later, it was found that the high concentration of the chlorine produced air in the bottom around the area near the crystal chlorine. The sand bottom had to be processed again; this time the sand was thoroughly stirred by a blender driven by an electrical hand drill to get rid of the air, and leveled again. After the process, the solution of dissolved crystal chlorine was added into the tank regularly instead of using crystal chlorine directly in the tank, thus no air was produced since.

4.5 Electronic instruments

4.5.1 Signal generator and pulse generator

A Function Generator FG1 (FARNELL INETRUMENTS LTD) was used as signal generator. Pulse signal was generated by a pulse generator (PG73N Bipolar Pulse Generator LYONS INSTRUMENTS). The frequency of the signal was 411kHz. The pulse length was 150μs according to the calculation given in appendix A.

4.5.2 Power amplifiers

Two power amplifiers were used in the experiment. One is self made, which was used to drive a directional transmitter (see section 4.9). The other one is a B&K 2713 Power Amplifier, which is used to drive a B&K 8103 hydrophone as an omnidirectional transmitter.

The diagram for the self made power amplifier is shown in Fig. 4.3. It is consist of one emitter follower, two common emitter amplifiers and one push-pull power amplifier. The input signal is coupled through C_1 into the base of T_1. As a emitter follower, T_1 has a high input impedance, which reduce the demanding for signal power output from the signal generator. This can keep the input of the power amplifier steady, so a stable output is obtained. In order to get enough power to drive the push-pull amplifier, T_2 and T_3 are employed as pre-driving and driving amplifiers, both are common emitter amplifiers. The signal output from T_1 is amplified by T_2, and further amplified by T_3. R_{11} and C_5 provide a feedback in order to make the whole circuit steady and improve the signal quality of the output. The output of T_3 is split into two equal amplitude but opposite phase signals by Tr_1, then are fed to the bases of the push-pull amplifier T_4 and T_5. The output of T_4 and T_5 are combined by transform Tr_2 and sent to the matching transform Tr_3. The output of Tr_3 is used to drive the transmitter.

This power amplifier can amplify signal 70dB, and the maximum output is above 20 Watts.

The B&K power amplifier 2713 is designed to work at the frequencies from 10Hz-200kHz. Since the signal frequency was 411kHz, the power amplifier had to be tested to see if it can be used at this frequency. The output response of power amplifier vs frequency was tested with a constant amplitude input. Fig. 4.4 shows that the output is constant over frequencies less than 100kHz, ant it drops slowly between 100kHz-200kHz, and it drops more quickly when frequency is over 200kHz. Because a narrow band signal was used in the experiment, the dropping of the signal amplitude over the band was negligible. So the power amplifier was able to be used in the experiment at the frequency.

4.5.3 Amplifiers and filter

In order to obtain enough signal gain and low noise, two amplifiers and one filter were used in the experiment. One amplifier is Ultra low noise preamplifier 5004, ORTEC Brookdeal, which has a fixed 60dB voltage gain. The other amplifier is System Amplifier TYPE 451, Brookdeal Electronics Ltd, which has a continuously changeable gain from 40dB-80dB. A band filter (KH model 3100 filter) was used to eliminate the noise outside the signal band.

4.5.4 Envelope detector

The envelope detector is used to obtain the signal's amplitude. It contains two major parts. One part is a tuned-amplifier with a buffer, the other part is diode rectifier and a two-pole Butterworth low

pass filter followed by a RC filter. By the envelope detector, the received signals are further amplified and filtered, then the envelopes of the signals are obtained by passing the signals through the rectifier and eliminating the carrier with the low pass filters. The diagram of the envelope detector is shown in Fig. 4.5.

The central frequency of the tuned-amplifier is 412.7kHz, the band width is 39.8kHz, the gain is 18dB. The buffer which itself has 0dB gain gives a good isolation for the amplifier and also provides a large amplitude output through the transform B_3. In order to obtain a good linearity for the envelope detecting, the load of the rectifying diode which is the R_{11}//the input impedance of the low pass filter is chosen so that the load is much greater than the dynamic impedance of the diode, i.e. the impedance of the diode is negligible comparing with the load. Since the dynamic impedance of the diode will increase if the input signal becomes small, it is necessary to make the input signal level as high as possible to satisfy the condition that the impedance of the diode is negligible. Under such conditions, the nonlinearity caused by the diode will be reduced.

According to the design calculation, the Butterworth filter should have a cutoff frequency 53kHz determined by the capacitor C_7, C_8 and resistor R_{12}, R_{13} used in the circuit. A measured frequency response is shown in Fig. 4.6. The cutoff frequency is only 39kHz. The reason is that the capacitor C_7 and C_8 are quite small, the distribution capacitors will add a comparably large proportion to the total capacitors, therefore the cutoff frequency becomes lower than that calculated frequency. To prove this, bigger capacitors and smaller resistors are used for the same cutoff frequency, the frequency response shown in the same picture as previous one indicates that the cutoff frequency is higher than previous one, but it is still lower than the calculated value. This means that as the capacitors used in the filter increase, the effect of the distributed capacitors decrease. Since a high impedance load is needed for the rectifier, the resistors of the filter have to be large and the capacitors have to be small to satisfy the requirement for a good linearity of the circuit. Passing the Butterworth filter, the carrier frequency will be 40dB lower. An RC low pass filter is used after the Butterworth filter to reduce the carrier 20dB further more.

The output response corresponding to the input signal level for the envelope detector is illustrated in the Fig. 4.7. When the input signal is large, the linearity of the output is good, but it becomes worse when the signal is smaller. According to the measurements, the variance is 4dB away from a linear response when the input is 5dB (ref. 7.5mV). The dynamic range above the point is 33dB, which is enough for the experiment. The maximum error introduced by nonlinearity of the diode will

be 4dB.

4.5.5 Sample and Hold

The connection of the Sample and Hold AD585 is shown in Fig. 4.8. The input signal is fed from the Envelope Detector. The S/H control signal that comes from interface 1 is sent to the HOLD end. When S/H command is high, the circuit is in sample mode, it is a buffer with gain equal to +1. When S/H is changed from high to low, the circuit is switched to the hold mode, the value of the input signal at this moment, is held in the circuit. An 150p additional capacitor is used in the circuit to reduce the dropping rate.

4.5.6 Interface for signal transmitting and receiving (Interface 1)

The diagram of the interface for signal transmitting and receiving (interface 1) is shown in Fig. 4.9. The function of the circuit is to send trigger signals to the pulse generator and the sample and hold circuit from the Apricot XI computer.

In the circuit, TTL components are used whose speeds are high enough to be compatible with the computer. In order to achieve precisely time delay between two pulses, the circuit is connected directly to the expansion slot of the computer and assembly language is used. Since the IEEE-488 bus is also connected with the computer through the same expansion slot. It is possible that this interface may be trigged when the computer is using the other devices on the IEEE-488 bus, thus the measurement may effected in two ways. One is that it will make the pulse generator transmit signals in some improper times. In this case, the signal of interest may be contaminated by some unwanted signals which add errors to the measurement. The other way is that the sample and hold will be trigged not in the right time, so the measured values are not valid. The interface is designed to avoid these problems by using a 8-input NAND, which can reduce the possibility of misactions taking place, and by using one shot circuits to ensure that each time just two pulses are sent, one is to the pulse generator to start signal transmitting, and another one is to the sample and hold during the time period from the beginning of the signal transmitting until the measured result being read into the computer. The time width of the one shot is adjustable by using different resistors and capacitors in the circuit.

Fig. 4.10 shows the logic relations for the inputs and outputs. The signals are input from data line 4 and data line 8, all control lines of IEEE-488 are used as one control end through the 8-input NAND. When the computer sets up EOI, DAV, NEFD, NDA, IFC, and ATN low, SQR and REN

high, the output of the NAND gate becomes low, if a positive pulse is fed to 4 or 8, the NOR gates will output a positive pulse, the inverters change the positive pulse to negative pulse. The rising edge of the output PG is used to trig the pulse generator, while the falling edge of the output of SH is used to trig the sample and hold circuit.

4.5.7 Stepper motor controlling interface (Interface 2)

The diagram of stepper motor controlling interface (Interface 2) is shown in Fig. 4.11. By using this interface, the computer can provide the clock signals and the direction control to the stepper motor drive boards to control the stepper motors. There are four stepper motors controlled by the computer. The motor 1 moves the hydrophone up and down, the motor 2 moves the carriage on the gantry in r direction (across the tank), the remaining two motors work synchronistically as motor 3 to drive the gantry moving in z direction (along the tank).

The interface is made of C-MOS. It is connected with the IEEE-488 bus. Since the stepper motor drive boards are C-MOS or Open Collector TTL compatible. The logic inputs, 0 (low) and 1 (high), corresponding voltages are 0V and 12V for the boards. But the logic high for the IEEE-488 Bus is only 3V, it is not capable to make the C-MOS and the stepper motor drive boards whose logic high is 12V work. In order to cope with this problem the transistors T_1-T_7 are used as buffers which can provide high voltage outputs to drive C-MOS and the boards. The REN is the control line of the interface. Data line 1 and data line 5 are used as clock signal and direction control inputs for motor 1, data line 2 and data line 6 are for motor 2, and data line 3 and data line 6 are for motor 3, respectively. C_1 and D_1 are the outputs of the clock signal and the direction control to the stepper motor drive board for motor 1, C_2 and D_2 are to the board for motor 2, and C_3 and D_3 are to the board for motor 3. Fig. 4.12 shows how the interface works. When the input REN is 1 (high), T_1 is 0 (low), this makes AG_1, AG_2, and AG_3 output 0s, no clock signal can be sent to the boards, all stepper motors stay still. When REN is changed to 0, t_1 becomes 1, the input of AG_1, AG_2, and AG_3 are 1, if a clock signal is sent to input 2 by the computer, it will go through T_2, AG_2 to the analogue switch S_1 and S_2, then it is sent to the stepper motor drive board to drive the motor 2 which moves the gantry across the tank. The outputs of D_1, D_2, D_3 are used to control the directions of the motors. Because the gantry driven by the motors can only move within limited distances both along and across the tank. The limit switches LS_1, LS_2, LS_3, and LS_4 have to be employed to stop the the gantry at the distances. The analogue switches are under control of both limit switches and the outputs of the direction control. Usually the limit switches are turned on to 1. Since the outputs of the AG_4 and AG_5

are complementary, so either S_1 is on, S_2 is off or S_1 is off, S_2 is on to provide a path for the clock signal from AG_2 to the board unless limit switch LS_1 or LS_2 is switched to 0 to stop the motor. The process for controlling the motor 3 is the same as for the motor 2, but it is more simple for the motor 1 because there is no limit switch in use.

4.6 Apricot XI Microcomputer

The Apricot XI Microcomputer is used to compute the sound field, control signal transmitting and receiving, control the gantry which carries the receiver to move three-dimensionally, and collect and store the data measured in the experiment. By means of an IEEE-488 bus, the computer can control the movement of the gantry and read the measured data in the sample and hold circuit. Through the interface 1, the computer can trig the signal generator and the sample and hold to transmit signal and receive signal. The computer can be connected to the mainframe such as GOULD by means of KERMIT through the serial interface RS232C. This provides a convenient way to use some sophisticated facilities on the mainframe. Most programs used for the experiment are written in FORTRAN language. In order to set the sample time precisely, assemble language is used to generate the pulses which are the triggers for the pulse generator and the sample and hold circuit. The time delays from signal transmitted to signal received were calculated by the computer. Although The sample and hold circuit should be trigged according to the exact time delays, the computer can only give discontinuous time delays due to the limit of the time period of its clock. A minimum time interval about 1.3μs is achieved on the computer. There was no problem caused by such a small discontinuity of the sample time in this experiment.

4.7 IEEE-488 bus

The IEEE-488 bus is an international standard which enables multiple devices, such as computer, electronic test and measurement instrumentation, computer peripherals etc. to be easily integrated into a complete system.

A 16 line bus is used to interconnect up to 15 separate devices each connected in parallel to the bus. Eight of the 16 lines are used to transmit data bytes, and the other eight lines are divided so that 3 are used to for a positive "handshake" to permit asynchronous operation of the devices, while the remaining 5 lines are used to for control purposes. The pin connections of the IEEE-488 connector are described as in Table 4.1.

Table 4.1. Pin connections of IEEE-488 connector

Function	Pin	Pin	Function
Data line 1	1	13	Data line 5
" 2	2	14	" 6
" 3	3	15	" 7
" 4	4	16	" 8
EOI	5	17	REN
DAV	6	18	GND for DAV
NRFD	7	19	GND for NRFD
NDAC	8	20	GND for NDAC
IFC	9	21	GND for IFC
SRQ	10	22	GND for SRQ
ATN	11	23	GND for ATN
Shield	12	24	Signal GND

Where EOI, DAV, NRFD, NDAC, IFC, SRQ, ATN, and REN are control lines.

The IEEE-488 bus is connected to the computer through one expansion slot on the computer. There is one 8-bit A/D converter in the IEEE-488 bus which is used to read measured data from the sample and hold. By using the IEEE-488, The computer can also send commands and data to control the speeds and the directions of the stepper motors to move the gantry which carries the receiver to the positions where the sound field is going to be measured in the experiment.

4.8 Hydrophone and its head-amplifier

Usually, when a hydrophone is used to measure the sound pressure in a acoustic field, the output is considered as the value of the pressure at the "acoustic center" of the hydrophone. Since any hydrophone is not a point, it has a certain size, so the value measured by the hydrophone is not equal to the pressure at its acoustic center point, it is an integration of the pressure on the surface of the hydrophone. To achieve a high spatial resolution, the hydrophone should be as small as possible. But the sensitivity of the hydrophone will be very low if the hydrophone is too small. To make a valid measurement, the sensitivity should be high enough to provide a satisfactory signal to noise ratio. Therefore it is a compromise to choose a hydrophone with a relatively small size and an acceptablely

low sensitivity.

The hydrophone that is employed in the experiment is a cylindrical ceramic hydrophone which is 0.4mm in diameter and 0.7mm in length. It is mounted on the top of a thin needle with a diameter just about 0.6mm. Since the wave length is 3.65mm, the dimensions of the hydrophone are smaller than the half wave length, it can provide a satisfactory spatial resolution for the measurement. The scattering caused by the needle will be negligible because the wave length is many times greater than the diameter of the needle. There was a head-amplifier which was built for the hydrophone with 10dB gain. In the test measurements, it was found that the Signal to Noise Ratio was not high enough to give satisfactory results. The noise mainly came from the head-amplifier. Then, another head-amplifier, a low noise emitter follower was built to provide a good impedance matching between the hydrophone and the amplifier.

The emitter follower was built with a low noise transistor, one C type battery was used for its power. The head-amplifier is put into an aluminium alloy diecast box with a size of 89mm×35mm×30mm. It can increase signal to noise ratio about 6dB higher than the previous one.

In order to protect the hydrophone from damage when measurements were carried out in the sand, a thin epoxy layer was coated over the hydrophone. The sensitivity of the hydrophone was slightly affected, but it would not raise any serious problem to the measurements because all the measurements were done are relative.

4.9 Transmitters

Two types of transmitters were employed as sources for different purposes in the experiment, one is directional, another one is omnidirectional.

4.9.1 Directional transmitter

A directional transmitter has been made with a piece of VERNITRON Ltd. PZT-4 piezoelectric ceramic. The ceramic is 20mm×20mm×4mm in dimensions, the resonant frequency of the ceramic is 500kHz. Since the water column is very shallow in the experiment, the transmitter should be small enough to be put in the water column without touching either the surface or the bottom. So that the ceramic is cut into a smaller piece with dimensions 10mm×10mm×4mm. This piece of ceramic is put into a perspex case, the working face is glued at the front side of the perspex case which is a quarter wave length thick in order to obtain maximum sound energy output. The back of the ceramic is stuck

on a piece of graphite material which is highly absorbent to improve the performance of the transmitter. Comparing this transmitter with another one which is the same except that it is air backing, the band width is wider, therefore a better wave-shape is obtained. The impedance characteristics of the transmitter in water is shown in Fig. 4.13

The beam pattern of the transmitter was measured. The result is shown in Fig. 4.14 with the thicker line. To make a comparison, the beam pattern of an ideal square-shaped transmitter is also drawn in thinner line. It can be seen that the main beam is slightly wider, and the first side-lobes of the transmitter is higher than the ideal one. A possible explanation is that the epoxy resin used to stick the ceramic to the perspex case formed a joint at the edges of the ceramic, which may introduce some focusing effect which results in the high side-lobes.

4.9.2 B&K hydrophone 8103

To observe mode pattern in the wedge, an omnidirectional source is needed. A B&K hydrophone 8103 is used as an omnidirectional transmitter in the experiment. Since B&K hydrophone 8103 is designed to work at frequencies from 0.1Hz-200kHz, it is necessary to know its directivity at frequency 411kHz to see if possible to use it as an omnidirectional transmitter in the experiment. The tested result is shown in Fig. 4.15, it indicates the transmitter has a maximum distortion about 1dB in the horizontal section. So that it is quite safe to say the transmitter is still omnidirectional at such a frequency.

4.10 Acoustic properties of the water and the sand bottom

4.10.1 The density of the water and the sound velocity in the water

Tap water was used in the experiment. The density of the water is 1g/cm^3. The sound velocity in the water was predicted by Wilson formula[70] as follow

$$c_0=1449.14+4.5721T-0.044532T^2-0.00026045T^3+0.160272P+$$

$$+1.39799(S-35)+0.00169202(S-35)^2-0.011244T(S-35)+\cdots\cdots \quad (4.1)$$

where c_0 is the sound velocity in the water in meters per second m/s, T is temperature in degrees centigrade °C, P is pressure in kilograms per square centimeter kg/cm^2, and S is salinity in parts per thousand °/$_{oo}$. The high order terms are neglected here. This formula is applicable in the ranges -4°C<T<30°C, 1kg/cm^2<P<1000/cm^2, and 0 °/$_{oo}$<S<37 °/$_{oo}$ with a standard deviation from the

mean within 0.3m/s. For the water used in the experiment, $S = 0$, $P = 1$ (since the water was very shallow, only a few centimeters, the pressure in the water was considered as a constant that was equal to 1kg/cm^2, *i. e* one atmospheric pressure), then the sound velocity was a function of the temperature, two values were predicted at two different temperatures according to the Eq. (4.1), the results are in Table 4.2.

Table 4.2 Sound velocity in the water

Temperature (°C)	Pressure (kg/cm^2)	Salinity (°/$_{oo}$)	Sound velocity (m/s)
17.5	1	0	1474.29
18.5	1	0	1477.39

c_0 was also measured in a test run under the same condition. The arrangement for the measurement as shown in Fig. 4.16, the transmitter was fixed half way from the water surface to the bottom, the hydrophone was put at same depth and about L_o=380mm away from the transmitter at the initial range first, pulse signal was transmitted and received under the control of the computer, then the hydrophone was moved a distance ΔL=149.25mm away from the previous position, transmitting the signal and recording the arrived signal again. In order to avoid the interference from the reflected signals, and to count the time of the signal travelling more precisely, 3μs short pulse was used. The times for the signals propagating from the source to the receiver at different distances were figured out by counting the time delays from signal transmitting to receiving set by the computer (details in appendix B) Δt, thus The sound velocity was obtained as $c_0=\Delta L/\Delta t$. At 17.5°C, the measured sound velocity was 1477m/s. This value is quite close to the predicted value by Eq. (4.1). The difference in the measured value is mainly caused by the inaccurate time reading which is about 0.57%. Thus we choose sound velocity in the water equal to 1477m/s as a parameter in the prediction of the sound field.

4.10.2 The density of the sand bottom and the sound velocity in the sand bottom

The density of the sand bottom was obtained by measuring the weight and the volume of a certain amount of water-saturated sand. The result is in Table 4.3.

Table 4.3 The density of the sand bottom

Weight (g)	Volume (ml)	Density (g/cm^3)
807.2	425	1.899

To predict sound velocity in sediment, a number of empirical formulas[71,72] are available if some parameters such as the mean diameter of the grain in the sediment or porosity of the sediment can be found. Here, the empirical formula given by Hamilton[71] is used, which is expressed as

$$c_1=1936.2-87.33(m_\phi)+4.45(m_\phi)^2 \tag{4.2}$$

where c_1 is sound velocity in sediment, and m_ϕ is a average diameter of the grain size of the sedimental materials in ϕ-scale, the definition of ϕ is

$$\phi=-\log_2(\text{ of grain diameter in milimeters}) \tag{4.3}$$

For the sand used in the experiment, the mean diameter is 50μm[73], and m_ϕ is 4.32, substituting this value into Eq. (4.2), the sound velocity in the sand bottom is predicted to be 1641.9m/s.

It is not like the sound velocity predicted by Eq. (4.1), the sound velocity predicted by Eq. (4.2) is less accurate. Although the value can provide a reference, a more accurate value is needed for the comparison between the experimental results and theoretical model. In order to obtain the right sound velocity in the bottom, an experiment was carried out to measure Rayleigh reflection coefficient of the bottom. The Rayleigh reflection coefficient V from a plane surface is given[65] by

$$V=\frac{\frac{\rho_1}{\rho_0}\cos\phi_0-\frac{c_0}{c_1}\cos\phi_1}{\frac{\rho_1}{\rho_0}\cos\phi_0+\frac{c_0}{c_1}\cos\phi_1} \tag{4.4}$$

where c_0 and c_1 are the sound velocity in the water and in the bottom, ρ_0 and ρ_1 are the density of the water and the bottom, ϕ_0 and ϕ_1 are the angles of incidence and refraction, respectively. At the normal incidence of wave ($\phi_0=\phi_1=0$), Eq. (4.4) gives

$$V=\frac{\rho_1 c_1-\rho_0 c_0}{\rho_1 c_1+\rho_0 c_0} \tag{4.5}$$

Rearrange Eq. (4.5), one can have

$$c_1=\frac{(1+V)\rho_0}{(1-V)\rho_1}c_0 \tag{4.6}$$

If the reflection coefficient V, the densities of the water and the bottom ρ_0 and ρ_1, the sound velocity in the water c_0 are known, the sound velocity in the bottom can be calculated by Eq. (4.5).

At the normal incidence of wave, the amplitude of the reflected wave p_{br} from the bottom is

$$p_{br}=Vp_i \tag{4.7}$$

where p_i is the amplitude of the incident wave, and the wave reflected from the water surface is

$$p_{sr}=-p_i \tag{4.8}$$

With the same amplitude of the incident wave, the reflection coefficient can be found as

$$|V|=\left|\frac{p_{br}}{p_{sr}}\right| \tag{4.9}$$

An experiment was done to measure the reflection from the bottom and the surface in normal direction, therefore the reflection coefficient of the bottom was able to be worked out by comparing the amplitudes of the reflected signals from the bottom and the surface. Fig. 17 shows the setup for the measurements. The directional transmitter was used in the measurement. It was fixed on the carriage and faced down to the bottom, the distance from the transmitter to the bottom was 87.5mm. By means of a transmitting and receiving interchange switch, the transmitter also worked as a hydrophone to receive the signal reflected from the bottom. To examine the bottom thoroughly, its reflections in normal direction were measured point by point over an area. The measured area was 0.7164m×0.7164m (200λ×200λ), and the distance for two neighboring sample points in r-direction or in z-direction was 10.75mm (3λ). The amplitudes of reflected signals were recorded and stored in the computer. It is found that the amplitude of the reflected signals fluctuated at different positions. This indicated the bottom was inhomogeneous, so the sound velocity had to be calculated by taking the mean value of the reflected pressure signals. After measuring the reflection from the bottom, the transmitter was put to face up to the water surface to measure the reflection from the surface with a distance 87.5mm between the transmitter and the the surface. The results are in Table 4.4.

Table 4.4 Amplitudes of reflected waves and the bottom reflection coefficient

Bottom reflection $\bar{p}_{br}(v)$	surface reflection $p_{sr}(v)$	reflection coefficient $\lvert\bar{V}\rvert$	relative deviation ε_v
3.97	3.584(-10dB)	0.369	0.04562

With the reflection coefficient in Table 4.4 and Eq. (4.6), the sound velocity is worked out, which is 1687m/s. Comparing the value predicted by Eq. (4.2), the difference is obvious. To select a more reasonable value of the sound velocity in the bottom, the sound field as a function of distance from the source in a shallow water channel with horizontal bottom was measured. The field contains only the first two normal mode at long distance. In order to compare the measured result, shallow water theory[12] is used to predict the sound field in the channel with a sound velocity in the bottom equal to 1665m/s. Very good agreement is found in the interference pattern of the two normal modes between the experimental result and the theoretical prediction (details in Appendix C). This suggests the sound velocity in the bottom should be about 1665m/s. The relative errors between the this value and the predicted values by Eq. (4.2) and (4.6) are about 1.4% and -1.3%, respectively. So that it is a reasonable value.

4.11 The procedures of the experiment

Firstly, the tank was lifted at one long end to form a wedge-shaped water column, the desired angle was reached by adjusting the height of the lifted end relatively to the other end. The angles used in the experiment were 1, 2, and 3 degree with deviations less than 3%.

To form an apex by the sand bottom and the water surface, the water was put into the tank with the surface a little lower than the sand bottom at the lifted end. Because of the evaporation, the water level becomes lower and lower. In order to keep the water level in the tank unchanged, a tap was used to add water all the times, the opening of the tap was so that the added water was about equal to the water evaporated.

The transmitter was placed at the position determined by the area where the measurement was going to be done as calculated in Appendix 1. The hydrophone was placed at the initial position.

Finally, the measurement was started after the following parameters were input into the computer;

1. Distance from the transmitter to the apex
2. Initial position of the hydrophone
3. Step lengths corresponding to neighbored measuring points in r-direction, in z-direction, and in depth direction
4. Sound velocity in the water
5. Pulse length of the signal (in microsecond)
6. Measured ranges in r-direction, in z-direction, and in depth direction
7. Angle of the wedge
8. Waiting time for the system settling down
9. Measured times for receiving a reliable datum
10. Allowed deviation

The pulse length and the measured ranges in r-direction and in z-direction were determined by the size of the tank and the position of the transmitter as in Appendix A. Since the moving of the gantry caused mechanical vibrations, measurement could not be started immediately after the gantry moving the hydrophone to a new position, a waiting time was given in order to reduce the inteference from the mechanical vibrations. Because of unavoidable noise interferences, the measured values were changed from time to time. In order to get reliable values, the sound pressure in one position was measured several times (given by parameter 9), the computer examined the measured values, if the deviation (given by parameter 10) was greater than allowed value, the sound pressure had to be measured again, if the deviation was within the allowed range, the average value of the measured values was taken and stored in the computer.

When the measurement was started, the computer sent the first pulse to trig the pulse generator, a long pulse signal was transmitted, the signal was received by the hydrophone, amplified and filtered, the envelope of the signal was obtained by a rectifier and a low-pass filter, after a time delay which

was the time for the signal propagating from the source to the receiver, plus the pulse length and the response time of the receiving system, the computer sent the second pulse to trig the sample & hold circuit, the sampled value was the amplitude of the sound pressure at hydrophone's position. The above process was repeated till a satisfactory value was obtained. It took about 10 seconds to get one valid value. Then the hydrophone was moved to next position to measure the sound pressure there until it reached the final position. For a complete measurement of the sound pressure on a plane in a wedge, it took several hours.

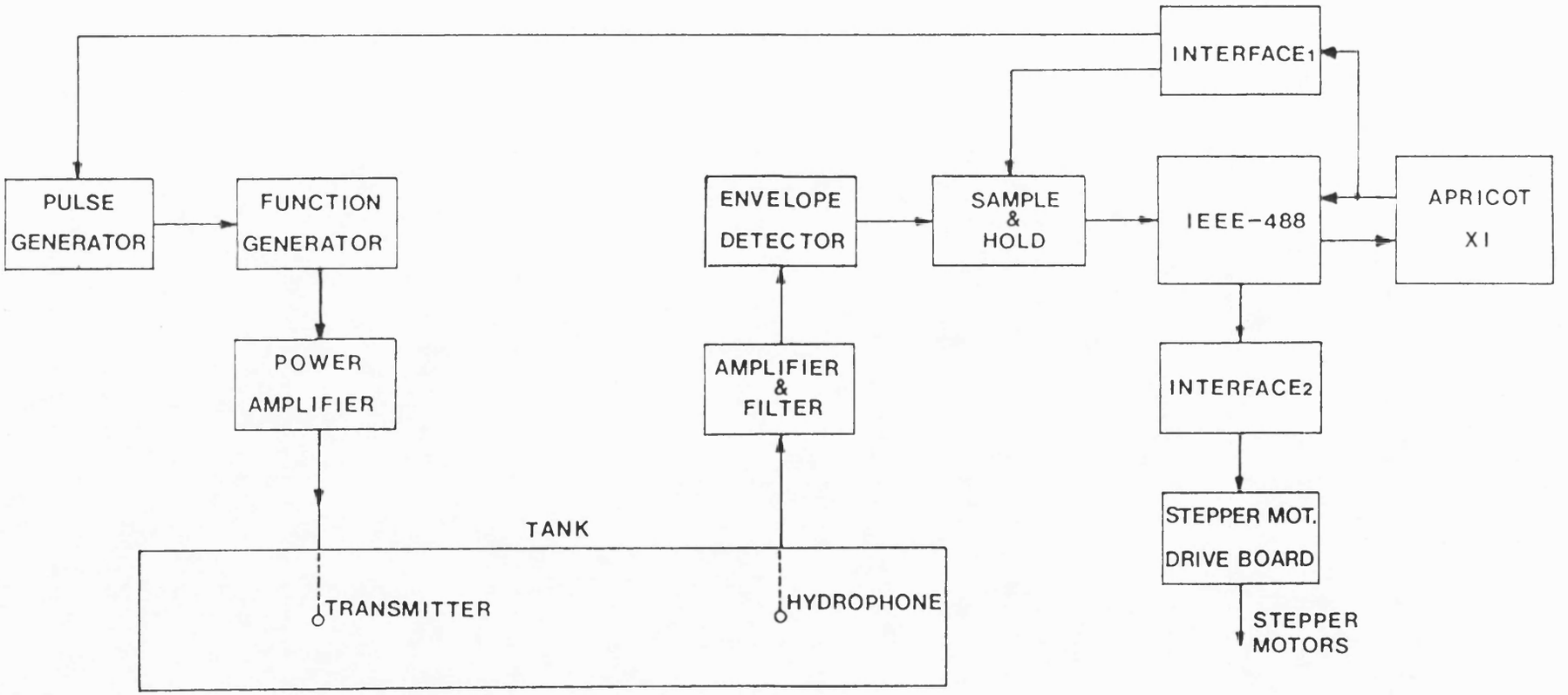

Fig. 4.1 Configuration of the experiment.

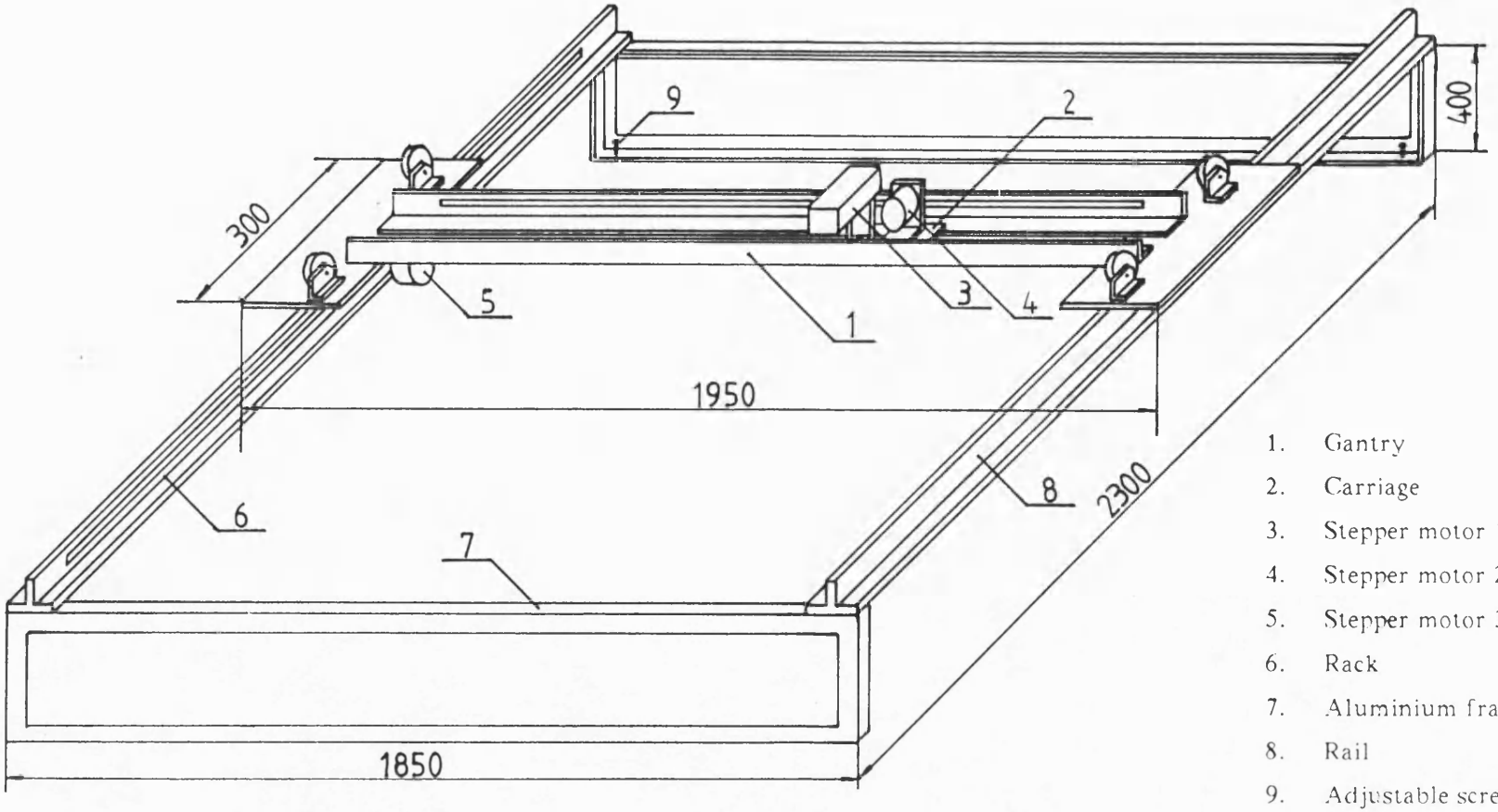

1. Gantry
2. Carriage
3. Stepper motor 1 and its gear box
4. Stepper motor 2
5. Stepper motor 3
6. Rack
7. Aluminium frame
8. Rail
9. Adjustable screw

Fig. 4.2 Schematic drawing of the gantry.

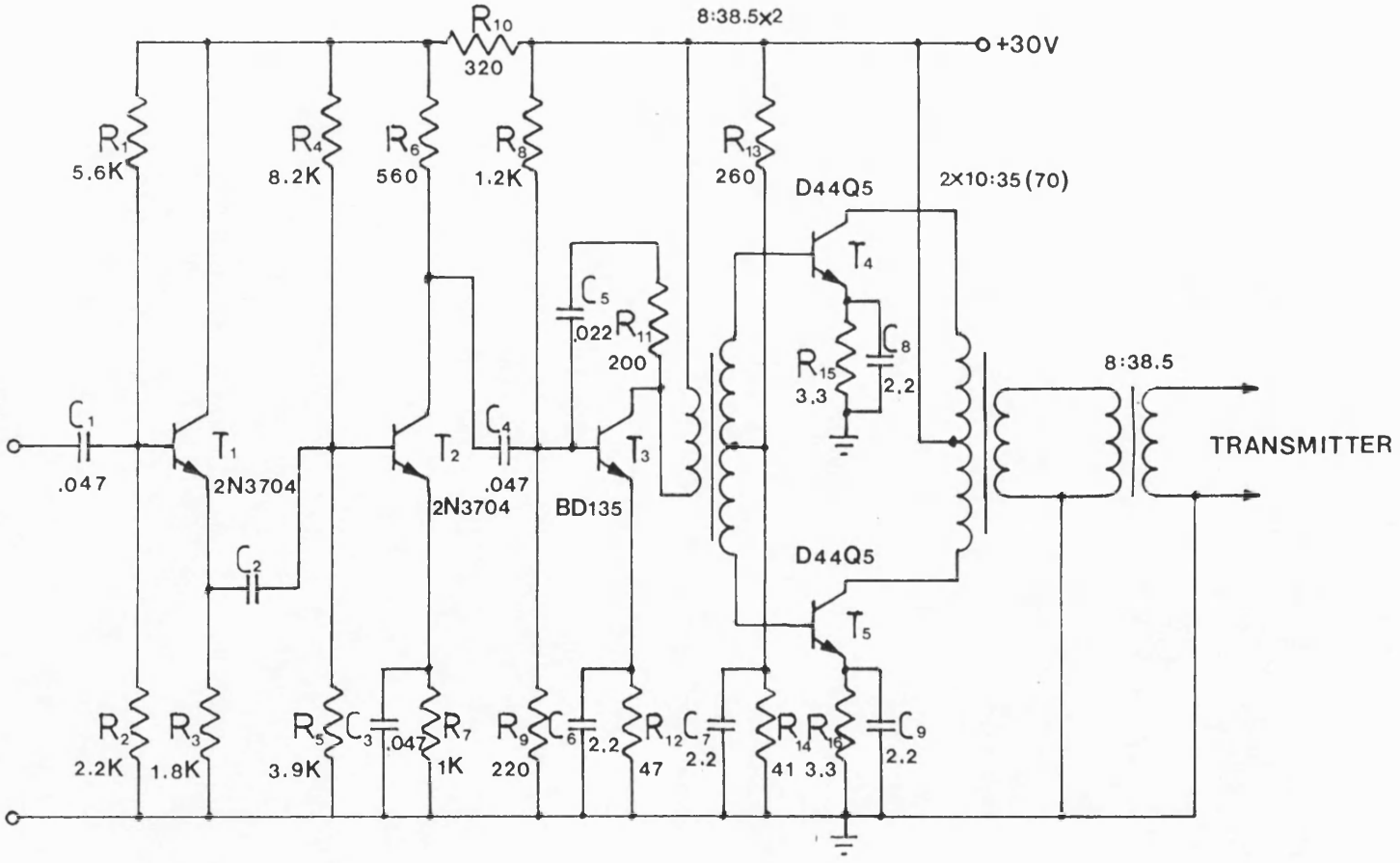

Fig. 4.3 Schematic diagram of the power amplifier.

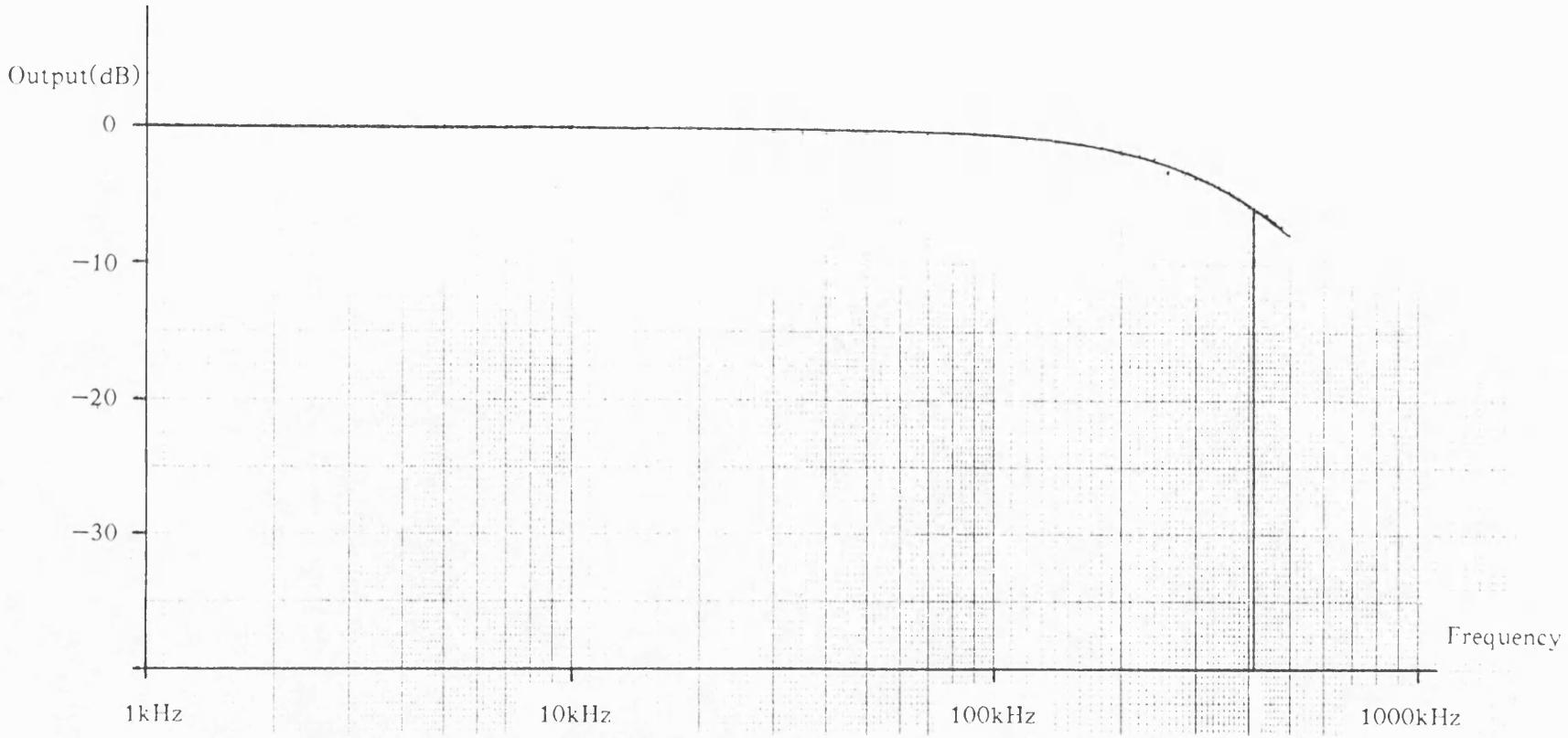

Fig. 4.4 Output response of the B&K power amplifier 2713 vs frequency.

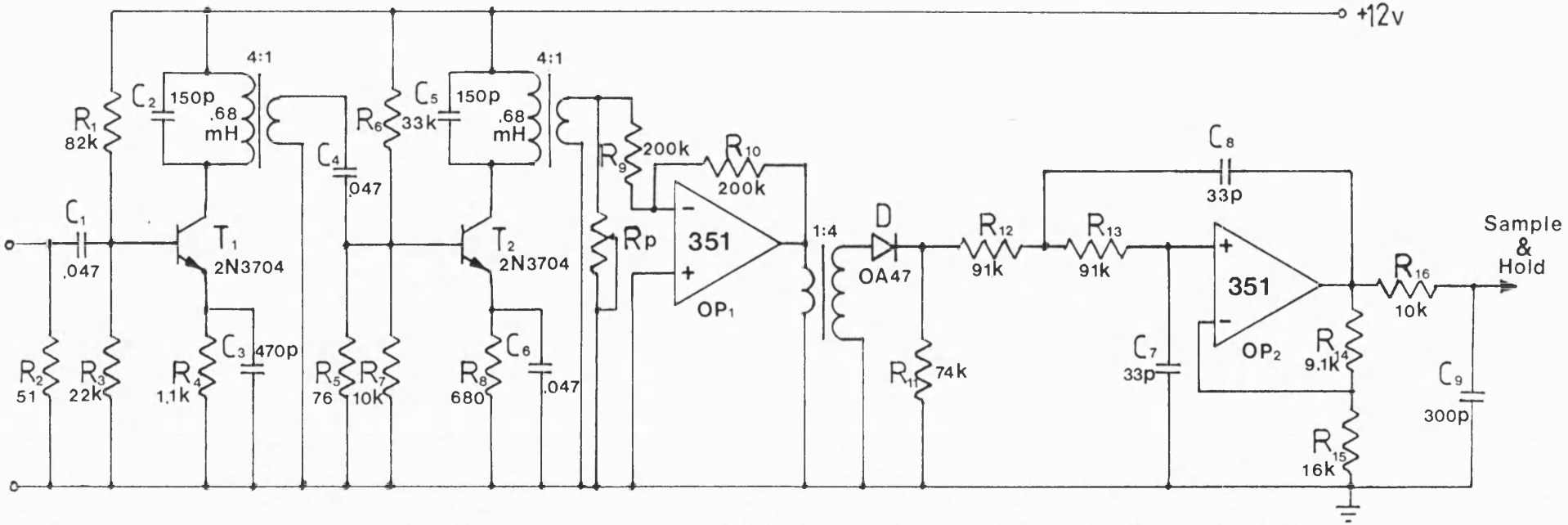

Fig. 4.5 Schematic diagram of the envelope detector.

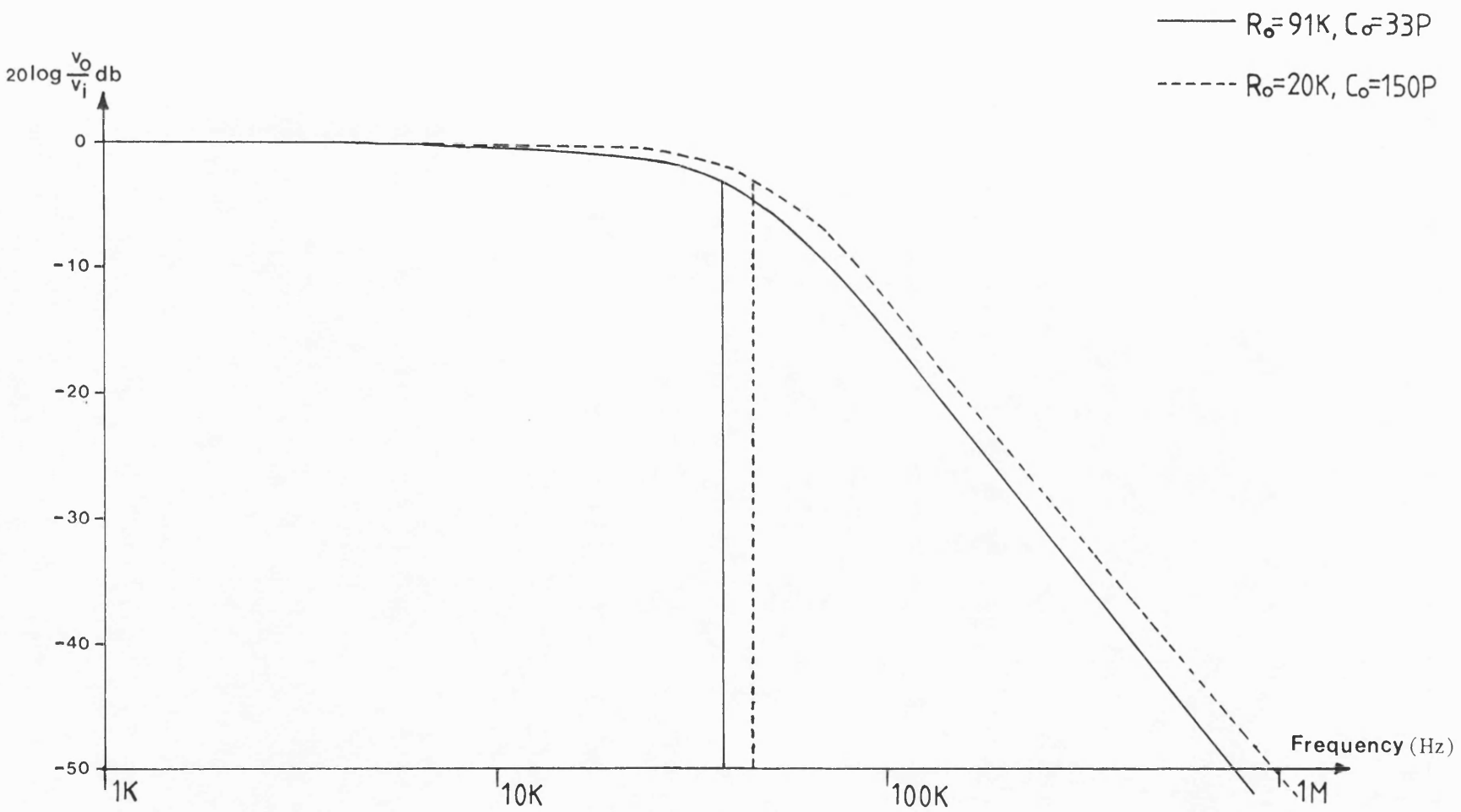

Fig. 4.6 Frequency response of the low-pass Butterworth filter.

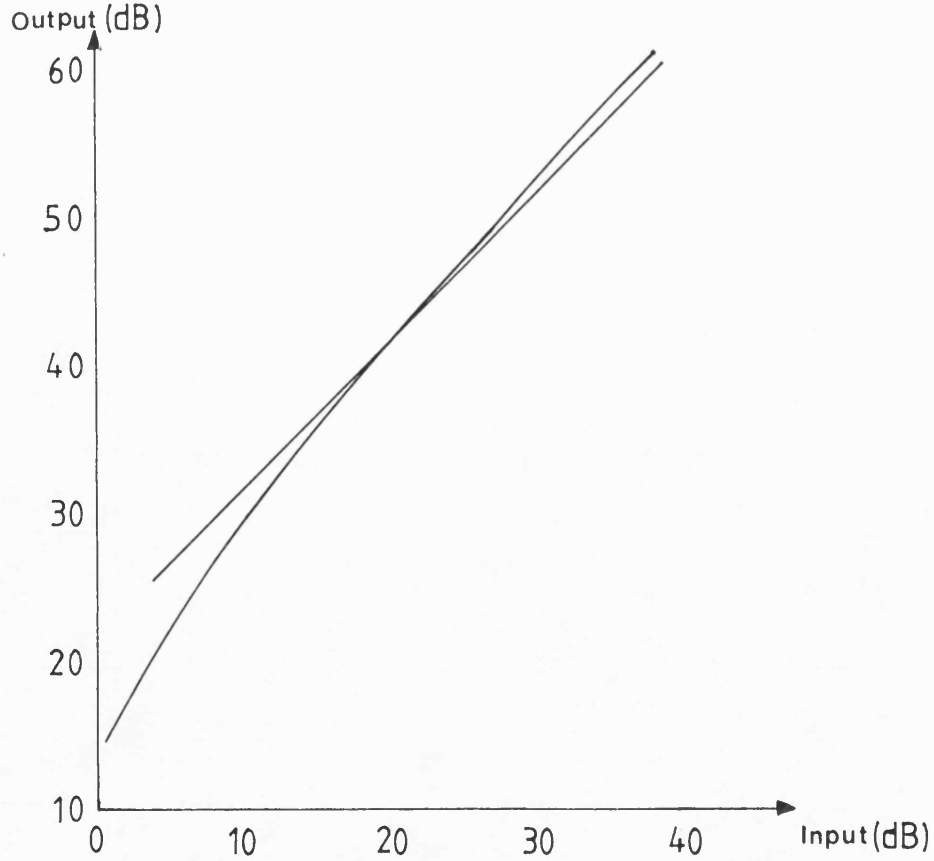

Fig. 4.7 Output vs input of the envelope detector.

Fig. 4.8 Connection diagram of the sample and hold AD585.

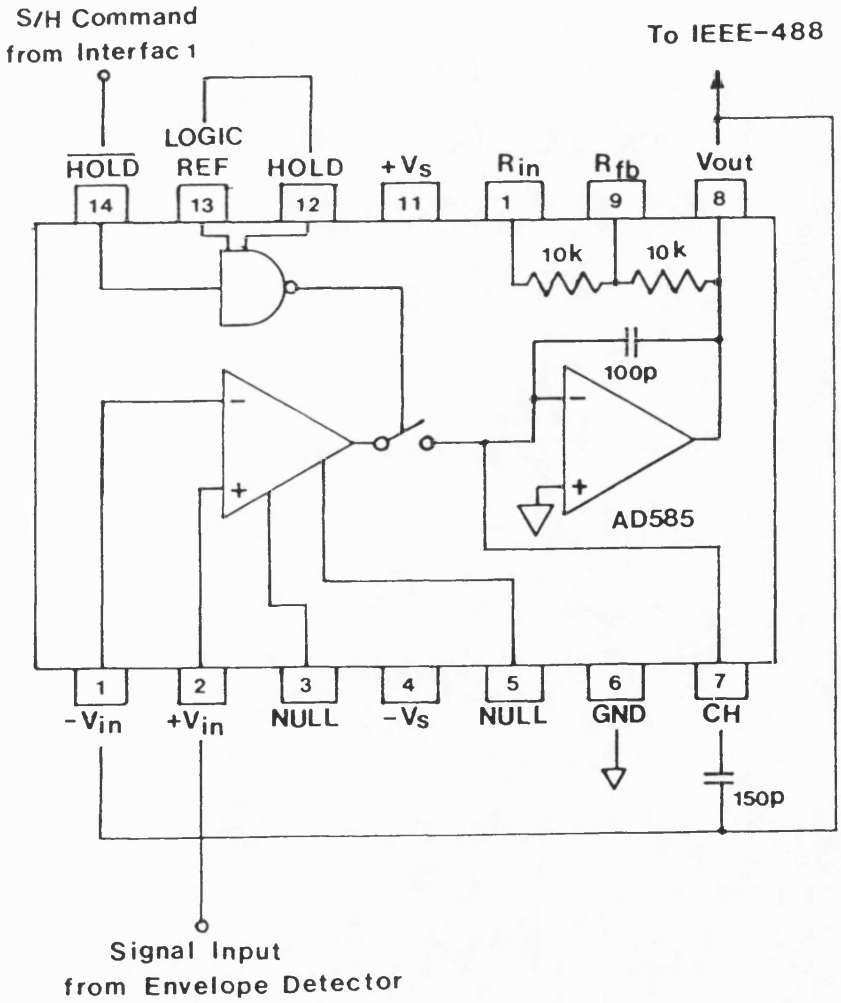

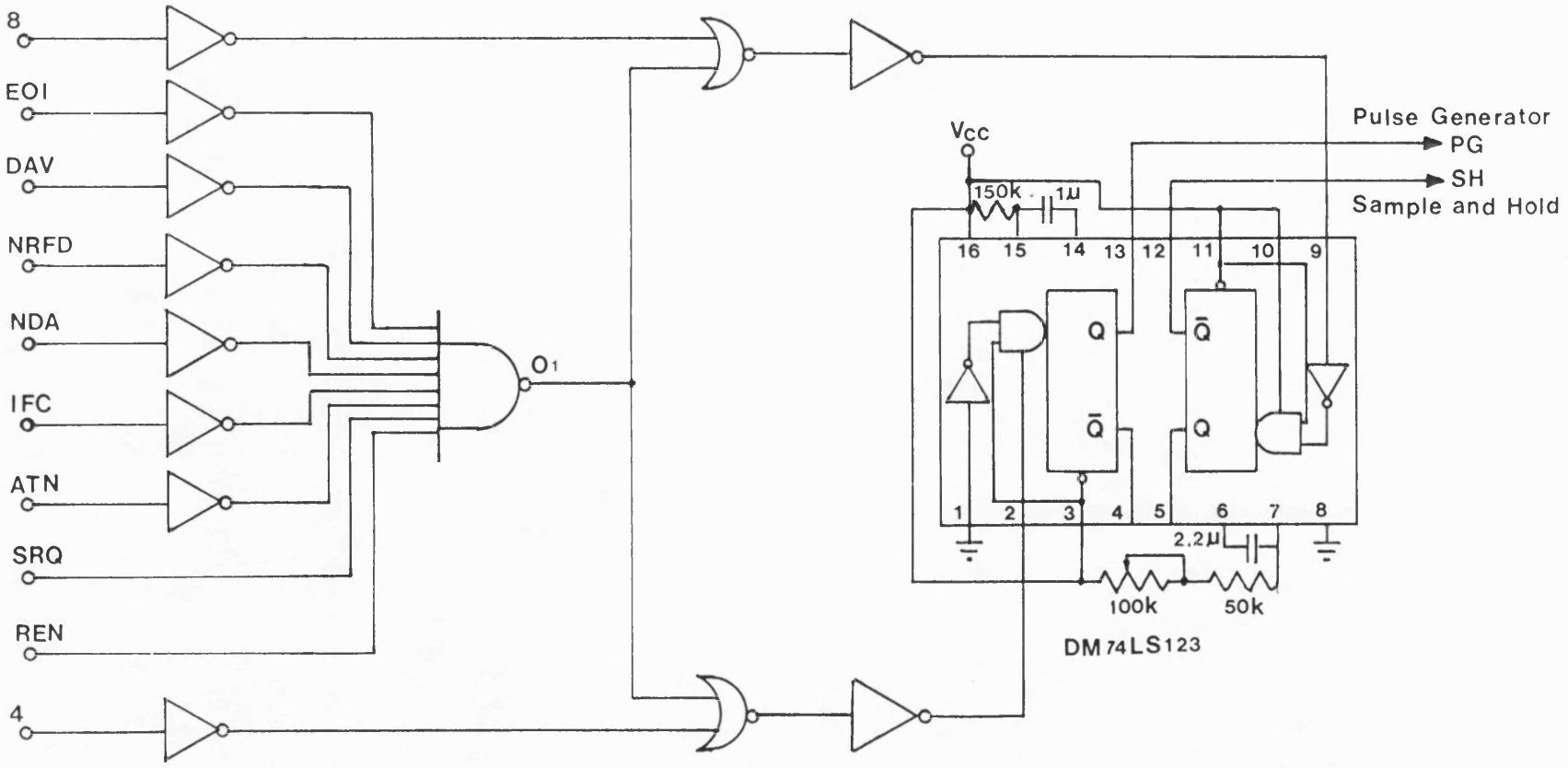

Fig. 4.9 Schematic diagram of the interface 1.

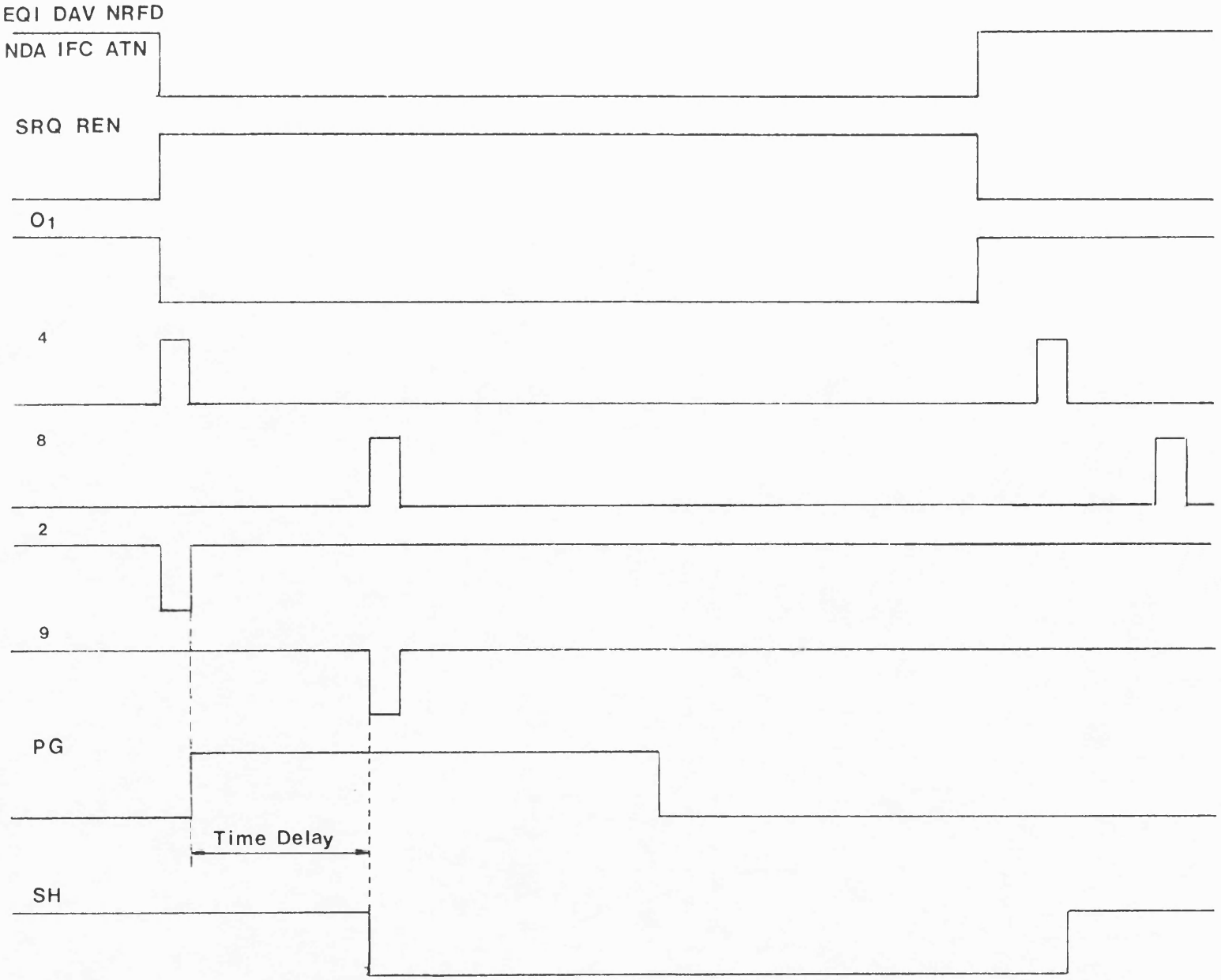

Fig. 4.10 Input and output scheme of the interface 1.

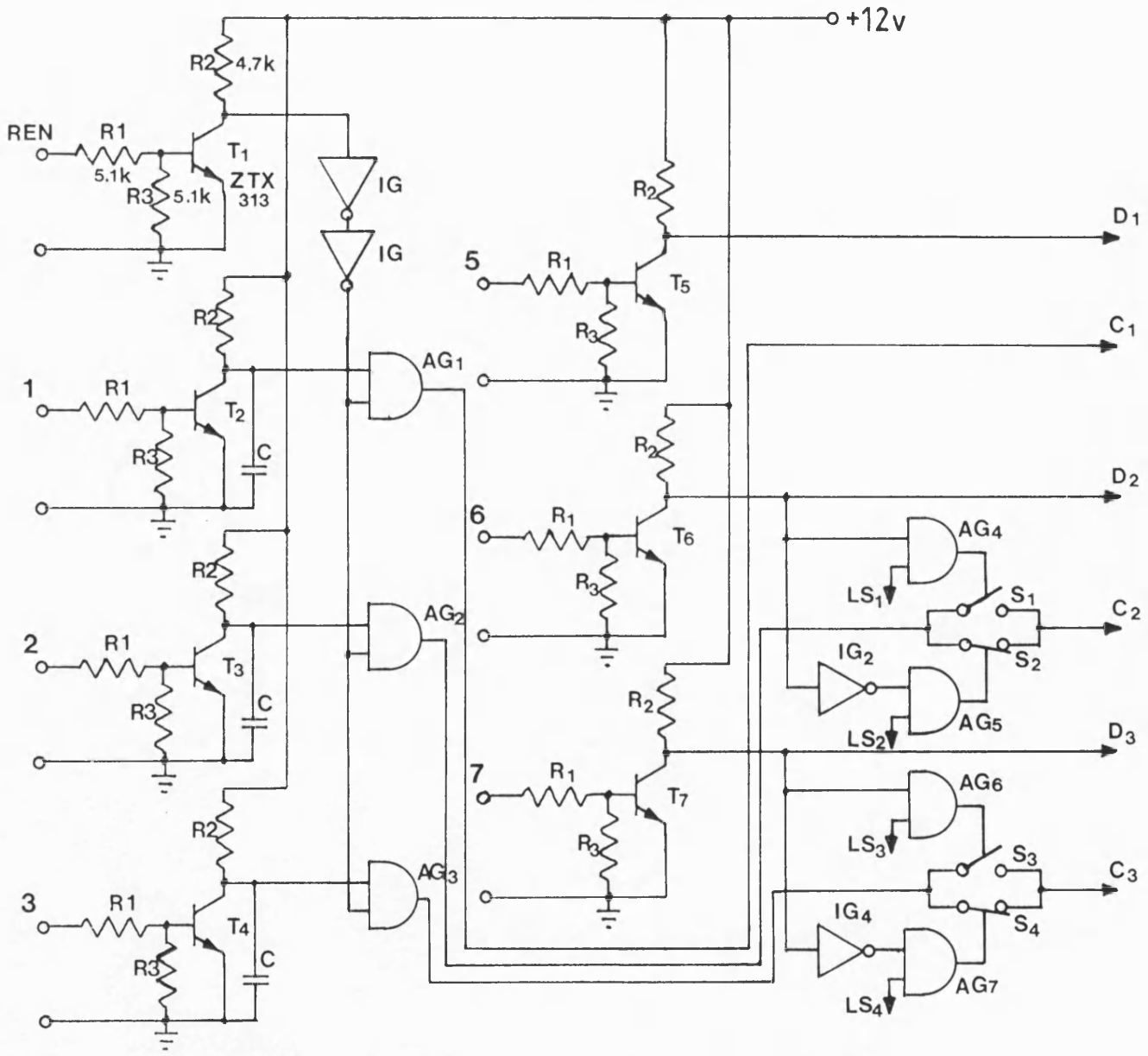

Fig. 4.11 Schematic diagram of the interface 2.

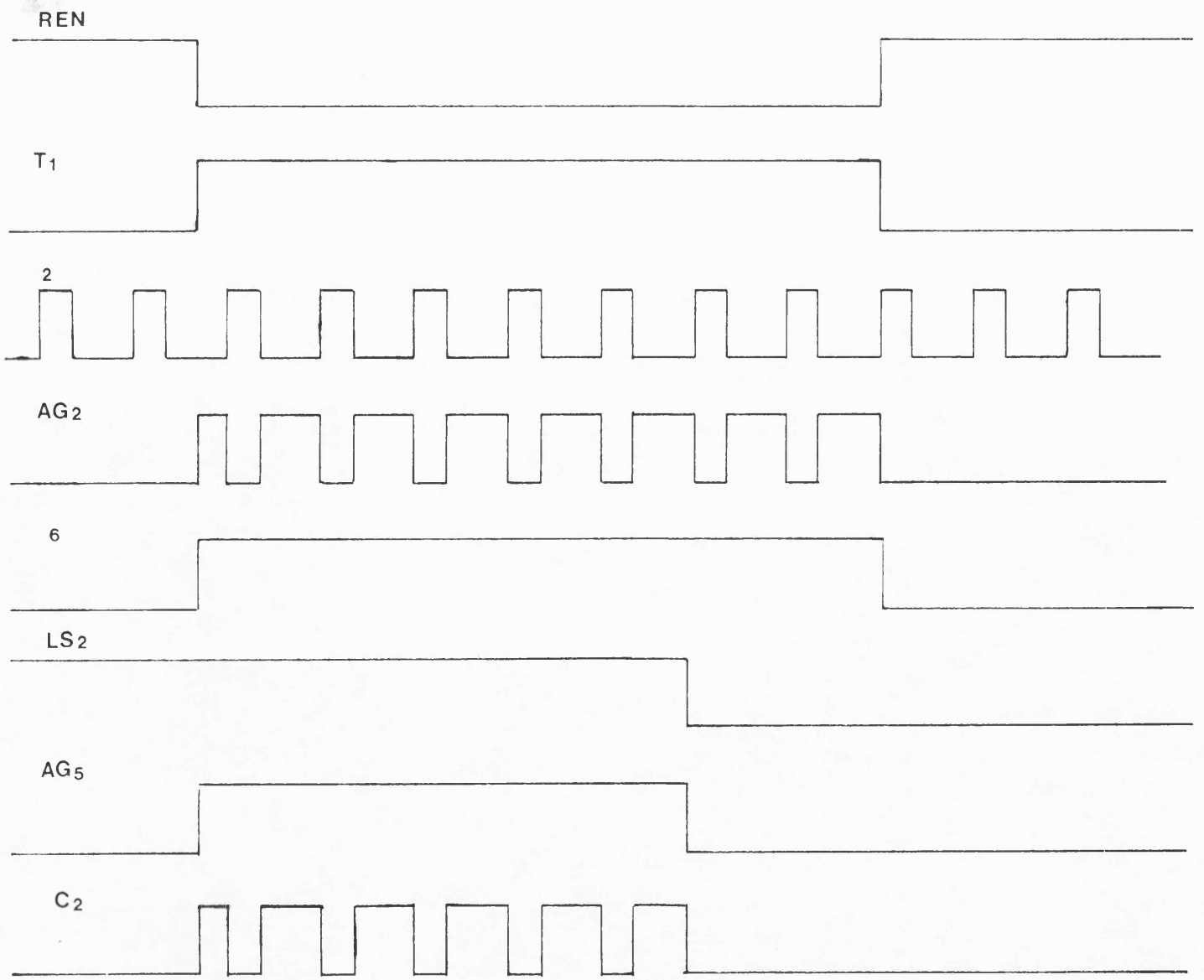

Fig. 4.12 Input and output scheme of the interface 2.

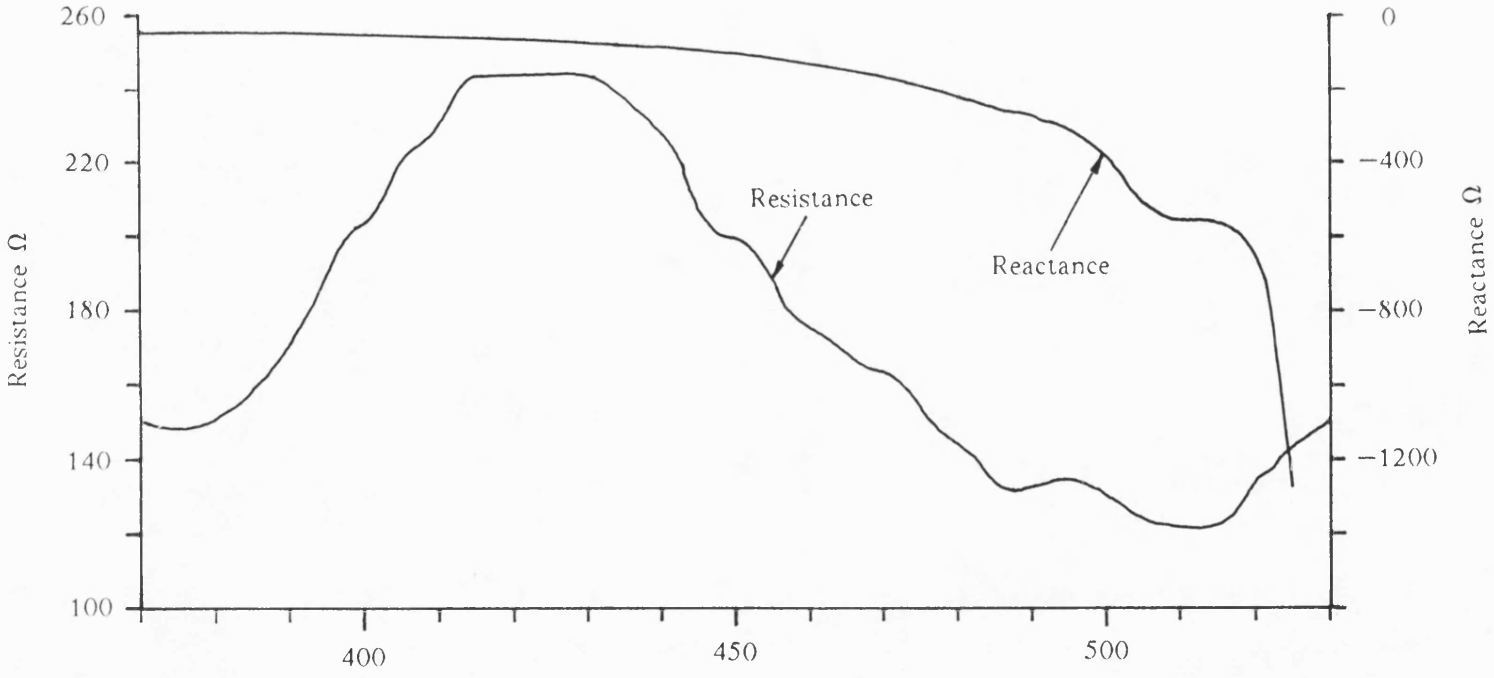

Fig. 4.13 Impedance characteristics of the directional transmitter.

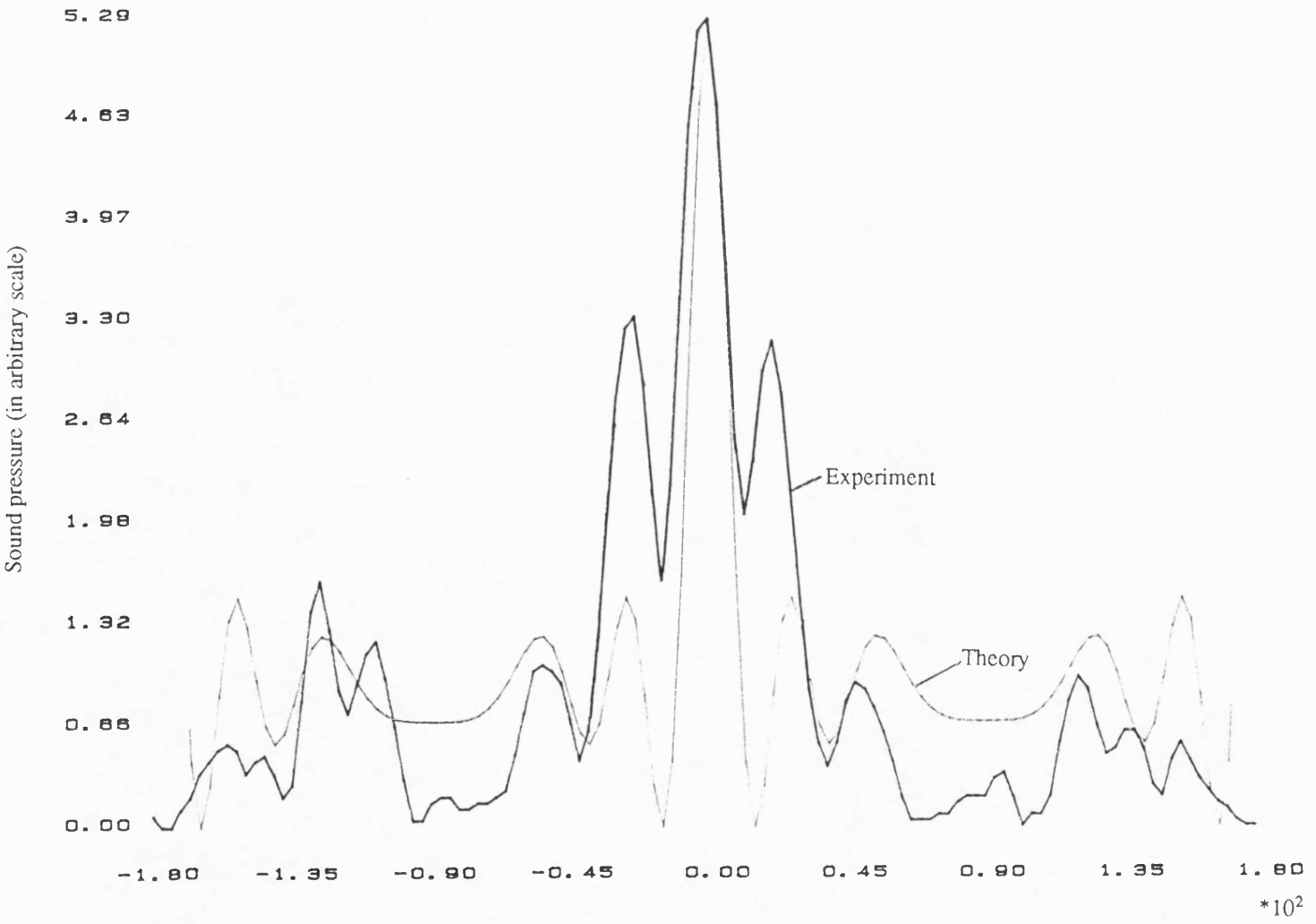

Fig. 4.14 Directivity of the directional transmitter.

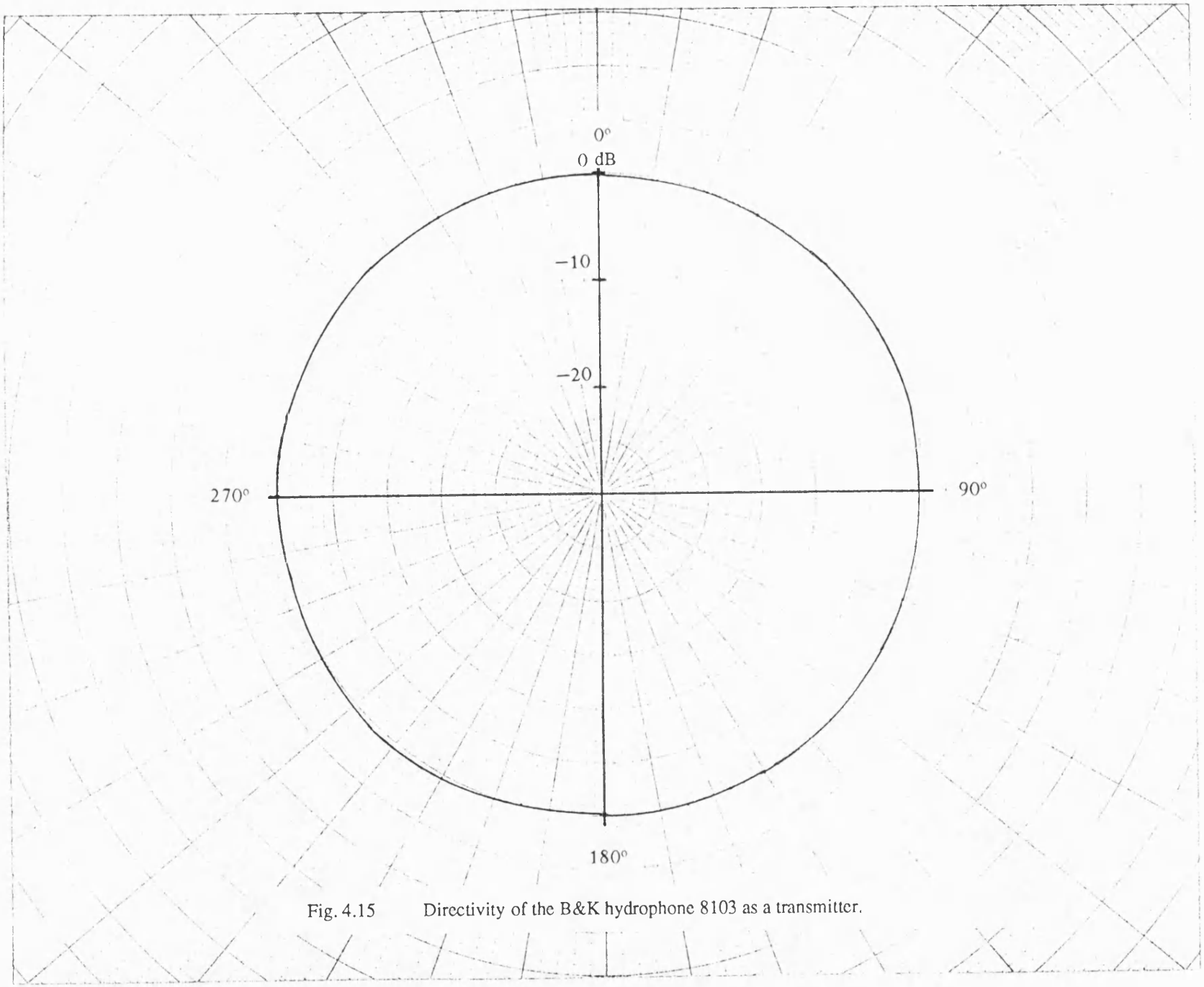

Fig. 4.15 Directivity of the B&K hydrophone 8103 as a transmitter.

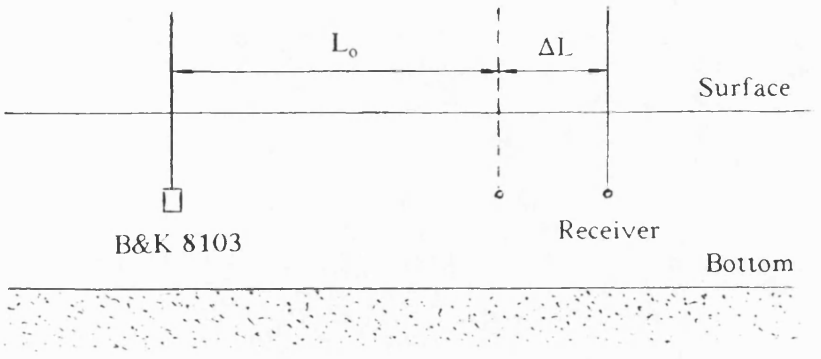

L_o = 380mm, ΔL = 149.25mm

Fig. 4.16 Measuring sound velocity in the water.

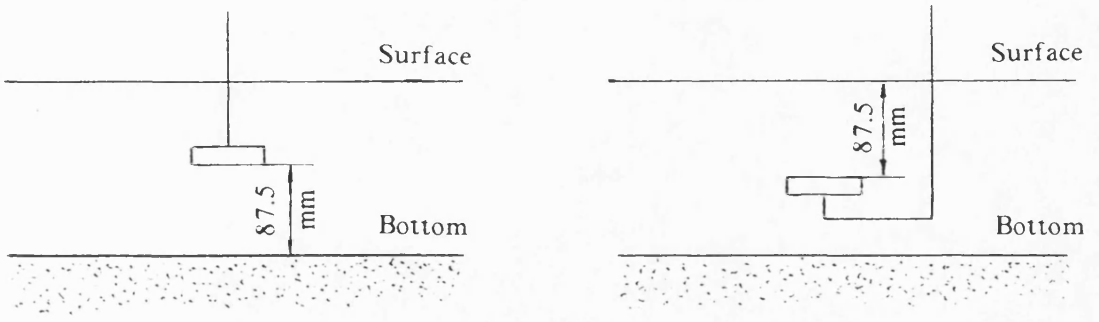

a. Measuring the bottom reflection

b. Measuring the surface reflection

Fig. 4.17 Measuring the reflections from the bottom and the water surface.

Chapter 5. NUMERICAL RESULTS

5.1 Introduction

The sound fields as a function of range and cross range, and as a function of range and water depth in ideal wedges and penetrable wedges are predicted by the approximate representations of the analytical solutions given in Chapter. 3. Since the wedge angle and the source position will determine the field in a wedge, they are used as parameters in the computing. Because most wedges in the oceans have small wedge angles, only small wedge angles are used in the predictions of the fields. In order to examine the effect of the wedge angle on the structures of the fields, three different angles are used, namely 1°, 2°, and 3° respectively. Different source positions are used to demonstrate the change of the field in a wedge. Consider the symmetry of the field about $z = 0$ plane, the prediction is carried out for $z \geq 0$. In order to make comparison with the experimental results, the region of interest for the fields is 0-75λ in range and 0-400λ in cross-range. There will be few modes sustained in the region under the given conditions, therefore the features of the fields can be demonstrated more clearly. For the penetrable wedge, the critical angle is 27.5°.

5.2 Ideal wedge

Since evaluation of the analytic solution in Eq. (2.21) for the acoustic field in an ideal wedge is time consuming, the approximate representation is used to predict the field. Firstly, the number of the modes which can be excited by a source at range 150λ away from the apex in an ideal wedge needs to be determined according to Eq. (3.47) that, $m=E\{2r'\theta_0/\lambda\}$, for a wedge with an angle 1°, one has $m=E\{300\pi/180\}=5$, so there may be 5 modes at most in the wedge. The caustics of the modes are determined by Eq. (3.44), the first three are shown in Fig. 5.1. They form a group of hyperbola, the higher modes nest in the lower modes. For each individual mode, its caustic divides the wedge into shadow zone and bright zone. The first mode which is the lowest mode has the narrowest shadow zone. Fig. 5.1 can be interpreted from the ray theory point of view combined with the mode theory. A ray may be repeatedly reflected by the surface and the bottom in a wedge, its heading is changed each time by the bottom reflection because of the slope, this change brings the horizontal refraction of the ray, any ray that runs up the slope, sooner or later, is turned to down slope direction, seen in the x–z plane (the surface plane of the wedge), the ray path is a hyperbola according to the Ray-Invariant given by Harrison[7] as

$$(1-\sin^2\gamma_0\cos^2\beta_0)x^2=\left[\frac{z(1-\sin^2\gamma_0\cos^2\beta_0)}{\sin\gamma_0\cos\beta_0}+x_0\cos\beta_0\cos\gamma_0\right]^2+x_0^2\sin^2\beta_0 \qquad (5.1)$$

where β_0 and γ_0 are the initial elevation angle and the initial azimuthal (angle to the down slope direction in the horizontal plane) at the source. If there is no limit on the elevation angles of the rays, they may ensonify anywhere in a wedge since the rays with very small elevation angles will not interact with bottom, therefore there is no change in their heading at all. This is the result given by pure ray theory. It is contrary to the mode theory, which predicts there is a shadow zone where sound can not ensonify. Consider the ray-mode equivalence, a restriction can be put on the elevation angles of the rays, that is the rays can only have their initial elevation angles at the source equal to the mode angles at the source. Therefore these rays are referred as the eigenrays of the modes. The eigenrays of a mode have the same elevation angle at the source, they can no longer reach anywhere in a wedge because they will be reflected by the boundaries at such an elevation angle, the reflection on the sloping bottom results in the refraction of the rays in the horizontal plane, so that the rays are confined in a certain region in the horizontal plane, which is the bright zone of the mode, beyond the region, there is the shadow zone of the mode where no ray corresponds to the mode can ensonify. The boundary of the bright zone and the shadow zone is the caustic of the mode given by Eq. (3.44), which is also the envelope of all rays corresponding to the mode. Fig. 5.2 shows some ray paths in the horizontal plane correspond to the first mode given by Eq. (5.1) and the envelope of the mode. Since higher modes have greater elevation angles as given in Eq. (3.49), the rays corresponding to these modes suffer sharper change in their headings because they are reflected more frequently from the sloping bottom, therefore, the higher the mode, the wider the shadow zone. The lowest mode has the narrowest shadow zone, so that the shadow zone of the field is determined by the lowest mode.

Fig. 5.3 shows the field as a function of range and cross range at depth $1/4\lambda$ in an area $1\text{-}75\lambda$ in range and $0\text{-}400\lambda$ in cross range with the source at mid depth in the wedge ($\theta'=0.5°$). As shown in Fig. 5.1 that only the first two modes may be sustained in the area, the higher modes are cutoff before reaching the area. When the source is at mid depth in the wedge, the second mode is absent, therefore only the first mode exists in the area. It can be seen that the field has a high intensity at the caustic, a shadow zone between the apex and the caustic, and a bright zone in which even with only one mode, the field shows a complicated interference pattern, which means there is intramode interference. This is a special feature of the sound field in an ideal wedge. Because of the successive bottom reflections, an upslope propagation wave will finally becomes a downslope propagation wave, which interferences with the upslope propagation wave. Fig. 5.4 shows the first mode coefficient as a function of range r. Near the apex, there is a shadow zone which sound energy can not reach, then the caustic occurs where the mode has a maximum interference peak, enter the bright zone from the

caustic towards deeper water, there is a strong spatial oscillation which has an increasing number of cycles as range increases. To explain the behaviour of the mode in Fig. 5.4, recall the theory mentioned in Sec. 3.2 that, a mode can be considered as a total contribution of two rays from the "virtual images" determined by stationary points, which interference to each other, the two rays have the same path when they arrive at caustic, but they have different paths apart from the caustic. The distances from the virtual images to the field point at range r in $z = 0$ plane are

$$d_{s1}=\sqrt{r'^2+r^2-2r'r\cos\sigma_1} \tag{5.2a}$$

$$d_{s2}=\sqrt{r'^2+r^2-2r'r\cos\sigma_2} \tag{5.2b}$$

where $\sigma_{1,2}$ are the stationary points given by Eq. (3.33). The difference $\Delta d = d_{s2}-d_{s1}$ of the two paths is a function of range r. Take the derivative of Δd with respect to r, one obtains

$$\frac{d(\Delta d)}{dr}=\left\{\frac{\sqrt{v^4-k^2R_0^2v^2+k^4r'^2r^2}+(k^2r'^2-v^2)}{d_{s2}}\right.$$

$$\left.-\frac{k^2(k^2r'^2-v^2)(r^2-r'^2)}{d_{s1}[\sqrt{v^4-k^2R_0^2v^2+k^4r'^2r^2}+(k^2r'^2-v^2)]}\right\}\frac{r}{\sqrt{v^4-k^2R_0^2v^2+k^4r'^2r^2}} \tag{5.3}$$

When $r < r'$, $\frac{d(\Delta d)}{dr} > 0$, therefore, the difference between the paths becomes greater as r increases, which results in an increasing oscillating. When $r > r'$, $\sigma_1 \to 0$ and $\sigma_2 \to \pi$, so that $\Delta d=2r'$, and no intramode interference will be found.

Fig. 5.5 shows the field at depth 1/4λ as a function of range and cross range in the same area as in Fig. 5.3 when the source has an angle 0.3 ° with the surface. The second mode is excited in the case as would be expected. The intermode interference can be seen in the area where the second mode exists. The second mode can penetrate less area than the first mode because it has a greater elevation angle at source, therefore it suffers more sharply changes in its heading.

Figs. 5.6a and 5.6b show the field as a function of range and water depth, the field contains only the first mode when the source angle $\theta' = 0.5°$ as shown in Fig. 5.6a, so there is one maximum in depth. When the source angle is 0.3°, the second mode can be seen clearly, and two maximum are found at the area where the second mode exists in Fig. 5.6b. Near the surface and the bottom, the pressure is low as shown in the figures. The caustics of the first and the second modes are

demonstrated by the high sound levels. As range r decreases, an increasing trend in sound level is observed in Figs. 5.6a and 5.6b which means the wedge has a focus effect on sound energy when upslope propagation happens.

There are 10 modes which can be excited in a 2° ideal wedge according to Eq. (3.47), the caustics of the first 5 modes are shown in Fig. 5.7, the higher modes can not be seen in the interest area. Comparing with Fig. 5.1, it can be found there are more modes in 2° wedge than in 1° wedge in the same area, the shadow zone of the first mode in this case is narrower too, the distances between the adjacent caustics are smaller.

When the source angle is 1°, the even number modes are absent, the field as a function of range and cross range at depth $1/4\lambda$ is shown in Fig. 5.8a. Fig. 5.8b shows the field with the source angle 0.5°, the second mode emerges, but the fourth mode is still absent. Comparing with Figs. 5.3 and 5.5, the interference patterns are more complicated since more modes are sustained in the wedge.

Figs. 5.9a and 5.9b show the field as a function of range and water depth. Fig. 5,9a corresponds to the source with an angle 1°, and Fig. 5.9b corresponds to a source with an angle 0.5° to the surface. The caustics of the first, the third and the fifth modes are clearly recognized by their caustics as in Fig. 5.9a, in addtion to all the modes in Fig. 5.9a, the second mode is seen in Fig. 5.9b.

In an ideal wedge with an angle θ_0=3°, there may be 15 modes in the wedge. Fig. 5.10 shows the caustics of the first 8 modes in this case. It is apparent that the caustics of the different modes are closer comparing with 1° and 2° wedge, and the shadow zone is even narrower.

The fields in r–z plane with the source angle $\theta' = 1.5°$ and $\theta' = 1.25°$ are shown in Figs. 5.11a and 5.11b, respectively. No even number modes can be found in Fig. 5.11a since the source is located at the null of these modes.

The fields in $z = 0$ plane as a function of range and water depth are shown in Figs. 5.12a and 5.12b, corresponding to 1.5° and 1.25° source angle respectively. As the field in r–z plane, there is no even number mode in Fig. 5.12a. The distance between the caustics is narrower.

Comparing the results given above, it is found that for a source at a fixed range from apex, more modes may be excited and sustained in a wedge with a large wedge angle than that with a small wedge angle, and the shadow zone is narrower.

In an ideal wedge, the field is determined only by the source position. The previous results show that when the source position varies in angle with a fixed range r', the excitation amplitudes of the modes change accordingly. If the source position is changed in range in a wedge, the maximum mode number in the wedge will change according to Eq. (3.47), the larger the range, the more the modes. The position of the caustic for different modes will also change except at $z = 0$ plane as given by Eq. (3.44). Fig. 5.13 shows the caustics of the first mode for a source at range $100\lambda, 150\lambda$ and 200λ in a 2° ideal wedge. It can be seen the cutoff range at the $z = 0$ plane is the same for the source at any range, the caustic becomes wider as the source is moved towards deeper water, consequently, the shadow zone becomes narrower. Since the elevation angle of the mode given by Eq. (3.49) decreases as the source moves away from the apex, it makes the change of the headings of all the rays corresponding to the mode slow, therefore, the caustic becomes wider. So that, for a receiver located far away the apex will have a broad view over a large area in a wedge.

5.3 Penetrable wedge

The fields in penetrable wedges are predicted by the approximated analytic solution in Sec. 3.3. The number of the modes in a penetrable wedge is determined in a different way from that in a perfect wedge. The wedge is considered as local flat at the source, then the number of the modes can be found according to the shallow water theory, *i.e.*, considering a shallow water channel with a uniform depth the same as the depth at source in the wedge, the number of the modes in the shallow water channel is decided by the depth, the sound velocities in the water and in the bottom, and the densities of the water and the bottom, by comparison, the same number modes can be excited by the source in the wedge. For small angle wedges, this approximation is reasonable. For a penetrable wedge with 1° wedge angle and a critical angle 27.5°, there are two modes sustained. Similar to the perfect wedge case, the caustics of the modes in a penetrable wedge can be determined according to Eq. (3.97), which takes the change of the coordinates into account. Fig. 5.14 shows the caustics of the modes. They are hyperbolic too. They are closer to and even cross the apex of the wedge because of the shift Δ from the real bottom to the effective bottom.

Fig. 5.15 shows the field with a source at $S(150\lambda, 0.5°, 0)$ in a 1° wedge. The field has a simple pattern in the central part where is referred as inner zone, outside the inner zone, there is an outer zone where the field has a rather complicated pattern that includes a high intensity region as shown in Fig. 5.15. Comparing with the field in an ideal wedge as shown in Fig. 5.3, the field in a penetrable wedge has a narrower shadow zone, the caustic for the first mode is less apparent.

Since the bottom of the penetrable wedge is not an ideal reflector, some sound rays may be kept in the wedge if the incident angles are greater than the critical angle. When the incident angle is less than the critical angle, the ray will penetrate the water/bottom interface into the bottom. In the central part, all the rays have incident angles less than the critical angle, therefore, penetration occurs, unlike an ideal wedge, there is only up-slope propagation wave which eventually penetrates into the bottom as the wave reaches its cutoff range, so there is no down-slope propagation here, consequently, no intramode interference can be found, and the pattern of the field looks more simple than that in an ideal wedge. Apart from the central part, the rays' incident angles become greater than the critical angle due to the horizontal refraction, so that there are both up slope and down slope propagation waves in this region, a high peak of sound level can be seen at the caustic of the first mode, which results from the interference of these two waves. To make comparison, the first mode coefficient as a function of range in $z = 0$ plane, and as a function of cross range at range 25λ away from apex, both in an ideal wedge and a penetrable wedge with 2° wedge angle, are shown in Figs 5.16 and 5.17. In Fig. 5.16a, the mode shows a strong spatial oscillation in the ideal wedge because of the intramode interference. In Fig. 5.16b, The mode is smooth since there is no intramode interference, the cutoff range for the mode in the penetrable wedge as indicated in the picture is estimated according to the shallow water theory. The cutoff process in the penetrable wedge takes place slowly over a long distance, it starts at the place where the incident angle of the sound ray is less than the critical angle, finally the ray totally penetrate into the bottom as the incident angle get less and less, it contrasts to that in an ideal wedge which is rather quick since the cutoff of the mode at the place where the sound ray changes its heading from upslope direction to downslope direction as shown in Fig. 5.16a and 5.16b. In Fig. 5.17a, the same as in in Fig. 5.16a, the mode shows a strong spatial oscillation. To compare with Fig. 5.17a, Fig. 5.17b shows the feature of the mode in a penetrable wedge, a smooth part in the inner zone, strong interference in the outer zone, and a quick fall in the shadow zone.

It is also different from the field in an ideal wedge, the field with a source at θ_0=0.5° in a 1° penetrable wedge contains the second mode, The excitation amplitude of the mth mode in a penetrable wedge is determined by the term $\sin\nu\theta'$ in Eq. (2.32), where $\nu=m\frac{\pi}{\theta_0}$ and $\theta'=\theta'/(1+\frac{\pi}{2kr'\theta_0\sin\alpha_c})$. For the given parameters, the excitation amplitude is 0.96 for the first mode, 0.51 for the second mode. Although the second mode can not be distinguished by the caustic, the interference pattern gives evidence that second mode exists in the interest area. A cross section of the field in Fig. 5.15 is shown in Fig. 5.18a, it can be seen there is a weak intermode interference at the

deep end of the wedge. As the water becomes shallow, the field is smooth because the second mode is cutoff. Fig. 5.18b shows the field with the source at S(150λ,0.3°,0), since the excitation amplitude of the first mode is 0.7, and the second mode is 1, a stronger intermode interference can be seen.

In a wedge with 2° wedge angle, the number of the modes is determined by the same way as for 1° wedge. There may be five modes in the wedge for a source at $r' = 150\lambda$. The caustics of the modes are shown in Fig. 5.19. As the wedge angle increases, there are more modes sustained in the wedge, the shadow zone of the field is narrower, the caustics get closer to each other. The field as a function of range and cross range at a depth 1/4λ in a 2° wedge is shown in Fig. 5.20. The excitation amplitudes of the first three modes for a source at mid depth in the wedge are 0.99, 0.29, and 0.9. Though the second mode is small in amplitude, it is clearly seen when the source is at mid depth in the wedge. Because the third mode is in the inner zone in the interest area, the caustic can not be seen in spite of the high excitation amplitude. A cross section of the field in Fig. 5.20 is shown in Fig. 5.21. Comparing with Figs. 5.18, the cutoff range corresponding to each mode is shorter, and more modes are sustained which results in a more complicated interference pattern.

The number of the modes in a 3° penetrable wedge is seven for a source at $r' = 150\lambda$, the caustics of the modes are drawn in Fig. 5.22. The excitation amplitudes of the first five modes are 0.99, 0.2, 0.95, 0.39, and 0.87 when the source is at mid depth in the wedge. All the even number modes have small excitation amplitudes since the source is near the nulls of these modes. The field as a function of range and cross range at 1/4λ depth for a 3° wedge is shown in Fig. 5.23. The second mode is lower in amplitude comparing with the first mode and the third mode as the source is at mid depth in the wedge as would be expected. The field as a function of range and water depth in $z = 0$ plane is shown in Fig. 5.24.

Comparing the results for the ideal wedges and the penetrable wedge, some common features are found; wedges with large angles can sustain more modes in the same range, the shadow zones of the fields are narrower. The differences are, there is no intramode interference in the inner zone of the penetrable wedge, and the shadow zones are even narrower for the penetrable wedge.

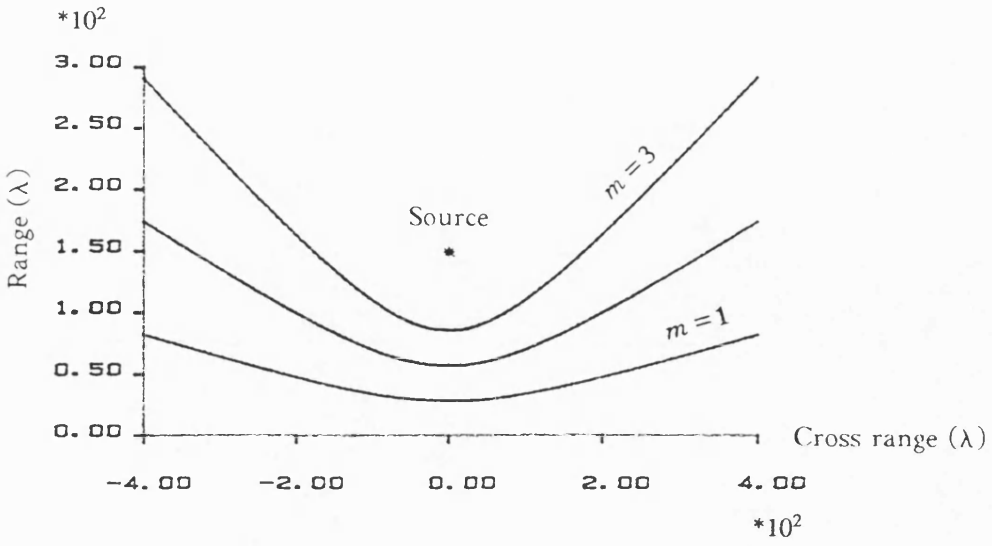

Fig. 5.1 The caustics of the first three modes in a 1° ideal wedge for a source at range $r = 150\lambda$, cross range $z = 0$.

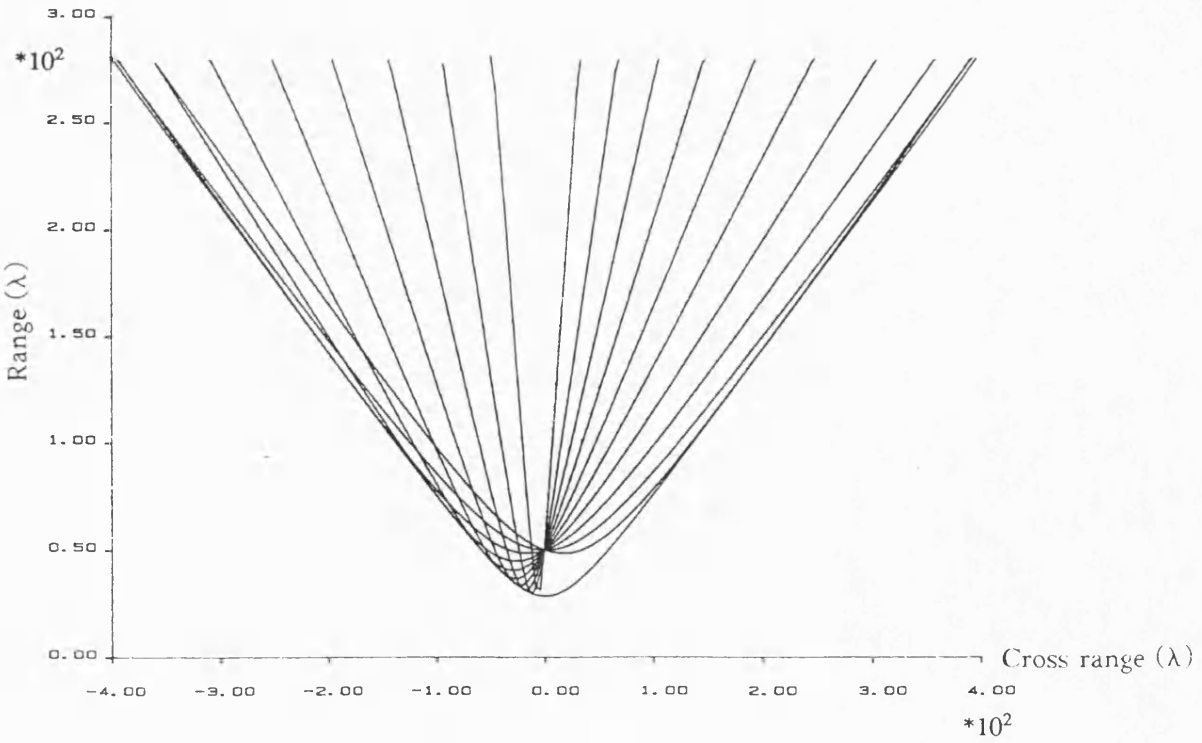

Fig. 5.2 Ray paths in horizontal plane and their envelope of the first mode for a source at range $r' = 50\lambda$ and cross range $z = 0$ in a 1° ideal wedge.

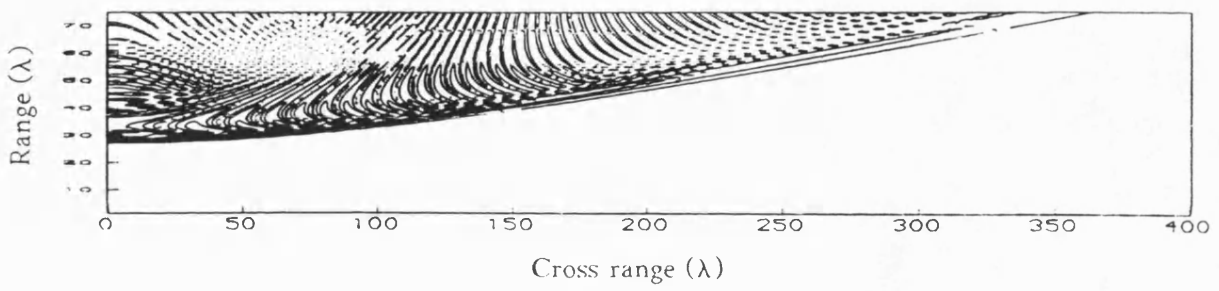

Fig. 5.3 Field $|\Phi(r,\theta,z)|$ at depth 1/4λ as a function of range (1-75λ) and cross range (0-400λ) for a 411kHz source at S(150λ,0.5°,0) in a 1° ideal wedge.

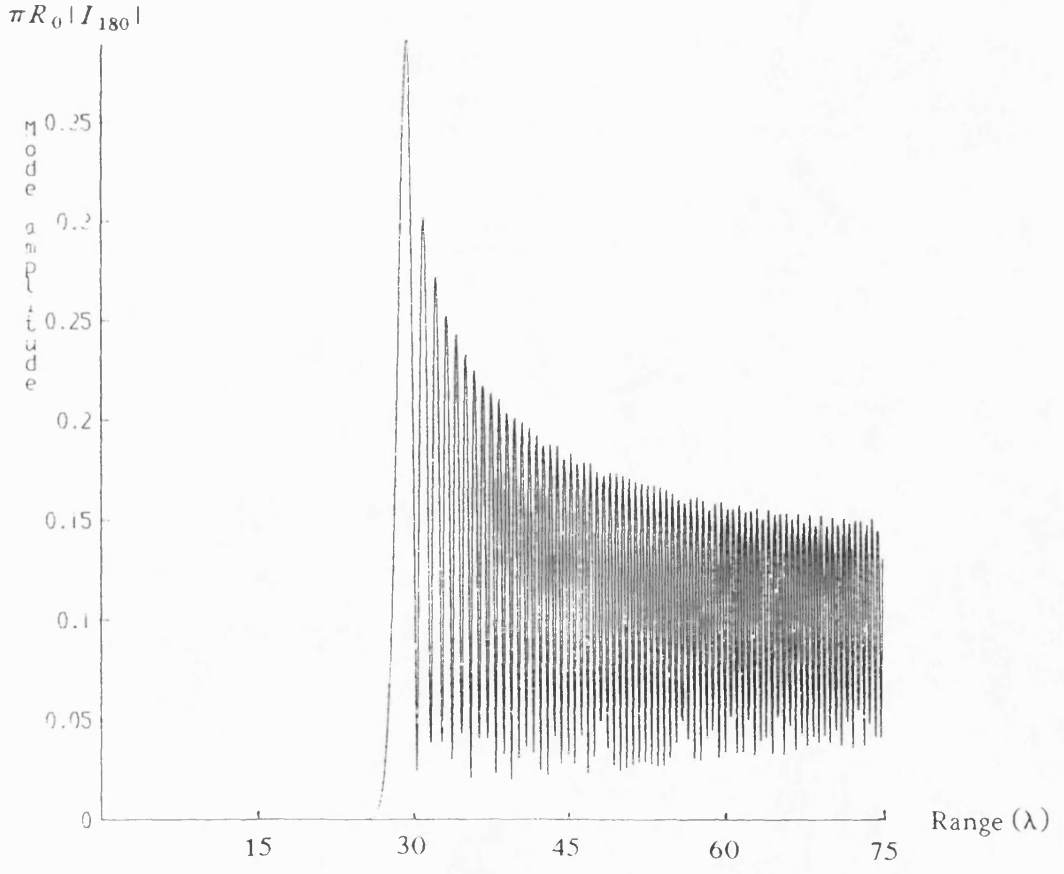

Fig. 5.4 The first mode coefficient $|I_{180}|$ at $z = 0$ plane as a function of range in a 1° ideal wedge.

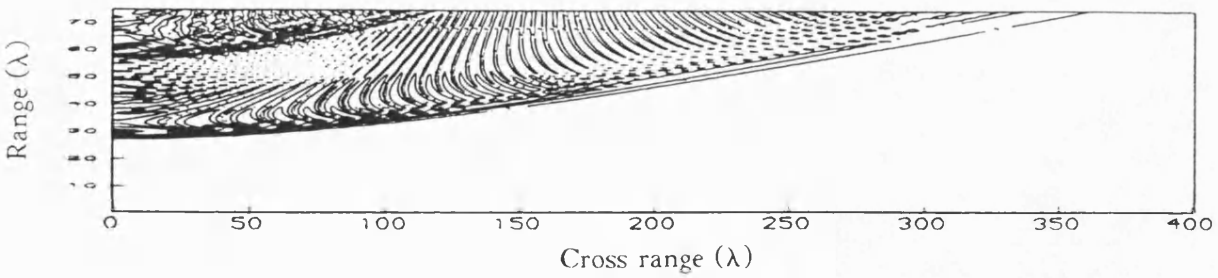

Fig. 5.5 Field $|\Phi(r,\theta,z)|$ at depth 1/4λ as a function of range (1-75λ) and cross range (0-400λ) for a 411kHz source at S(150λ,0.3°,0) in a 1° ideal wedge.

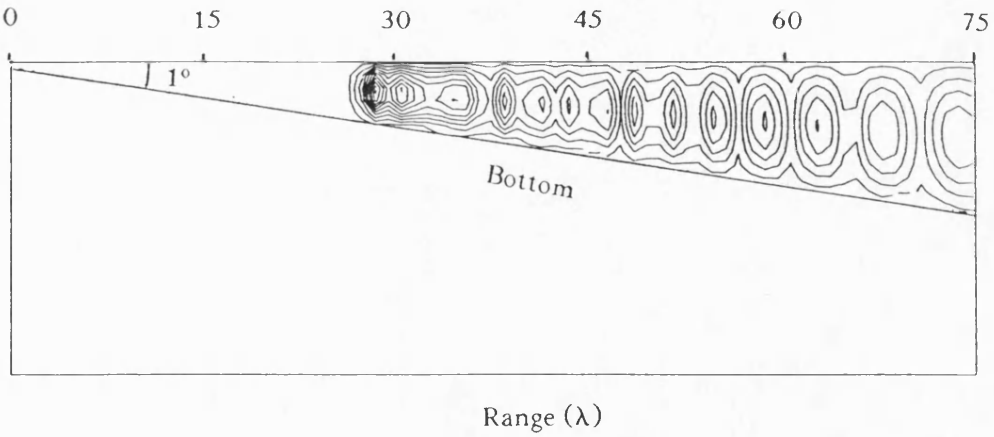

Fig. 5.6a Field $|\Phi(r,\theta,z)|$ at $z = 0$ plane as a function of range (1-75λ) and water depth, for a source at S(150λ,0.5°,0) in a 1 ° ideal wedge.

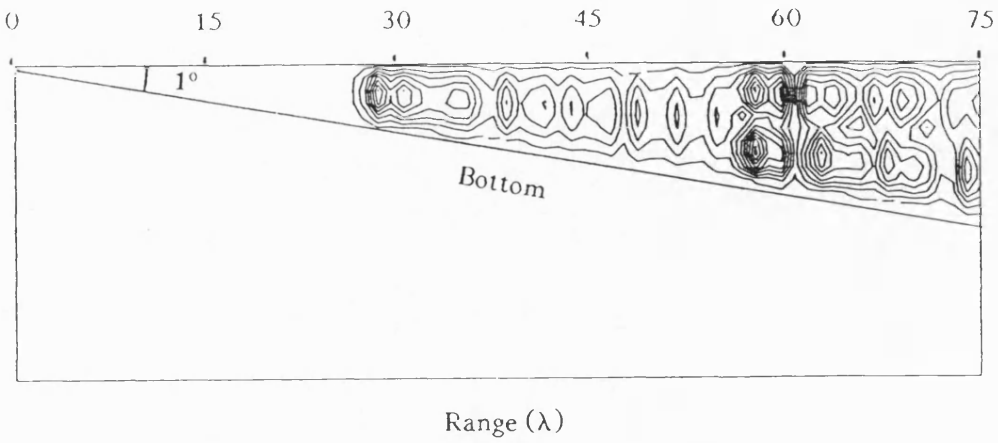

Fig. 5.6b Field $|\Phi(r,\theta,z)|$ at $z = 0$ plane as a function of range (1-75λ) and water depth, for a source at S(150λ,0.3°,0) in a 1 ° ideal wedge.

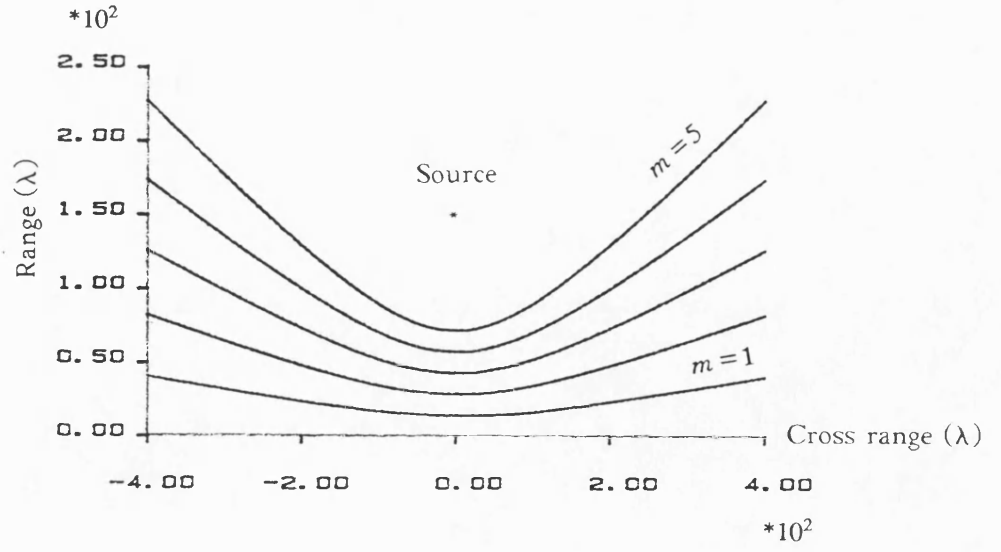

Fig. 5.7 The caustics of the first five modes in a 2° ideal wedge for a source at range $r = 150\lambda$, cross range $z = 0$.

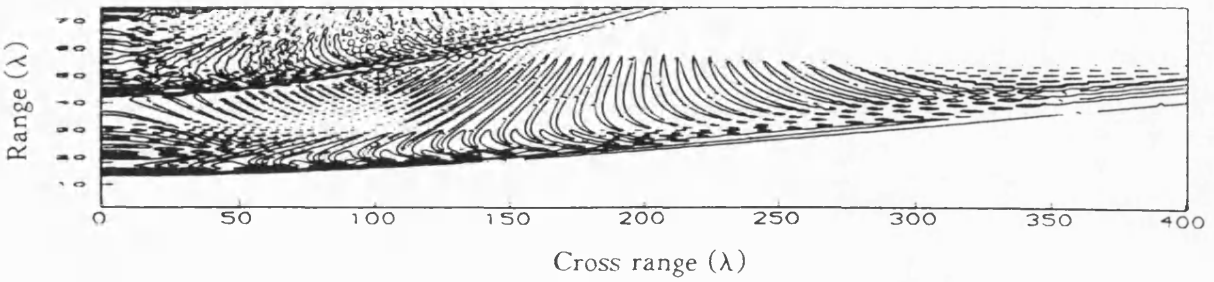

Fig. 5.8a Field $|\Phi(r,\theta,z)|$ at depth 1/4λ as a function of range (1-75λ) and cross range (0-400λ) for a 411kHz source at S(150λ,1°,0) in a 2° ideal wedge.

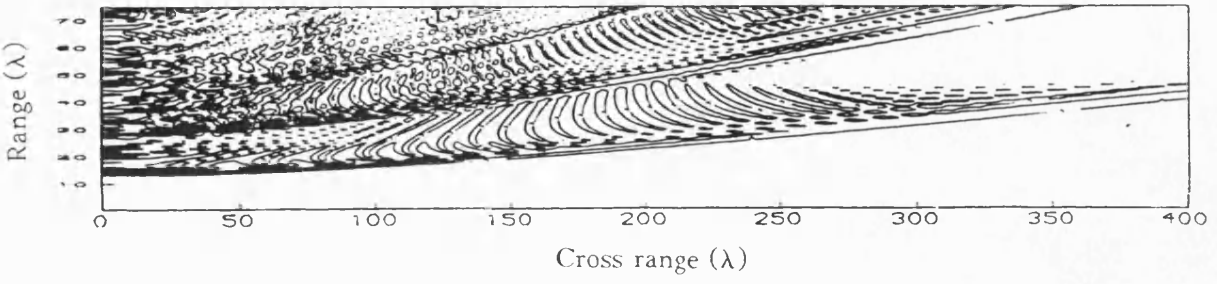

Fig. 5.8b Field $|\Phi(r,\theta,z)|$ at depth 1/4λ as a function of range (1-75λ) and cross range (0-400λ) for a 411kHz source at S(150λ,0.5°,0) in a 2° ideal wedge.

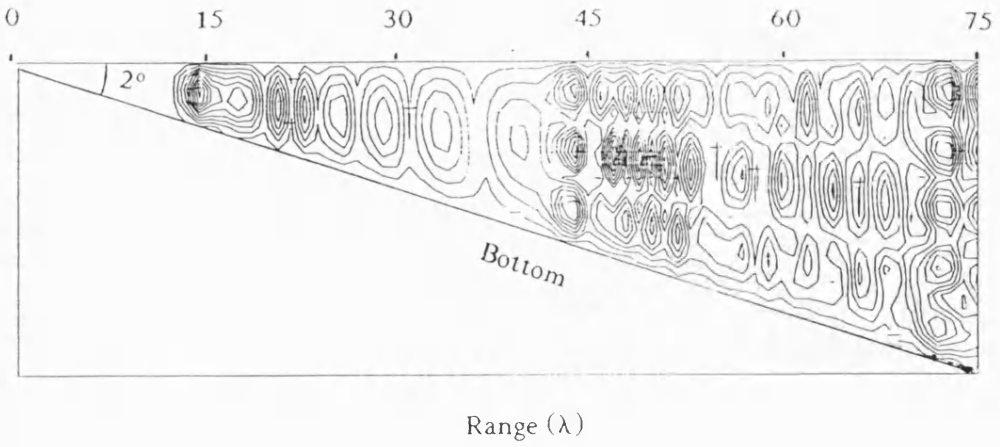

Fig. 5.9a Field $|\Phi(r,\theta,z)|$ at $z = 0$ plane as a function of range (1-75λ) and water depth, for a source at S(150λ,1°,0) in a 2 ° ideal wedge.

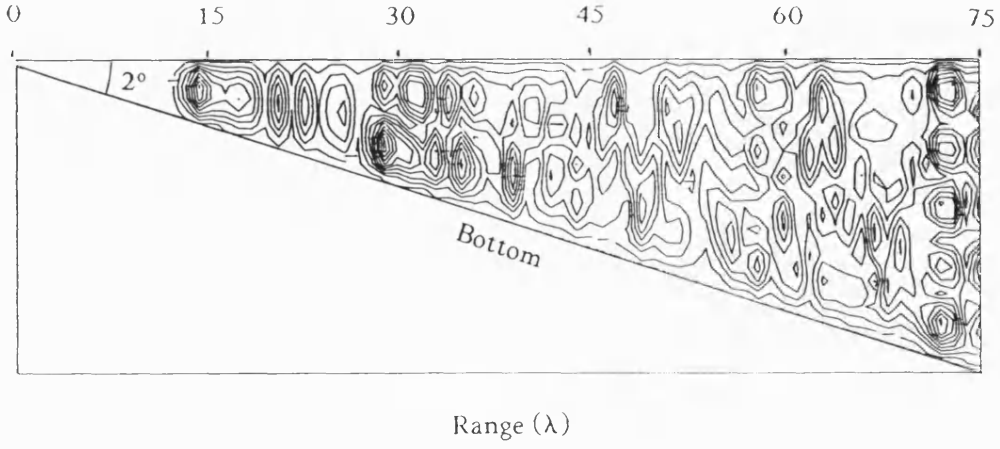

Fig. 5.9b Field $|\Phi(r,\theta,z)|$ at $z = 0$ plane as a function of range (1-75λ) and water depth, for a source at S(150λ,0.5°,0) in a 2 ° ideal wedge.

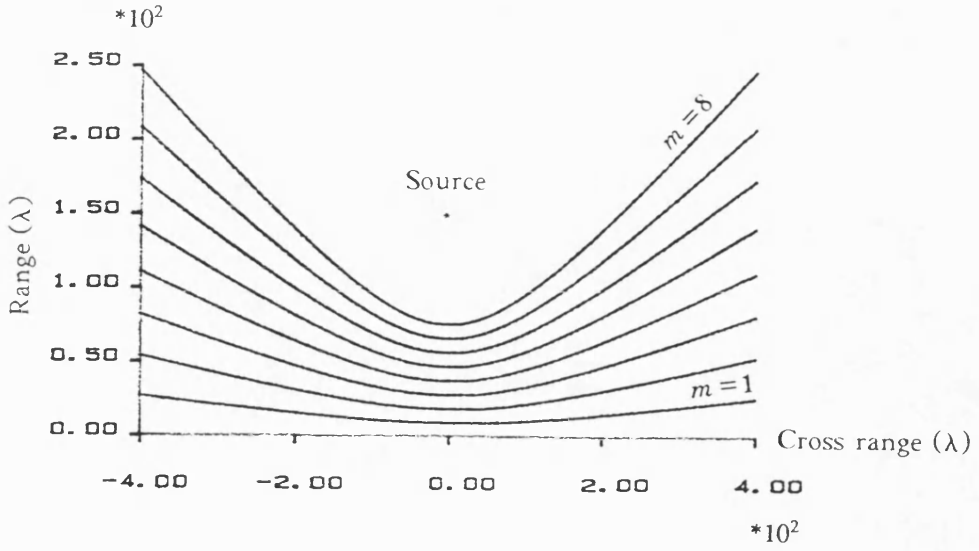

Fig. 5.10 The caustics of the first eight modes in a 3° ideal wedge for a source at range $r = 150\lambda$, cross range $z = 0$.

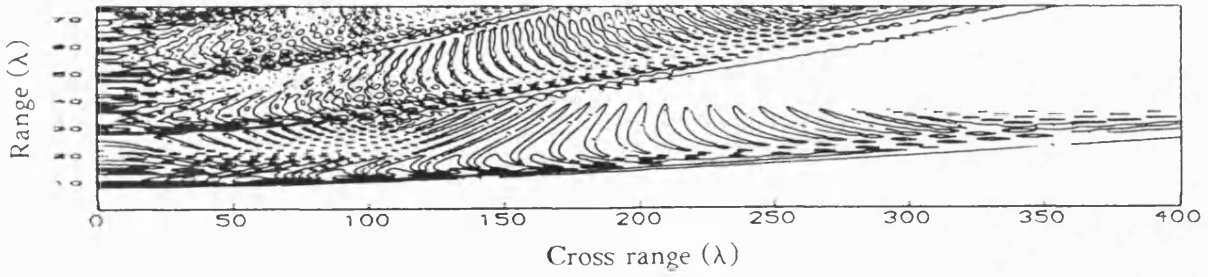

Fig. 5.11a Field $|\Phi(r,\theta,z)|$ at depth $1/4\lambda$ as a function of range ($1\text{-}75\lambda$) and cross range ($0\text{-}400\lambda$) for a 411kHz source at S(150λ,1.5°,0) in a 3° ideal wedge.

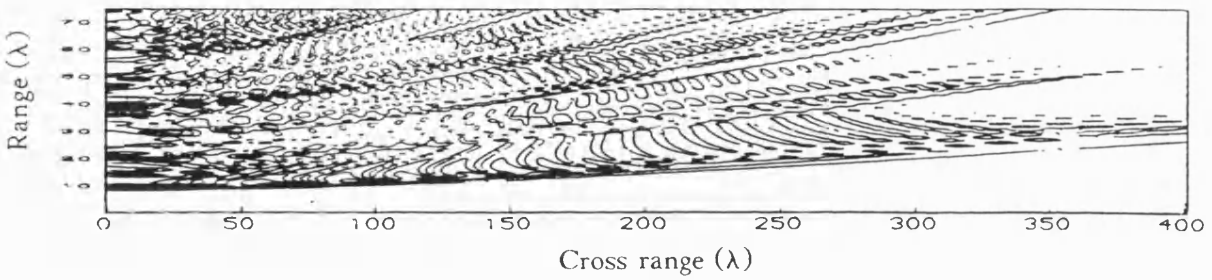

Fig. 5.11b Field $|\Phi(r,\theta,z)|$ at depth 1/4λ as a function of range (1-75λ) and cross range (0-400λ) for a 411kHz source at S(150λ,1.25°,0) in a 3° ideal wedge.

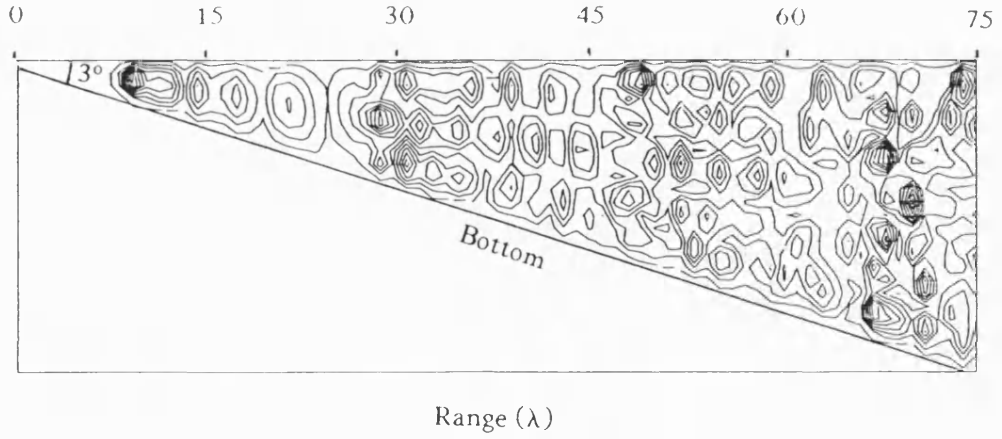

Fig. 5.12a Field $|\Phi(r,\theta,z)|$ at $z = 0$ plane as a function of range (1-75λ) and water depth, for a source at S(150λ,1.5°,0) in a 3 ° ideal wedge.

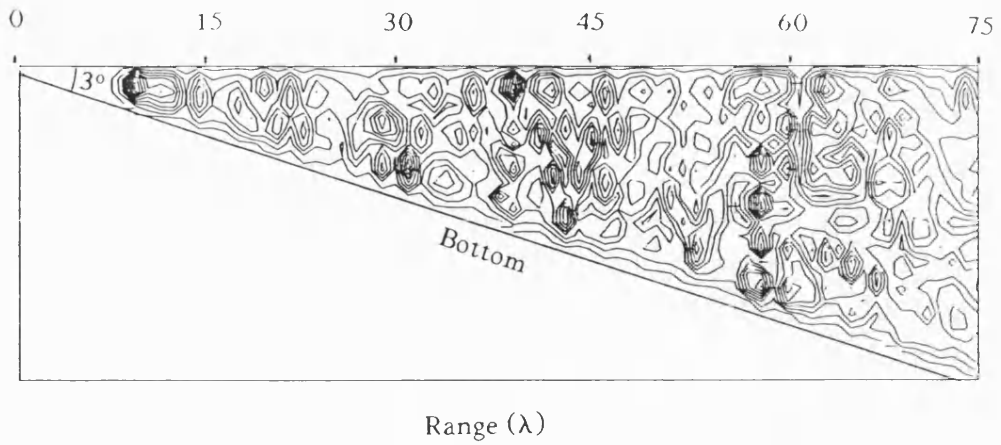

Fig. 5.12b Field $|\Phi(r,\theta,z)|$ at $z = 0$ plane as a function of range (1-75λ) and water depth, for a source at S(150λ,1.25°,0) in a 3 ° ideal wedge.

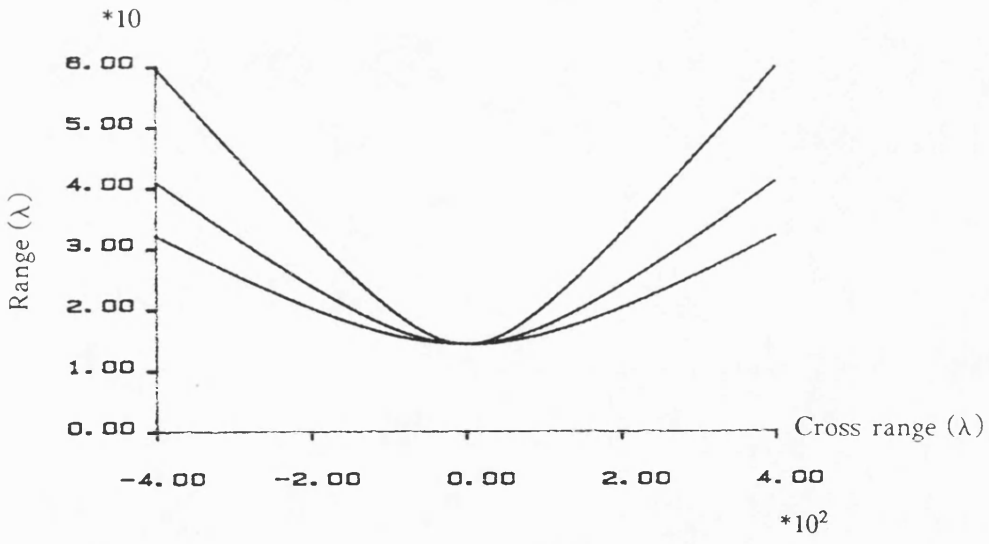

Fig. 5.13 The caustics of the first mode correspond to the source at range $r = 100\lambda, 150\lambda$, and 200λ in a 2° ideal wedge.

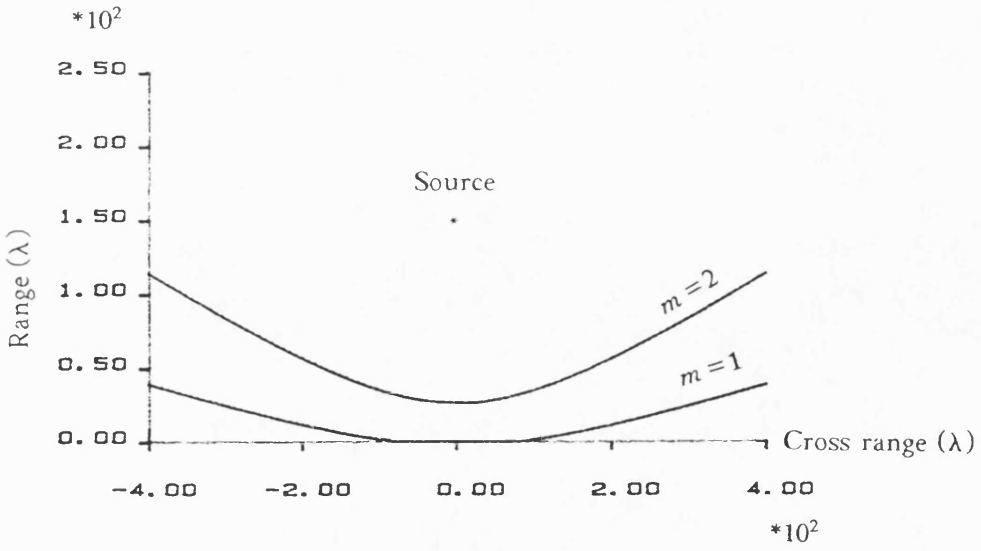

Fig. 5.14 The caustics of the modes in a 1° penetrable wedge for a source at range $r' = 150\lambda$, cross range $z = 0$.

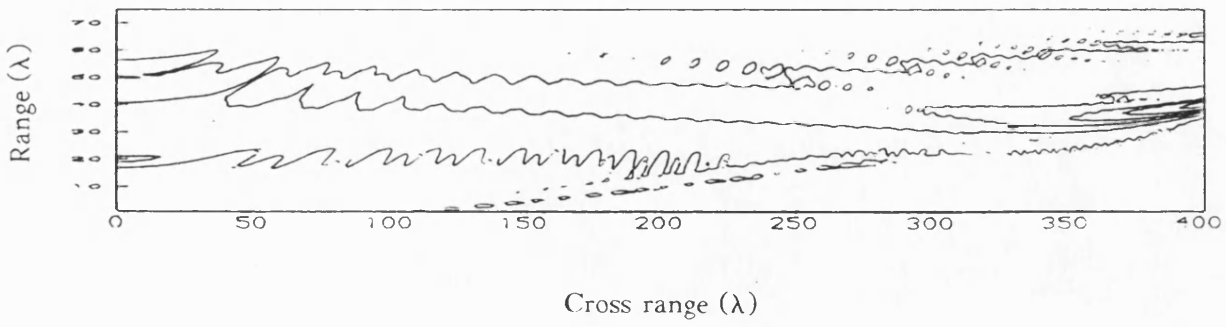

Fig. 5.15 Field $|\Phi(r,\theta,z)|$ at depth $1/4\lambda$ as a function of range ($1\text{-}75\lambda$) and cross range ($0\text{-}400\lambda$) for a 411kHz source at **S**(150λ,0.5°,0) in a 1° penetrable wedge.

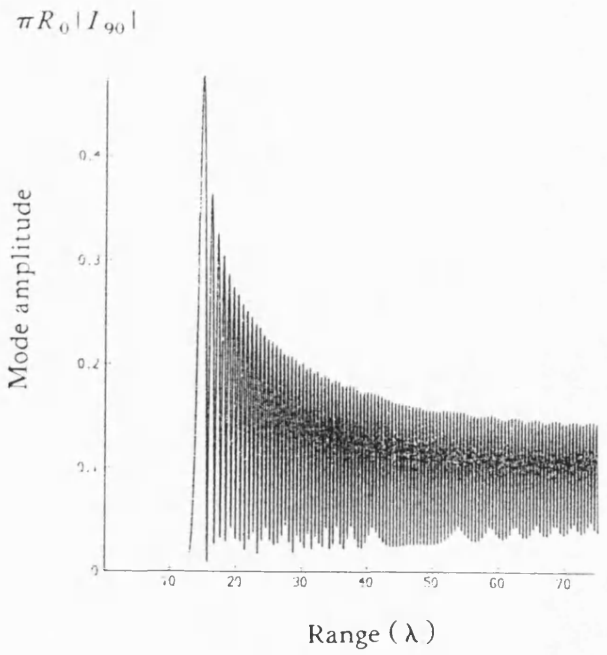

Fig. 5.16a The first mode coefficient at $z = 0$ plane as a function of range (1-75λ) for a source at range $r' = 150\lambda$ in a 2° ideal wedge.

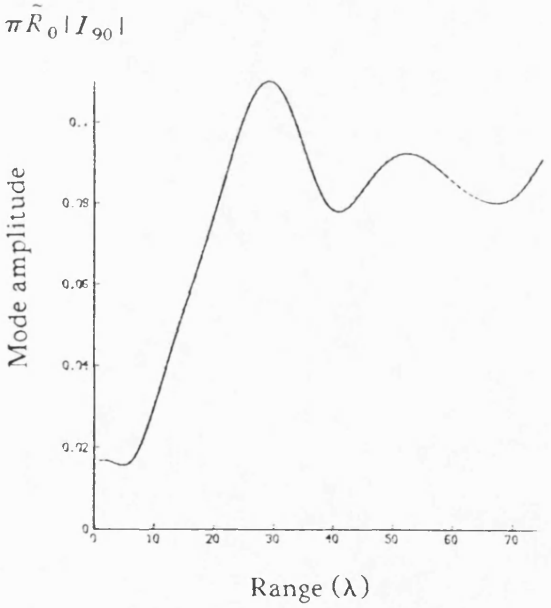

Fig. 5.16b The first mode coefficient at $z = 0$ plane as a function of range (1-75λ) for a source at range $r' = 150\lambda$ in a 2° penetrable wedge with a critical angle $\alpha_c = 27.5°$.

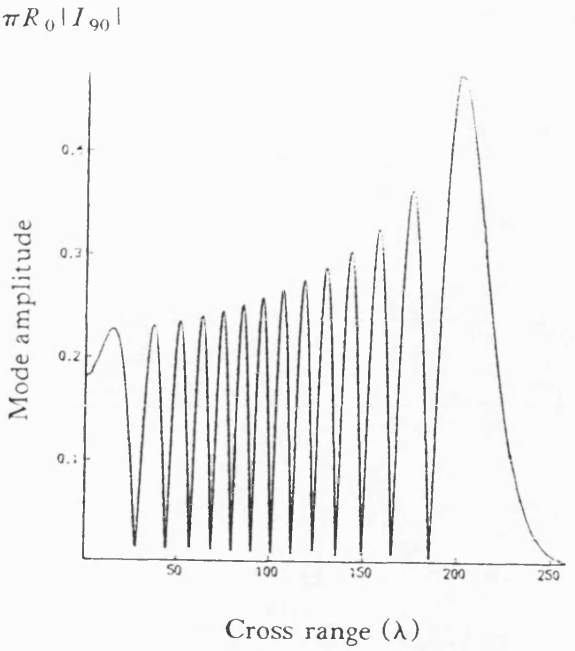

Fig. 5.17a The first mode coefficient at range $r = 25\lambda$ as a function of cross range (0-260λ) for a source at range $r' = 150\lambda$ in a 2° ideal wedge.

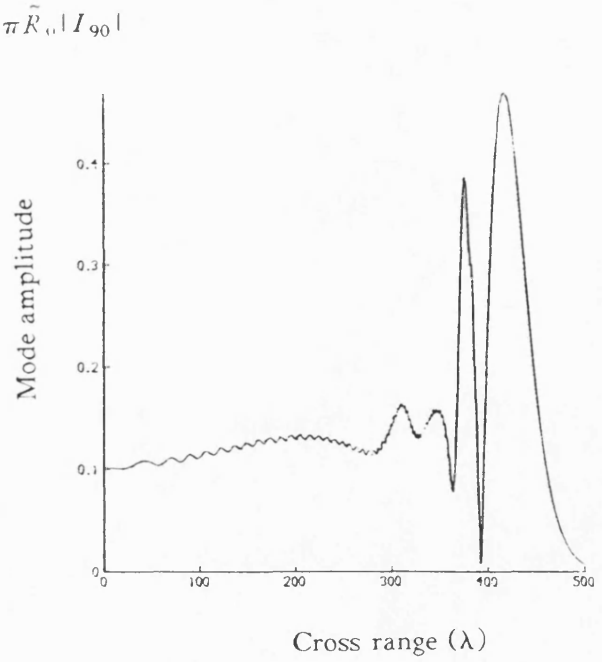

Fig. 5.17b The first mode coefficient at range $r = 25\lambda$ as a function of cross range (0-500λ) for a source at range $r' = 150\lambda$ in a 2° penetrable wedge with a critical angle $\alpha_c = 27.5°$.

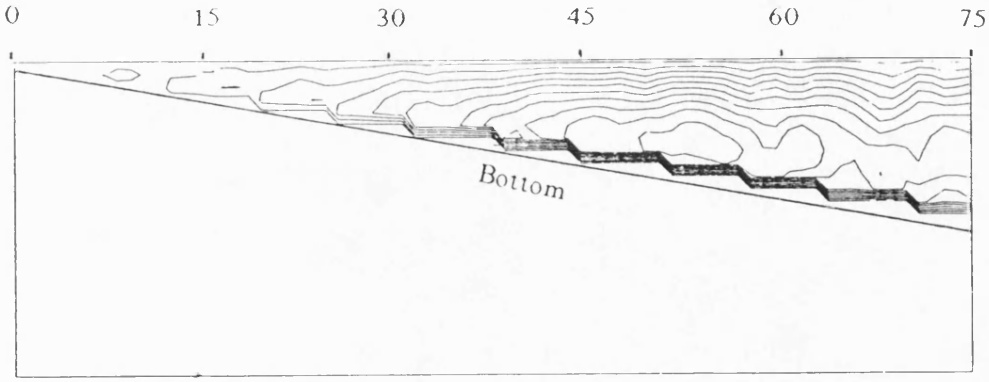

Fig. 5.18a Field $|\Phi(r,\theta,z)|$ at $z = 0$ plane as a function of range (1-75λ) and water depth, for a source at S(150λ,0.5°,0) in a 1 ° penetrable wedge.

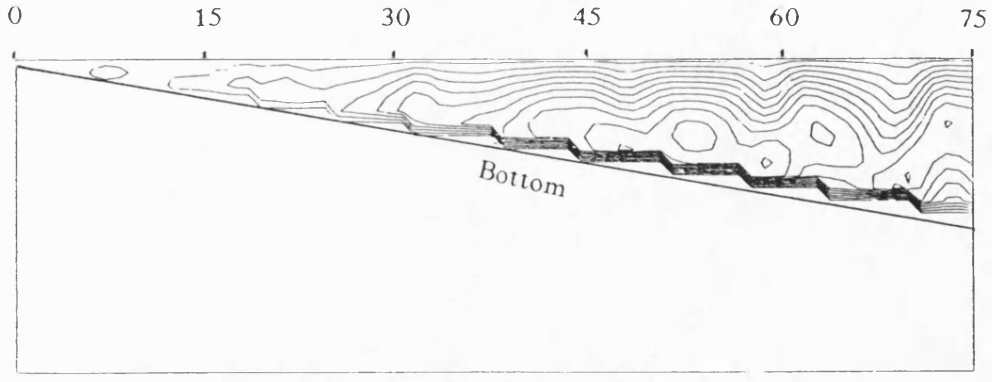

Fig. 5.18b Field $|\Phi(r,\theta,z)|$ at $z = 0$ plane as a function of range (1-75λ) and water depth, for a source at S(150λ,0.3°,0) in a 1 ° penetrable wedge.

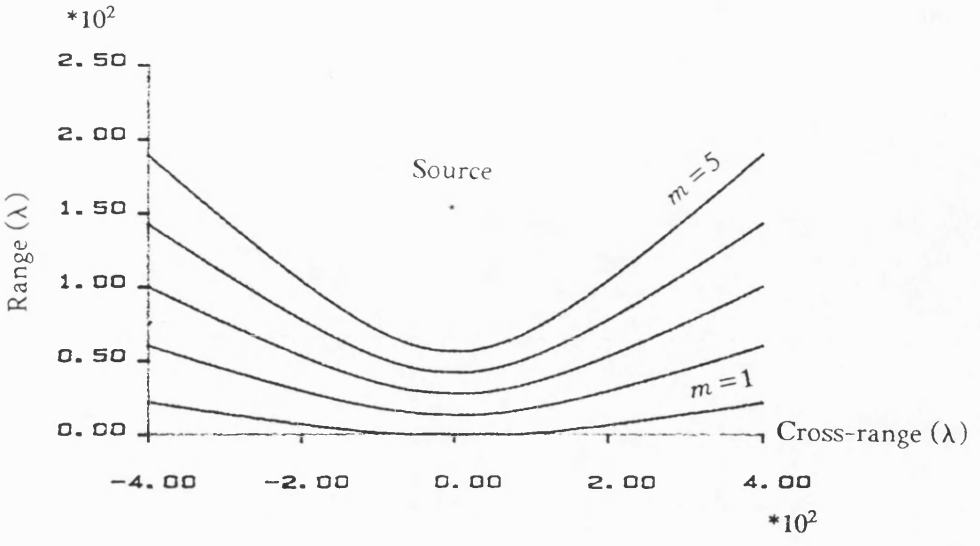

Fig. 5.19 The caustics of the modes in a 2° penetrable wedge for a source at range $r' = 150\lambda$, cross range $z = 0$.

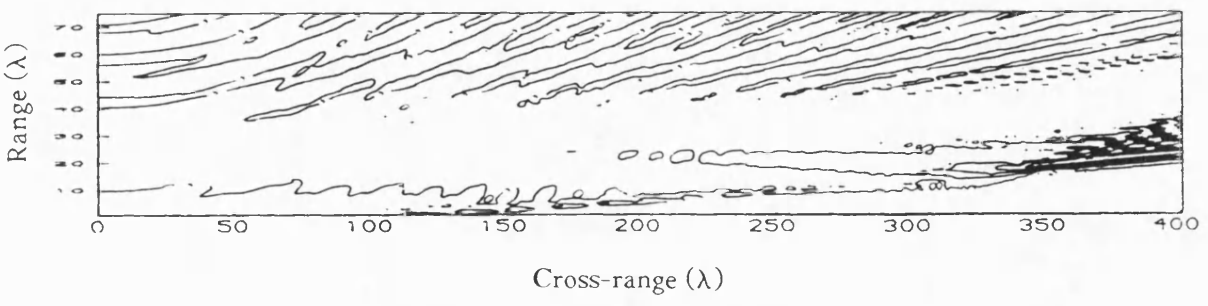

Fig. 5.20 Field $|\Phi(r,\theta,z)|$ at depth 1/4λ as a function of range (1-75λ) and cross range (0-400λ) for a 411kHz source at S(150λ,1°,0) in a 2° penetrable wedge.

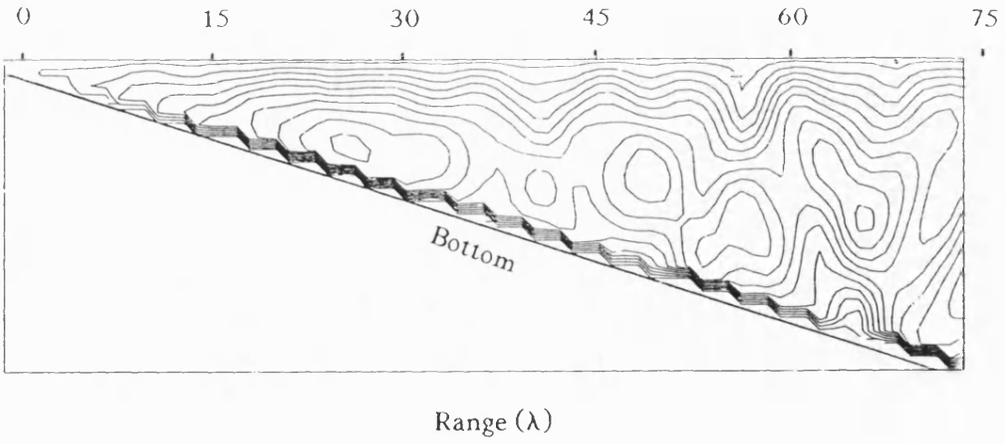

Fig. 5.21 Field $|\Phi(r,\theta,z)|$ at $z = 0$ plane as a function of range (1-75λ) and water depth, for a source at S(150λ,1°,0) in a 2° penetrable wedge.

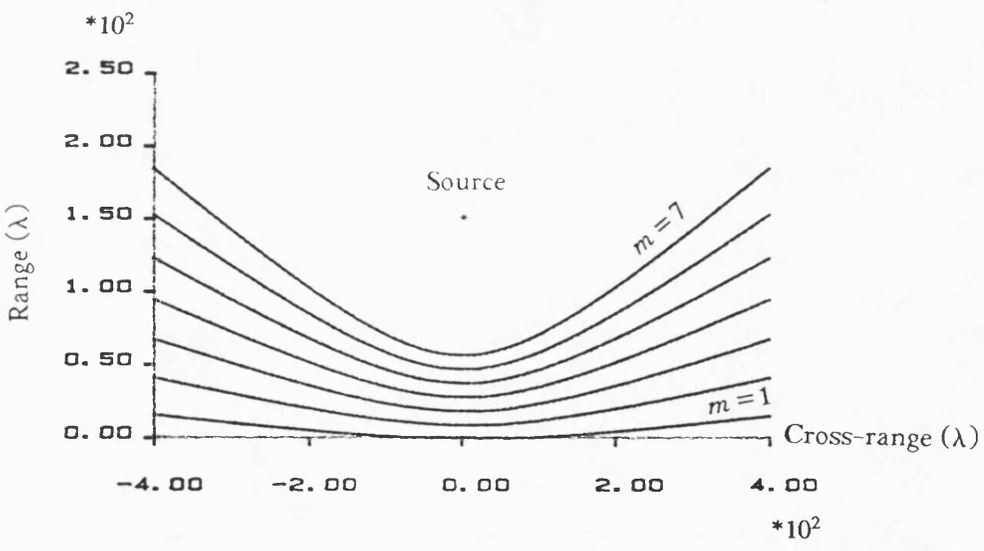

Fig. 5.22 The caustics of the modes in a 3° penetrable wedge for a source at range $r' = 150\lambda$, cross range $z = 0$.

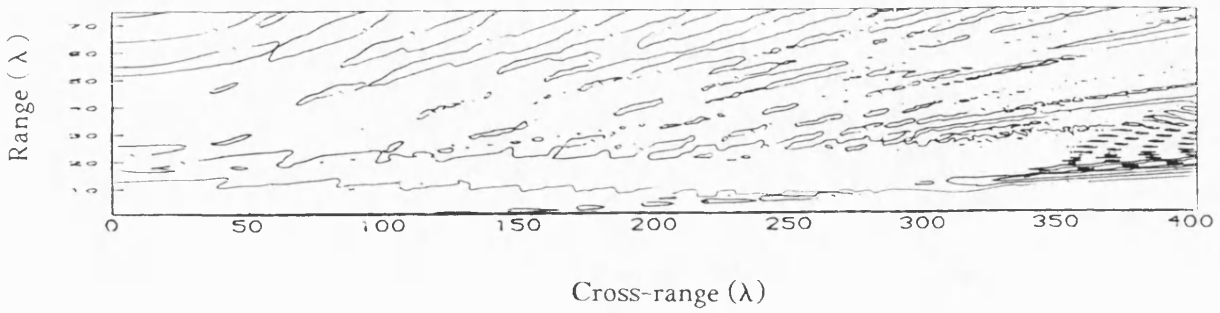

Fig. 5.23 Field $|\Phi(r,\theta,z)|$ at depth 1/4λ as a function of range (1-75λ) and cross range (0-400λ) for a 411kHz source at S(150λ,1.5°,0) in a 3° penetrable wedge.

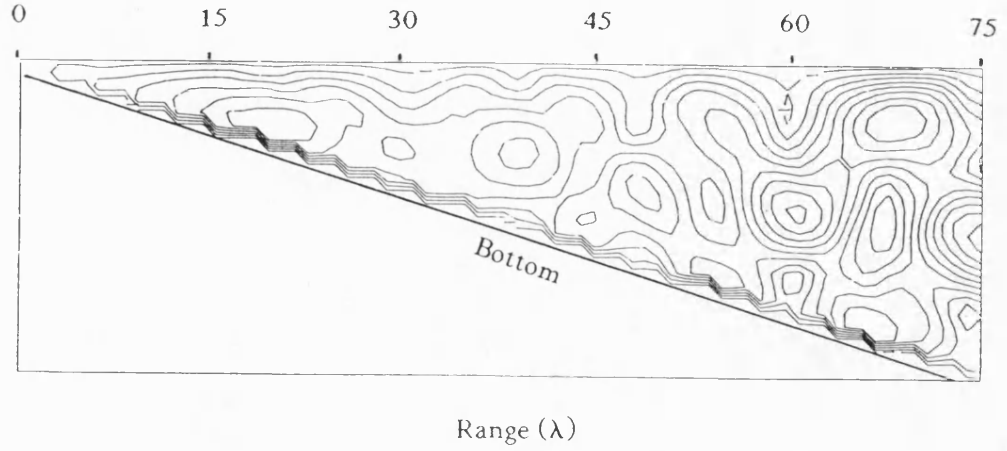

Fig. 5.24 Field $|\Phi(r,\theta,z)|$ at $z = 0$ plane as a function of range (1-75λ) and water depth, for a source at S(150λ,1.5°,0) in a 3° penetrable wedge.

Chapter 6. EXPERIMENTAL RESULTS AND DISCUSSIONS

6.1 Introduction

Sound pressure as a function of range and cross range, and as a function of range and water depth in wedges with a sand bottom have been measured in the tank as described in Chapter 4. In order to test the performance of the experimental apparatus, some preliminary measurements have also been carried out in a shallow water channel and in a wedge-shaped channel before the sand bottom was put into the tank. In order to explain the mode propagation in water channel, sound pressure in shallow water channels with the sand bottom parallel to the water surface was measured. To observe the sound penetration into the bottom, sound pressure was also measured in the bottom. The results of the measurements are demonstrated here and compared with the theoretical predictions. The scale of the sound pressure shown in this chapter is arbitrary.

6.2 Preliminary results

To model a shallow water channel, the tank was put horizontally on the bench. The water depth in the tank was 3cm (8.4λ). In contour map, Fig. 6.1 shows the acoustic field at the half depth of the water for the directional transmitter as a source which is also at the half depth of the water. The measured area is 0.9m×0.9m (250λ×250λ) in range (Special attention must be paid to that the range is origin at the source in this section and the next section) and cross range, the minimum range from the transmitter is 0.38m (106λ), and the cross range from the transmitter is from -0.45m to 0.45m (125λ). The range and the cross range are sampled every 2cm (5.6λ). To view the field more clearly, Fig. 6.2 demonstrates the same field as in Fig. 6.1 in isometric projection seen in two different angles. It can be seen that the field is symmetric with respect to the acoustic axis of the transmitter, high peaks occur at the central part of the field where is the main beam of the transmitter, away from the center, sound intensity decreases and side lobes are found. Although there are multipath propagations in the shallow water channel, the directivity of the transmitter is very similar to that in a free space. The sound pressure is decreasing as the distance is increasing from the transmitter. Intermode interference is demonstrated by the alternative high and low pressure distribution along the propagation path in range direction.

Replacing the directional transmitter with the omnidirectional transmitter, the field was measured in an area of 0.6m×1.2m (167λ×334λ) under the same condition, the minimum range is 0.34m (95λ), and the cross range is from -0.6m to 0.6m. As it can be seen in Figs. (6.3) (contour map) and 6.4 (isometric projection), the field is cylindrically symmetric, but no directivity can be seen as it would

be expected, there are alternatively high and low intensity circle rings centered at the transmitter which indicate there are intermode interference.

To measure the fields in a wedge shaped water channel, the tank was lifted at one side to form a 2° water wedge. The directional transmitter was placed so that the direction of its acoustic axis is parallel to the apex of the wedge. The measurement was made in the same manner in Fig. 6.1 except the depth of the receiver was 2mm, the result is shown in Figs. 6.5 (contour map) and 6.6 (isometric projection). The field is not symmetric any more, although the main beam is still in the central part of the field, all the sound rays tend to propagate towards deeper water due to the refraction caused by the sloping bottom. Figs. 6.7 (contour map) and 6.8 (isometric projection) show the field for the omnidirectional transmitter in an area of 0.3m×1.37m (83.5λ×381λ) in the wedge. The shadow zone can be seen at the place where is far away from the transmitter and near the apex of the wedge. The field near the apex is quite smooth since only the first mode exists there, the sound intensity reaches the peak at the caustic then drops very quickly in the shadow zone, no intramode interference is found in this part of the field, so that the bottom of the tank (made of polypropylene) is not perfect reflecting according to the penetrable wedge theory. In the deeper water, there are more modes sustained, intermode interference occurs as it can be seen. As predicted by the normal mode theory in Sec. 3.2, the basic pattern of the field are hyperbolic, near the apex, where only lower modes can reach, there are wider hyperbolic beams, in the deeper water, high modes form narrow hyperbolic beams. Although no quantitative comparison about the sound intensity can be made because the acoustic property of the bottom is not known, the measured results which provide good views of the field in these cases show some qualitative agreement with the theory.

6.3 The fields in water channels with a horizontal sand bottom

In order to demonstrate the mode propagation in a water channel, the sound pressure as a function of range and depth is measured in shallow water channels. The theoretical model of the problem is briefly given in Appendix C. Fig. 6.9 shows a result of the measurement, which was taken in a water channel with water depth 6.9mm (1.92λ). The water depth was sampled every 0.3mm (0.0835λ). The starting range of the measurement is 200mm (56λ), and the pressure was sampled every 10.75mm (3λ) over a distance of 718mm (200λ). It can be found that there are two modes sustained in the channel according to the characteristic equation in Appendix C. The grazing angles and the phase velocities of the two modes are 11.5° and 24.3° and, 1507.2m/s and 1621.1m/s, respectively. The results of the experiment agree very well with the prediction of the theoretical model as shown in

Appendix C. Here the detail structure of the field is revealed. At the short range from the source, two modes strongly interference with each other to form alternative high and low pressure zone in a zig-zag fashion. As the range increases, the second mode decays quicker than the first mode because the second mode has a steeper grazing angle than the first mode, consequently, it suffers more attenuation as it is reflected from the lossy bottom. It seems that the mode is stripped away as sound propagates outward from the source. At the far end of the figure, the second mode almost can not be seen, only the first mode exists. In practice, the effect of the attenuation in bottom will be significant for a long range shallow water propagation, so that the first mode is the most important since all the other modes decay quicker that the first mode.

Fig. 6.10 shows another measured result carried out in a channel with water depth 10mm (2.78λ). The other conditions were the same as in Fig. 6.9. We can see there are more modes in the channel as the sound pressure has a complicated distribution in the water column. By the prediction of the theory in Appendix C, there should be three modes in the channel. The grazing angles and the phase velocities of the three modes are 8.46°, 17.51° and 27.04° and, 1493m/s, 1548.8m/s and 1658.2m/s, respectively. These also agree very well with the experimental result. As mentioned before, the third mode is first stripped away due to the attenuation after 150λ, and only the first and the second modes were sustained in the channel. So the field is similar to that in Fig. 6.9. Comparing with the result in Fig. 6.9, the interference period of the first mode and the second mode is longer. The interference corresponding to two modes with 2π phase difference can be found as

$$\left(\frac{2\pi f}{c_{pm}}-\frac{2\pi f}{c_{pn}}\right)\Delta r=2\pi$$

or

$$\Delta r=\frac{c_{pn}c_{pm}}{(c_{pn}-c_{pm})f} \tag{6.1}$$

where f is frequency, c_{pm} and c_{pn} are the phase velocities of the m*th* and the n*th* mode. We can see from the above equation that the distance corresponding to two modes with 2π phase difference is determined by the difference of the phase velocities of the two modes, the smaller the difference in phase velocities, the longer the interference period. When the water depth becomes deeper, more modes will be sustained in the channel, and the phase velocities of two adjacent modes are closer to each other, therefore it results in a "thinner" interference pattern as in Fig 6.10 comparing with that in Fig. 6.9. For the given phase velocities of the first two modes in Figs. 6.9 and 6.10, the interference

periods are 14.5λ and 28.1λ respectively, according to Eq. (6.1). These results agree well with the experimental results which are indicated in the figures.

6.4 The field as a function of range and depth

Although there are many theoretical models which can be used to predict the sound field as a function of range and depth in a wedge, which basically is a two dimensional problem, there are not adequate experimental results to demonstrate the features of the field, especially in up slope propagation case. Here some results that the fields are measured as functions of range and depth at $z = 0$ plane are presented, which is equivalent to the theoretical model of an infinite line source parallel to the apex in a wedge. All the measured results here are the up slope propagation field of a point source. According to the adiabatic approximation theory that, for a small angle of slope, the normal modes will adjust to the local water depth with negligible coupling of energy to other modes. Consider a mode propagating in up slope direction, as the water depth becomes shallower and shallower, the mode can no longer adjust to the local depth at a certain range from the apex, therefore the mode becomes a leaking mode from a trapped mode, the range corresponding to the change is the cutoff range. The depth of the water in the wedge at which the mode is cutoff can be found by shallow water theory as if the mode is in a shallow water channel with the same depth, then the cutoff range can be determined.

6.4 a. In the water column

Fig. 6.11 shows the result of a measurement of the sound pressure in water column carried out in $z = 0$ plane for a source at $r' = 297\lambda$ in a 1° wedge, the measurement was made over a range 200λ sampled every 3λ in range and 0.056λ in depth. The measurement was made only in the water column. The cutoff ranges as indicated in the figure are 32λ for the first mode, 94λ for the second mode, and 154.6λ for the third mode within the measured range. As the part of the result in Fig. 6.11, the measured sound pressure as a function of range at depth 0.14λ is shown in Fig. 6.12. It can be seen from Figs. 6.11 and 6.12 that the field has a shadow zone which is up to about 16λ at range from the apex of the wedge, after the shadow zone, there is only the first mode till about 70λ, the amplitude of the first mode drops a little as it approaches towards the apex at range from 60λ to 35λ due to the attenuation in the bottom. At the range less than 32λ, the first mode becomes a leaking mode from a trapped mode, Fig. 6.12 shows the amplitude of the sound pressure decreases as the mode passes the cutoff range towards the apex. Comparing with the first mode in a perfect wedge in Fig. 5.4, the cutoff process is much slower in a penetrable wedge. As we can understand that the

cutoff for a mode in a perfect wedge is related with the rays corresponding to the mode turning round from up slope direction to down slope direction when the grazing angle of the rays exceed 90° (normal incidence). In a penetrable wedge, the cutoff of a mode starts at the range where a ray corresponding to the mode has a incident angle greater than the critical angle which is about 27.5° in this case, far less than the normal incidence, therefore the cutoff range is greater. It seems that the end of the cutoff process should also occur at the place where all rays turn round as in the perfect wedge. This is not the case because the lateral wave is excited at the beginning of the cutoff. Some introductions will be given in next section about the lateral wave and its effect in up slope propagation. Although the contribution from the lateral wave makes the cutoff process more complicated, a rough estimation can be still made as suggested before about the end of the cutoff process, that is it ends as the ray with an angle equal to the critical angle at the cutoff range turns round from the up slope direction to the down slope direction. Fig. 6.13 shows the cutoff process of the eigenray of a mode in a penetrable wedge.

Between the range from 70λ to 120λ, the measured field shows there are only the first mode and the second mode are sustained, since it is a typical interference pattern that results from two modes interfering with each other as shown in Fig. 6.9. But it is different from the shallow water channel with a horizontal bottom since the period of the interference is changed in a wedge propagation. It becomes shorter if the modes propagate in up slope direction as it can be seen. This indicates that the modes adjust to the water depth as they propagate in the wedge, so that the phase velocities of the modes are changed accordingly. The interference period is a function of the difference of the phase velocities. It does not change in a water channel with parallel boundaries since the phase velocity of a mode will not change as can be seen in Eq. (6.1). Because the phase velocities of all the modes vary in a penetrable wedge, the interference period which depends on the difference of the phase velocities will change as demonstrated in Fig. 6.12. Beyond the range over 120λ towards deeper water, the field becomes complicated because of the successive emergences of the third mode and the forth mode.

Fig. 6.14 shows the measured field as a function of range and depth in $z = 0$ plane up to 160λ in range for a source at range $r' = 261\lambda$ in a 2° wedge. The result was taken only in the water column. The cutoff ranges are 16λ for the first mode, 47λ for the second mode, 77λ for the third mode, 109λ for the forth mode, and 139λ for the fifth mode as indicated in the figure. A part of the measured sound pressure as function of range at depth 0.14λ is shown in Fig. 6.15. Comparing with Fig.6.12, the cutoff process for the first mode is shorter in a 2° wedge than that in a 1° wedge. Since a ray

corresponding to a mode changes its heading quicker in a wedge with a greater wedge angle, therefore, the range for a ray starts to penetrate into the bottom until it turns round is shorter in 2° wedge than in 1° wedge. The range for the ray corresponding to the first mode turning round in $z = 0$ plane can be estimated by Eq.(3.50) with the grazing γ of the first mode at source position computed by shallow water theory. γ is equal to 8.9° in 1° wedge and 4.9° in 2° wedge. Thus the turning point is at range 23.2λ in 1° wedge and 12.7λ in 2° wedge.The range for mode cutoff taking place is 8.8λ in 1° wedge and 3.2λ in 2° wedge. Comparing with Fig. 6.11, it can be seen that the cutoff ranges for different modes are closer, more modes are sustained in a 2° wedge. So the experimental results confirm the prediction by the theoretical model.

Comparing with the result in Fig. 5.21, it is found that the agreement is good between the experimental result and the theoretical prediction in the region where only the first mode is trapped in the wedge. As the range increases, the interference patterns of the two results become different. One reason for the discrepancy is that the transmitter used in the experiment is not a point source, so that there could be some uncertainty in its position in the wedge. The another reason is that all the partial reflections in the penetrable wedge are excluded from the field predicted by the theoretical model as mentioned in chapter 2. In fact the partial reflection wave at the region near the cutoff range of a mode is quite important, as we can see from the experimental results. Therefore the mode interfering demonstrated in the predicted field is less strong than that in the experiment.

Fig 6.16 shows the measured field as a function of range and depth in $z = 0$ plane up to 75λ in range for a source at range $r' = 150\lambda$ in a 3° penetrable wedge. There are four modes sustained in the region. The cutoff ranges for the sustained modes are 10.6λ for the first mode, 31.1λ for the second mode, 51.5λ for the third mode, and 73λ for the forth mode. Comparing with Figs. 6.11. and 6.12, there are one mode in 1° wedge and three modes in 2° wedge sustained in the same region. As would be expected, the measured result is different from the predicted result in Fig. 5.24 at the region where more than one mode sustained because of the uncertainty of the source position in the experiment and the absence of the contribution from the partial reflection wave in the theory.

6.4 b. In the water column and in the bottom

Sound penetration into the bottom is an important feature of the field in a penetrable wedge. To investigate this phenomenon, the measurements were carried out not only in the water column, but also in the bottom as mentioned in Chapter 4. Fig. 6.17 shows the field in $z = 0$ plane for a source at $r' = 150\lambda$. The measured range is 74λ, which is sampled every 2λ. The measured depth is 6.7λ, which

is sampled every 0.28λ. The sloping bottom is indicated by the dash line.

First, we examine the field in the water column. It corresponds to the beginning part (0-75λ) of the field shown in Fig. 6.11, but gives more detail about the field. The cutoff range of the first mode is indicated in the figure. It can be seen that at the range greater than the cutoff range the first mode adjusts to the water depth as described by the adiabatic approximation. The second mode, though been cutoff, still makes some contribution to the field at range about 70λ. The contribution contains two parts, one is from the partial reflection of the wave explained in the previous section, another one is from the lateral wave. The generation of the lateral wave will be explained later.

The field in the bottom gives some very interesting results. At the range further than 50λ from the apex, the field in the bottom has a very obvious interference pattern. At the shorter range, there are two beams in the bottom, one major beam occurs at range between 18-26λ, and the other beam is quite small which is at range less than 18λ.

Fig. 6.18 shows the measured field as a function of range and depth in the water column and in the bottom of a penetrable wedge with a 2° angle. The measured range is 74λ, which is sampled every 2λ. The measured depth is 6.7λ, which is sampled every 0.28λ. The sloping bottom is indicated by the dash line. there are two modes sustained in the water column. The cutoff range of the each mode is indicated in the figure. The penetration of the first mode is clearly seen as in the 1° wedge case shown in Fig. 6.17. There is a major beam at the cutoff range, and there is also a small beam proceed the major beam in the bottom.

The penetration of the second mode in both the experimental results shown in Figs. 6.17 and 6.18 does not give a clear beam pattern in the bottom as some numerical results suggested[35]. The interference pattern in the place where there should be the penetration beam of the second mode indicates that there is not only the second mode but the first mode.

To explain the result obtained above, the phenomenon of the lateral wave needs to be explained first. It is well known that a sound wave incident on the interface of the bottom with an angle near the critical angle produces a wave that travels parallel to the interface in the bottom. As it propagates at the bottom sound velocity, it continually excites a wave in water called lateral wave or head wave, which is radiated at the critical angle from the bottom. In a penetrable wedge, when a trapped normal mode propagates in up slope direction, the incident angle of the mode becomes steeper and steeper, it will reach the critical angle at the cutoff range, at this point, the lateral wave will be excited by the

mode. Though the lateral wave decays quickly for a long range propagation compared with trapped mode, its contribution to the field at short distance is not negligible.

There will be two partially reflected waves at the range shorter than the cutoff range produced by the first mode, one is the specular reflection from the critical incident, another one is the lateral wave. In the process of the penetration, these two waves form two beams in the bottom. The major beam is is due to the specular reflection of the eigenray corresponding to the first mode at the cutoff range, which can be predicted as in the previous section in ray theory. After entering the bottom, the eigenray forms a beam to propagate into the bottom. The width of the beam on the bottom should be equal to the range between the places that the ray corresponding to the mode starts to penetrate into the bottom and that the ray turns its heading to deeper water as shown in Fig.6.13, which is referred to as the penetration aperture. The penetration beam would be confined within this aperture if there were no lateral wave. However, the sound energy penetration into the bottom is continued beyond the aperture towards the apex. It is obvious that this phenomenon can not be explained as higher mode coupling into lower mode since the mode we observed is the lowest mode. Therefore, the small beam which is closer to the apex results from the lateral wave which is reflected from the water surface and into the bottom again. Because the lateral wave decays rapidly as the it propagates towards the apex, a shadow zone can be found as demonstrated in the experimental results.

As pointed out in chapter 2, the theoretical model used here can not describe the field in the bottom, therefore, no more detail comparison can be made with the measured results.

6.5 The field as a function of range and cross range

Fig. 6.19 shows the measured sound pressure as a function of range and cross range at a fixed depth in a penetrable wedge with 1° wedge angle. The area in which the data were taken is 75λ in range and 393λ in cross range. The depth of the receiver is $1/4\lambda$. The source was put at about the middle of the wedge, so the amplitude of the second mode is small. There is only the first mode sustained in the measured area according to the shallow water theory. The second mode is cutoff at a range 94λ in the $z = 0$ plane as mention in Sec. 6.4a. In the measured result, the trace of the second mode can be seen as in Fig. 6.19. The interference pattern indicates that the second mode has a hyperbolic envelope as the theory predicted in Chapter 3. Most part of the area is insonified only by the first mode. The field is rather smooth in the area where only the first mode exists, the amplitude of the field is decreasing as the cross range is increased, near the apex of the wedge, there is the shadow zone.

Comparing with the numerical result in Fig. 5.15, there is no high intensity interference pattern in the region where is far in cross range at the caustic of the first mode in the measured field as predicted by the penetrable theory, *i. e.* there is no intramode interference, and the amplitude of the pressure decreases quicker as the distance from the source increases than that predicted by the theoretical model. Since the sand bottom used in the experiment is a highly absorbent one, when the sound propagates in the wedge, a substantial amount of attenuation is introduced by the bottom, thus a higher propagation loss is found in the measured result. The high attenuation in the bottom can explain why no intramode interference is found in the experimental result. In the region where only the first mode exists, the field at any point can be considered as the total contribution from two rays as mentioned in the Chapter. 3, one ray is the direct ray from the source to the receiving point and the other ray is the indirect ray. The indirect ray is a ray which travels in a direction closer to the up slope direction, so that it is refracted to the receiving point by more reflections from the surface and the bottom. In the inner zone, both the direct ray and the indirect ray have incident angles greater than the critical angle, they will penetrate into the bottom, since the indirect ray interacts with bottom more times than the direct ray, it decays quicker in the water column as its energy transmits into the bottom, so only the direct ray has contribution to the field. In the outer zone, though the indirect ray can no longer penetrate into the bottom because its incident angle is greater than the critical angle, it still suffers higher attenuation than the direct ray as it undergoes more bottom reflections, its amplitude is smaller than the direct ray, therefore the direct ray is dominant and no obvious intramode interference is found.

Fig. 6.20 shows the measured field as a function of range and cross range in a 2° penetrable wedge. The measured area is 75λ in range and 393λ in cross range. The receiver was at 1/4λ below the water surface, and the source was at about the middle of the wedge. The shadow zone of the field is narrower. More modes are sustained in this case as it can be seen that a complicated interference pattern appears. There are two modes in the measured area, and the third mode is just outside the area predicted by shallow water theory. The hyperbolic patterns in the picture indicate the basic structure of the mode propagation in a wedge as predicted by the theory in Chapter 3. Here the second mode insonifies more region comparing with that in 1° wedge, and the smooth part where only the first mode exists becomes narrower. Comparing with the numerical result in Fig. 5.20, the intramode interference predicted by the penetrable wedge theory in Sec. 3.3 is not found in the measured result, the amplitude of the pressure decreases as the distance between the source and the receiver increases no matter the receiver is in the inner zone or outer zone defined by Eqs. (2.42) and (2.46), this is the

same as in 1° wedge. The intermode interference predicted by the effective wedge model is similar to the measured result in the pattern, though it is not as strong as measured result. As mentioned in Sec. 6.4a, the predicted field does not take the partial reflection wave into account, this results in less mode interfering as seen in Fig.5.20.

Increasing the wedge angle up to 3°, Fig. 6.21 shows the measured field as a function of range and cross range in a 3° penetrable wedge. The other conditions are the same as in Figs. 6.19, and 6.20. As would be expected, the more modes are sustained in the wedge, according to the shallow water theory, there are 4 modes in this area. It can be seen that the shadow zone is even narrower, the gap between the second mode and the first mode is narrower comparing with the result in Fig. 6.20. Compared with the numerical result in Fig. 5.23, the measured field also has a apparent mode propagation structure, but there is no intramode interference in the measured result, and the intermode interference is stronger.

It can be seen that there are distinct shadow zones in Figs. 6.19, 6.20 and 6.21. Comparing with the result given in Fig. 5.14, it is found the positions of the envelopes predicted by the effective bottom model are too close to the apex, and even cross the apex of the wedge. This does not agree with the experimental results. Another way to predict the envelopes is to use Eq. (3.50) with the elevation angle γ computed by shallow water theory. Figs. 6.22 show the comparison between the measured envelopes of the fields and that predicted by Eq. (3.50) in 1°, 2° and 3° wedges. Linear regression method is used to determine the envelopes of the shadow zone with the experimental data. It is found that there are still big differences for the positions of the envelopes. This is because the ray invariant considers only the eigenray of a mode, it can predict the envelopes of the eigenray. But the experimental results give the envelopes of the shadow zone which are determined by the lateral wave as mentioned in Sec. 6.4, these envelopes are closer to the apex. Even though the positions of predicted by Eq. (3.50) are further from the apex, which are at least 5λ as it can be seen from the comparison, it gives a better estimate about the shadow zone edge in a penetrable wedge than that given by Eq. (3.97).

6.6 The field as function of range and cross range with a rough surface

In the previous section, the measured sound pressure field as a function of range and cross range demonstrate the special features of the point source field in penetrable wedges with smooth boundaries. In practice, both boundaries of a wedge may not be smooth such as a rough water surface caused by wind. It is interesting to make a comparison between the fields for a point source in a

penetrable wedge with a smooth water surface and in a penetrable wedge with a rough water surface. Fig 6.23 shows the field as a function of range and cross range in a penetrable wedge with a rough surface. The wedge angle is 2°. The measured area is the same as in Fig. 6.20. To make a rough surface expanded polystyrene beads are spread on the water surface randomly in the tank. The average diameter of the beads is about 4.5mm. The fluctuation of the surface caused by the beads is less than 1mm in depth. As it can be seen from the experimental result that the mode interference is not clear any more. The hyperbolic pattern which results from the intermode interference has disappeared. However, in the area where is far from the source, the field shows the scattering becomes less and less, and the first mode is still recognizable. This is because sound rays with steeper grazing angles which correspond to the higher modes undergo more surface scattering, some scattered rays will penetrate into the bottom if their grazing angles are greater than the critical angle, they decay very quickly. The rays corresponding to the first mode suffer less scattering, therefore, they insonify more area. Fig. 6.24 shows parts of the results in Figs. 6.20 and 6.23, which are normalized sound pressure at range 75λ as a function of cross range from $z = 0$ to $z = 390\lambda$ in a smooth wedge and in a rough wedge. There is a clearly distinguishable interference pattern shown in Fig. 6.24a for the field in a smooth wedge. Two modes exist at the far end as it can be seen. The field in a rough wedge fluctuates very rapidly, no intermode interference is found as shown in Fig. 6.24b, less fluctuation at the far end indicates the second mode is less important around this part.

6.7 Taking the bottom absorption into account in the analytic solution for the penetrable wedge

As it can be seen from the the comparisons between the predicted and the measured sound fields in chapter 5 and this chapter, there is a significant attenuation in the measured field due to the absorption in the sand bottom. The effect of the bottom absorption on the amplitude of the sound pressure is investigated in the appendix C. There are two mechanisms of attenuation in the bottom, one is the absorption, and the other one is due to the shear wave generation. Since the absorption is the most important effect as we can see from appendix C, so that only the absorption is considered here. Taking the absorption into account, the sound propagation in a shallow water channel can be predicted by shallow water theory very well as demonstrated in the appendix C. Unfortunately, in a penetrable wedge, the analytic solution Eq. (2.32) can not give a good prediction of the sound field if there is a bottom absorption. Here a simple modification to the solution is made which concerns the effect of the attenuation in the bottom.

Consider a mode in a shallow water channel with a lossy bottom, its amplitude decays exponentially, the attenuation coefficient of the mode is a function of the absorption in the bottom and grazing angle of the mode, the greater grazing angle, the larger attenuation coefficient. Analogous to the shallow water channel, a mode in a penetrable wedge suffers the bottom attenuation in the same way. Since the grazing angle of the mode varys as the local water depth changes, the attenuation coefficient of the mode is changed accordingly. Suppose the mode travels a distance dr, then the attenuation over the distance is $\alpha_r dr$, where α_r is the local mode attenuation coefficient. The total attenuation of the mode propagating from the source to the receiver can be found by an integration over the distance

$$a_t=\int \alpha_r dr \tag{6.2}$$

In practice, the integral can be approximate by a sum

$$a_t \approx \sum \alpha_r \Delta r = \Delta r \sum \alpha_r \tag{6.3}$$

The local mode attenuation coefficient α_r can be obtained as if the mode in a shallow water channel with the depth equal to the local depth of the wedge. The sound field in a wedge with a penetrable and lossy bottom can be represented by

$$\Phi(\tilde{r},\theta,z)=\frac{Q}{\theta_0}\sum_v I_v(\tilde{r},\theta,z)\sin\mu\theta\sin\mu\theta' e^{-a_l} \tag{6.4}$$

Fig. 6.25 show the comparison between Eqs. (2.32) and Eq. (6.4), which is the field as a function of the cross range at range 80λ and depth $1/4\lambda$. The dot dash line in the figures is the result without bottom attenuation. The solid line is the result with bottom attenuation, the first figure in Fig. 6.25 shows the absorption is $1dB/\lambda$ and, the second one shows the absorption is $1.48db/\lambda$. The predicted field without attenuation shows many small fluctuations over some intermode interference pattern, which comes from the higher modes. But the sound pressure decreases quicker and, an obvious intermode interference pattern can be seen when the bottom has absorption, all the higher modes decay quickly in this case. This result is close to the experimental result as in Fig. 6.24.

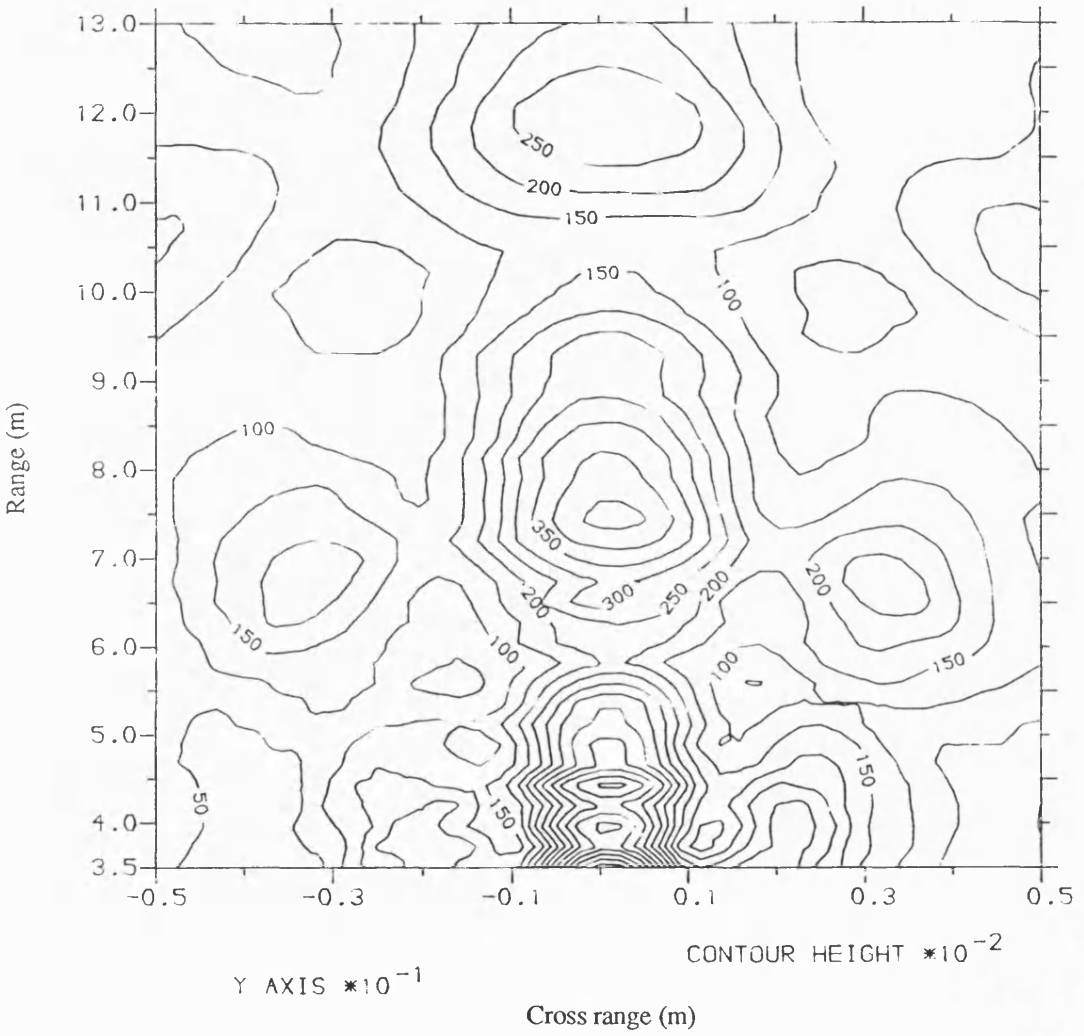

Fig. 6.1 Sound pressure field (contour map) at a fixed depth for a directional source in a shallow water channel.

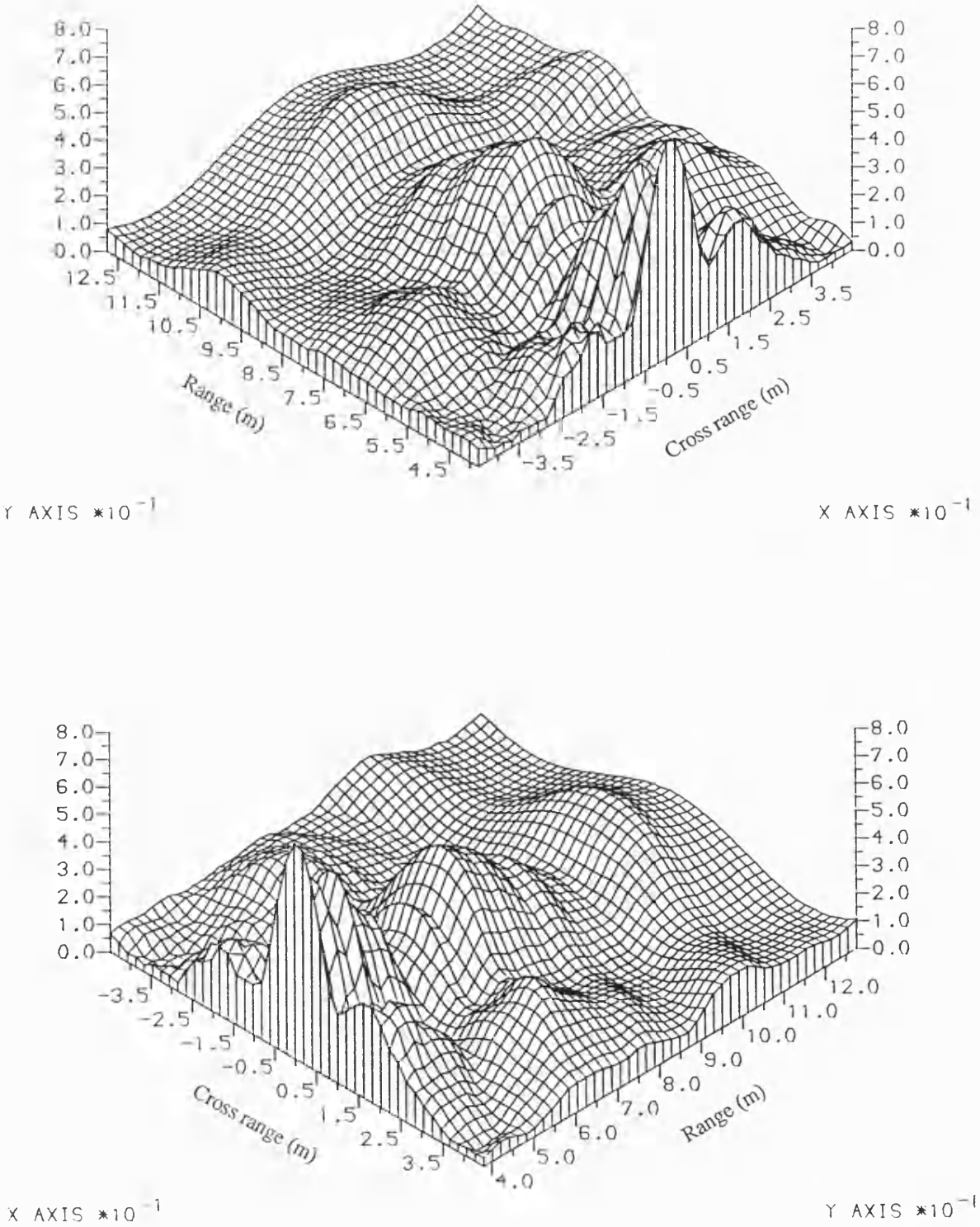

Fig. 6.2 Sound pressure field (isometric projection in two view angles) at a fixed depth for a directional source in a shallow water channel.

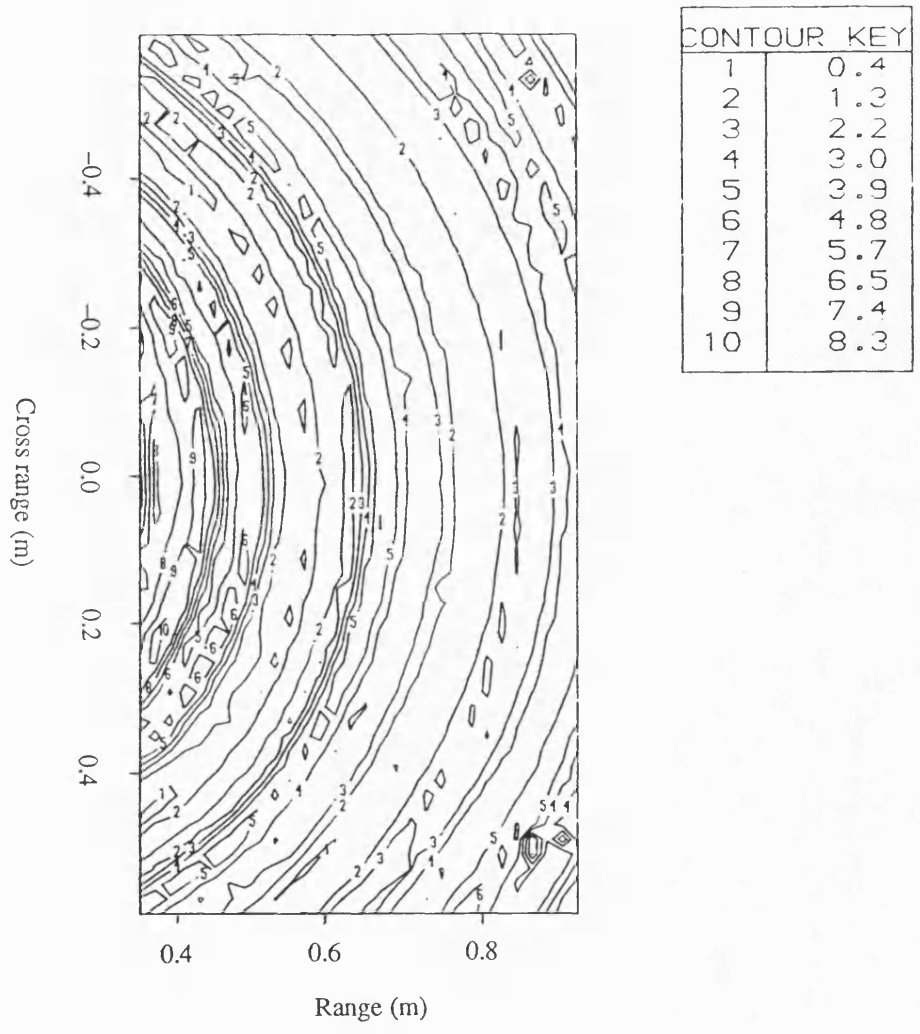

Fig. 6.3 Sound pressure field (contour map) at a fixed depth for an omnidirectional source in a shallow water channel.

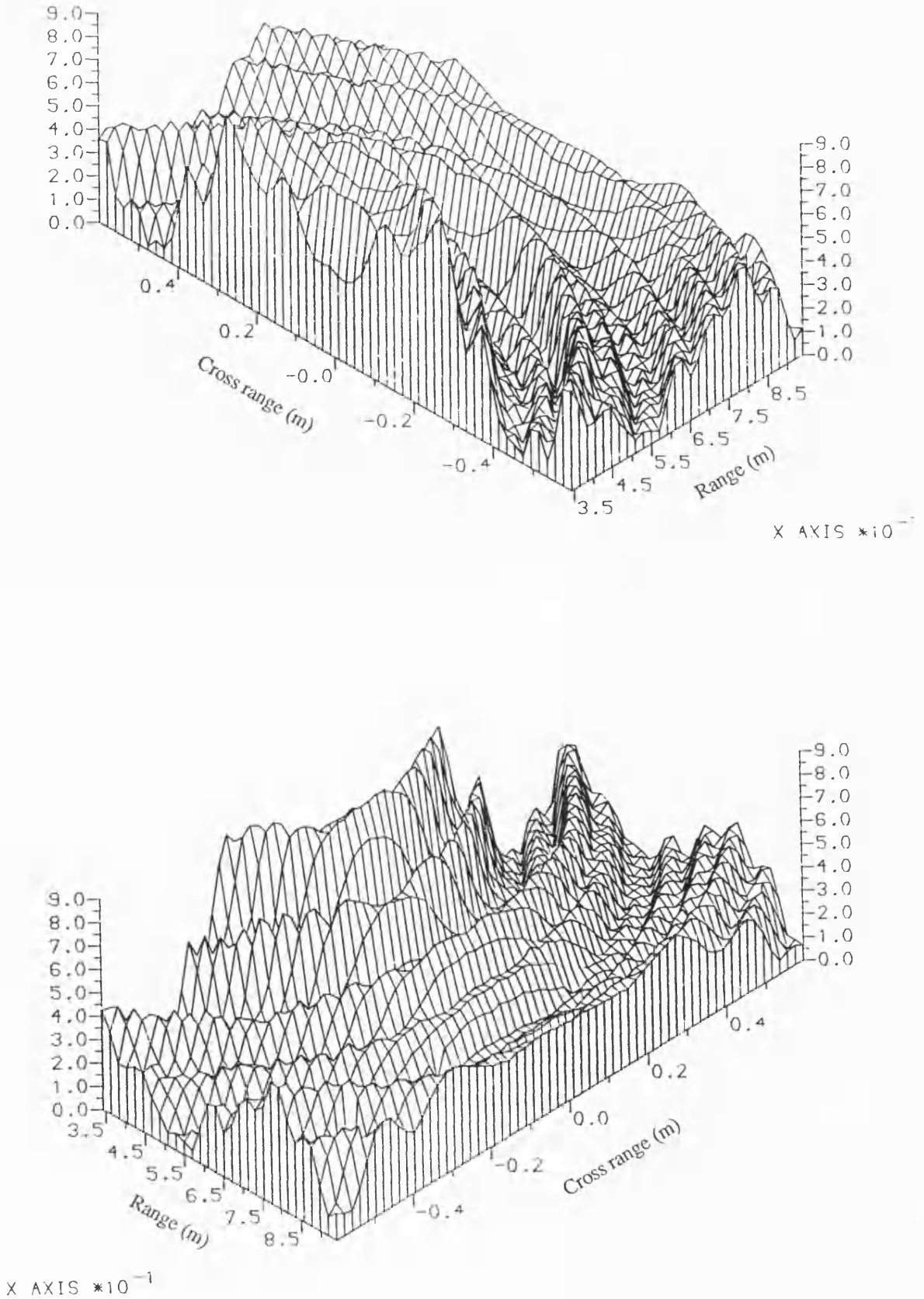

Fig. 6.4 Sound pressure field (isometric projection in two view angles) at a fixed depth for an omnidirectional source in a shallow water channel.

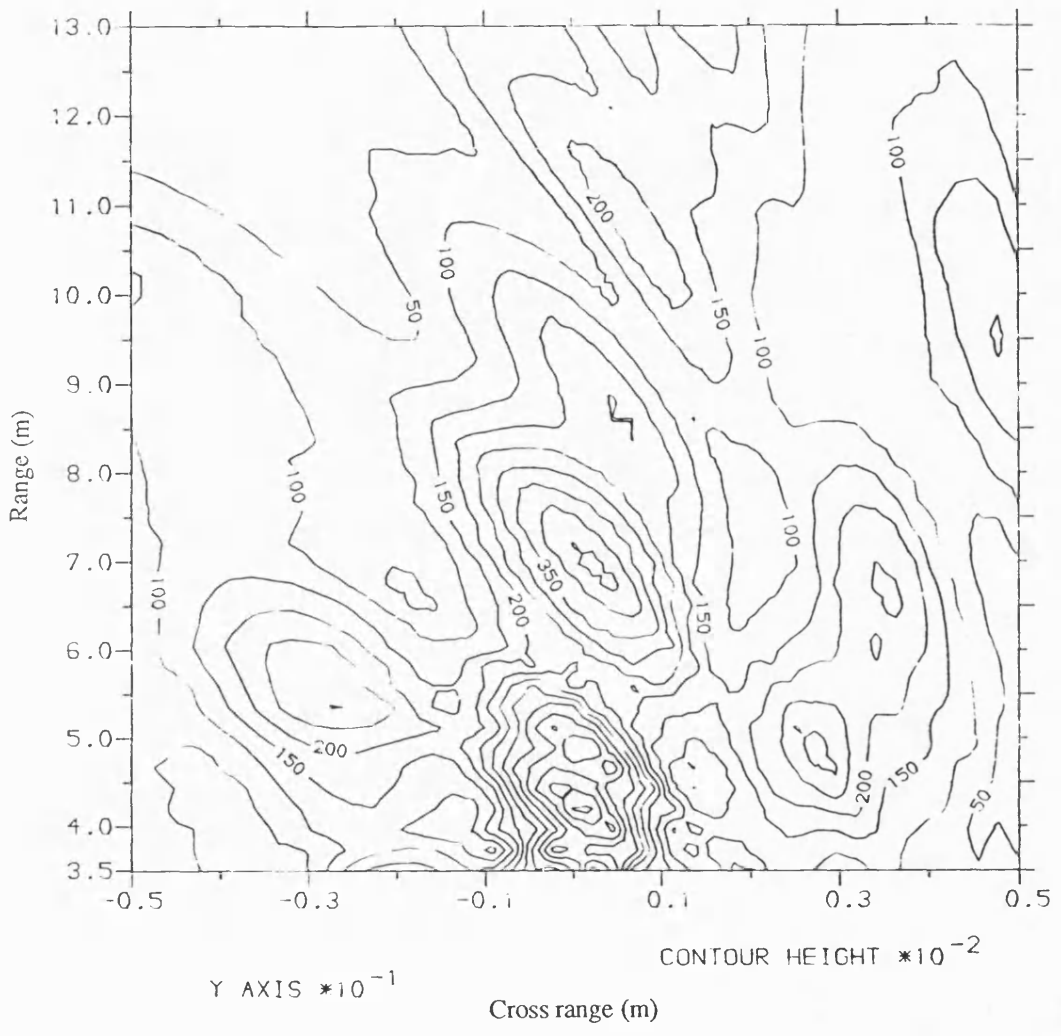

Fig. 6.5 Sound pressure field (contour map) at a fixed depth for a directional source in a wedge water column.

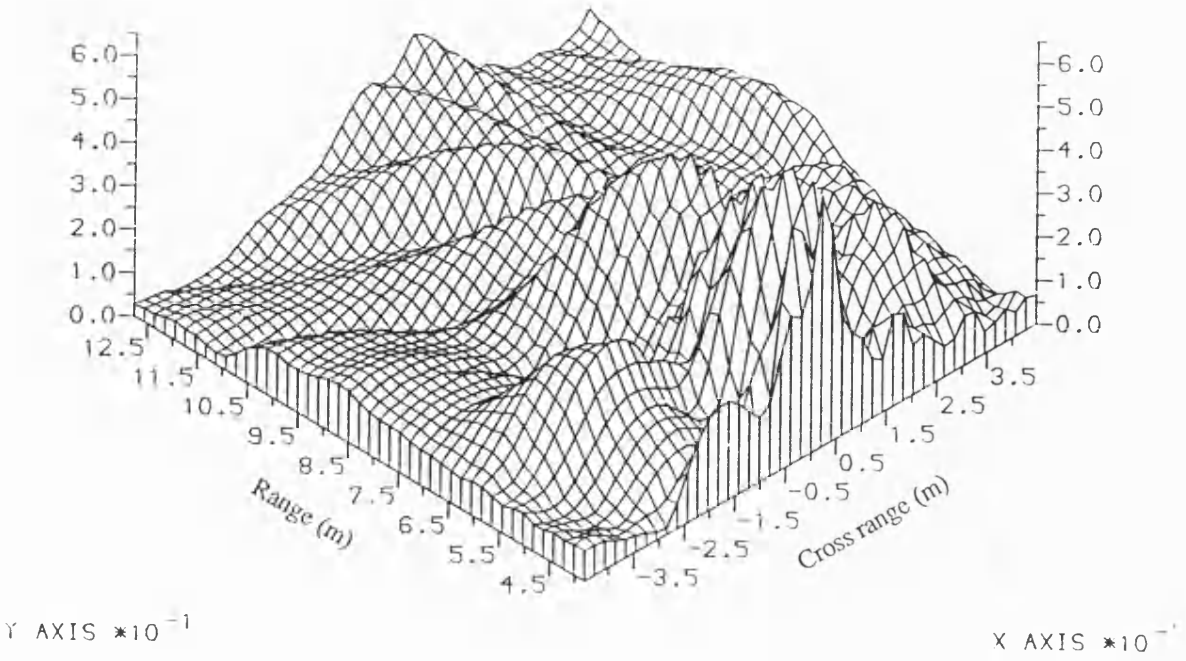

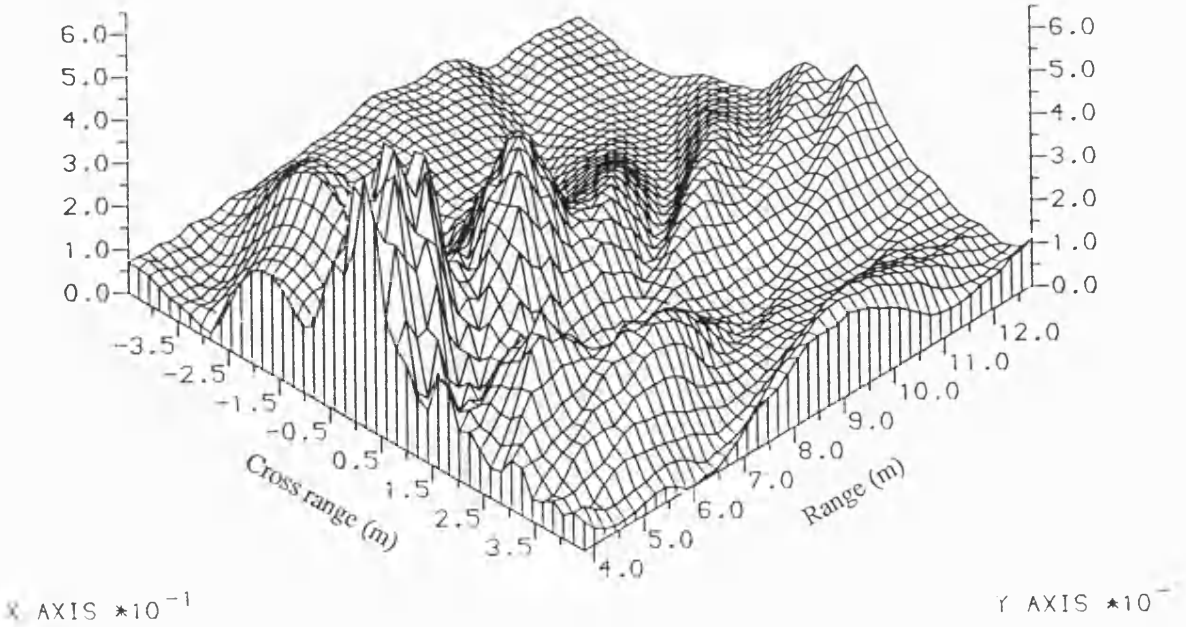

Fig. 6.6 Sound pressure field (isometric projection in two view angles) at a fixed depth for a directional source in a wedge water column.

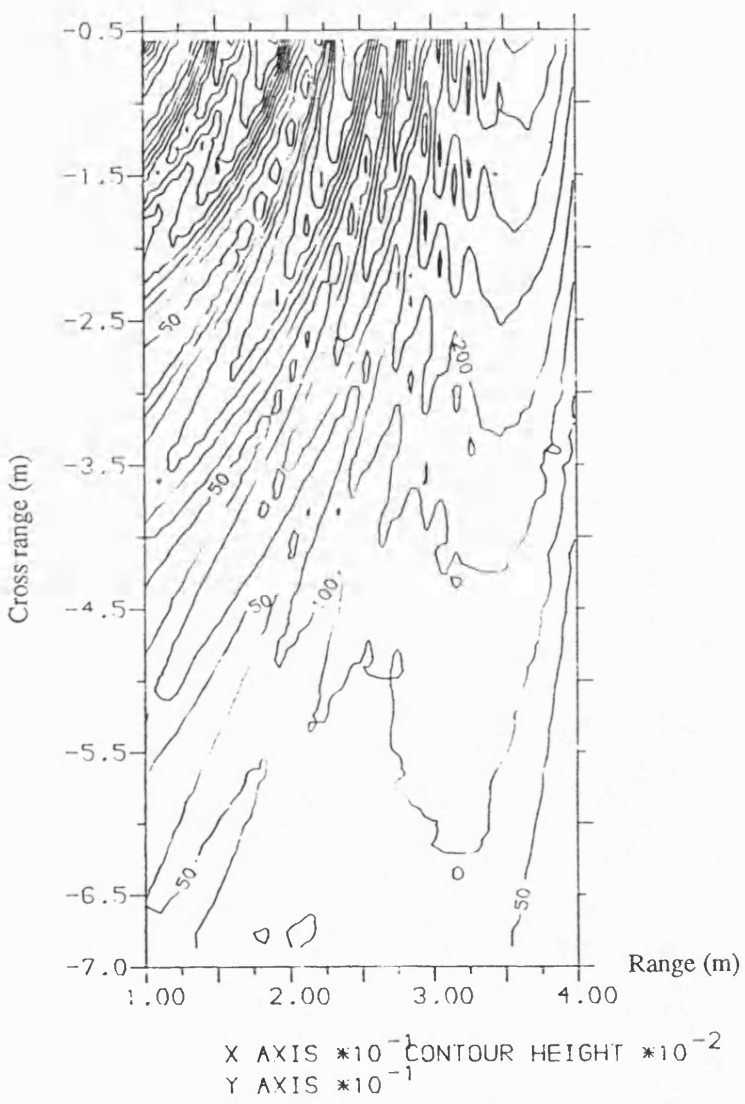

Fig. 6.7 Sound pressure field (contour map) at a fixed depth for an omnidirectional source in a wedge water column.

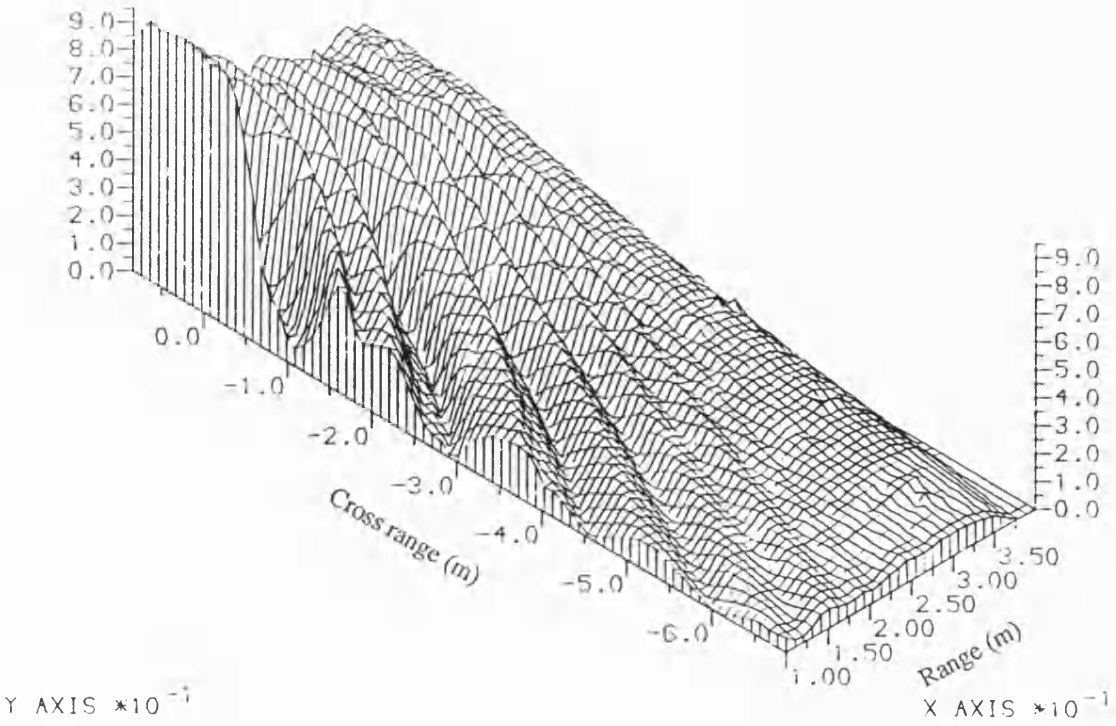

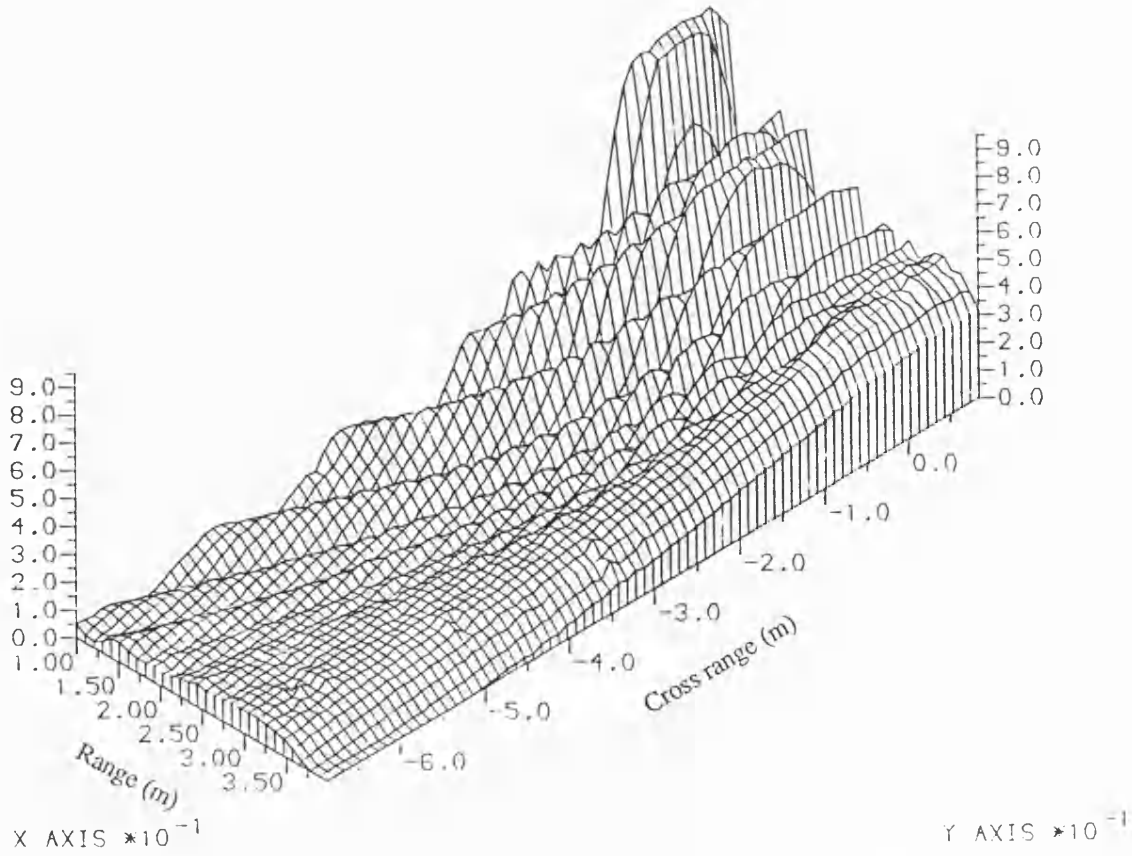

Fig. 6.8 Sound pressure field (isometric projection in two view angles) at a fixed depth for an omnidirectional source in a wedge water column.

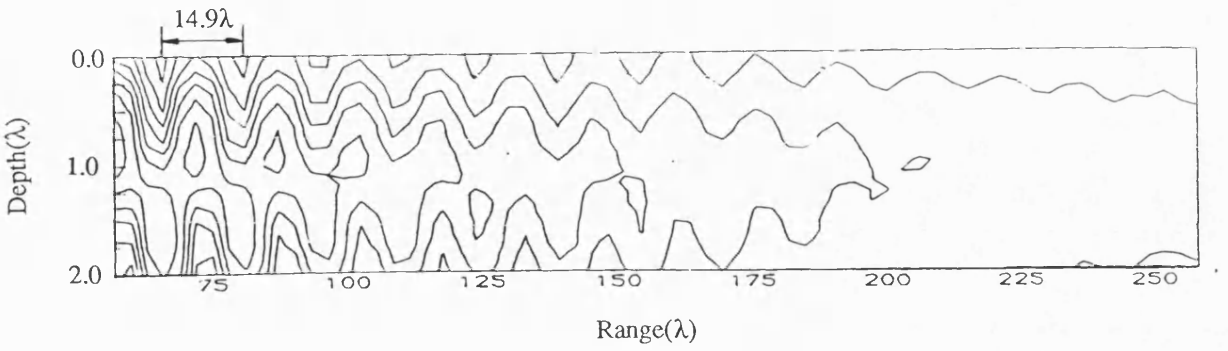

Fig. 6.9 Sound field as a function of range and depth in a shallow water channel with the sand bottom. The water depth is 6.9mm (1.92λ).

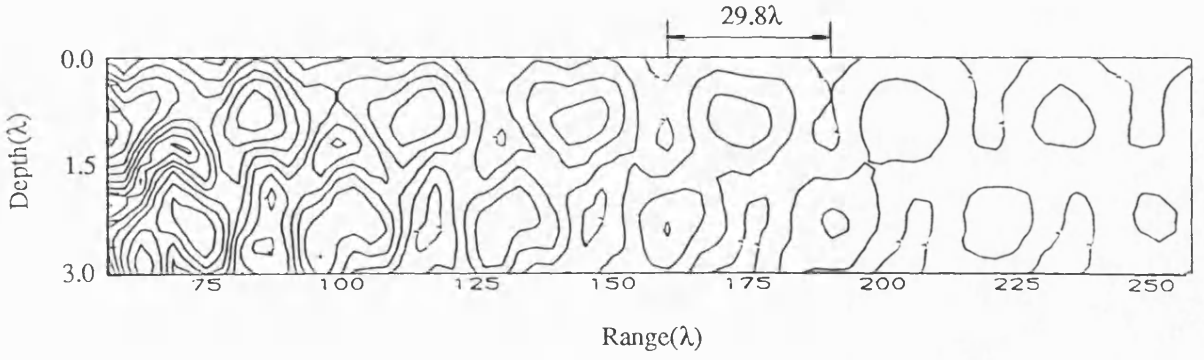

Fig. 6.10 Sound field as a function of range and depth in a shallow water channel with the sand bottom. The water depth is 10mm (2.78λ).

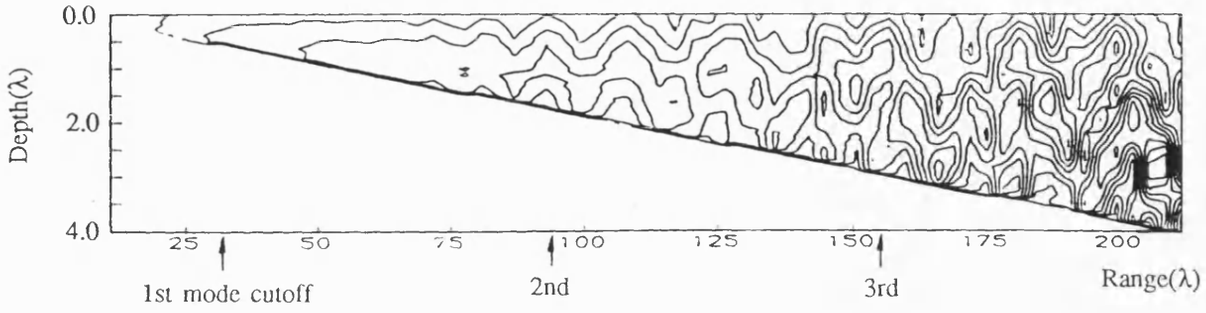

Fig. 6.11 Sound field in $z = 0$ plane as a function of range and depth in a penetrable wedge with 1° wedge angle.

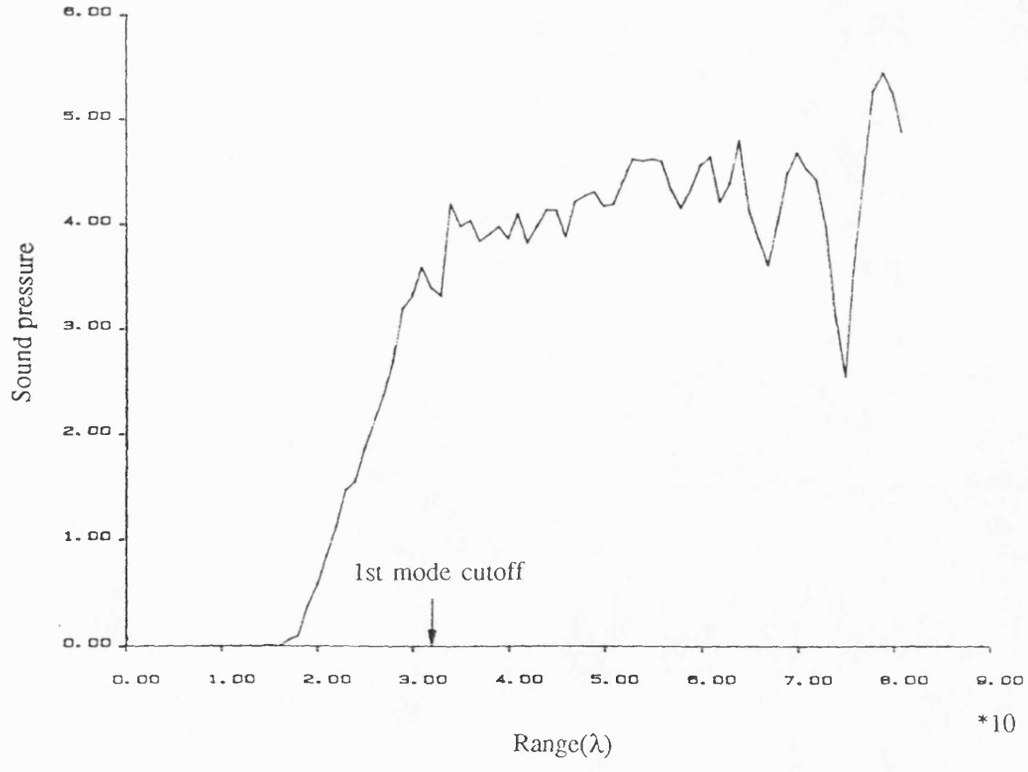

Fig. 6.12 Sound field at the depth 0.14λ in $z = 0$ plane as a function of range in a penetrable wedge with 1° wedge angle.

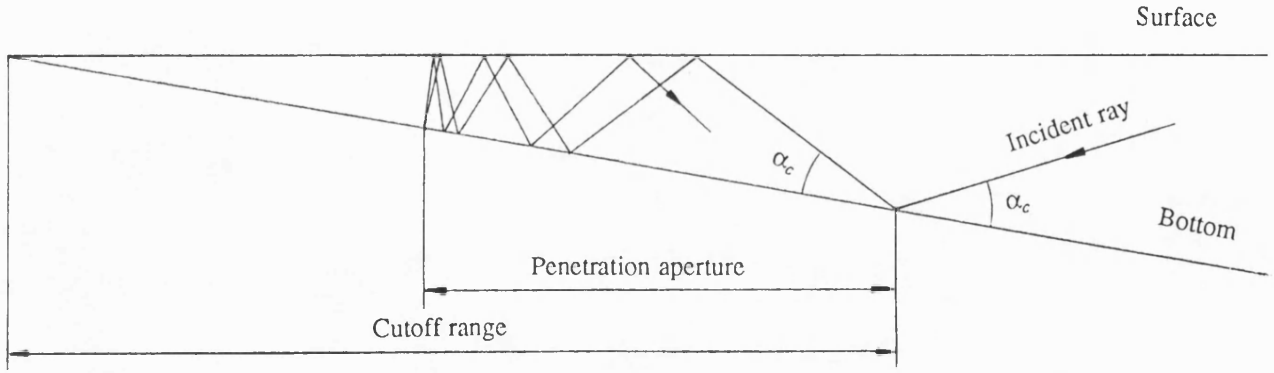

Fig. 6.13 A mode cutoff process illustrated in a sound ray.

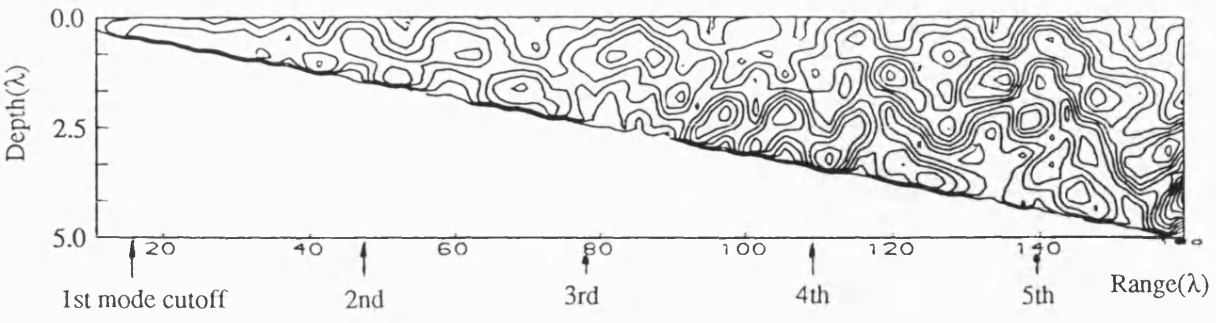

Fig. 6.14 Sound field in $z = 0$ plane as a function of range and depth in a penetrable wedge with 2° wedge angle.

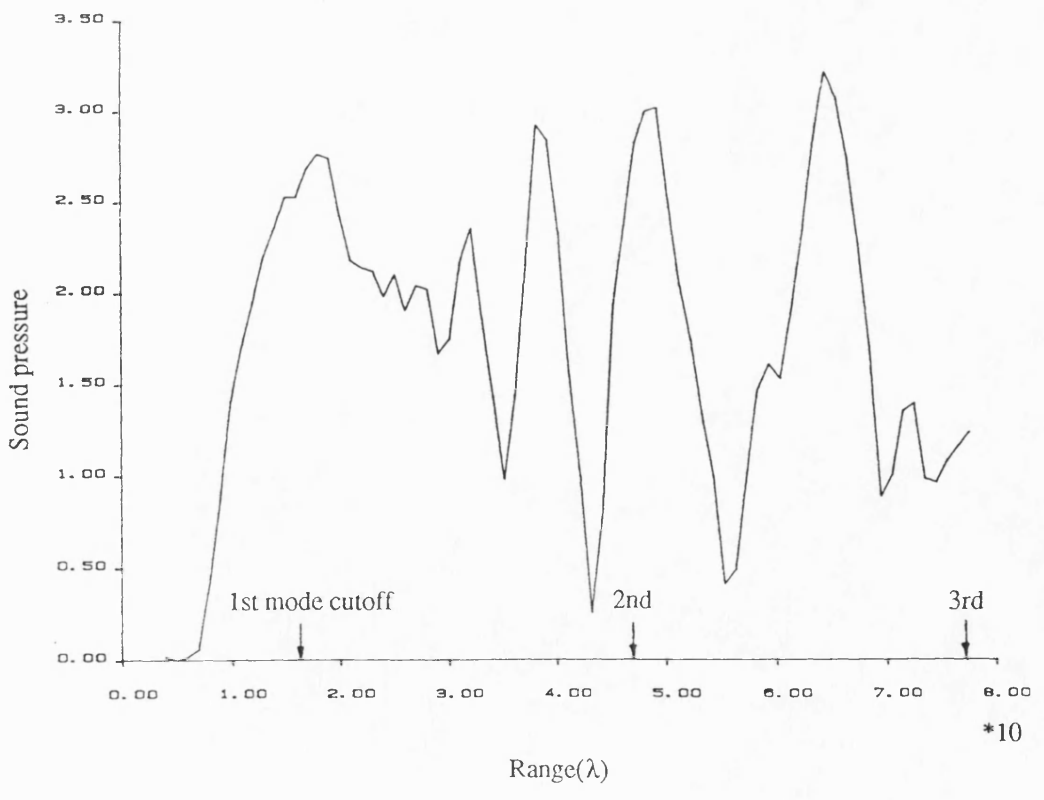

Fig. 6.15 Sound field at the depth 0.14λ in $z = 0$ plane as a function of range in a penetrable wedge with 2° wedge angle.

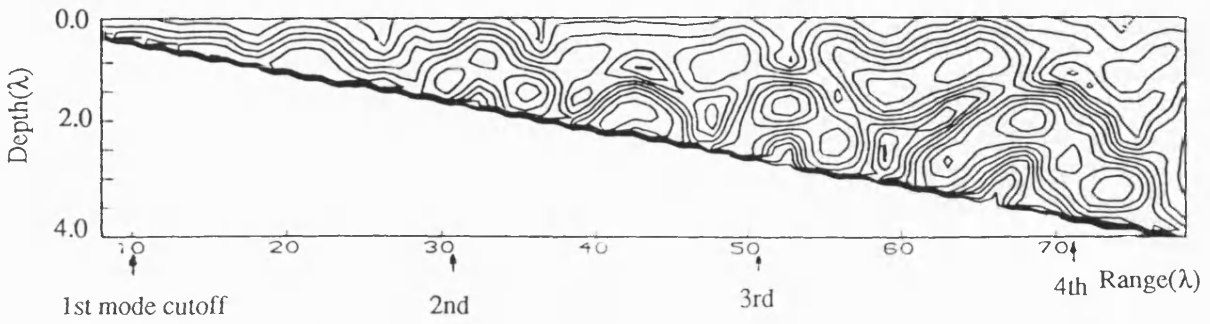

Fig. 6.16 Sound field in $z = 0$ plane as a function of range and depth in a penetrable wedge with 3° wedge angle.

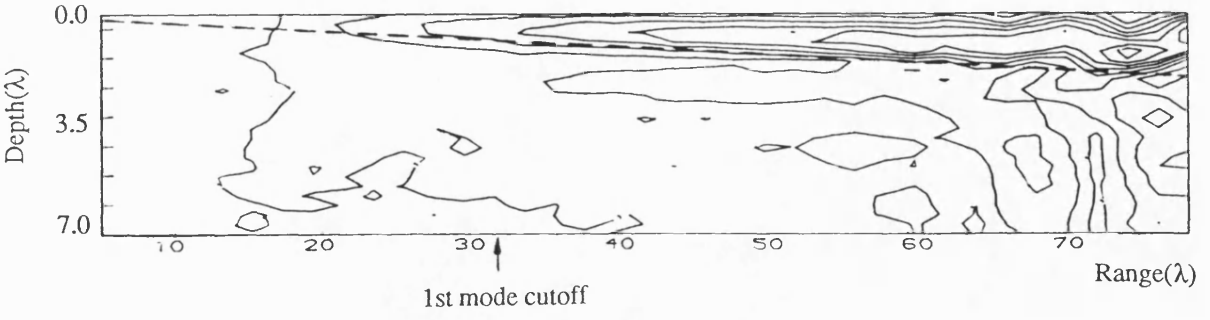

Fig. 6.17 Sound field in the water column and in the bottom as a function of range and depth in a 1° penetrable wedge.

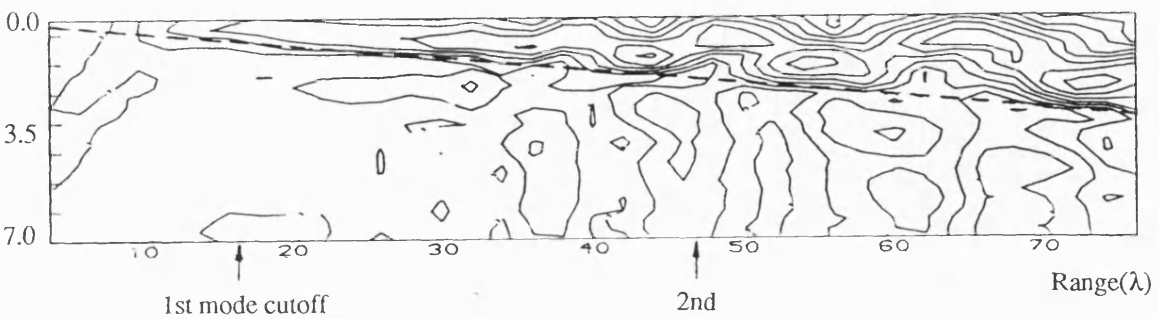

Fig. 6.18 Sound field in the water column and in the bottom as a function of range and depth in a 2° penetrable wedge.

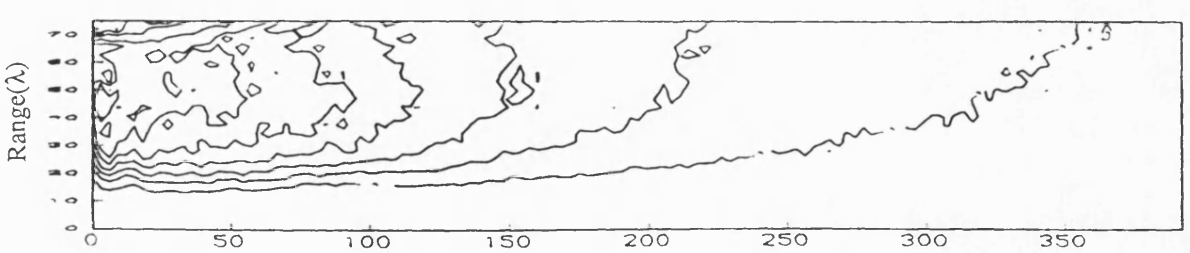

Fig. 6.19 Sound field at the depth 1/4λ as a function of range and cross range in a 1° penetrable wedge.

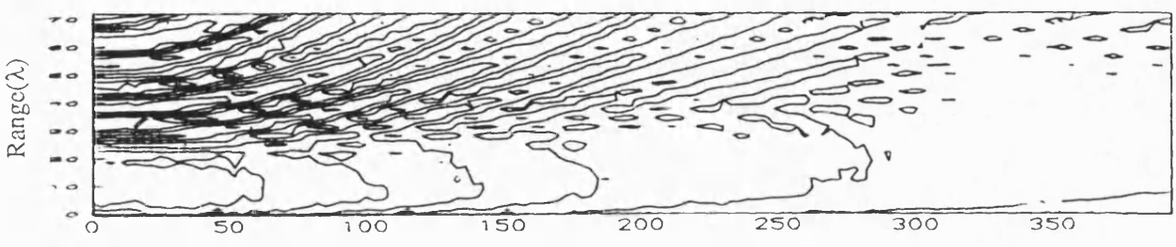

Fig. 6.20 Sound field at the depth 1/4λ as a function of range and cross range in a 2° penetrable wedge.

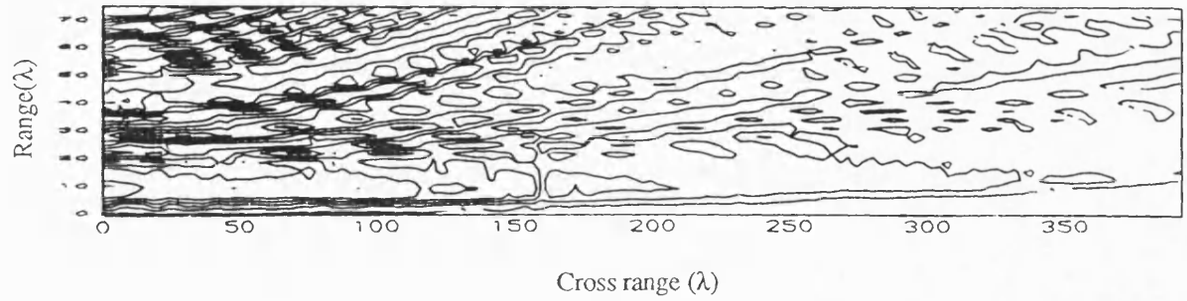

Fig. 6.21 Sound field at the depth 1/4λ as a function of range and cross range in a 3° penetrable wedge.

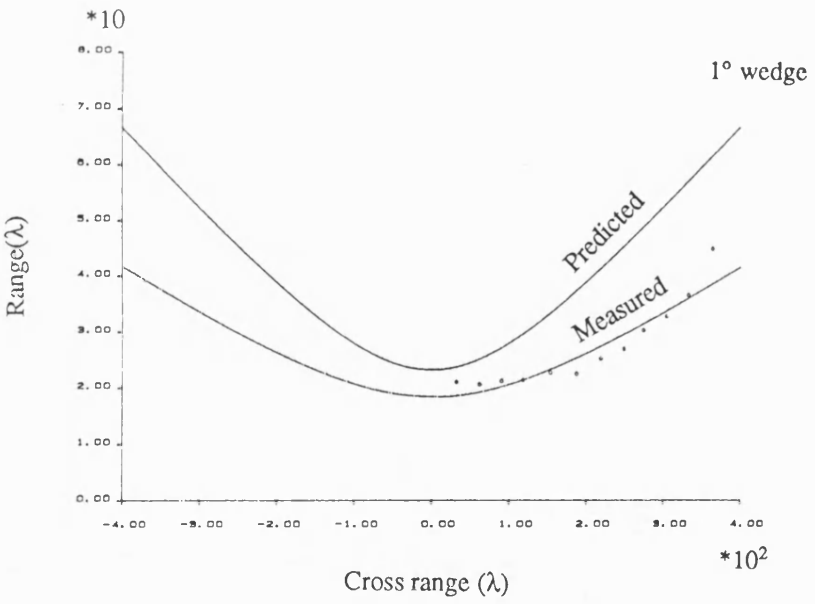

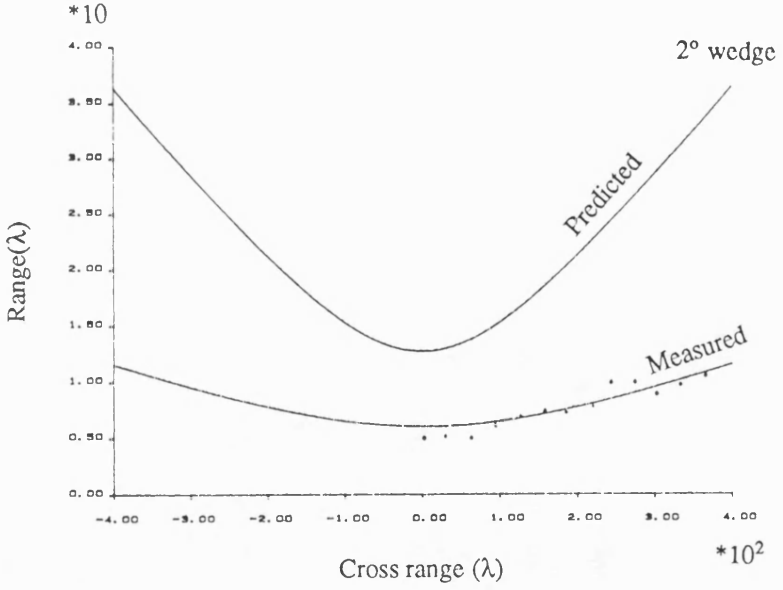

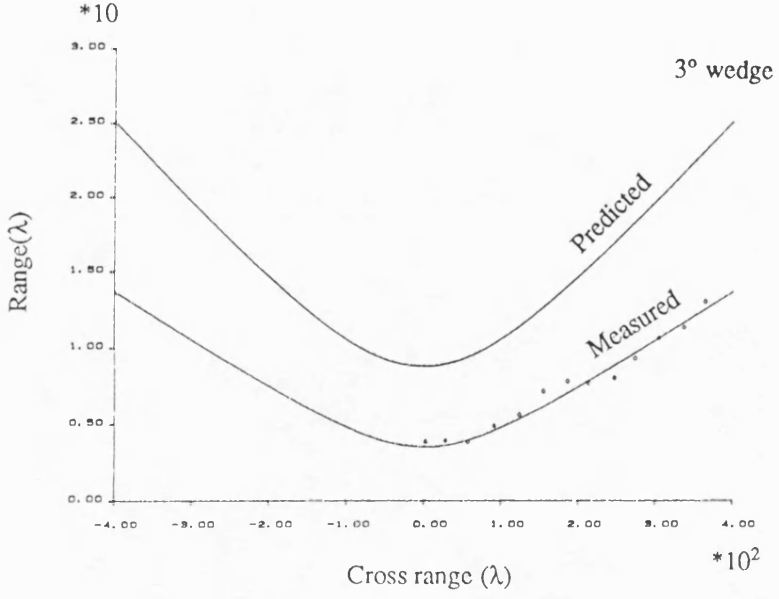

Fig. 6.22 The measured envelopes of the sound fields and the predicted by ray invariant in 1°, 2° and 3° wedges.

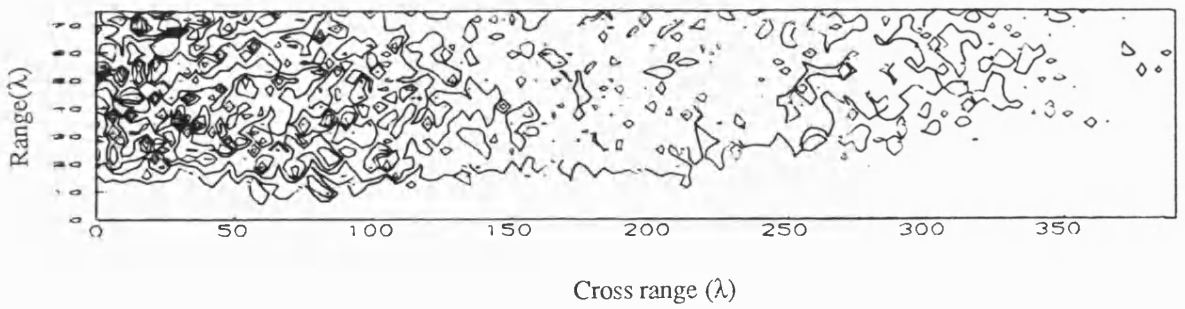

Fig. 6.23 Sound field at depth 1/4λ as a function of range and cross range in a 2° penetrable wedge with a rough water surface.

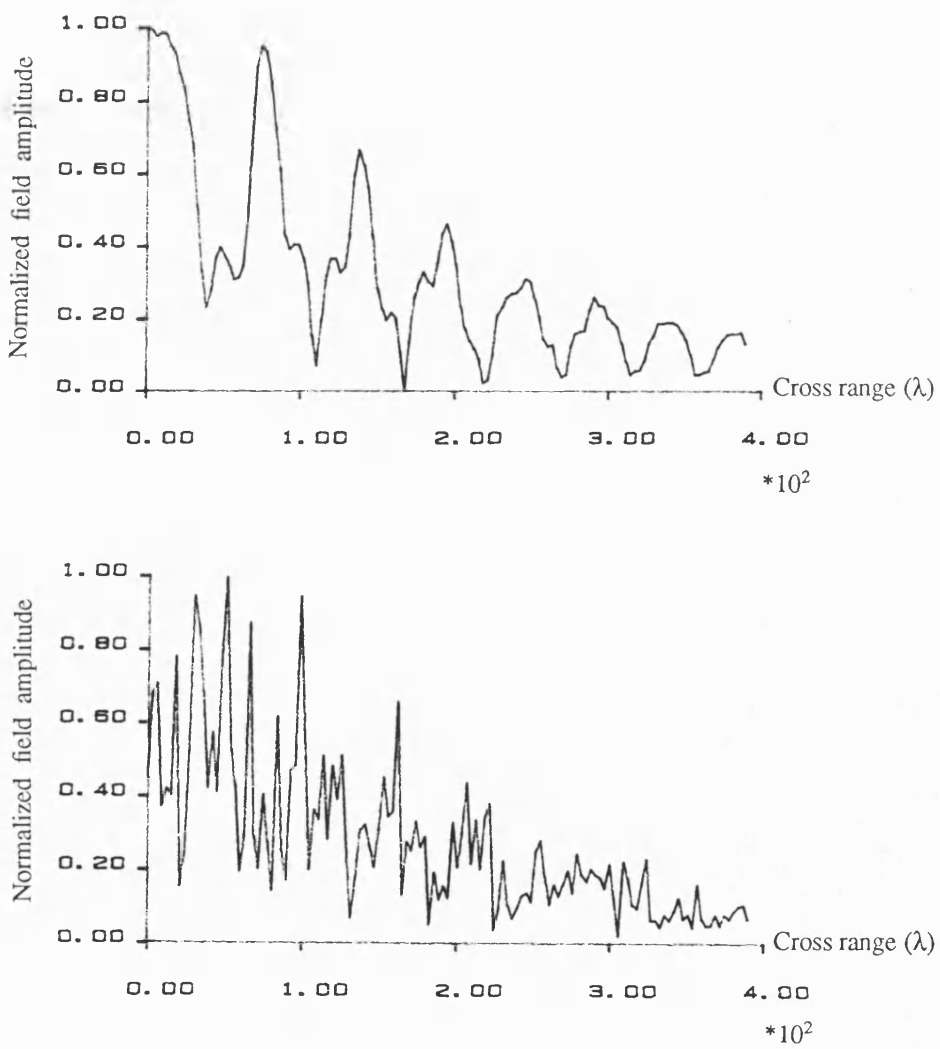

Fig. 6.24 Comparison of the sound field at range 75λ as a function of cross range in a wedge with a smooth water surface and in a wedge with a rough water surface.

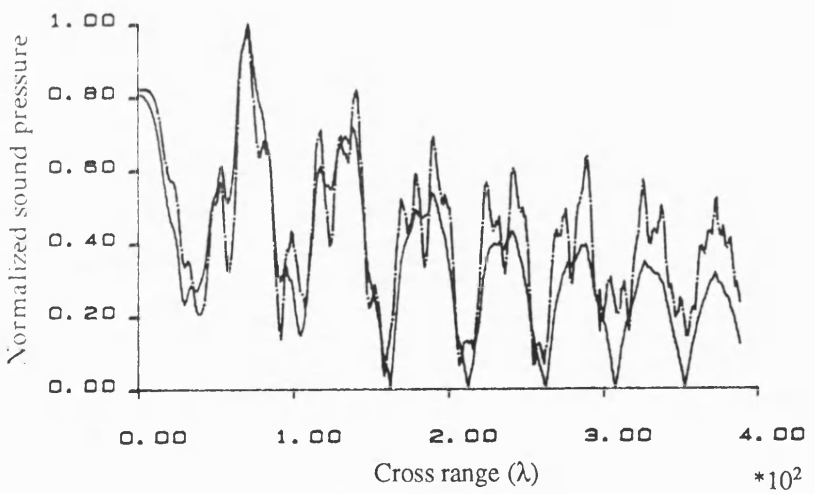

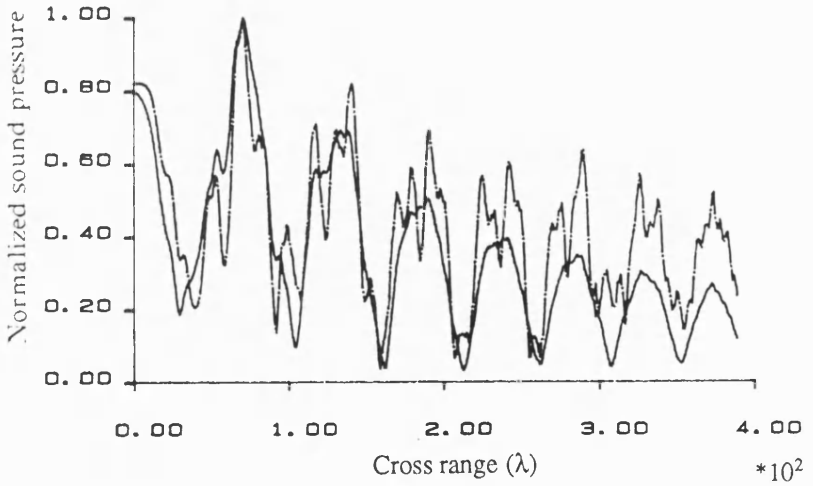

Without bottom attenuation

With bottom attenuation 1dB/λ

Without bottom attenuation

With bottom attenuation 1.48dB/λ

Fig. 6.25 Sound fields as a function of cross range at range 80λ and depth 1/4λ in a 2° penetrable wedge with and without bottom attenuation

Chapter 7. CONCLUSIONS

In this chapter, some general conclusions of this research project are given. Before doing so, a summary of the thesis is presented, which is in the order of the thesis presentation, the review of the previous works, the theoretical models and the implementation, the experimental work, the predicted sound fields, the experimental results and discussions.

7.1 Summary of the thesis

Chapter 1 introduces the wedge problem and the history of the study. The various theoretical approaches are discussed briefly. Generally, there are three different methods used most frequently to describe the wedge problem, they are ray theory, normal mode theory and parabolic equation (PE) approximation. Both ray theory and normal mode theory can give exact solutions of the sound field in a perfect wedge. PE approximation is capable of handling the penetrable wedge problem. No exact analytic solution can be found because the Helmholtz equation is not separable in a penetrable wedge due to the boundary condition on the bottom. However many approximate solutions such as the extension of the normal mode theory to the range dependent environment have been developed which can deal with the penetrable wedge problem. So far the complexity of describing the sound field 3-dimensionally in a penetrable wedge results in very few theoretical models yet available, all of them are approximate representations and remain to be examined. In this thesis, Buckingham's analytic solutions[51,52] are used to predict the field in a penetrable wedge since they can describe the sound field in water column 3-dimensionally. An experiment is carried out to measure the sound pressure in a model tank with a sand bottom to display the mode propagation in penetrable wedges. The results of the experiment will give an insight of the wedge problem and can also verify the theoretical model[51,52].

The geometry of the wedge problem is shown in chapter 2. Starting with a point source in a perfect wedge, Buckingham's analytic solution[17] is introduced. It is a sum of normal modes with the mode coefficients expressed by a finite integral which can not be expressed explicitly. Then his analytic solution[51,52] for a penetrable wedge is introduced, which has the same expression as that in the perfect wedge but in a different coordinate system introduced by the effective bottom, and a different upper integration endpoint which is a function of the critical angle and range and cross range.

Since the integral for the mode coefficients can not be expressed explicitly, a simple way to evaluate it is by numerical method. This proved to be extremely time consuming because the

integrand of the integral is highly oscillatory. To exploit the property of the integrand, stationary phase method (SPM) is used to evaluate the integral approximately in chapter 3. The integrals are changed into the forms which can be evaluated by SPM. The stationary points are given, and their significance is interpreted. The contribution of a mode to the sound field can be characterized into a bright zone, a caustic and a shadow zone depending on the stationary points being real but not equal or, real and equal or complex. The caustic of each mode can be found at the place where two real stationary point coalesce into each other. A uniformly asymptotic approximation of the analytic solution for perfect wedge is obtained. When the stationary points are far away from each other, the approximation gives a representation of the contributions to the field from two isolated first order stationary points. Since the endpoints of the integrals for mode coefficients in a perfect wedge and a penetrable wedge are finite, the contributions from the endpoints have to be taken in to account. Considering kR_0 is large, using integration by parts to the integrals can give the first order approximation of the contributions from the endpoints in a perfect wedge. Since the upper endpoint of the integral for mode coefficients is a function of the critical angle and range and cross range in penetrable wedge, the stationary point may be close to the endpoint, in the case the integration by parts can not be used. The approximate representations is derived for this case, which is expressed in terms of the incomplete Airy integral. The approximate representations can predict the sound field rapidly with a satisfactory accuracy. The differences of the "wedge mode" and the "shallow water mode" are pointed out. Finally, the restrictions on using the approximate representations are discussed.

A laboratory experiment which measured sound pressure in a tank with a sand bottom is detailed in chapter 4. Pulse signals are used in the experiment. The pulse length of the signals are determined so that they can be considered as a continuous sine wave, and the interferences from the side walls of the tank can also be eliminated during the measurement. A detail of the calculation of the pulse length according to the geometry of the tank and the band width of the signal receiving system is given in appendix A. A gantry system was built, which is able to carry a receiver to measure sound pressure 3-dimensionally. The sand used in the experiment has an average diameter of 0.05mm. The sand was degassed before being put into the tank. The sound velocity in the sand bottom was determined by measuring the relative reflection coefficient and the density of the water saturated sand. The result was confirmed by comparing the measured shallow water propagation of normal modes with the theoretical prediction (The theory of normal mode propagation in shallow water is introduced in appendix C). The whole process of measuring sound pressure was under the control of

an Apricot XI computer, which triggers the signal generator to transmit signals, calculates the time delay from the transmitter to the receiver and triggers the sample and hold accordingly. The timing control by the computer is given in appendix B. The amplitude of the sound pressure was stored in the computer. Since the tank can be easily lifted at the one end to form a wedge shaped water column with an angle of interest, the sound field in different wedges was measured. The measurement was made in the water column and in the sand bottom as well.

Chapter 5 gives some predicted fields in perfect wedges and penetrable wedges by the approximate representation derived in chapter 3. The fields in perfect wedges are useful to demonstrate the main features of sound propagation in perfect wedges. The intramode pattern is explained in terms of ray theory. In the prediction of the fields in penetrable wedges, the parameters used were the same as that in the experiment. The predicted fields in penetrable wedges show that the first mode can reach to the apex of the wedges, and there are intramode interference. The intermode interference pattern indicates the caustic of the mode are hyperbolic. The effects of the wedge angle on the structure of the field in a wedge are investigated.

The experimental results are given in chapter 6. The sound pressure as a function of range and water depth in the water column in penetrable wedges with different angles are demonstrated. In order to help to interpret the results, the sound fields in shallow water channels are also demonstrated. The mode propagating in a penetrable wedge proved to be adiabatic before reaching its cutoff range. The cutoff range of a mode estimated according to the shallow water theory agrees well with the experimental results. In order to investigate the penetration of the sound into the bottom, the sound field was measured in the water column and in the sand bottom. Two penetration beams are found after the first mode cutoff in the experimental results. The major beam occurs at the place centred at the cutoff range, and the small beam is after the major beam toward the apex. The sound pressure as a function of range and cross range in penetrable wedges with different angles are given. The results show that the basic structure of the field is similar to the predicted field. But the intramode interference which predicted by penetrable wedge theory is not found in the experiment. There is a clear shadow zone , which position differs from the prediction by penetrable theory. A better estimate is made according to ray invariant with the elevation angle of the first mode given by shallow water theory. The sound field in a wedge with a rough surface is measured. Comparison is made between the fields in a wedge with a smooth surface and a wedge with a rough surface. There is no clear intermode interference in the wedge with a rough surface, and the propagation loss is greater than that in a wedge with a smooth surface.

In chapter 6, a modification to the analytic solution for a penetrable wedge is made to take the bottom absorption into account. It is analogous to the mode propagation in a shallow water channel with a lossy bottom. Instead of a constant attenuation for a mode in shallow channel, a variable attenuation is used in the computing of the field, which is a function of the water depth in the wedge. The improvement is obvious.

7.2 Conclusions

Finally, some conclusions can be drawn from the present work here.

The evaluation of the analytic solutions for the sound fields in both a perfect wedge and a penetrable wedge by stationary phase method (SPM) provides the approximate representations which can be used to predict the sound fields with a very satisfactory accuracy and hundred times faster compared with the numerical method.

The sound field for a point source in a penetrable wedge can be interpreted in terms of normal modes. A point source in a penetrable wedge produces a pressure field with a hyperbolic envelope at the shadow zone edge where the first mode is cutoff, and the higher modes also have hyperbolic envelopes at the their own cutoff ranges as demonstrated in the numerical and the experimental results. The position of the envelope can be estimated by ray invariants with the elevation angle given by shallow water theory. Compared with the experimental results, the estimated position of a mode envelope is further away from the apex of the wedge. The shadow zone of the field is narrower in a wedge with a greater angle than that in a wedge with a smaller wedge angle. At the same range from the apex, there will more modes sustained in a wedge with a greater angle than that with a smaller angle.

In the water column, it can be seen from the experimental results that a mode adiabatically propagates in up slope direction in a penetrable wedge before passing the cutoff range. The partially reflected wave has an important contribution to the field around the adjacent region of the cutoff range. The cutoff process of a mode is slow in a penetrable wedge and it depends on the wedge angle.

In the bottom, the penetration of a mode is examined by experiment. It is found that the penetration does take place at the place predicted by the shallow water theory. The process of the penetration proves to be a complicated one as the lateral wave is excited at the critical incidence of the wave propagating in up slope direction. Two beams are found in the bottom after the first mode cutoff because of the sound energy transmitting from the water column into the bottom. The major

beam is associated with the specular reflection of the wave incident at the bottom with the critical angle, and the small beam is considered to be the contribution from the lateral wave. Although the main beam of the mode penetration into the bottom has been predicted by many theoretical models, the small beam has not been predicted yet.

Compared with the experimental results, the field predicted by the penetrable wedge theory is in general agreement with the shape of the shadow zone edge and, the hyperbolic interference pattern caused by the mode interference. But discrepancies are found in the details such as the relative amplitude of the sound pressure and, the position of the mode envelopes. There is a number of reasons for the discrepancies. One is the penetrable wedge theory will fail as a mode approaches its cutoff. Another is the field predicted by the theory does not take partial reflection into account. Further the bottom attenuation has not been taken into account either. Because of the attenuation in the sand bottom, there is no intramode interference found in the outer zone in the experimental results, which has been predicted by the penetrable wedge theory.

A modification can be made to the analytic solution for the field in a wedge with a penetrable and lossy bottom to take the bottom absorption into account in a manner analogous to the shallow water case. The propagation loss given by the modification is close to the experimental result.

7.3 Suggestions

Some suggestions should be made here as the future work according to the present work carried out.

Because the penetrable theory used here can only describe the field in the water column in a wedge, it is suggested that some 2-D range dependent models should be used to predict the field both in the water column and in the bottom with the same condition as in the experiment in order to make a detailed comparison with the experimental results obtained here. This will give more insight to the wedge problem.

The penetrable wedge model may be improved by taking partial reflection into account.

Appendix A

The pulse length and the valid measured area

Theoretically, a single frequency continuous sine wave signal should be used in the experiment. But the reflected waves from the walls of the tank would introduce errors to the measurement if continuous wave were used in this experiment since the dimensions of the tank are limited. One alternative way is to use pulse sine signal to avoid this kind of interference. To obtain a valid measurement by using pulse signal instead of continuous signal, the pulse length of the signal must be long enough to ensure the measuring system is settled down and all the signals from different paths arrive at the receiver within the time period of the pulse.

Since the measuring system has a finite bandwidth, it needs a time to response an input signal, the responsing or settling time is determined by the bandwidth of the system as

$$T_s=\frac{1}{B_s} \tag{A.1}$$

where B_s is the bandwidth of the system.

To determine the travelling time of the signals from different paths, the geometry of a wedge is shown in Fig. A1, where $S(r',0,0)$ is the source, the virtual images distribute continuously on a circle with a radius r' centered at the apex $\overline{O}$ of the effective wedge, **I** is a virtual image with an elevation angle σ, $R(r,0,z)$ is the receiver. Provided the source and the receiver are on the same plane as mentioned in Sec. 2.4, the distances from the source **S** and the virtual image **I** to the receiver are

$$d_1=\sqrt{(r'-r)^2+z^2} \tag{A.2}$$

$$d_2=\sqrt{(r'\sin\sigma)^2+(r'\cos\sigma-r)^2+z^2}$$

$$=\sqrt{r'^2-2r'r\cos\sigma+r^2+z^2} \tag{A.3}$$

From Eqs. (A.2) and (A.3) we can see that all ray paths from the virtual images longer than the ray path from the source. The different between the two distances is

$$d=d_2-d_1$$

$$=\sqrt{r'^2-2r'r\cos\sigma+r^2+z^2}-\sqrt{(r'-r)^2+z^2} \tag{A.4}$$

It is obvious that d decreases as the receiver moves parallelly to the apex away from $z=0$ plane, and it has a maximum when the receiver is at $z=0$ for any ray path from the images. For a fixed receiver, d will increase as the elevation angle of I increases. These suggest that the maximum time differences of the signal travelling from the source and the virtual images to the receiver occurs at $z=0$ plane with the image at $\sigma=\pi$ as indicated by the dash line shown in Fig. A1. In a penetrable wedge, any ray path with an incident angle less than the critical angle will penetrates into the bottom, so only the rays with incident angle greater than the critical angle need to be concerned as mentioned in Sec. 2.4, the corresponding images are those on the circle with their elevation angle σ less than σ_c. Hence, the longest ray path of interested will be the one from the image with angle σ_c in this case, and the difference between the shortest path and the longest path is

$$d_c=\sqrt{r'^2-2r'r\cos(\sigma_c)+r^2+z^2}-\sqrt{(r'-r)^2+z^2} \tag{A.5}$$

where σ_c is given according to the positions of the source and the receiver, and the critical angle by Eqs. (2.41), (2.45), or (2.47) in Sec. 2.4. The virtual image with the angle σ_c is called "critical image" here. It can be seen that the time delay from the source and the images to the receiver will be less or at most be equal in a penetrable wedge then that in a perfect wedge according to Eq. (A.5), since $\sigma_c \le \pi$. Near $z=0$, d_c is small because σ_c is small. This is different from that in a perfect wedge where the maximum d occurs at $z=0$. As the receiver is moved away from $z=0$ plane, d_c will increase first, then decrease which is decided by the change of σ_c.

Now we can determine the signal length, which has to satisfy the condition as follow,

$$T_0 \ge T_s+T_c \tag{A.6}$$

where T_0 is the signal length, T_s is the system settling time given by Eq. (A.1), and T_c is the maximum time delay between the ray path from the source and the ray path from the critical image, which is given by

$$T_c=\frac{d_c}{c_0} \tag{A.7}$$

where d_c is given by Eq. (A.5), and c_0 is the sound velocity in the water.

Consider the source is at the position of 150λ out from the apex of the wedge, the maximum measured distance out from the apex of the wedge is 75λ, the cross range is 400λ, the sound velocity is 1477m/s in the water, 1665m/s in the sediment, the critical angle is 27.49°, the system bandwidth is

39kHz, the signal frequency is 411kHz, the maximum difference d_c can be found by Eq. (A.5), which is d_c=41λ.

T_s=0.025ms

T_c=0.1ms

$T_0 \geq$ 0.125ms

So that the pulse length is at least 125μs. In the experiment, the pulse length used is T_0=150μs.

The field is symmetric about the z=0 plane, the measurement only needs to be carried out at $z \geq 0$ area, this also gives an advantage that a larger part of the field can be measured in a limit area. So the source is put near one side of the tank as shown in Fig. A2, the position of the source is determined so that the difference of the path lengths of the direct ray at the plane which is perpendicular to the apex through the source and the ray reflected from the side wall nearby should be at least as long as the signal length. For a source at the range 150λ with pulse length 150μs, the maximum measured range r_m=75λ from the apex, it is found that the distance l_1 from the wall to the source is about 75λ, thus a valid measurement can be made within a cross range z_m at least 400λ with the tank. The area in which the measurement was carried out is also shown in Fig. A2.

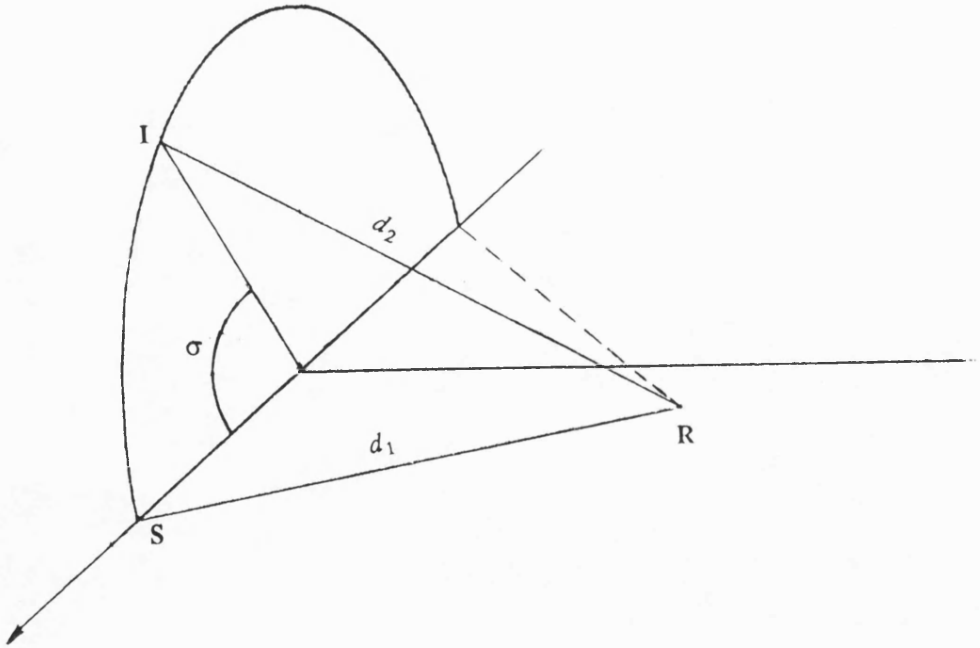

Fig. A1 Ray paths from source S and image I to receiver R.

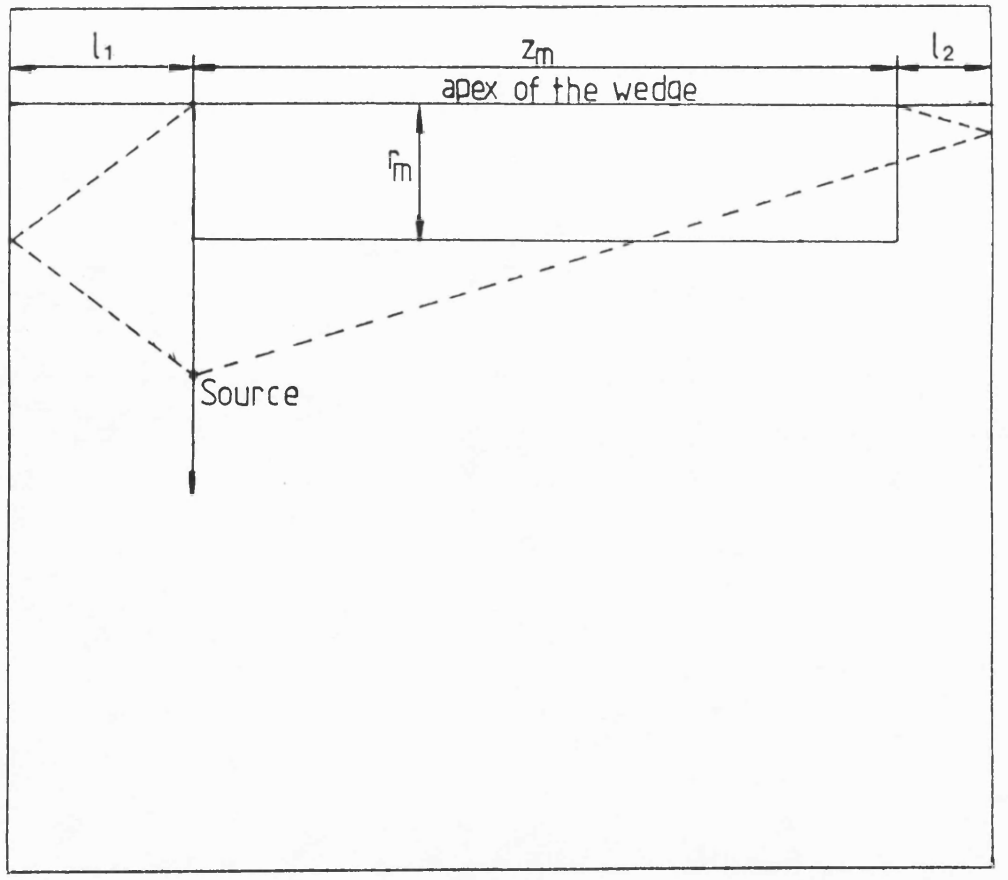

Fig. A2 Source position and valid measuring area in the tank.

Appendix B

Signal transmitting and receiving controlled by the computer

In order to avoid the interference by the reflected signals from the side walls of the tank, pulse signals were used in the experiment. The pulse length of the signal is determined as mentioned in appendix A. To measure the sound field in the tank as a function of position, the receiver was moved 3-dimensionally from one point to another in the tank while the source was fixed. So that the relative distance from the source to the receiver was changing for different positions. In this case, it is important to sample the received signals at a proper time delay after the signal transmitting to obtain valid data. The proper time delay needed for a particular position of the receiver should include the time of the signal propagating from the source to the receiver in the water column and the pulse length given in appendix A. During the measurement, the pulse length can be preset up in the computer and, the time of the signal propagating can be calculated according to the relative position of the source and the receiver for a given sound velocity in the water.

Once the time delay is worked out, the only way to realize the time delay as precise as possible on the computer is to use the assembly language. By means of the assembly language, the computer can generate a trigger for transmitting signal and a trigger for receiving signal after the time delay. The programme named as "TRIG" which fulfills these tasks is given at the end of this appendix. A description about the programme is detailed here. There is one parameter needed in the programme, which is an integer. Firstly, this parameter is sent to the count register (CX) of the CPU. Secondly, a pulse is sent to the port (address 90h) which connects the interface for signal transmitting and receiving, the falling end of the pulse is used to trig the pulse generator to transmit a pulse sine signal. A time delay is obtained by a loop operation which reduces the content of the count register (CX) to zero. The minimum time delay is about 5.3μs by this method since the execution of a loop command needs 17 clocks of time period if the content of CX is not zero. A finer time resolution is achieved by adding two times operations of decreasing data register (DX) successively, which can produce a minimum time delay up to 1.3μs, and four times gives a double minimum time delay. For any given time delay corresponding to the relative positions of the source and the receiver, it can be divided as an integer times of 5.3μs plus a small mount less than 5.3μs. The small mount can be further divided as an integer times of 1.3μs. Therefore, the time delay is approximated by these two digitized times, which error is less than 1.3μs. In the programme, the parameter needed is the integer obtained by dividing the time delay with 5.3μs. Finally, after the time delay generated by the loop operation plus the time delay caused by a number of operations decreasing DX accordingly, a pulse is

sent the port (address 90h), which trigs the sample and hold with the raising end to sample the received signal.

Programme "TRIG"

```
data    segment public 'data'
data    ends

dgroup  group           data
code    segment 'code'
        assume          cs:code,ds:dgroup,ss:dgroup
public  trig

trig    proc            far

        push            bp              ; save framepointer on the stack
        mov             bp,sp
        les             bx,[bp+6]       ; es,bx := addr of the parameter
        mov             cx,es:[bx]      ; move the parameter into CX
        mov             ax,0a008h
        out             90h,ax
        mov             ax,0a000h
        out             90h,ax          ; trigger for signal generator
next:   loop            next            ; main time delay
        dec             dx              ; optional time delay
        dec             dx              ; optional time delay
        mov             ax,0a0f7h
        out             90h,ax          ; trigger for sample and hold
        mov             sp,bp
        pop             bp
        ret
        trig            endp
        code            ends

end
```

Appendix C

Sound propagation in a shallow water channel with an absorbing bottom

To confirm the sound velocity in the bottom obtained by measuring the normal reflection coefficient from the bottom as described in Sec. 4.10.2, sound propagation in a horizontal shallow water channel with the sand bottom was measured.

Shallow water propagation with a liquid bottom was treated by Pekeris[12]. The geometry of the problem is shown in Fig. C1. Point source and point receiver are in a non-absorbing water of constant depth H. The density ρ_0 and sound velocity c_0 in the water are respectively less than ρ_1 and c_1 in the underlying bottom which extends downward to infinity. The acoustic field can be described by

$$\Delta\psi+k^2\psi=-4\pi\delta(\vec{r}-\vec{r}_0) \qquad 0<z<H \tag{C.1a}$$

$$\Delta\psi+k_1^2\psi=0 \qquad z>H \tag{C.1b}$$

$$\psi\,|_{z=0}=0 \tag{C.1c}$$

$$\left[\rho\psi\right]_{H-0}^{H+0}=0 \qquad \left[\frac{\partial\psi}{\partial z}\right]_{H-0}^{H+0}=0 \tag{C.1d}$$

where $k=\frac{\omega}{c_0}$ is the wave number in the water, and $k_1=\frac{\omega}{c_1}$ is the wave number in the bottom. Solving Eqs. (C.1) results in the representation of the acoustic field in the water as

$$\psi(r,z)=\int_{-\infty}^{+\infty}\frac{\sin(k_z z)[e^{jk_z z_0}-Ce^{-jk_z z_0}]}{k_z(1-C)}H_0^{(1)}(\mu r)\mu d\mu \qquad 0<z<z_0$$

$$=\int_{-\infty}^{+\infty}\frac{\sin(k_z z_0)[e^{jk_z z}-Ce^{-jk_z z}]}{k_z(1-C)}H_0^{(1)}(\mu r)\mu d\mu \qquad z_0<z<H \tag{C.2}$$

where $1-C$ is called as characteristic equation and

$$C=\frac{k_{1z}\rho_0-k_z\rho_1}{k_{1z}\rho_0+k_z\rho_1}e^{j2k_zH} \tag{C.3}$$

and

$$k_z=\sqrt{k^2-\mu^2}, \qquad k_{1z}=\sqrt{k_1^2-\mu^2} \tag{C.4}$$

which are the vertical components of the wave numbers in the water and in the bottom, $H_0^{(1)}(\mu r)$ is the zero-order Hankel function of the first kind.

Eq. (C.2) can be solved by Cauchy's theorem. Consider that

$$H_0^{(1)}(\mu r)\approx\left\{\frac{2}{\pi\mu r}\right\}^{1/2} e^{j(\mu r-\frac{\pi}{4})} \qquad \mu r\to\infty \tag{C.5}$$

the closed integration path is chosen on the upper half μ plane with branch cuts at $\mu=\frac{\omega}{c_1}$ and $\mu=\frac{\omega}{c_0}$ as in Fig. C2. Thus Eq. (C.2) is expressed as

$$\psi(r,z) = 2\pi j\sum(\text{residues}) + I_{\text{branch}} \tag{C.6}$$

where

$$\sum(\text{residues})=\sum_{n=1}\frac{\sin(k_{zn}z_0)\sin(k_{zn}z)}{k_{zn}\left[\frac{\partial C}{\partial\mu}\right]_{\mu_n}}H_0^{(1)}(\mu_n r)\mu_n \tag{C.7}$$

where μ_n is the nth residue, and from Eq. (C.4), $k_{zn}=\sqrt{k^2-\mu_n^2}$. Eq. (C.6) indicates that the acoustic field in the water is consist of two parts, the first part is a sum of normal modes, and the second part is known as the lateral wave. The normal modes are determined by the roots of the characteristic equation as

$$1-C = 1-\frac{k_{1zn}\rho_0-k_{zn}\rho_1}{k_{1zn}\rho_0+k_{zn}\rho_1}e^{j2k_{zn}H} = 0 \tag{C.8}$$

There are two kinds of roots in Eq. (C.8), a finite number of real roots and an infinite number of complex roots. The modes corresponding to real roots are called proper mode, the modes corresponding to the complex roots are called improper mode or evanescent mode.

Consider the field far from the source, the lateral wave is less significant [65], the improper modes are also attenuated very quickly, so the main contribution to the field comes from the proper normal modes. Thus only the real roots which satisfies $k<\mu_n<k_1$ needs to be found from Eq. (C.8). Rewriting Eq. (C.8) as

$$\rho_0\sqrt{k^2-k_1^2-k_{zn}^2}\sin(k_{zn}H)+\rho_1 k_{zn}\cos(k_{zn}H)=0 \tag{C.9}$$

It can be seen that the roots of Eq. (C.9) are functions of frequency, sound velocities and densities in the water and in the bottom, and the depth of the water. Provided that all these parameters are known, the roots can be found by numerical method.

When $\mu_n r$ is large, the field is represented by Eqs. (C.5) and (C.7) as

$$\psi(r,z)=2\pi j\sum_{n=1}F_n(r,z)e^{j(\mu_n r-\frac{\pi}{4})} \tag{C.10}$$

where

$$F_n(r,z)=\left\{\frac{2}{\pi\mu_n r}\right\}^{1/2}\frac{\sin(k_{zn}z_0)\sin(k_{zn}z)}{k_{zn}\left[\frac{\partial C}{\partial\mu}\right]_{\mu_n}}\mu_n \tag{C.11}$$

which is the amplitude of the nth normal mode. Eq. (C.10) indicates that for a fixed source, a receiver at a constant depth moving in r direction will receive two different modes interferencing to each other with the maximum values at

$$(\mu_n-\mu_m)r=2l\pi \tag{C.12}$$

where l is an integer. Since μ_n and μ_m are functions of frequency, sound velocities and densities in the water and in the bottom, and the depth of the water, for given sound velocity and density in the water and, density in the bottom and water depth, the interference pattern is determined only by sound velocity in the bottom. According to this point, the sound velocity in the bottom can be found by measuring the sound pressure in r direction and comparing the result with theoretical prediction by Eq. (C.10) or Eq. (C.12).

A measurement was made in a shallow water channel which is just deep enough to sustain the first two modes. The result is shown as the curve 1 in Fig. C3, the parameters used are, frequency f=411kHz, the water depth H=7mm, the source depth z_0=3.3mm, the receiver depth z=2.1mm, the starting range r_s=0.2m, and the final range r_f=0.92m. With the sound velocity in the bottom c_1=1665m/s as obtained by measuring the reflection coefficient mentioned in Sec. 4.10.2, the sound velocity in water c_0=1477m/s as calculated in Sec. 4.10.1, the densities in the water and in the bottom ρ_0=1g/cm^3 and ρ_1=1.9g/cm^3, a theoretically predicted propagation loss against the distance r by Eq. (C.10) with the same parameters as in the measurement is also shown as the curve 2 in Fig.

C3. The interference patterns predicted by Eq. (C.10) and measured agree very well at the places where maximum pressure occurs. It means that the value of the sound velocity used in the theoretical prediction is reasonable, and it confirms the sound velocity obtained in Sec. 4.10.2 is reasonable. But a poor agreement at the amplitudes of the two results is found here. The discrepancy comes from that the bottom absorption is not taken into account in the theoretical model. The sand bottom used in the experiment has a large attenuation coefficient[73], it will have an important contribution to the propagation loss. A modification is needed to deal with this case.

To examine the sensitivity of the interference pattern with respect to the sound velocity in the bottom, taking partial derivative of Eq. (C.12) with respect to c_1, one has

$$\frac{\frac{\partial r}{\partial c_1}}{r}=-\frac{\frac{\partial \mu_n}{\partial c_1}-\frac{\partial \mu_m}{\partial c_1}}{\mu_n-\mu_m} \tag{C.13}$$

where $\frac{\partial \mu_n}{\partial c_1}$ can be obtained by differentiating the characteristic equation in Eq. (C.8) with respect to c_1, which is given as

$$\frac{\partial \mu_n}{\partial c_1}=-\frac{\frac{k_1^2}{c_1\sqrt{\mu_n^2-k_1^2}}}{\mu_n\left(H\frac{\rho_0}{\rho_1}\frac{\mu_n^2-k_1^2}{k_0^2-\mu_n^2}+\frac{1}{\sqrt{\mu_n^2-k_1^2}}+\frac{\sqrt{\mu_n^2-k_1^2}}{k_0^2-\mu_n^2}+\frac{\rho_1}{\rho_0}H\right)} \tag{C.14}$$

Eq. (C.13) gives the relative distance change at the interference maximum with respect to the sound velocity in the bottom. For the given parameters as in Fig. C3, a 1% change of c_1 will cause a 1.5% change in the interference pattern in Eq. (C.12), which is equal to about a quarter cycle at the maximum range in Fig. C3. Comparing the measured and predicted results, the difference is less than a quarter cycle at the maximum range, therefore, the error of the sound velocity in the bottom used in the prediction is about 1%, which justifies the determination of the sound velocity in Sec. 4.10.2.

As noticed in Fig. C3, higher propagation loss is found in the measured result, which comes from the bottom absorption. When the absorption in the bottom is taken into account, the wave number k_1 becomes complex as

$$k_1=k'_1+jk''_1 \tag{C.15}$$

which will result in complex roots k_{zn} in Eq. (C.9). Let $k_{zn}=k'_{zn}+jk''_{zn}$, where k'_{zn} and k''_{zn} are real and imaginary parts of k_{zn}, substitute k_{zn} and Eq. (C.15) into Eq. (C.9), one has

$$\rho_0\sqrt{k^2-k'^2_1-2jk'_1k''_1+k''^2_1-k'^2_{zn}-2jk'_{zn}k''_{zn}+k''^2_{zn}}$$

$$\left[\sin(k'_{zn}H)\cosh(k''_{zn}H)+j\cos(k'_{zn}H)\sinh(k''_{zn}H)\right]$$

$$+\rho_1(k'_{zn}+jk''_{zn})\left[\cos(k'_{zn}H)\cosh(k''_{zn}H)-j\sin(k'_{zn}H)\sinh(k''_{zn}H)\right]=0 \qquad \text{(C.16)}$$

If $k''_1 \ll k'_1$, the imaginay part of k_{zn} must be very small comparing with the real part, *i.e.* $k''_{zn} \ll k'_{zn}$, Eq. (C.16) can be approximated by

$$\rho_0\sqrt{k^2-k'^2_1-k'^2_{zn}}\sin(k'_{zn}H)+\rho_1k'_{zn}\cos(k'_{zn}H)=0 \qquad \text{(C.17a)}$$

$$\rho_0\sqrt{k^2-k'^2_1-k'^2_{zn}}\left[\cos(k'_{zn}H)\sinh(k''_{zn}H)-\sin(k'_{zn}H)\cosh(k''_{zn}H)\frac{k'_1k''_1+k'_{zn}k''_{zn}}{k^2-k'^2_1-k'^2_{zn}}\right]$$

$$+\rho_1\left[k''_{zn}\cos(k'_{zn}H)\cosh(k''_{zn}H)-k'_{zn}\sin(k'_{zn}H)\sinh(k''_{zn}H)\right]=0 \qquad \text{(C.17b)}$$

Eq. (C.17a) is the same as for a non-absorbing bottom case. Solving Eq. (C.17a) by numerical method, the real part of the root k'_{zn} can be found, then put the solution in Eq. (C.17b), therefore the imaginary part of the root k''_{zn} can be also found by numerical method. The horizontal component of the wave number μ_n in the water for the nth mode is derived from Eq. (C.4) as

$$\mu_n=\mu'_n+j\mu''_n=\sqrt{k^2-k_{zn}^2}\approx\sqrt{k^2-k'^2_{zn}}-j\frac{k'_{zn}k''_{zn}}{\sqrt{k^2-k'^2_{zn}}} \qquad \text{(C.18)}$$

From Eqs. (C.17a) and (C.18), it is found as it would be expected, the horizontal propagation velocity is not altered to the first order of the approximation by the presence of a small bottom attenuation and, with the imaginary part μ''_n, the acoustic field is attenuated quicker than in the non-absorbing bottom case.

The acoustic field in a water channel with bottom attenuation can be predicted by Eq. (C.10) with the μ_n in Eq. (C.18). Suppose the attenuation $\alpha_b(f)$ of sound through the sand has the form[73]

$$\alpha_b(f)=k_bf^N \qquad \text{(C.19)}$$

where k_b is the attenuation coefficient in dB/mkHz and f is frequency in kHz. The index N is close to unity. Thus the complex wave number k_1 can be written as

$$k_1=k'_1+jk''_1\approx\frac{\omega}{c_1}+j\frac{k_b f^N}{20\log e} \tag{C.20}$$

For the sand used in the experiment, k_b = 0.47dB/mkHz and N=1, sound velocity c_1=1665m/s, the wave number in the bottom at frequency f = 411kHz is

$$k_1=1538.1+j22.2 \tag{C.21}$$

It can be seen that the imaginary part is far less than the real part. So that the approximations in Eqs. (C.17) are applicable in this case.

In practice, the attenuation in the bottom has a large range variation depending on the type of the bottom, a value between zero and 1dB per wave-length is acceptable. Some comparisons are made with different attenuations in the bottom as shown in Figs. C4, C5, C6 and C7. In Fig. C4 and C5, the same parameters are used as in Fig. C3 except the water depth is H=4.7mm, so only the first mode is sustained in the water. In Fig. C4, the curve 1 is the normalized sound pressure without attenuation, it follows the cylindrical spreading, the curve 2 is the normalized measured result, which indicates the bottom attenuation causes more propagation loss in the water channel. In Fig. C5, the bottom attenuation is taken into account, two values are used, the curve 1 with 0.78dB/λ attenuation in the bottom and the curve 2 with 1dB/λ, the results show a great improvement over the model without attenuation comparing with Fig. C4, comparing with the measured result as the curve 3, 1dB/λ is likely to be a desired value. With the same parameters as in Fig. C3, the normalized sound pressure in the water which sustains only the first two modes in this case are labeled as the curve 1, with 0.78dB/λ and 1dB/λ bottom attenuation in Fig. C6 and C7, the theoretical results are close to the experimental result which are labeled as the curve 2 as seen in the figures. It should be pointed out that the interference patterns with attenuation in the bottom have been changed very little as it can be seen from the figures.

There are still differences between the experimental and theoretical results as shown in Figs. C5, C6 and C7. The propagation loss is still greater in the measured result than the predicted by theoretical model with attenuation in the bottom. The main reason for the discrepancies is the shear wave in the bottom is not taken into account in the theoretical model. Because the bottom is made of sand, it will support a small mount of shear wave[74]. The shear wave velocity is less than the sound velocity in the water, so the incident wave from the water excites shear wave which propagates with a greater angle from the interface down to the bottom can never return to the water again, therefore, more propagation loss is introduced by the shear wave. A simple model can be used to estimate the

propagation loss caused by shear wave in the bottom according to the reflection coefficient of sound wave on the water-bottom interface by assuming no attenuation in both media. Consider two half infinity media, one is liquid and the other one is solid, with a liquid-solid interface, an incident plane wave with a grazing angle α in the upper medium is partly reflected by the interface, and partly transmitted into the lower medium. Since the lower medium can support compressional and shear waves, both waves are excited by the incident wave and propagate in the lower medium as shown in Fig. C8. The reflection coefficient V from liquid-solid interface is given by Brekhovskikh[65]:

$$V=\frac{Z_c\cos^2(2\gamma_1)+Z_s\sin^2(2\gamma_1)-Z}{Z_c\cos^2(2\gamma_1)+Z_s\sin^2(2\gamma_1)+Z} \tag{C.22}$$

where γ_1 is the refraction angle of the shear wave in the solid and, Z, Z_c and Z_s denote respectively the impedances of sound waves in the liquid, and compressional and shear waves in the solid:

$$Z=\frac{\rho_0 c_0}{\cos(90-\alpha)},\quad Z_c=\frac{\rho_1 c_1}{\cos(90-\alpha_1)},\quad Z_s=\frac{\rho_1 b_1}{\cos(\gamma_1)} \tag{C.23}$$

where b_1 is the shear wave velocity. Here, one has $b_1 < c_0 < c_1$. Consider the grazing angle α less than critical angle, $\cos(90-\alpha_1)$ becomes complex and so does Z_c, thus the modular of the reflection coefficient $|V|$ is written as

$$\begin{aligned}|V| &= \left\{\frac{[Z_s\sin^2(2\gamma_1)-Z]^2+|Z_c|^2\cos^4(2\gamma_1)}{[Z_s\sin^2(2\gamma_1)+Z]^2+|Z_c|^2\cos^4(2\gamma_1)}\right\} \\ &= \left\{1-\frac{4ZZ_s\sin^2(2\gamma_1)}{[Z_s\sin^2(2\gamma_1)+Z]^2+|Z_c|^2\cos^4(2\gamma_1)}\right\}\end{aligned} \tag{C.24}$$

It can be seen that although the compressional wave in the solid undergoes totally internal reflection, the amplitude of reflected wave is less than that of incident wave because of the shear wave.

In most cases, the shear wave velocity in sediment is far less then sound velocity in water[74], *i.e.* $b_1 \ll c_0$, therefore γ_1 is a small angle as it can be seen from Eq. (C.23). Substitute $\cos(\gamma_1)=1$ and $\sin(\gamma_1)$ with $\sin(\gamma_1)=\frac{b_1}{c_0}\cos(\alpha)$ into Eq. (C.24), one has

$$|V| = \left\{1-\frac{16Z\cos^2(\alpha)}{c_0[Z^2+|Z_s^2|\cos^4(2\gamma_1)]}\right\} \tag{C.25}$$

It indicates the reflection coefficient V is proportional to the third power of the shear wave velocity b_1 if the condition $b_1 \ll c_0$ is satisfied.

For a certain range r, the propagation loss caused by shear wave in the bottom can be found by multiplying the reflection coefficient as many times as the wave reflected by the bottom along the propagation path. As shown in Fig. C9, the distance Δr corresponding to two adjacent reflections from the bottom can be determined according to the water depth, the displacement of the incident ray as mentioned in Sec. 3.3, then the reflect time is found by dividing the range r with the distance Δr.

In the bottom used in the experiment, the shear wave velocity is an unknown quantity, generally speaking, it is not a constant as in a solid medium according to many investigations about sediments in the past. Hamilton[74] gives some regression equations to predict the shear wave velocities in sediments, which shows the shear wave velocity is a function of the depth in sediments. However, it is reasonable to use a constant shear wave velocity for an estimation of the propagation loss caused by shear wave in sand bottom. Some data are obtained based on the above idea to demonstrate the contribution from the shear wave. Assume the shear wave velocity is 170m/s, which is far less than sound velocity in water, for the given parameters as in Fig. C4, the amplitude of the plane wave is decreased 4% at range r=0.92m, for the given parameters as in Fig. C3, the amplitudes of the first mode and the second mode are decreased 2.5% and 1.4% respectively at range r=0.92m. Taken the attenuations into account, the differences between the measured results and the predicted by Eq. (C.10) become smaller, it is the result as expected.

It is possible to derive a complete analytic solution which includes the bottom attenuation and shear wave. Since it is not the major concern of present subject, no further work is done here.

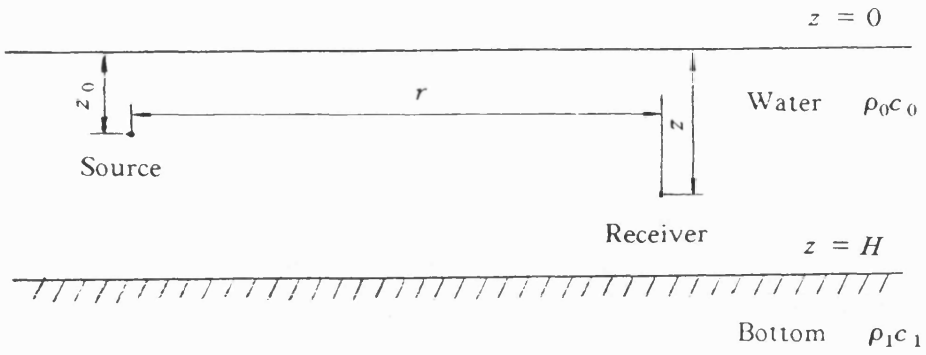

Fig. C1 Geometry of the Pekeris problem.

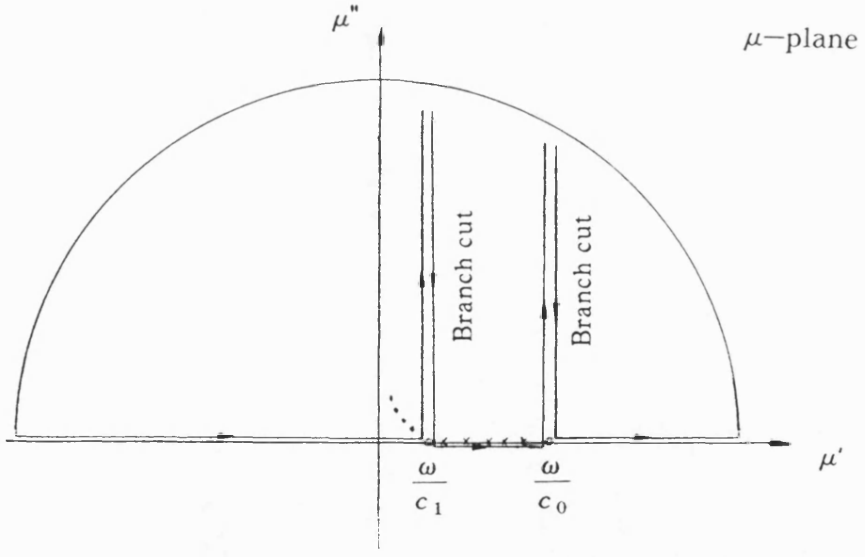

Fig. C2 The integration path for the evaluation of Eq. (C.2) with branch cuts at $\mu = \frac{\omega}{c_1}$ and $\mu = \frac{\omega}{c_0}$. The roots of Eq. (C.8) indicated by the crosses on the real axis are for the proper modes, the complex roots indicated by the dots in the first quadrant are for the improper modes.

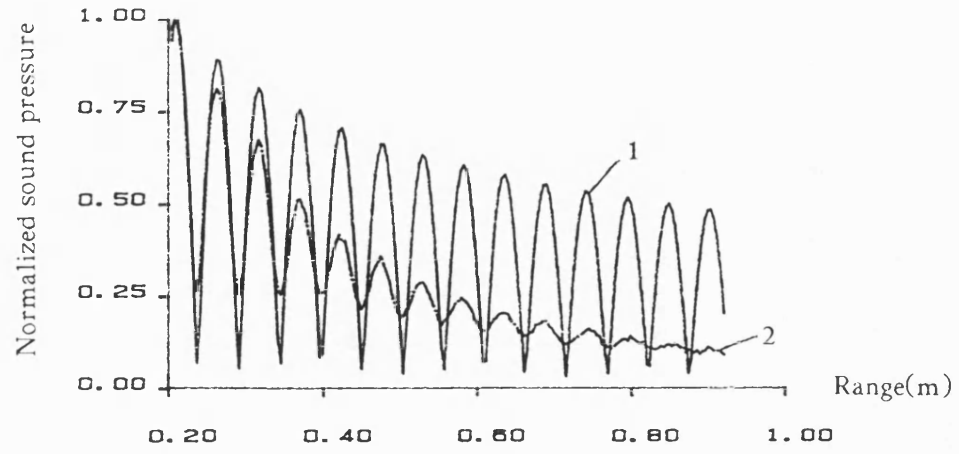

Fig. C3 The normalized sound pressure in the water channel with depth H = 7mm. 1 --- Predicted sound pressure by Eq. (C.10) with sound velocity in the bottom equal to 1665m/s, 2 --- Measured sound pressure.

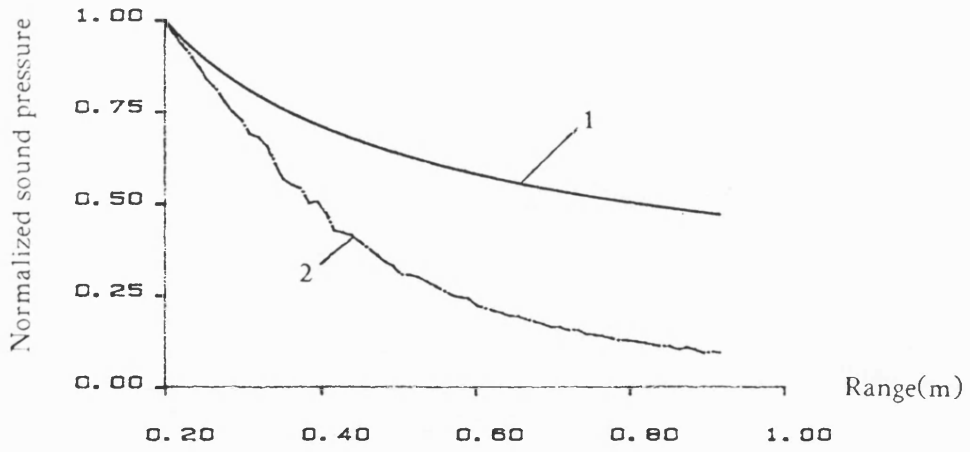

Fig. C4 The normalized sound pressure in the water channel with depth H = 4.7mm. 1 --- Predicted sound pressure by Eq. (C.10) with sound velocity in the bottom equal to 1665m/s, 2 --- Measured sound pressure.

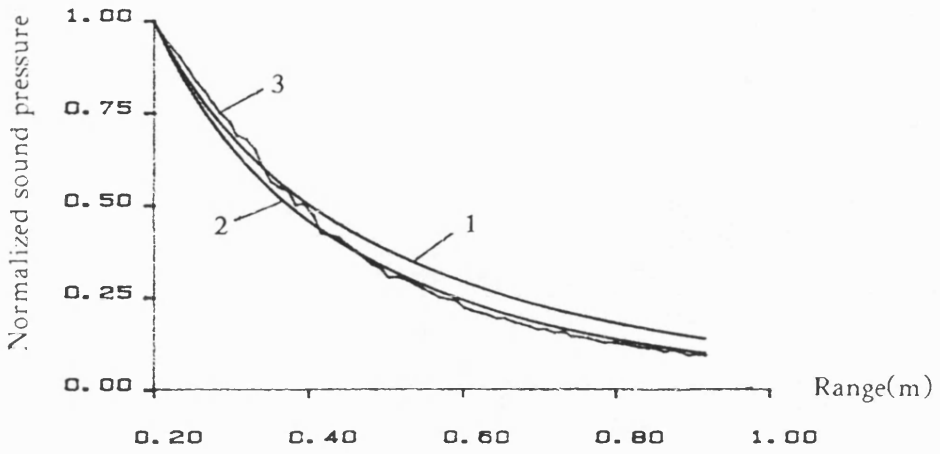

Fig. C5 The normalized sound pressure in the water channel, the parameters are the same as in Fig. C4. 1 --- Predicted sound pressure by Eq. (C.10) with 0.78dB/λ attenuation in the bottom, 2 --- Predicted sound pressure by Eq. (C.10) with 1dB/λ attenuation in the bottom, 3 --- Measured sound pressure.

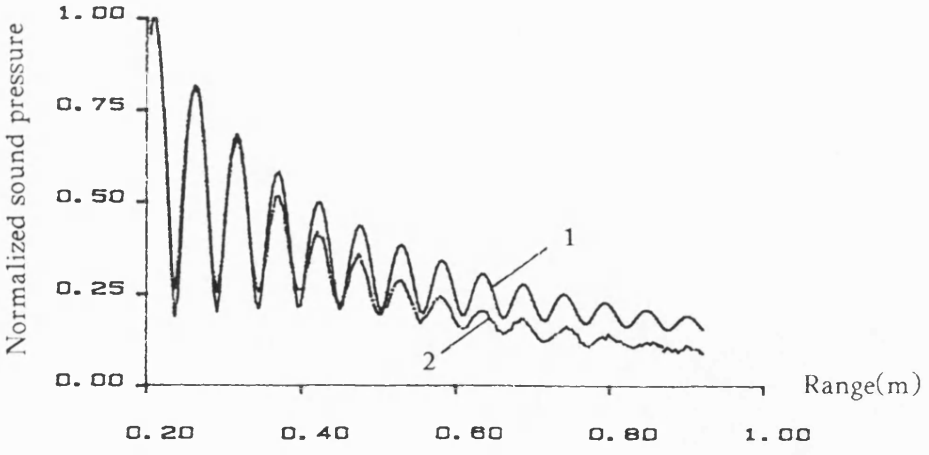

Fig. C6 The normalized sound pressure in the water channel, the parameters are the same as in Fig. C3. 1 --- Predicted sound pressure by Eq. (C.10) with 0.78dB/λ attenuation in the bottom, 2 --- Measured sound pressure.

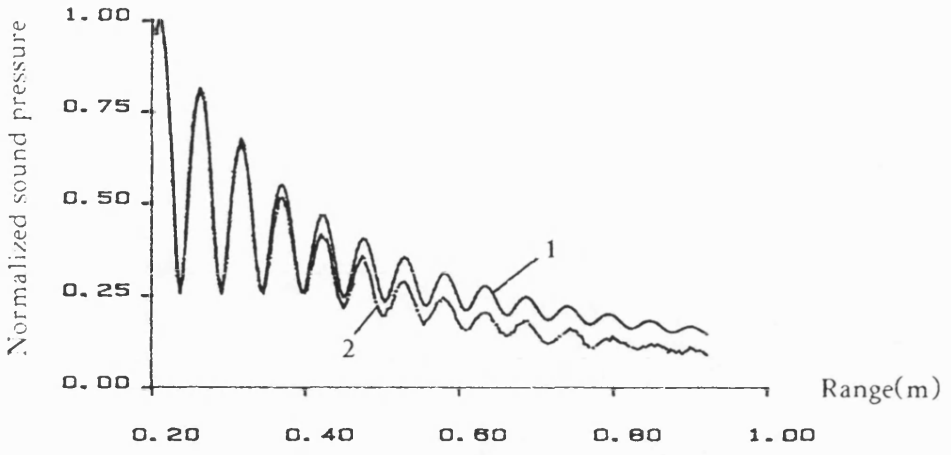

Fig. C7 The normalized sound pressure in the water channel, the parameters are the same as in Fig. C3. 1 --- Predicted sound pressure by Eq. (C.10) with 1dB/λ attenuation in the bottom, 2 --- Measured sound pressure.

List of References

1. A. Sommerfeld, "Mathematische Theorie der Diffraction," Math. Ann. **47**, 317-341 (1896).

2. T. J. Bromwich, "Diffraction of Waves by a Wedge," Proc. Lond. Math. Soc. (Series 2), **14**, 450-463 (1914-1915).

3. H. S. Carslaw, "Diffraction of Waves by a Wedge of Any Angle," Proc. Lond. Math. Soc. (Series 2), **18**, 291-306 (1919-1920).

4. D. E. Weston, "Horizontal Refraction in a Three Dimensional Medium of Variable Stratification," Proc. of the Phys. Soc. **78**, 46-52 (1961).

5. V. K. Kuznetsov, " A New Method for Solving the Problem of the Sound Field in a Fluid Wedge," Sov. Phys. Acoust. **5**, 171-176 (1959).

6. H. Weinberg and R. Burridge, "Horizontal Ray Theory for Ocean Acoustics," J. Acoust. Soc. Am. 55, 63-79 (1974)

7. C. H. Harrison, "Three-Dimensional Ray Paths in Basins, Troughs, and near Seamounts by Use of Ray Invariants," J. Acoust. Soc. Am. **62**, 1382-1388 (1977).

8. C. H. Harrison, "Acoustic Shadow Zones in the Horizontal Plane," J. Acoust. Soc. Am. **65**, 56-61 (1979).

9. D. E. Weston, "Guided Propagation in a Slowly Varying Medium," Proc. Phys. Soc. Lond. 73, 365-384 (1959).

10. C. T. Tindle and G. B. Deane, "Sound Propagation over a Sloping Bottom Using Rays with Beam Displacement," J. Acoust. Soc. Am. **78**, 1366-1374 (1985).

11. T. H. Rousseau, M. J. Jacobson, and W. L. Siegmann, "Ray Transmissions over a Sloping Bottom in a Shallow Water," J. Acoust. Soc. Am. **78**, 1713-1726 (1985).

12. C. L. Pekeris, "Theory of Propagation of Explosive Sound in Shallow Water," Geol. Soc. Am. Memoirs 27, (1948).

13. M. P. Sakharova, "Asymptotic Representation of the Sound Field of a Point Source in a Wedge-Shaped Region," Sov. Phys. Acoust. **5**, 214-219 (1959).

14. A. Sommerfeld (F. Frank and R. Mises), "Differential and Integral Equations of Mathematical Physics," [Russian translation] (ONTI, 1937), Chapt.20.

15. D. L. Bradley, "The Propagation of Sound in a Wedge-Shaped Shallow Water Duct," Ph.D. thesis (Catholic Univ. of America, Washington, DC, 1970).

16. D. L. Bradley and A. A. Hudimac, "The Propagation of Sound in a Wedge-Shaped Shallow Water Duct," Naval Ordinance Laboratory, Tech. rep. NOLTR 70-325 (November 1970).

17. M. J. Buckingham, "Acoustic Propagation in a Wedge-Shaped Ocean with Perfectly Reflecting Boundaries," in *Proceedings of the NATO Advanced Research Workshop on Hybrid Formulation of Wave Propagation and Scattering*, edited by L. B. Felsen, IAFE, Castel, Gandolpho, Rome, Italy, 30 August-3 September 1983 (Nijhoff, Dordrecht, 1984), pp. 77-105; and NRL rep. 8793 (March 1984).

18. D. R. Delbalzo, J. E. Matthews, J. V. Soileau, and C. Feuillade, "Acoustic Propagation over a Large-Scale Linear Ocean Slopes," Proc. of a SACLANT ASW Research Center symposium, San Terenzo di lerici, La Spezia, Italy, 10-14 June, 1985.

19. V. K. Kuznetsov, "Refraction of Normal Waves at a Wedge Lying on a Half-Space," Vestnik, Moscow Univ., Ser. Fiz. -Astron., No. 3, 293-300 (1972)

20. R. K .Eby, A. O. Williams, Jr., R. P. Ryan, and P. Tamarkin, "Study of Acoustic Propagation in a Two-Layered Model," J. Acoust. Soc. Am **32**, 88-99 (1960).

21. A. D. Pierce, "Extension of the Method of Normal Modes to Sound Propagation in an Almost Stratified Medium," J. Acoust. Soc. Am. **37**, 19-27 (1965).

22. D. M. Milder, "Ray and Wave Invariants for SOFAR Channel Propagation," J. Acoust. Soc. Am. **46**, 1259-1263 (1969).

23. R. D. Graves, A. Nagl, and H. Überall," Range-Dependent Normal Modes in Underwater Sound Propagation: Application to the Wedge-shaped Ocean," J. Acoust. Soc. Am. **58** 1171-1177 (1975).

24. S. T. McDaniel, "Coupled Power Equations for Cylindrically Spreading Waves," J. Acoust. Soc. Am. **60**, 1285-1289 (1976).

25. S. T. McDaniel, "Mode Conversion in Shallow-Water Sound Propagation," J. Acoust. Soc. Am. **62**, 320-325 (1977).

26. F. S. Chwieroth, A. Nagl, and H. Überall, "Mode Coupling in a Sound Channel with Range-Dependent Parabolic Velocity Profile," J. Acoust. Soc. Am. **64**, 1105-1112 (1978).

27. A. Nagl, H. Überall, A. J. Haug, and G. L. Zarur, "Adiabatic Mode Theory of Underwater Sound Propagation in a Range-Dependent Environment," J. Acoust. Soc. Am. **63**, 739-749 (1978).

28. R. A. Koch, S. R. Rutherford, and S. G. Payne, "Slope Propagation: Mechanisms and Parameter Sensitivities," J. Acoust. Soc. Am **74**, 210-218 (1983).

29. R. A. Koch, "Underwater Acoustic Propagation Dependence on Sediment Type for a Sloping Bottom," in Conference proceedings *Acoustics and the Sea-Bed*, edited by N. G. Pace, 1983, pp. 261-269.

30. C. T. Tindle, H. Hobaek, and T. G. Muir, "Downslope Propagation of Normal Modes in a Shallow Water Wedge," J. Acoust. Soc. Am. **81**, 275-286 (1987).

31. C. H. Tindle, H. Hobaek, and T. G. Muir, "Normal Mode Filtering for Downslope Propagation in a Shallow Water Wedge," J. Acoust. Soc. Am. **81**, 287-294 (1987).

32. H. Hobaek and E. K. Westwood, "Measurements of upslope wave-front curvature in a sand-bottom wedge," J. Acoust. Soc. Am. **84**, 1787-1790 (1988).

33. K. E. Gilbert, R. B. Evans, S. A. Chin-Bing, D. White, W. A. Kuperman, "Some new models for sound propagation in bottom-limited ocean environments," in *Proceedings of the Institute of Acoustics Underwater Acoustics Group Conference on Acoustics and the Sea-Bed*, edited by N. G. Pace, Bath University, UK, 6-8 April 1983, pp. 243-250.

34. J. R. Wait and P. K. Spies, "On the calculation of mode conversion at a graded height change in the earth-ionosphere waveguide at VLF," *Radio Science* **3**, 787-791 (1968).

35. F. D. Tappert, "The parabolic Approximation Method," in *Wave propagation and Underwater Acoustics*, edited by J. B. Keller and J. S. Papadakis(Springer, New York 1977).

36. F. B. Jensen and W. A. Kuperman, "Sound Propagation in a Wedge-Shaped Ocean with a Penetrable Bottom," J. Acoust. Soc. Am. **67**, 1564-1566 (1980).

37. E. Topuz and L. B. Felsen, "Intrinsic Modes: Numerical Implementation in a Wedge-Shaped Ocean," J. Acoust. Soc. Am. **78**, 1735-1745 (1985).

38. A. D. Pierce, " Augmented Adiabatic Mode Theory for Upslope Propagation from a Point Source in Variable Depth Shallow Water Overlying a Fluid Bottom, " J. Acoust. Soc. Am. **74**, 1837-1847 (1983).

39. A. Kamel and L. B. Felsen, "Spectral Theory of Sound Propagation in an Ocean Channel with Weakly Sloping Bottom," J. Acoust. Soc. Am. **73**, 1120-1130 (1983).

40. J. M. Arnold and L. B. Felsen, "Rays and Local Modes in a Wedge-Shaped Ocean," J. Acoust. Soc. Am. **73**, 1105-1119 (1983).

41. S. T. McDaniel, "Propagation of Normal Mode in the Parabolic Approximation," J. Acoust. Soc. Am. **57**, 307-311 (1975).

42. D. Lee and K. E. Gilbert, "Recent Progress in Modeling Bottom-Interacting Sound Propagation with Parabolic Equations," in *OCEANS 82 Conference Record*, Washington, D. C., Sept. 1982, PP. 172-177.

43. D. J. Thomson and N. R. Chapman, "A Wide-Angle Split-Step Algorithm for the Parabolic Equation," J. Acoust. Soc. Am. **74**, 1948-1954 (1983).

44. G. Botseas, D. Lee, and K. E. Gilbert, "IFD: Wide Angle Capability," NUSC tech. rep. 6905 (1983).

45. S. E. Dosso and N. R. Chapman, "Measurement and Modeling of Downslope Acoustic Propagation Loss over a Continental Slope, " J. Acoust. Soc. Am. **81**, 258-268 (1987).

46. W. L. Siegmann, G. A. Kriegmann, and D. Lee, "A Wide-Angle Three-Dimensional Parabolic Wave Equation," J. Acoust. Soc. Am. **78**, 659-664 (1985).

47. J. S. Perkins and R. N. Baer, "An Approximation to the Three-Dimensional Parabolic-Equation Method for Acoustic Propagation," J. Acoust. Soc. Am. **72**, 515-522 (1982).

48. A. D. Pierce, "Simplified Three-Dimensional Parabolic Equation Underwater Sound Propagation Algorithm Incorporating Horizontal Refraction and Focusing Effects," J. Acoust. Soc. Am. Suppl. 1 **71**, S65 (1982).

49. M. H. Schultz, D. Lee, and K. R. Jackson,"Application of the Yale Sparse Technique to Solve the 3-Dimensional Parabolic Wave Equation," in *Recent Progress in the Development and Appication of the Parabilic Equation*, edited by P. D. Scully-Power and D. Lee (Naval Underwater Systems Center, New London, CT, 1984), TD7145.

50. R. N. Baer, "Propagation Through a Three-Dimensional Eddy Including Effect on a Array," J. Acoust. Soc. Am. **69**, 70-75 (1981).

51. M. J. Buckingham, "Acoustic Propagation in a Wedge-Shaped Ocean," The A. B. Wood Memorial Lecture, *Proceedings of the Institute of Acoustics Underwater Acoustics Group Conference on Acoustics and the Sea-Bed*, edited by N. G. Pace, Bath University, UK, 6-8 April 1983, pp. 251-259.

52. M. J. Buckingham, "Theory of Three-dimensional Acoustic Propagation in a Wedgelike Ocean with a Penetrable Bottom," J. Acoust. Soc. Am. **82**, 198-210 (1987).

53. Yih-Hsing Pao, Franz Ziegler, and Yi-Sun Wang, "Acoustic waves generated by a point source in a sloping fluid layer," J. Acoust. Soc. Am. **85**, 1414-1426 (1989).

54. Evan K. Westwood, "Complex ray methods for acoustic interaction at a fluid-fluid interface," J. Acoust. Soc. Am. **85**, 1872-1884 (1989).

55. Evan K. Westwood, "Ray methods for flat and sloping shallow-water waveguides," J. Acoust. Soc. Am. **85**, 1885-1894 (1989).

56. H. Schmidt and F. B. Jensen, "A full wave solution for propagation in multilayered viscoelastic media with application to Gaussian beam reflection at fluid-solid interfaces," J. Acoust. Soc. Am. **77**, 813-825 (1985).

57. F. B. Jensen and C. M. Ferla, "Numerical solutions of range-dependent benchmark problems in ocean acoustics," SACLANT Undersea Research Centre Report SR-141, September 1988.

58. A. B. Wood, "Model Experiments on Sound Propagation in Shallow Seas," J. Acoust. Soc. Am. **31**, 1213-1235 (1959).

59. V. K. Kuznetsov, "Emergence of Normal Modes Propagating in a Wedge on a Half-Space from the Former into the Latter," Sov. Phys. Acoust. **19**, (3), 241-245 (1973).

60. J. A. Borchardt, "Measurement of the Acoustic Pressure Everywhere over a Modeled Continental Slope," M. S. Thesis, Naval Postgraduate School, Monterey, CA, Dec. 1985.

61. A. B. Coppens, *Personal Communication,* Naval Postgraduate School, Monterey, CA, 1984.

62. R. Doolittle, A. Tolstoy, and M. Buckingham, "Experimental Confirmation of Horizontal Refraction of Sound Propagation in a Wedge-Like Ocean," Proceedings of a SACLANT AWS Research Center Symposium, San Terenzo di Lerici, La Spezia,Italy. pp. 169-178 (1985).

63. R. Doolittle, A. Tolstoy, and M. Buckingham, "Experimental Confirmation of Horizontal Refraction of CW Acoustic Radiation from a Point Source in a Wedge-shaped Ocean Environment," J. Acoust. Soc. Am. **83**, 2117-2125 (1988).

64. S. A. L. Glegg and J. R. Yoon, "Model Experiments for 3-Dimensional Propagation Characteristics in a Wedge-Shaped Ocean," ASA Meeting, Miami, 16-20 November 1987.

65. L. M. Brekhovskikh, *Waves in Layered Media*, Academic Press, Inc., (1960). New York.

66. D. L. Bell and W. J. Porter, "Remote Sediment Classification Potential of Reflected Acoustic Signals," *Physics of Sound in Marine Sediments*, edited by L. Hampton, pp. 319-355 (1974). New York: Plenum Press.

67. C. Chester, B. Friedman, and F. Ursell, "An extension of the method of steepest descents," Proc. of Cambridge Phil. Soc. **53** (1957), pp 599-611.

68. L. B. Felsen and N. Marcuvitz, *Radiation* and *Scattering of Waves*, Prentice-Hall, Englewood Cliffs, NJ, 1973.

69. A. Tolstoy, R. Doolittle, and B. Decina, "Exact but Computationally Intensive Prediction for CW Point Source in an Ideal Wedge," *COMPUTATIONAL ACOUSTICS: Algorithms* and *Applications*, edited by D. Lee, R. L. Sternbery, and M. H. Schultz, Elsevier Science Publishers B. V. (North-Holland), IMACS, 1988, pp. 199-207.

70. W. D. Wilson, "Equation for the speed of sound in sea water," J. Acoust. Soc. Am. **32**, 1357 (1960).

71. E. D. Hamilton, "Sound Velocity and Related Properties of Marine Sediments, North Pacific," Journal of Geophysical Research **75**, 4423-4446 (1970).

72. T. Akal, "Acoustical Characteristics of the Sea Floor: Experimental Techniques and Some Examples from Mediterranean Sea," *Physics of Sound in Marine Sediments*, edited by L. Hampton, pp. 447-480 (1974). New York: Plenum Press.

73. P. R. Thomas and N. G. Pace, "Broadband measurements of acoustic attenuation in water-saturated sands," ULTRASONICS pp. 13-17. January 1980.

74. E. D. Hamilton, "Geoacoustic modeling of the sea floor," J. Acoust. Soc. Am. **68**, 1313-1340 (1980).